NASA-CR-161677

AUG 0 1981

NOV 0 1 1983

Dual Nozzle Aerodynamic And Cooling Analysis Study

Contract NAS 8-33553
Final Report 33553-F
27 February 1981

Prepared For:
National Aeronautics And Space Administration
George C. Marshall Space Flight Center
Marshall Space Flight Center, Alabama 35812

By:
G. M. Meagher

Property
AEDC
F40600-81-C-0004

PROPERTY OF U.S. AIR FORCE
AEDC TECHNICAL LIBRARY
ARNOLD AFB, TN 37389

Aerojet
Liquid Rocket
Company

1. Report No.	2. Government Accession No.	3. Recipient's Catalog No.
33553F		

4. Title and Subtitle	5. Report Date
Dual Nozzle Aerodynamic and Cooling Analysis Study	27 February 1981
	6. Performing Organization Code

7. Author(s)	8. Performing Organization Report No.
G. M. Meagher	
	10. Work Unit No.

9. Performing Organization Name and Address	11. Contract or Grant No.
Aerojet Liquid Rocket Company P.O. Box 13222 Sacramento, California 95813	NAS 8-33553
	13. Type of Report and Period Covered
12. Sponsoring Agency Name and Address	Contractor Report, Final
National Aeronautics and Space Administration Washington, D.C. 20546	14. Sponsoring Agency Code

15. Supplementary Notes

Project Manager, F. Braam, Propulsion Division
NASA-Marshall Space Flight Center
Marshall Space Flight Center, Alabama 35812

16. Abstract

During this study, analytical models to predict performance and operating characteristics of dual-nozzle concepts have been developed and improved. Aerodynamic models are now available to define flow characteristics and bleed requirements for both the dual-throat and dual-expander concepts. Advanced analytical techniques were utilized to provide quantitative estimates of the bleed flow, boundary layer, and shock effects within dual-nozzle engines. Thermal analyses were performed to define cooling requirements for baseline configurations, and special studies of unique dual-nozzle cooling problems defined feasible means of achieving adequate cooling.

As a result, analytical models for the dual-throat concept are now in place which can be used in conjunction with a hot-fire experimental verification program to define the performance capabilities and design characteristics of this advanced engine concept. Though less developed than those for the dual throat, and though they have not been substantiated with empirical aerodynamic correlations, similar analysis techniques for the dual-expander concept are now available. A summary of these results is contained in the following paragraphs, and the technical details are provided in the technical discussion of this report.

17. Key Words (Suggested by Author(s))	18. Distribution Statement
	Unlimited

19. Security Classif. (of this report)	20. Security Classif. (of this page)	21. No. of Pages	22. Price*
Unclassified	Unclassified	249	

* For sale by the National Technical Information Service, Springfield, Virginia 22161

FOREWORD

The work described herein was performed at the Aerojet Liquid Rocket Company under NASA Contract NAS 8-33553, with Mr. Fred Braam, NASA-Marshall Space Flight Center, as Project Manager. The ALRC Program Manager was Mr. Jeffery W. Salmon, and the Project Engineer was Mr. Gregory M. Meagher.

The technical period of performance for this study was from 9 July 1979 to 31 October 1980. The overall objective of this study was to upgrade performance and heat transfer analysis techniques for the dual-throat and dual-expander combustion chamber concepts.

The author wishes to acknowledge the efforts of the following personnel for their significant contributions:

Dick Ewen, ALRC	Gary Nickerson, SEA Inc.
Jerry Pieper, ALRC	Irwin Alber, Consultant
Jim Duey, ALRC	Joe Hoffman, Purdue University

This report presents the Summary, Section I - Introduction, Section II - Conclusions and Recommendations, and Sections III, IV, V and VI - Technical Discussion.

TABLE OF CONTENTS

		Page
Summary		1
I.	Introduction	8
II.	Conclusions And Recommendations	15
III.	Dual Throat Aerodynamic Model and Performance Prediction Improvement	18
	A. Literature Survey	19
	B. Aerodynamic Bleed Flow Model	20
	1. Shear Layer Modeling	24
	2. Aerodynamic Bleed Flow Model Computer Program	37
	3. Model Calibration	41
	4. Parametric Analysis	46
	C. Mode II Boundary Layer Loss Verification	58
	1. Previous Simplified Approach	58
	2. BLIMP Analysis	61
	D. Shock Model	66
	E. Secondary Nozzle Contour Optimization	81
	1. Design Method	86
	2. Optimization Analysis Results	87
	F. Dual Throat Performance	91
	1. Baseline Design Performance	92
	2. Comparison of Simplified Performance Parametrics	92
	G. Recommendations	98
	1. Design Approach	98
	2. Test Programs	100
	3. Model Improvements	100
IV.	Dual Expander Analysis	103
	A. Preliminary Geometric Analysis	103
	B. Dual Expander Aerodynamic Bleed Flow Model	121
	1. Model Development	121
	2. Model Calibration	128

TABLE OF CONTENTS (cont.)

		Page
	C. Dual Expander Flow Field Analysis	131
	1. Calculations for Mode II Operation	134
	2. Performance Calculations for Mode I Operation	147
	D. Recommendations	150
	1. Mode II Performance Prediction Program	150
	2. Flow Model	152
	3. Overall Numerical Algorithm	152
V.	Preliminary Heat Transfer Analysis	154
	A. Special Studies	155
	1. Lip Regions	155
	2. Secondary Throat Analysis for Dual Throat Mode II	162
	B. Channel Design Procedures	167
	C. Dual Throat	171
	1. Baseline Design	171
	2. Parametric Study	179
	D. Dual Expander	182
	1. Baseline Designs	182
	2. Parametric Study	193
	E. Summary of Results	193
VI.	Hot-Fire Data Analysis	198
	A. Pre-Test Analysis	198
	B. Test Results	202
	1. Data Evaluation	202
	2. Model Comparison	208
	3. Engine Performance	211
References		215
Appendices:		
A	Program Input, Aerodynamic Model	218
B	Derivation of Dual Expander Equations	230
C	Input Description, Dual Expander Shear Layer Model	241

LIST OF TABLES

Table No.		Page
III-I	Summary of Literature Search - Aerojet Dual Nozzle Analysis	21
III-II	Effect of Bleed Flow Properties on Required Bleed Flowrate	47
III-III	Dual Throat Baseline Geometry	49
III-IV	Variation in Nozzle Spacing	51
III-V	Variation in Primary Nozzle Area Ratio	53
III-VI	Variation in Primary Nozzle Size	56
III-VII	Bleed Flow Thermodynamic Properties Effects	57
III-VIII	Comparison of Boundary Layer Loss Calculations	63
III-IX	Comparison of Nozzle Divergency Efficiencies for Two Types of Optimum Nozzle Contours	91
III-X	Dual Throat Baseline Operating Point	93
III-XI	Comparison of the Dual Throat and Conventional Gas-Generator Engine Concepts	94
IV-I	Dual Expander Cases Analyzed	104
IV-II	Parametric Analysis Results	105
IV-III	Dual Expander Geometric Influences	122
IV-IV	Base Flow Study, Summary of Results	135
IV-V	Mode II Operating Conditions	136
IV-VI	Summary of Results, Mode II Performance Prediction	144
IV-VII	Mode I Operating Conditions	147
V-I	Baseline Channel Layout Summary	175
V-II	Dual Throat Baseline Cooling Circuits, Interface Area Ratio = 1.58	181
V-III	Dual Throat Parametric Design Summary	183
V-IV	Dual Expander Baseline Cooling Circuits, Interface Area Ratio = 2.34	190
V-V	Dual Expander Baseline with Oxygen-Cooled Secondary Interface Area Ratio = 1.66	191
V-VI	Dual Expander Parametric Study Design Points	194
V-VII	Dual Expander Parametric Design Summary	195

LIST OF TABLES (cont.)

Table No.		Page
VI-I	Dual Throat Thruster MSFC In-House Test Summary	200
VI-II	Hot-Fire Tests Performance Measurement	212
VI-III	Performance Comparison of Hot-Fire Tests/ Aerodynamic Model	214

LIST OF FIGURES

Figure No.		Page
I-1	Dual Throat Thrust Chamber Configuration and Flow Fields for Modes I and II	11
I-2	Dual Expander Modes of Operation	12
III-1	Mode II, Sustainer Mode Operation	22
III-2	Shear Layer Streamlines and Velocity Profile	25
III-3	The "d" and "j" Streamlines Within the Shear Layer	25
III-4	Flow Chart For the Aerodynamic Bleed Flow Model Computer Program	38
III-5	Model Improvements Allowed More Accurate Predictions for Smaller Nozzle Spacing	43
III-6	Model Predictions Became Less Accurate With Increasing Nozzle Spacing	43
III-7	Model Accuracy Improved By Changing Plume Scaling Factor	43
III-8	Nozzle Spacing Influence on Plume Scaling Factor	44
III-9	Base Pressure Versus Bleed Flow	45
III-10	Dual Throat Baseline Configuration	50
III-11	Effect of Nozzle Spacing For 0% W_s/W_p	52
III-12	Effect of Varying Primary Nozzle Area Ratio on Plume Attachment for 0% W_s/W_p	55
III-13	Effect of Varying Primary Nozzle Size on Plume Attachment for 0% W_s/W_p, $\varepsilon = 2.71$	57
III-14	NAS 8-32666 Boundary Layer Loss Methodology	60
III-15	Effect of Nozzle Inlet Conditions on the Momentum Thickness for a Cooled Nozzle Wall	65
III-16	Conventional Nozzle Upstream Velocity Vector Plot	69
III-17	Conventional Nozzle Downstream Velocity Vector Plot	70
III-18	Conventional Nozzle Upstream Mach Number Plot	71
III-19	Conventional Nozzle Downstream Mach Number Plot	72
III-20	Conventional Nozzle Upstream Pressure Plot	73
III-21	Conventional Nozzle Downstream Pressure Plot	74
III-22	Dual Throat Baseline Upstream Velocity Vector Plot	75

LIST OF FIGURES (cont.)

Figure No.		Page
III-23	Dual Throat Baseline Downstream Velocity Vector Plot	76
III-24	Dual Throat Baseline Upstream Mach Number Plot	77
III-25	Dual Throat Baseline Downstream Mach Number Plot	78
III-26	Dual Throat Baseline Upstream Pressure Plot	79
III-27	Dual Throat Baseline Downstream Pressure Plot	80
III-28	Dual Throat Baseline Zero Bleed Flow Velocity Vector Plot	82
III-29	Dual Throat Baseline Zero Bleed Flow Pressure Profile	83
III-30	Dual Throat Baseline Zero Bleed Flow Mach Number Profile	84
III-31	Dual Throat Baseline Zero Bleed Flow Wall Pressure Profile	85
III-32	Secondary Nozzle Optimization Program Procedure	88
III-33	Dual Throat Secondary Nozzle Contour Comparison	90
III-34	Mode I Delivered I_{sp} Versus Thrust Ratio	96
III-35	Dual Throat Engine Throat Radius As A Function of Thrust Ratio	97
III-36	Percent Bleed Flow Versus Primary Nozzle Area Ratio	99
III-37	ISOBARS, Characteristic Lines and Flow Field Regions	101
IV-1	Engine Efficiency Versus Thrust Ratio	107
IV-2	Engine I_{sp} Versus Thrust Ratio	108
IV-3	Engine Area Ratio Versus Thrust Ratio	109
IV-4	Throat Area Versus Thrust	110
IV-5	Engine I_{sp} Versus Thrust	111
IV-6	Mode I Nozzle Size Versus Chamber Pressure Ratio	112
IV-7	Throat Area Versus Chamber Pressure	113
IV-8	Engine I_{sp} Versus Chamber Pressure	114
IV-9	Nozzle Area Ratio Versus Exit Pressure	115
IV-10	Engine I_{sp} Versus Area Ratio	116
IV-11	Dual Expander Nomenclature	118
IV-12	Dual Expander Shear Layer Model	124
IV-13	Dual Expander Aerodynamic Model Geometry	125

LIST OF FIGURES (cont.)

Figure No.		Page
IV-14	Calculational Procedure for the Dual Expander Aerodynamic Model	126
IV-15	Axisymmetric Supersonic Base Pressure From Modified Conical Pressure Rise Method	130
IV-16	Trailing Wake Radius Versus Mach Number for $\delta = 1.4$	130
IV-17	Dual Expander Modes I and II Operation	132
IV-18	Dual Expander Thrust Chamber Geometry	138
IV-19	Annular Nozzle Throat Section Mach No. Contours	138
IV-20	Annular Nozzle Downstream Section Mach No. Contours	140
IV-21	Region IV Upstream Mach No. Contours, Case 2, Zero Truncation, 0% Bleed	142
IV-22	Region IV Downstream Mach No. Contours, Case 2, Zero Truncation, 0% Bleed	143
IV-23	Inner and Outer Wall Pressures (Predicted)	149
IV-24	Dual Expander Geometry and Flow Field Model	151
V-1	Typical Lip Region Heat Flux Variation	156
V-2	Dual Throat Lip Region Design	157
V-3	Dual Expander Design	158
V-4	Lip Region 3-D Thermal Model	160
V-5	Dual Throat Lip Region Wall Temperatures	161
V-6	Primary Plume Impingement In Secondary Throat Region With No Bleed Flow	164
V-7	Freestream Velocity Distribution Mode II Secondary Throat Region With No Bleed Flow	165
V-8	Cycle Life/Creep Wall Temperature Criteria	169
V-9	Schematic of Wall Conduction Model	170
V-10	Zr-Cu Chamber Wall Strength Criteria	172
V-11	Dual Throat Coolant Flow Schematic	173
V-12	Dual Throat Baseline Cooling Circuit Pressure Drop Characteristics	178
V-13	Comparison of Secondary Throat Region Heat Fluxes	180

LIST OF FIGURES (cont.)

Figure No.		Page
V-14	Dual Throat Parameter Study Effect of Chamber Pressure on Coolant Pressure Drop and Mach Number	184
V-15	Dual Throat Parameter Study Effect of Thrust Split on Coolant Pressure Drop and Mach Number	185
V-16	Dual Expander Coolant Flow Schematic	186
V-17	Dual Expander Baseline Cooling Circuit Pressure Drop Characteristics	188
V-18	Dual Expander Transpiration Cooling	192
VI-1	Existing Dual Throat Test Article	199
VI-2	Predicted Trend in Bleed Flowrates Versus Nozzle Spacing	201
VI-3	Wall Pressure Profile, Nozzle Spacing = 5.062, GH_2 Bleed Flow	203
VI-4	Wall Pressure Profile, Nozzle Spacing = 3.979, GH_2 Bleed Flow	204
VI-5	Wall Pressure Profile, Nozzle Spacing = 2.897, GH_2 Bleed Flow	205
VI-6	Wall Pressure Profile, Nozzle Spacing = 5.062, GN_2 Bleed Flow	206
VI-7	Comparison of the Hot-Fire and Cold-Flow Pressure Profiles	207
VI-8	Experimental Results Have Verified Aerodynamic Model Predictions	209
VI-9	Hot-Fire Results Verified Nozzle Spacing Trends Correlated from Cold-Flow Tests	210

NOMENCLATURE

ALPHABETIC SYMBOL	DEFINITION
A^*	Nozzle throat area
C	Crocco number
C_p	Specific heat at constant pressure
C_v	Specific heat at constant volume
H	Enthalpy
I	Integral of shear layer properties
ℓ	Length of shear layer measured along its center line from its point of origin
M	Mach number
N	Nash recompression factor
P	Pressure
$\hat{P}$	Pressure on the downstream side of an oblique shock
r_w	Radial distance measured from the primary flow center line to the shear layer center line
R	Gas constant
$\tilde{R}$	Universal gas constant
T	Temperature
U or u	Velocity
W	Mass flow rate
y	Distance measured normal to the shear layer center line
Y	Species mass fraction

NOMENCLATURE (cont.)

GREEK SYMBOL

α	Ratio of primary to secondary species mass fractions in the recirculation region
γ	Ratio of specific heats
η	Nondimensional length measured normal to the shear layer center line
Λ	Enthalpy ratio
υ	Prandtl-Meyer turning angle
$\P$	3.14159265
ρ	Density
σ	Shape factor for the shear layer
ϕ	Nondimensional velocity ratio

SUBSCRIPTS

b	At the invisid jet boundary
bleed	For the bleed flow at point of entry into the shear layer
d	At dividing streamline
e	At the primary nozzle exit plane
j	At the jet boundary streamline
p	For the primary stream
r	In the recirculation region
s	For the secondary stream
o	At stagnation
∞	At a great distance

SUMMARY

A. STUDY OBJECTIVES AND SCOPE

The objective of this study was to expand and extend the analysis models and parametric studies previously performed for both the dual-throat and dual-expander engine concepts. This was accomplished within five basic tasks, including (1) improvements to the existing dual-throat aerodynamic and performance prediction computer model, (2) preliminary geometric analysis of the dual-expander concept, (3) preliminary flow field analyses of the dual-expander concept, (4) further preliminary heat transfer analysis of both concepts, and (5) engineering analysis of data from the NASA/MSFC hot-fire testing of a dual-throat thruster model thrust chamber assembly. As a result of this effort, a quantitative comparison of the aerodynamic, performance, and thermal design characteristics between the two dual-nozzle concepts can be derived.

B. STUDY RESULTS

During this study, analytical models to predict performance and operating characteristics of dual-nozzle concepts have been developed and improved. Aerodynamic models are now available to define flow characteristics and bleed requirements for both dual-throat and dual-expander concepts. Advanced analytical techniques were utlized to provide quantitative estimates of the bleed flow, boundary layer, and shock effects within dual-nozzle engines. Thermal analyses were performed to define cooling requirements for baseline configurations, and special studies of unique dual-nozzle cooling problems (i.e., lip and secondary throat regions) defined feasible means of achieving adequate cooling. Similar analysis techniques for the dual-expander concept are now available. However, these techniques are, in general, less developed than those for the dual-throat concept and have not been substantiated with empirical aerodynamic correla-

tions. A summary of these results is contained in the following paragraphs, and the technical details are provided in the technical discussion of this report.

The dual-throat aerodynamic model has been expanded to include effects not considered prior to the subject contract. Previously, the aerodynamic model was limited in its ability to predict the base pressure that developed within the exterior thrust chamber. As presented in Section III,B, the aerodynamic model computer program has been modified to include a procedure for predicting base pressure. This model assumes that the base pressure is controlled by the loss in total pressure which occurs when the shear layer flow passes through an oblique shock during attachment at the exterior thruster wall. An empirical constant, called the Nash factor, is used to calibrate the model with experimental data. A further development of the computer program has been to provide for dissimilar exhaust gases to be used for the interior and exterior (bleed) flow. Each stream is allowed to possess a given constant value for specific heat at constant pressure, molecular weight, and total temperature.

As a result, the aerodynamic model has been generalized so that it can be applied to studies of various dual-throat concepts, including tripropellant earth-to-orbit engines and bipropellant engine applications such as the Orbit Transfer Vehicle Engine (OTV-E) and liquid oxygen/hydrocarbon boosters for uprating the Space Shuttle. This model was also used to define test conditions and predictions in support of the MSFC hot-fire testing of a dual-throat thruster model. Subsequent analysis of these test results, as discussed in Section VI, has shown excellent agreement between model predictions and test measurements.

Summary (cont.)

The capability to optimize the dual-throat engine performance was enhanced through the development of a computer program that allows the design of an optimum nozzle wall contour for a given approach flow. This was achieved by modifying an existing Rao nozzle computer program, as described in Section III,E. As a result, it is now possible to design the contour downstream of the exterior nozzle throat so that it will provide maximum performance during Mode II operation. In order to accurately predict the performance of nozzles designed using these procedures, revisions were also made to the TDK computer program and to the aerodynamic model computer program. This procedure was used to define two secondary nozzle contours for the baseline configuration: one optimized for booster phase operation (Mode I) and one optimized for sustainer operation (Mode II). In this case, the performance for the operating mode in which the nozzle contour was optimized was about one (1) second greater than its performance with its non-optimum nozzle. Although a minor difference in this case, it shows that the capability now exists to optimize the performance for either mode of operation if this proves to be advantageous from a total mission standpoint.

Another analysis task conducted during this study assessed the effects of shock waves on nozzle performance. Shock waves are introduced in the supersonic expansion by the shape of the jet boundary and by its attachment to the exterior thruster wall. The resulting shock structure is inherently two-dimensional and, thus, a two-dimensional numerical procedure must be used to predict the flow field. The VNAP computer program was used for this purpose. The results of this study task, presented in Section III,D, indicate that shocks will have only a minor influence on the performance and thermal operating characteristics with properly designed bleed flows. This analysis was also used to define boundary conditions for the thermal analysis of the adverse condition of Mode II operation without any bleed flow.

The boundary layer analysis and performance loss of dual-throat engines was investigated further by using the JANNAF Reference computer code

BLIMP, in conjunction with the aerodynamic shear model (described in Section III,C). This procedure provided a rigorous method of assessing boundary layer influences, including the effects of bleed flow addition, and guided an improvement to the simplified boundary layer loss procedure.

Finally, all of the aforementioned improvements were incorporated into the existing dual-throat simplified performance model, and results were compared to previous performance predictions, as noted in Section III,F. In general, the revised model predicts lower specific impulse (~1%) for the baseline configuration in Mode II, but as a result of this investigation, the uncertainty of this prediction has been significantly reduced. Parametric trends with operating conditions proved similar; however, the variation of specific impulse with thrust split is altered and should be considered in future mission analysis studies.

As a second phase of this study, discussed in Section IV, performance models for dual-expander thrusters were developed. The dual expander is similar in concept to the dual-throat thruster and consists of an exterior, annular thrust chamber that surrounds a conventional thrust chamber. Two modes of operation are treated: Mode I, the booster mode of operation, during which both engines are on, and Mode II, the sustainer mode of operation, during which the annular thruster operates alone. During Mode II operation, a free shear layer develops along the jet boundary and is subsequently turned parallel to the axis of symmetry and transformed into a turbulent wake. Bleed flow can be used to control the shape and properties of this viscous region.

An aerodynamic model similar in concept to the dual-throat model was developed to determine the shear layer and base recirculation flow fields during Mode II operation. Use of this model showed that the bleed flow

requirements for a dual-expander nozzle were significantly influenced by the truncation point (Mach number) of the inner nozzle. The overall bleed flow required was, in general, 0 to 3%, which is significantly less than that required for the dual throat. In fact, it was concluded that the dual-expander engine could be designed and operated without bleed flow while still obtaining controllable aerodynamic flow characteristics.

A model for predicting shock losses and flow effects during Mode II operation was also applied to predict shock location and performance effects with varying inner nozzle truncation and bleed flow. The results indicated little performance differences with nozzle truncation and no significant shock influences over the range of bleed flows considered. However, the VNAP results were not sufficiently accurate in its present form to be used for performance prediction or for optimum nozzle design. To overcome this problem, development of a method of characteristics analysis with shock capability is recommended. Most of the point procedures required for this approach are available and could be used in assembling the new computer program.

Procedures were also developed to specify preliminary geometric design parameters for a dual-expander nozzle. These procedures are based on the criterion that the flow angle and static pressure must be matched at the primary nozzle lip during Mode I operation. During this study, the VNAP analysis was used to calculate the flow characteristics in the annular nozzle region. The subsequent results verified that the design criteria had been met.

Thermal design and parametric analyses, described in Section V, were performed for both dual-nozzle concepts. A satisfactory dual-throat baseline design was obtained by using three parallel cooling circuits.

Summary (cont.)

The primary circuit coolant flows from an area ratio of 1.58:1 in the primary nozzle to the primary injector. This circuit has the highest pressure drop requirement of the three parallel circuits, so its coolant flow fraction is selected to provide the minimum pressure drop. A separate circuit cools the inner annulus surface, the lip region, and the rest of the primary nozzle. The majority of the channel pressure drop in this circuit is required for the lip region, for which a three-dimensional SINDA model was developed. A counterflow circuit cools the outer surface of the secondary chamber; this circuit is a composite design which considers both Mode I and Mode II operation. The channel design over a short region upstream of the secondary throat is defined by the primary plume impingement associated with a bleed flow malfunction in Mode II. An exact solution for the inviscid plume impingement problem was obtained with the VNAP program. This solution provided edge conditions for an integral boundary layer analysis which defined the wall heat transfer edge conditions. The initial momentum thickness for the boundary layer analysis was varied in order to bound the problem, with the channel design based on the worst case. The maximum heat flux ranged from essentially the Mode I value to almost 50% higher.

Individual cooling circuit characteristics for the dual-throat baseline design have been defined. Although the fuel system pressure drop of 1160 psi is set by the primary circuit, the coolant Mach number is slightly higher in the secondary circuit when the latter is designed to accommodate the maximum postulated Mode II heat flux for the zero bleed flow case. Parametric study results indicate that it is the coolant Mach number, rather than pressure drop, which limits increases in chamber pressure and Mode I thrust split. Increasing the chamber pressures to 4500/3150 psia or the thrust split to 80/20 results in a primary circuit Mach number of 0.37 (an unacceptably high design value).

Summary (cont.)

The dual-expander designs, similar to those of the dual throat, are cooled with three parallel circuits. However, the inner annulus circuit is now a major circuit in terms of length and heat load and also includes a throat region. Regenerative cooling of the baseline design point with hydrogen only is difficult. Coolant flows in the secondary and inner annulus circuits must be selected to avoid minimum channel depth and Mach number limits, respectively, and the remaining flow available for the primary is less than optimum. As a result, the system pressure drop of 1720 psi is 130 psi above the minimum primary circuit value. Using oxygen to cool the secondary circuit and reducing the interface area ratio between the primary circuit inlet and the inner annulus circuit outlet allows the hydrogen pressure drop to be reduced to 1550 psi. Transpiration cooling the throat region of the primary chamber did not prove to be effective since the hydrogen flow fractions required for transpiration cooling, coupled with the flow requirements of the other circuits, severely limit the flow available for regeneratively cooling the remainder of the primary circuit. This results in relatively high pressure drops.

Parametric study designs of the dual expander could not be obtained with increased chamber pressures or increased Mode I thrust split, or with the secondary chamber pressure reduced to 1500 psia. The latter results from the high primary chamber pressure drop associated with reduced coolant inlet pressure. These results, along with the baseline design details, indicate that the baseline design point is near the optimum chamber pressure ratio and is very close to the chamber pressure versus thrust split characteristic which represents a practical cooling limit.

I. INTRODUCTION

Propulsion systems for future vehicles, such as the Single-Stage-to-Orbit (SSTO) and Heavy Lift Launch Vehicle (HLLV), may embrace such capabilities as dual-mode operation and in-flight changes in area ratio for altitude compensation. These vehicles benefit from dual-mode operation through reduced vehicle volume by taking advantage of relatively high bulk density propellants in one mode and lower density, but higher performing propellants in the other mode. Area ratio change during flight provides an increase in performance as ambient pressure decreases with altitude.

Dual-nozzle engines combine both operating capabilities in a single design. Their dual combustors allow use of either one or two propellant combinations and, with their two separate nozzle throats and a fixed nozzle exit area, allow for a shift in area ratio without resorting to nozzle translating mechanisms.

The dual-nozzle concept can be applied to both bipropellant and tripropellant engines with resultant advantages. The baseline engine application, analzyed in this and earlier studies, is a tripropellant single-stage-to-orbit (SSTO) engine. Dual nozzles could also be applied to bipropellant dual-thrust Orbit Transfer Vehicle (OTV) engine and Liquid Rocket Booster (LRB) engine designs. For OTV-E, a high-thrust priority payload and a low-thrust cargo transfer engine could be combined in a single thrust chamber. For a LOX/Hydrocarbon LRB, mission thrust tailoring and an area ratio increase at altitude could be achieved. This concept has been analyzed, with favorable results, during the recent Advanced Oxygen-Hydrocarbon Rocket Engine Study (Ref. 1).

Two types of dual-nozzle designs have been conceived -- the dual throat and the dual expander. An engine system preliminary analysis using the dual-throat concept was performed during Contract NAS 8-32967 to examine potential

power cycles and generate parametric data for a tripropellant SSTO vehicle engine. A preliminary performance prediction methodology based on a new aerodynamic bleed flow computer model was developed. This model was formulated by using the results of cold-flow tests conducted with a subscale dual-throat thruster configuration. The dual-expander engine concept, prior to the subject contract, has received less formal analysis. Some preliminary engine system parametric data have been generated, and a conceptual baseline engine system has been established.

A dual-throat thruster consists of a large thrust chamber assembly that contains within it a smaller thrust chamber. Because of this novel construction, dual-throat thrusters provide the means to obtain a large area ratio adjustment within a single thrust chamber assembly without the need for extendible nozzles. This area ratio adjustment is accomplished by changing the operating mode of the thruster. For example, in the high-thrust mode, the exterior and interior thrust chambers are both operating. When the exterior thrust chamber is extinguished, the low-thrust interior thrust chamber remains in operation, but now utilizes the exterior thrust chamber exhaust nozzle as its exhaust expansion contour. In this manner, the interior thruster is caused to operate at a high expansion ratio. The attachment of the interior thruster exhaust to the exterior thruster wall contour can be controlled by injecting mass flow into the exterior chamber, thereby creating a free shear layer that develops along the jet boundary. Mass injection will raise the base pressure in the chamber of the exterior thruster and move the jet attachment point downstream. Proper location of the free jet can serve to lower the losses in interior chamber performance that are caused by aerodynamic effects.

The sustainer mode of operation, as described above, is called Mode II, and the booster mode of operation is called Mode I. The dual-throat thrust chamber configuration and flow fields for Mode I and II of the tripropellant

SSTO engine case are illustrated in Figure I-1. During Contract NAS 8-32967, the baseline engine design gas generator flow was employed as the Mode II bleed flow. During Mode I, the gas generator flow would be dumped in the nozzle exhaust.

The dual expander is similar in concept to the dual-throat thruster. The dual expander consists of an exterior annuluar thrust chamber that surrounds a conventional thrust chamber. Figure I-2 illustrates the two modes of operation for the SSTO engine application that are treated in this study. Mode I is the booster mode of operation during which both engines are on. The annular thruster uses a LOX/H_2 propellant combination, and the interior thruster uses LOX/RP-1. Thus, in the dual expander, the exterior chamber is the sustainer thruster whereas, in the dual-throat design, the interior chamber is the sustainer thruster. Mode II is the sustainer mode of operation during which the annular thruster operates alone. During Mode II operation, a free shear layer develops along the jet boundary and is subsequently turned parallel to the axis of symmetry and transformed into a turbulent wake. Bleed flow can be used to control the shape and properties of this viscous region.

Technological investigation of the dual-throat nozzle concept was initiated in 1975 by the NASA George C. Marshall Space Flight Center. In July of 1976, the NASA and the Aerojet Liquid Rocket Company (ALRC) collaborated on an analytical/empirical program to evaluate the concept. A bailment agreement was established wherein NASA hardware was supplied for use on an ALRC-sponsored cold-flow program. Aerodynamic analyses were conducted, and the cold-flow test program was completed. After the promising aerodynamic features had been confirmed, NASA contracted ALRC (NAS 8-32666, Ref. 1) to expand the data base and to initiate development of a dual-throat performance prediction model.

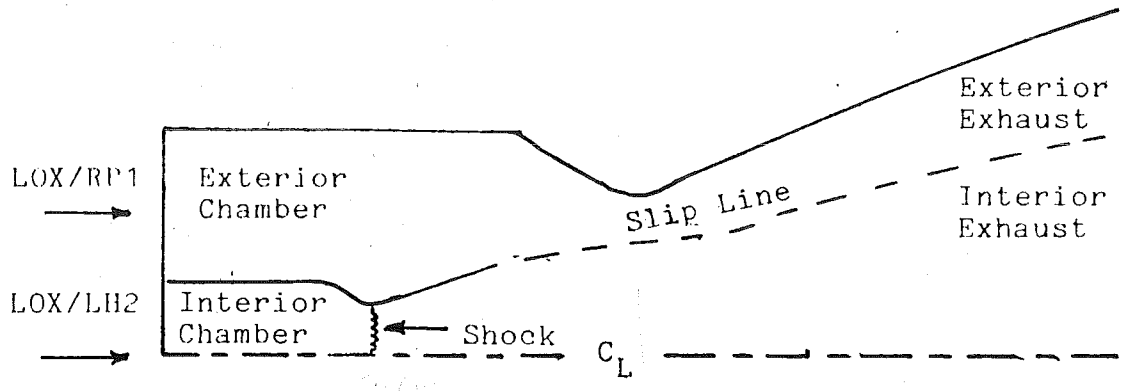

a. MODE I, BOOSTER MODE OPERATION
DUAL-THROAT THRUSTER

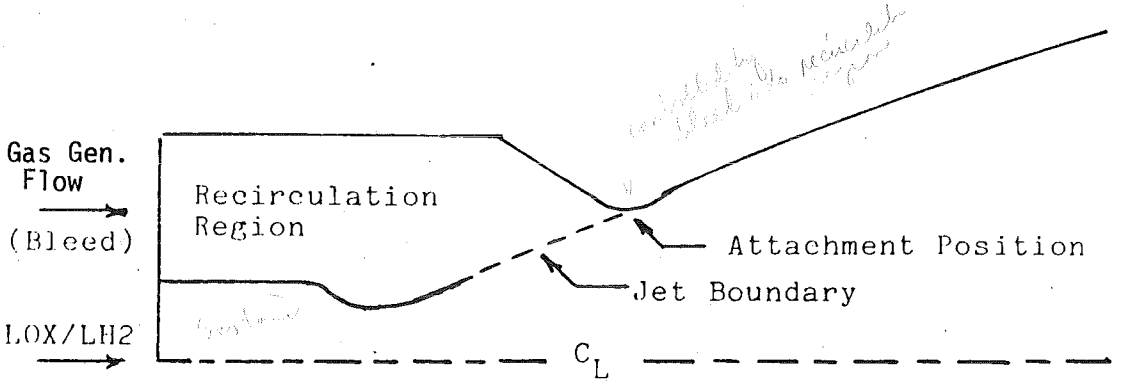

b. MODE II, SUSTAINER MODE OPERATION
DUAL-THROAT THRUSTER

Figure I-1. Dual-Throat Thrust Chamber Configuration and Flow Fields for Modes I and II

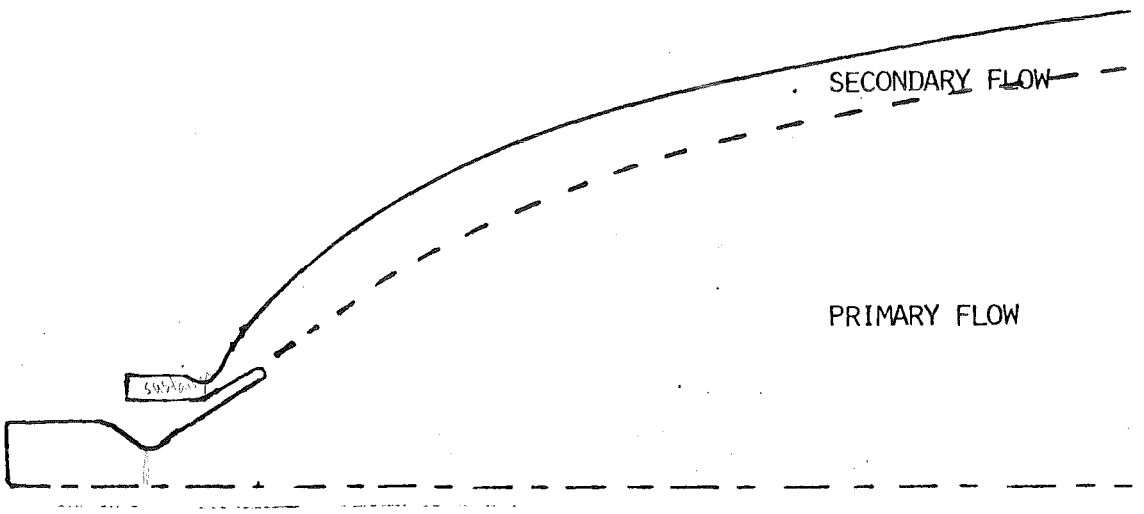

a. DUAL-EXPANDER MODE I OPERATION
BOTH ENGINES ON

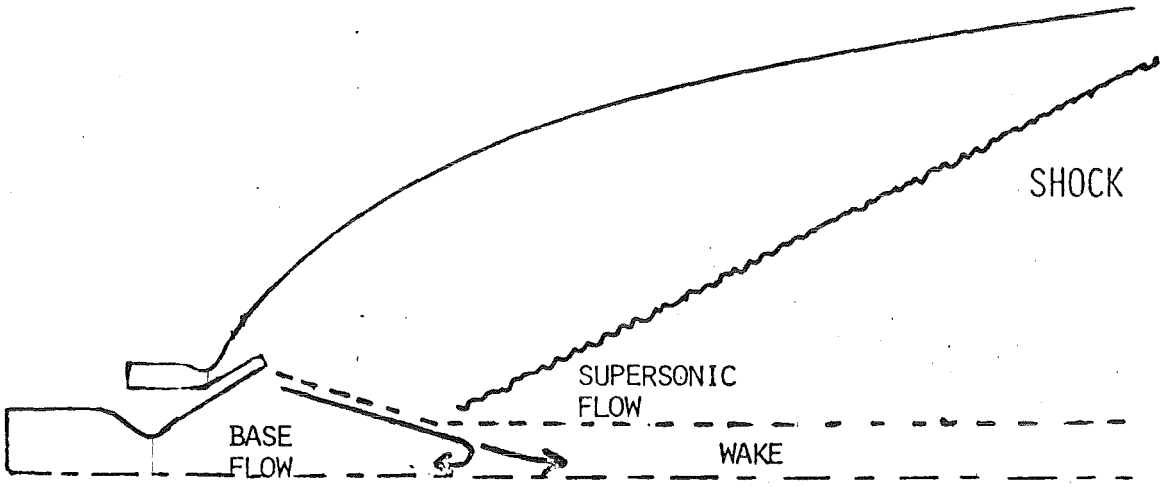

b. DUAL-EXPANDER MODE II OPERATION
OUTER ENGINE ON, INNER ENGINE OFF

Figure I-2. Dual-Expander Modes of Operation

I, Introduction (cont.)

The Dual-Fuel, Dual-Throat Engine Preliminary Analysis Program (NAS 8-32967, Ref. 2) was subsequently conducted to determine dual-throat engine system parameters and vehicle/engine integration requirements for the tri-propellant SSTO engine application. This study concluded that while the dual-throat, dual-fuel engine was a viable SSTO candidate, a number of uncertainties remaining in the heat transfer and performance areas needed to be resolved. Also, as the Dual-Expander Engine had been conceived during this period (Ref. 3), there was a need to make accurate trades between the two dual-nozzle concepts. As a result, the effort described in this report was conducted.

To accomplish this, the Dual Nozzle Aerodynamic and Cooling Analysis study was conducted. The results are discussed in this report. The major objectives of the program were as follows:

(1) Improve the existing dual-throat aerodynamic bleed flow model and performance prediction methodology;

(2) Develop basic geometric and aerodynamic data defining performance for a dual-expander chamber;

(3) Conduct preliminary thermal analyses of both the dual throat and dual expander;

(4) Provide engineering analysis of data from government hot-fire testing of a dual-throat thruster model chamber.

I, Introduction (cont.)

The objectives were accomplished through a series of five tasks:

Task I: Dual-throat aerodynamic model and performance prediction improvements. This task resulted in improving the bleed flow model to analytically predict base pressure for dissimilar compositions of the primary and bleed flows. Secondly, a computer program was developed to optimally design the secondary nozzle contour for Mode II operation. Third, simplified procedures used to predict boundary layer and divergence losses were verified by a rigorous analysis. This analysis also investigated the influence of shocks on engine operation.

Task II: Dual-expander preliminary geometric analysis. A design criterion was established, and the interrelationships between nozzle geometry and engine operating characteristics were defined.

Task III: Dual-expander preliminary flow field analysis. The flow field characteristics of the dual-expander operation were investigated, verifying the design approach from Task II and identifying the insensitivity of nozzle performance to inner chamber truncation and the low bleed flow requirements of the dual expander.

Task IV: Preliminary thermal analysis of both dual throat and dual expander. This task showed that the lip regions of the inner nozzle in both concepts could be cooled. Completely regeneratively cooled designs were established for both engines.

Task V: Test data analysis. Hot-fire data analysis verified the improved aerodynamic bleed flow model.

II. CONCLUSIONS AND RECOMMENDATIONS

A. CONCLUSIONS

The major conclusions formed during conduct of the program are listed below.

1. The dual-throat aerodynamic bleed flow model has been verified on the basis of cold-flow and hot-fire data correlations and is ready for use as a general design tool.

2. The predictive accuracy of the aerodynamic bleed flow model could be bettered by improving the current plume shape calculational procedure.

3. Dual-throat engine performance is relatively insensitive as to whether or not the secondary nozzle contour is optimized for the Mode I or Mode II expansion.

4. The previous simplified technique for predicting the dual-throat Mode II boundary loss was inaccurate. The rigorous procedure employed during this program has resulted in significant improvement of the simplified prediction procedure.

5. Dual-throat nozzle performance in Mode I is comparable to that of a conventional nozzle. Mode II performance is approximately 1-2% lower than that of a conventional nozzle optimized for altitude (i.e., sustainer) operation.

6. Preliminary performance analysis results for the dual-expander nozzle indicate that high Mode II expansion efficiencies can be achieved. The results indicate low bleed flow requirements and insensitivity to the primary nozzle truncation area ratio.

7. There is a degree of uncertainty associated with the dual-expander performance results. The calculational procedures employed during this program (i.e., the VNAP computer model) should be replaced by a method of characteristics solution that treats shock waves.

8. Both the dual-throat and dual-expander baseline tripropellant SSTO engine designs can be cooled with three-circuit regenerative designs. The primary nozzle lip and secondary nozzle throat gas-side heat transfer coefficient assumptions should be verified through hot-fire testing.

B. RECOMMENDATIONS

The following recommendations for future work are made on the basis of the significant results obtained on this program. They are listed in the order of highest to lowest priority.

1. A demonstration program should be conducted to verify the major thermal design assumptions utilized during the study.

II, B, Recommendations (cont.)

2. The dual-expander flow field analysis results should be verified through conductance of a model cold-flow test program.

3. The dual-throat SSTO engine parametrics developed on Contract NAS 8-32967 should be updated on the basis of the improved performance prediction results obtained on this program.

4. A method of characteristics solution that treats flow field shocks should be developed for Mode II dual expander analysis.

5. The plume shape calculational procedure contained within the aerodynamic bleed flow model should be improved and correlated with existing test data.

6. A procedure for optimization of dual-expander secondary nozzle contour should be developed.

III. DUAL THROAT AERODYNAMIC MODEL AND PERFORMANCE PREDICTION IMPROVEMENT

The basic objectives of Task I were to improve the dual throat aerodynamic model's capability and verify the approaches used in the dual throat performance prediction methodology developed by ALRC for NASA/MSFC during Contract NAS 8-32666.

The specific objectives of Task I were as follows:

- Improve the base flow pressure and shear layer portion of the aerodynamic bleed flow model.
- Assess the approach used to calculate boundary layer loss for Mode II operation.
- Assess the approach used to calculate nozzle divergence efficiency for Mode II operation and determine how shocks affect it.
- Develop a Rao nozzle optimization program for the Mode II operation and determine the effect of Mode II contour optimization on the delivered performance of both modes.
- Assess changes in predicted performance based on the use of the improved aerodynamic model and update the performance model as required.
- Review the existing cold-flow data bank and define areas that would benefit from further cold-flow test data.

III, Dual Throat Aerodynamic Model and Performance Prediction Improvement (cont.)

A. LITERATURE SURVEY

In support of the improvement of the aerodynamic model, a computerized literature survey was conducted for the purpose of obtaining references that might be useful in formulating the analytical model as well as data that could be used for calibration of the model. Conducting a computerized literature search has the advantage of significantly reducing the amount of man-hours otherwise required for this task, thus significantly reducing cost and time as well.

The literature search was carried out via a remote data terminal to gain access to a computerized library. The method used involves the formulation of a search strategy based on key words or phrases. These may be combined using boolian operators to obtain all literature from a given data base. The search is conducted interactively on the main frame computer. For example, reference titles that contain a given key word, but not another key word, may be listed on the terminal. If a particular title appears to be of interest, a request by terminal is made and the abstract of the article is printed. If desired, the article can then be ordered over the terminal.

In order to prepare a search strategy, the initial computer session was spent in checking various key author names and key words for frequency of citation in the NTIS index. Titles obtained in this way were used to construct the boolian operators to be used in the general search. A strategy was established to be accomplished in two steps.

The first step was to identify those papers which make reference to the principal works in the field. This was accomplished with the Science Citation Index capability of SCISEARCH. Papers which referred to the works of Korst, Bauer, and Alber were sought in this way.

III, A, Literature Survey (cont.)

The second part of the literature search utilized various key words and employed six data bases. Information obtained in this manner is summarized in Table III-I, which gives the number of references found by category by source. Abstracts were obtained for these references. After reading the abstracts, approximately 30 papers were ordered.

B. AERODYNAMIC BLEED FLOW MODEL

The aerodynamic bleed flow model's capability of predicting the aerodynamics unique to Mode II operation has been expanded. The Mode II (sustainer mode) operation is illustrated in Figure III-1. The interior thrust chamber is called the primary thruster, and its exhaust is called the primary flow stream. A secondary flow stream (bleed flow) is injected into the exterior thrust chamber. The thruster expands the primary flow to a supersonic condition at the nozzle exit. Further expansion then occurs in the form of a Prandtl-Meyer fan at the nozzle lip. The result is an exhaust plume with a constant pressure boundary. Flow is introduced into the exterior chamber so as to control the location of the plume boundary in order to minimize reattachment shocks which occur when the flow impinges on the exterior thruster wall. The plume boundary is an exhaust streamline path and acts very much like a nozzle wall. However, a shear layer develops along this boundary due to viscous interaction of the exhaust jet and the gases recirculating in the exterior chamber. Analysis of this shear layer mixing region and of the phenomena described above are an important feature of the aerodynamic model.

The principal assumptions employed in the aerodynamic model are listed below:

- The flow leaving the primary nozzle is one-dimensional and supersonic.

TABLE III-I

SUMMARY OF LITERATURE SEARCH-AEROJET DUAL NOZZLE ANALYSIS

	DATA BASE					
	NTIS	COMPENDEX	ISMEC	SCISEARCH	DISSERTATIONS	CONFERENCES
SHEAR LAYERS	16			22		
SHEAR LAYERS * HEAT TRANSFER	4					
SHEAR LAYERS * (HT. TRANS. + ISOENERGETIC + REATTACHMENT)		22	8		2	
BASE FLOW + BASE PRESSURE	42		22	13	20	20
(BASE FLOW + BASE PRESSURE) * (SHEAR LAYERS + HT. TRANS. + REATT)		20				
REATTACHMENT	11					17
DUAL THROAT	2	1				2
DUAL NOZZLES	1	2				1
DUAL EXPANDER		1				
AEROSPIKE	4	5				6
AIR AUGMENTED ROCKETS	3	5				2
UNCONVENTIONAL ROCKETS						
EJECTOR * (ROCKETS + MEASUREMENTS)	15	20	4			

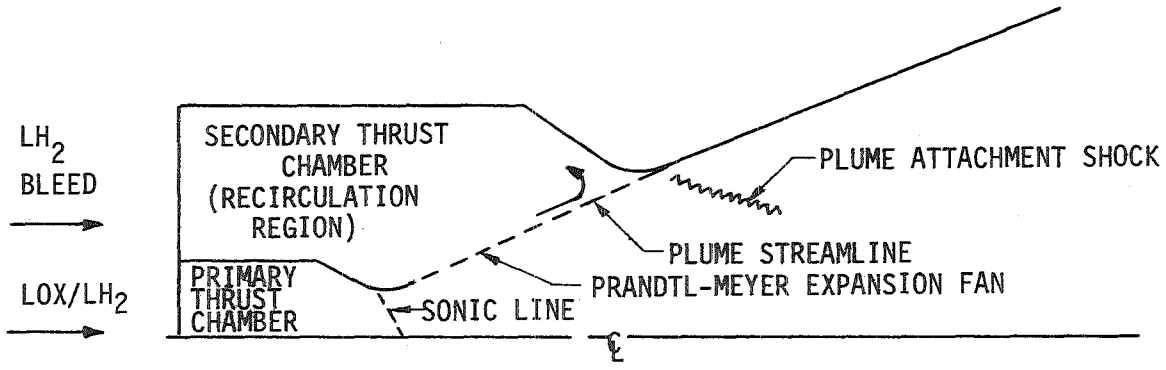

Figure III-1. Mode II, Sustainer Mode Operation

III, B, Aerodynamic Bleed Flow Model (cont.)

- The primary nozzle exhaust flow is represented by an ideal gas with constant specific heat and molecular weight.

- The bleed flow is represented by an ideal gas with constant specific heat and molecular weight. These values can differ from those of the primary exhaust stream. The total temperature of the bleed flow can also differ from that of the primary flow stream.

- The shear layer is represented by a model of the type developed by Chapman, Korst, Bauer, Chow and Addey, and others (see Refs. 5, 6, 7, 8, and 9). The model used here, however, is non-isoenergetic, as defined by the assumptions given above.

- The shear layer is treated as two-dimensional. This assumption has been shown to be accurate (see Bauer, Ref. 7), provided that the projected thickness of the mixing zone on the radius of symmetry is less than .3 of the radius of symmetry. This condition is always satisfied in dual throat thrusters.

- The boundary layer at the primary nozzle lip is thin.

- The shear layer is a constant pressure surface, both in cross section and along its entire length. At the inner edge of the shear layer, the gas velocity is negligible. At the outer edge of the shear layer, the velocity is constant and equal to the velocity of the plume boundary streamline.

- The shear layer is superimposed on the inviscid jet plume boundary.

III, B, Aerodynamic Bleed Flow Model (cont.)

- The plume boundary can be represented by the methods developed by Herron (Ref. 10).

1. Shear Layer Modeling

Some features of the free shear layer that develops along the jet boundary are shown in Figure III-2. The shear layer is assumed to begin at the exit of the primary nozzle where its thickness is negligible. It then develops as a turbulent shear layer along the boundary of the primary nozzle exhaust plume. Viscous interaction of the exhaust plume with gases recirculating in the chamber of the secondary nozzle form the shear layer. In steady-state operation, the system will maintain a stable equilibrium base pressure. This base pressure determines the plume boundary. The theory assumes that a streamline divides the shear layer such that gases on one side of the streamline are recirculated into the base region. This is the so-called "dividing streamline" concept. At steady-state operation, all of the gases exhausting from the primary nozzle will also exhaust from the secondary nozzle. Gases in the recirculating region (in this case the chamber of the secondary nozzle) have been trapped because they are degraded in total pressure to the extent that they cannot penetrate the static pressure rise produced by turning off the flow at the point where the shear layer impinges on the secondary nozzle wall. It is assumed, in this model, that the dividing streamline becomes a stagnation point at the secondary wall. This stagnation occurs abruptly either by a compression that is essentially isentropic, or by a non-isentropic compression through a shock structure. Details of this process govern the value that will be obtained for a base pressure, i.e., the pressure along the plume boundary.

The introduction of mass flow into the recirculation region will tend to raise the base pressure and shift the plume boundary downstream.

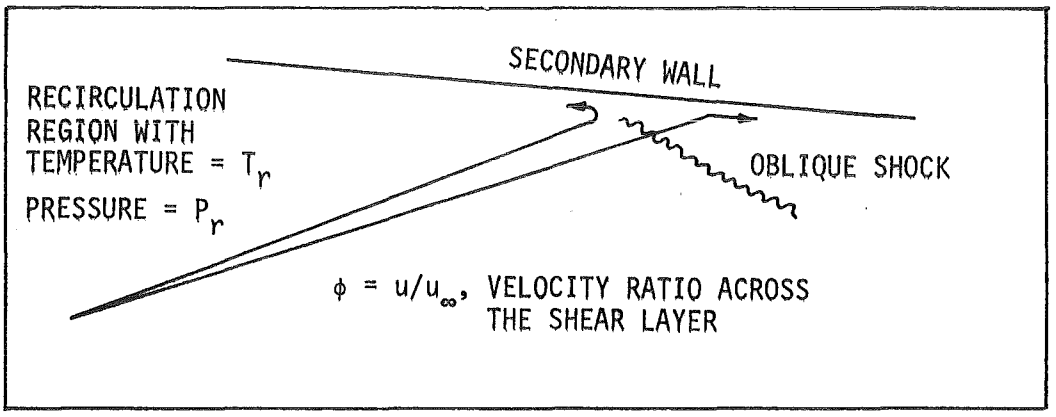

Figure III-2. Shear Layer Streamlines and Velocity Profile

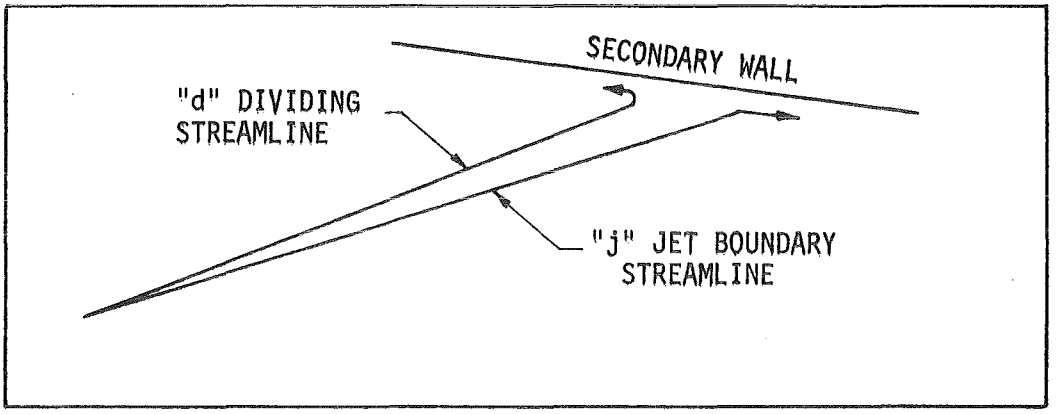

Figure III-3. The "d" and "j" Streamlines within the Shear Layer

III, B, Aerodynamic Bleed Flow Model (cont.)

Mass flow introduced into the recirculation region at a given rate must exit the nozzle at the same rate. If this flowrate is sufficiently small, all of the injected flow will become entrained within the shear layer. For this reason, the analysis used here is called a "small bleed flow" model.

Figure III-3 shows the location of two important streamlines within the shear layer. The "d" streamline is the so-called "dividing streamline" that separates the recirculation gases from the gases that exit the nozzle. The recirculation gases are assumed to be a mixture or primary and bleed flow gases. The "j" streamline, also shown in Figure III-3, is a limiting streamline for the bleed flow gas. On the primary side of the "j" streamline, there is "pure" primary flow, whereas, on the secondary side, there is "mixed" primary and secondary flow. All of the bleed flow introduced during steady-state operation must exit the nozzle and is contained between the "d" and "j" streamlines. The "d" and "j" streamlines coincide if the bleed flow is reduced to zero.

The velocity profile at any position across the shear layer will appear as shown in Figure III-2. The shear layer will be turbulent, but for either laminar or turbulent flow the velocity profile can be represented by

$$\bar{\phi} = (1 + \text{erf}\ \eta) / 2$$

where

$$\bar{\phi} = u/u_\infty \quad , \quad 0 < \bar{\phi} < 1$$

and erf is the error function, i.e.,

$$\text{erf}\ \eta = 2\pi \int_0^\eta \exp(-\eta^2)\, d\eta$$

III, B, Aerodynamic Bleed Flow Model (cont.)

η is the nondimensional mixing length

$$\eta = \sigma y/\ell$$

In the above equation, y is the distance measured normal to the centerline of the shear layer, and ℓ is the length of the shear layer measured along the centerline from its origin. The variable σ is known as the "shape factor" or "similarity parameter." The difference between laminar and turbulent mixing is reflected in the relationship used for σ. It is necessary to use an empirical expression for the shape factor. Numerous expressions for σ are available in the literature (see Refs. 6, 7, 9, 11), but the empirical expression given by Korst (Ref. 6) has been used here, i.e.,

$$\sigma = 12 + 2.758\ M_b$$

where M_b is the Mach number along the inviscid primary jet boundary.

Since the bleed flow gas properties can be different from those in the primary stream, it is necessary to assume a variation in properties across the mixing zone, i.e., across the shear layer from the base recirculation region to the "j" streamline. It is assumed that the distribution of mass fraction across the mixing zone is linear with respect to velocity ratio, thus:

$$\overline{C}_p = C_{pr}\ (1-\phi) + \phi C_{pp}$$

where C_{pr} is the specific heat in the recirculation region, i.e.,

$$C_{pr} = C_{ps}\ (1-Y_{pr}) + C_{pp}\ Y_{pr}$$

Y_{pr} is the amount of mass from the primary flow entrained in the recirculation region.

III, B, Aerodynamic Bleed Flow Model (cont.)

The gas constant in the mixing region is

$$\overline{R} = R_r (1-\phi) + \phi R_p$$

where R_r is the gas constant in the recirculation region, i.e.,

$$R_r = R_s (1-Y_{pr}) + R_p Y_{pr}$$

with

$$R_s = \tilde{R}/M_{ws}$$

and

$$R_p = \tilde{R}/M_{wp}$$

where R is the universal gas constant. The specific heat ratio in the mixing zone is

$$\overline{\gamma} = \overline{C}_p/(\overline{C}_p - \overline{R}),$$

Using the relations

$$R = C_p - C_v$$

$$\gamma = C_p/ C_v$$

it follows that

$$\overline{\gamma} = \frac{\gamma_r (1-\phi) + \gamma_p \frac{C_{vp}}{C_{vr}} \phi}{(1-\phi) + \frac{C_{pp}}{C_{pr}} \frac{\gamma_r}{\gamma_p} \phi}$$

III, B, Aerodynamic Bleed Flow Model (cont.)

In like manner, the specific heat ratio along the dividing streamline is found to be

$$\bar{\gamma}_d = \frac{\gamma_r (1-\phi_d) + \gamma_p \frac{C_{vp}}{C_{vr}} \phi_d}{(1-\phi_d) + \frac{C_{pp}}{C_{pr}} \frac{\gamma_r}{\gamma_p} \phi_d}$$

Next, the velocity ratio at the dividing streamline, ϕ_d, is sought. The energy equation is

$$C_p T + U^2/2 = C_p T_o$$

so that

$$U^2 = 2C_p (T_o - T)$$

and

$$U^2_d/U^2_\infty = C_{pd} (T_{od} - T_d)/C_{pp} (T_{op} - T_b)$$

where T_b is the temperature along the plume boundary. Defining the Crocco number as

$$C^2 = 1 - T/T_o$$

gives

$$\phi_d^2 = U^2_d/U^2_\infty = (C_d^2 C_{pd} T_{od})/(C_b^2 C_{pp} T_{op})$$

Expressing the Crocco number in terms of pressure gives

$$C_b^2 = 1 - (P_b/P_{op})^{(\gamma_p-1)/\gamma_p}$$

III, B, Aerodynamic Bleed Flow Model (cont.)

and

$$C_d^2 = 1 - (P_b/P_{od})^{(\bar{\gamma}_d-1)/\bar{\gamma}_d}$$

where P_{od} is the total pressure on the "d" streamline. However, at the shear layer attachment point, the "d" streamline is stagnated after passing through an oblique shock. The maximum strength of this shock corresponds to the deflection angle experienced by the plume boundary when turned abruptly by the nozzle wall, i.e.,

$$P_{od}/P_b = \hat{P}/P_b$$

where $\hat{P}/P_b$ is obtained from the oblique shock relations. On the other hand, if the shock imparts no loss in total pressure to the "d" streamline, then the flow is compressed isentropically and

$$P_{od} = P_b$$

It is assumed that the true recompression criterion falls between these two extremes, so that

$$P_{od} = N\hat{P} + (1-N)\, P_b$$

and

$$0 \leq N \leq 1.$$

The quantity, N, is known as the Nash factor (see Ref. 11, 12). In the analysis presented here, N is used to calibrate the shear layer model with experimental data.

III, B, Aerodynamic Bleed Flow Model (cont.)

Total enthalpy across the mixing layer is also assumed to vary linearly with respect to velocity ratio, i.e., at the "d" streamline

$$\frac{H_{od}}{H_{op}} = \frac{H_r}{H_{op}} + \left(1 - \frac{H_r}{H_{op}}\right) \phi_d$$

so that

$$\frac{C_{pd}\ T_{od}}{C_{pp}\ T_{op}} = \frac{C_{pr}\ T_r}{C_{pp}\ T_{op}} + \left(1 - \frac{C_{pr}\ T_r}{C_{pp}\ T_{op}}\right) \phi_d$$

From the definition of the Crocco number, and since $T_r = T_{od}$, it follows that

$$\phi_d^{\,2} = \frac{C_d^{\,2}}{C_b^{\,2}} \left[\frac{C_{pr}\ T_r}{C_{pp}\ T_{op}} + \left(1 - \frac{C_{pr}\ T_r}{C_{pp}\ T_{op}}\right) \phi_d\right]$$

Solving the above equations gives:

$$\phi_d = \frac{1}{2} \frac{C_d}{C_b} \left[\frac{C_d}{C_b}\left(1 - \frac{C_{pr}\ T_r}{C_{pp}\ T_{op}}\right) + \sqrt{\left(\frac{C_d}{C_b}\right)^2 \left(1 - \frac{C_{pr}\ T_r}{C_{pp}\ T_{op}}\right) + 4\ \frac{C_{pr}\ T_r}{C_{pp}\ T_{op}}}\right]$$

The expressions given above are sufficient to determine $\bar{\gamma}_d$, C_d^2, and ϕ_d^2 by means of numerical iteration, provided that conditions in the base recirculation region are known. The similarity coordinate of the "d" streamline is then given by

$$\eta_d = \text{erf}^{-1}\ (2\ \phi_d - 1)$$

III, B, Aerodynamic Bleed Flow Model (cont.)

The similarity coordinate for the "j" streamline, η, can be found from the mass and momentum conservation equations. Using these equations, it can be shown that for a two-dimensional shear layer*

$$\int_{-\infty}^{\eta_j} (\rho/\rho_\infty)\ \phi d\eta = \int_{-\infty}^{\infty} (\rho/\rho_\infty)\ \phi\ (1-\phi)\ d\eta$$

The term (ρ/ρ_∞), which is the ratio of the gas density across the shear layer to the density at the primary edge, ρ_b, can be evaluated as follows:

$$(\rho/\rho_\infty) = (\rho/\rho_b)$$

From the perfect gas law, and since the pressure is constant across the shear layer,

$$(\rho/\rho_b) = \frac{R_p}{R}\ \frac{T_b}{T} = \frac{R_p}{R}\ \frac{T_b/T_{op}}{T/T_o}\ \frac{T_{op}}{T_o}$$

Since

$$T/T_o = 1 - C^2$$

then

$$(\rho/\rho_b) = \frac{R_p}{R}\ \frac{1-C_b^2}{1-C^2}\ \frac{T_{op}}{T_o}$$

*For example, see Bauer (Ref. 7) and neglect the axisymmetric terms.

III, B, Aerodynamic Bleed Flow Model (cont.)

As shown previously, it follows directly from the energy equation that

$$\phi^2 = \frac{C^2 C_p T_o}{C_b^2 C_{pp} T_{op}}$$

Therefore,

$$(\rho/\rho_b) = \frac{R_p}{R} \frac{1-C_b^2}{1-C_b^2 \phi^2 \frac{C_{pp} T_{op}}{C_p T_o}} \frac{T_{op}}{T_o}$$

$$(\rho/\rho_b) = \frac{R_p}{R} \frac{1-C_b^2}{\frac{T_o}{T_{op}} - C_b^2 \phi^2 \frac{C_{pp}}{C_p}}$$

and

$$(\rho/\rho_b) = \frac{R_p}{R} \frac{C_p}{C_{pp}} \frac{1 - C_b^2}{\Lambda - C_b^2 \phi^2}$$

where Λ is the enthalpy ratio,

$$\Lambda = \frac{T_o C_p}{T_{op} C_{pp}}$$

and is assumed to vary linearly with velocity across the shear layer as follows:

$$\Lambda = \frac{C_{pr} T_r}{C_{pp} T_{op}} + \left(1 - \frac{C_{pr} T_r}{C_{pp} T_{op}}\right) \phi$$

III, B, Aerodynamic Bleed Flow Model (cont.)

where

$$C_p = C_{pr}\,(1-\phi) + \phi\, C_{pp}$$

$$R = R_r\,(1-\phi) + \phi\, R_p$$

The similarity coordinate, η, is then found from the following relationship:

$$\int_{-3}^{\eta_j} \frac{C_p}{C_{pp}} \frac{R_p}{R} \frac{\phi}{\Lambda - C_b{}^2 \phi^2}\, d\eta = \int_{-3}^{3} \frac{C_p}{C_{pp}} \frac{R_p}{R} \frac{\phi\,(1-\phi)}{\Lambda - C_b{}^2 \phi^2}\, d\eta$$

The far edges of the shear layer are taken as +3 and -3. The value for η_j is obtained by integrating the left-hand side of the above expression until it is equal in value to the right-hand side. For computational convenience, the followng functions are defined:

$$I_1\,(A) = \int_{-3}^{A} \frac{C_p}{C_{pp}} \frac{R_p}{R} \frac{\phi}{\Lambda - C_b{}^2 \phi^2}\, d\eta$$

$$I_3\,(A) = \int_{-3}^{A} \frac{C_p}{C_{pp}} \frac{R_p}{R} \frac{\phi^2}{\Lambda - C_b{}^2 \phi^2}\, d\eta$$

so that

$$\int_{-3}^{\eta_j} \frac{C_p}{C_{pp}} \frac{R_p}{R} \frac{\phi}{\Lambda - C_b{}^2 \phi^2}\, d\eta = \int_{-3}^{3} \frac{C_p}{C_{pp}} \frac{R_p}{R} \frac{\phi}{\Lambda - C_b{}^2 \phi^2}\, d\eta - \int_{-3}^{3} \frac{C_p}{C_{pp}} \frac{R_p}{R} \frac{\phi^2}{\Lambda - C_b{}^2 \phi^2}\, d\eta$$

$$I_1\,(\eta_j) = I_1\,(3) - I_3\,(3)$$

Next, a method is presented for determining the species concentrations in the base recirculation region. The shear layer to the left of the "d" streamline

III, B, Aerodynamic Bleed Flow Model (cont.)

is turned into the recirculation region at a height r_w above the primary flow centerline. By applying the mass and energy balance equations to a control volume surrounding the recirculation region, it can be shown that (Ref. 13) equation [18])

$$\dot{W}_s \, (Y_{PBleed} - Y_{pr}) = \int_{-\infty}^{y_d} 2\pi \, r_w \, \rho \, U(Y_{pr} - Y_p) \, dy$$

The bleed flow is entirely made up of the secondary flow species, so that

$$Y_{PBleed} = \rho_p / \rho_{bleed} = 0$$

Thus,

$$0 = Y_{pr} + \frac{2\pi r_w}{\dot{W}_s} \int_{-\infty}^{y_d} \rho U \, (Y_{pr} - Y_p) \, dy$$

For unity, Schmidt and Lewis No.

$$Y_p - Y_{pr} = \phi \, (1 - Y_{pr})$$

So that

$$0 = Y_{pr} + \frac{2\pi r_w}{\dot{W}_s} \int_{-\infty}^{y_d} \rho U \phi dy \, (1 - Y_{pr})$$

Changing to nondimensional coordinates, and proceeding as before, gives

$$0 = Y_{pr} + \frac{2\pi r_w}{\dot{W}_s} \left(\frac{\ell \rho_b U_b}{\sigma} \right) (1 - C_b^2) \, [I_3 \, (\eta_d) \, (1 - Y_{pr})]$$

III, B, Aerodynamic Bleed Flow Model (cont.)

It can be shown that the mass flow in the secondary stream is*

$$\dot{W}_s = 2\pi r_w \left(\frac{\ell \rho_b U_b}{\sigma} \right) (1-C_b^2) \left[I_1 (\eta_j) - I_1 (\eta_d) \right]$$

Combining the above two equations gives

$$\alpha = \frac{I_3 (\eta_d)}{I_1 (\eta_j) - I_1 (\eta_d)} \qquad (1)$$

where

$$\alpha = Y_{pr}/Y_{sr}$$

The total enthalpy in the base recirculation region is therefore

$$\frac{C_{ps} T_{os}}{C_{pp} T_{op}} = \frac{C_{pr} T_r}{C_{pp} T_{op}} + \left(\frac{C_{pr} T_r}{C_{pp} T_{op}} - 1 \right) \alpha \qquad (2)$$

The total mass flow from the primary nozzle is

$$\dot{W}_p = \frac{\gamma_p P_{op} A_p^*}{\sqrt{\gamma_p R_p T_{op}}} \left(\frac{2}{\gamma_p + 1} \right)^{\frac{\gamma_p + 1}{2(\gamma_p - 1)}}$$

Thus, the ratio of the secondary mass flowrate to the primary mass flowrate

$$\dot{W}_s/\dot{W}_p = \frac{2}{\sigma} \frac{\ell r_w}{(r_p^*)^2} M_b \left(\frac{P_b}{P_{op}} \right) (1-C_b^2)^{1/2} \left(\frac{\gamma_p + 1}{2} \right)^{\frac{\gamma_p + 1}{2(\gamma_p - 1)}} \left[I_1 (\eta_j) - I_1 (\eta_d) \right] \qquad (3)$$

*For example, see Bauer (Ref. 7) and neglect the axisymmetric terms.

III, B, Aerodynamic Bleed Flow Model (cont.)

Equations (1), (2), and (3) above form a system of three nonlinear simultaneous equations in three unknowns: Y_{pr}, P_b/P_{op}, and T_r/T_{op}. The aerodynamic bleed flow computer program numerically solves for these three unknowns, using input initial estimates of their values.

2. Aerodynamic Bleed Flow Model Computer Program

The small bleed flow model for the shear layer derived at in the previous subsection is used in the aerodynamic computer bleed flow program. A flow chart for this computer program is presented in Figure III-4. The procedures shown in Figure III-4 are discussed below.

At the beginning of the program, initial and default values are set and the input data is read, using FORTRAN NAMELIST. (See Appendix A for a description of the program input and a sample problem.) The primary and secondary wall geometries are then constructed. Both the primary and the secondary nozzles are assumed to have geometries that can be described analytically by the following parameters:

Chamber contraction ratio

Circular wall radius connecting the chamber and the nozzle inlet

Conical nozzle inlet

Circular wall radius upstream of the nozzle throat

Circular wall radius downstream of the nozzle throat

The nozzle wall geometries are defined by simple geometrical inputs such as wall slope, throat radius of curvature, etc. Complete shapes are specified so that the wall contours can be plotted as well as used in the analysis.

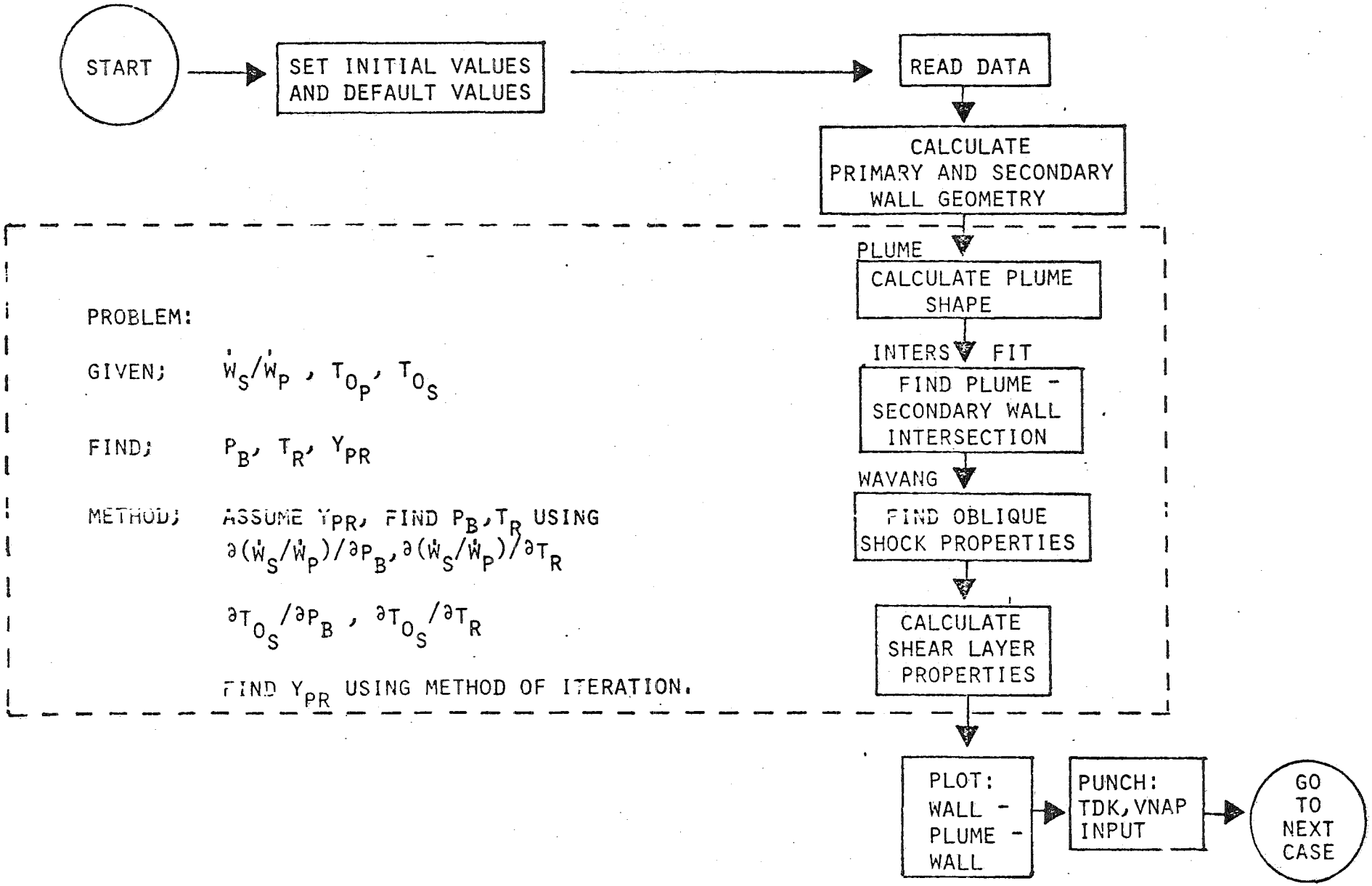

Figure III-4. Flow Chart for the Aerodynamic Bleed Flow Model Computer Program

In order to be used easily by the computer programs, the wall geometries are converted to finely spaced tables of points.

Next, an iterative procedure is initiated which consists of the steps enclosed in the dashed line rectangle shown in Figure III-4. The steps taken in this procedure are individually discussed below.

(1) Conditions at the exit of the primary nozzle are determined in the MAIN subroutine by using the one-dimensional relation between Mach number and area ratio, i.e.,

$$\varepsilon_p = M_e^{-1} \left[\frac{2}{\gamma_p+1} \left(1 + \frac{\gamma_p-1}{2} M_e^2 \right) \right]^{\frac{\gamma_p+1}{2(\gamma_p-1)}}$$

(2) The exhaust flow is turned at the nozzle lip and expands to equal the boundary Mach number M_b. The angle of this turn, $\Delta\upsilon$, is determined in the PLUME subroutine by using the Prandtl-Meyer relations for supersonic expansion at a point, as follows:

$$\nu = \nu_b - \nu_e$$

where

$$\nu_b = \left(\frac{\gamma_p+1}{\gamma_p-1} \right)^{1/2} \arctan \left[\frac{\gamma_p-1}{\gamma_p+1} \left(M_b^2 - 1 \right) \right]^{1/2} - \arctan \left[M_b^2 - 1 \right]^{1/2}$$

$$\nu_e = \left(\frac{\gamma_p+1}{\gamma_p-1} \right)^{1/2} \arctan \left[\frac{\gamma_p-1}{\gamma_p+1} \left(M_e^2 - 1 \right) \right]^{1/2} - \arctan \left[M_e^2 - 1 \right]^{1/2}$$

(3) The plume boundary is determined by using the modified method of Herron (Ref. 10). Since the plume boundary is a circular arc, all of its geometric properties (such as its position, arc length to any point, and slope at any point) are known analytically. This step is accomplished by using subroutine PLUME.

(4) The intersection of the plume with the secondary nozzle wall is determined geometrically by using subroutine INTERS.

(5) The shear layer model allows the shear layer profile to be determined exactly at the point of intersection of the plume boundary and the wall. All properties of the profile can be evaluated from various integrals of the error function, as described in Section III,B,1. These integrals are evaluated in subroutines IONEV, ITHRV, I1INVR, and IZEROS.

(6) The plume boundary is a streamline. The streamline will be turned abruptly (i.e., deflected) to follow the secondary nozzle wall, resulting in a shock structure. The cases of most interest correspond to solutions of the shock relations of the weak family. Cases where a lambda shock structure develops, so that the flow is shocked subsonically in part of the region, are of less interest since they correspond to aerodynamically poor designs. The obliquie shock relations are used to determine the rise in static pressure across the shock and the loss of total pressure across the shock. Since the development of shock structure in the nozzle is fundamentally a two-dimensional phenomenon, no attempt is

made to treat the flow in the nozzle downstream of the origin of the shock. The oblique shock relations are calculated by subroutine WAVANG.

The calculations described above require a first estimate for the variables P_b, T_r, and Y_{pr}. It is necessary to find converged values for these three variables that satisfy equations (1), (2) and (3) of Section III,B,1. Newton's method is used to obtain the next estimates for P_b, and T_r. Equations (2) and (3) are used to obtain the four partial derivatives required by Newton's method. The next estimate for Y_r is obtained by the method of iteration, using equation (1). Solutions are sought for each bleed flow given in an input table. Converged values for a solution are automatically used as first estimates for the next case.

The primary nozzle contour, the plume shape, and the secondary nozzle contour can be plotted. Punched card output is available for the outer streamline for the inviscid flow, i.e., the primary wall, the plume boundary, and the secondary wall downstream of the plume attachment point. The punched cards are in the input format required by the TDK program and/or the VNAP program (Refs. 3 and 4, respectively).

3. Model Calibration

Three empirical parameters exist in the bleed flow model which can be adjusted, as necessary, to improve the correlation between the Mode II bleed flow and the recirculation pressure and temperature. Two of these parameters were adjusted by using the cold-flow data and hardware geometry from NAS 8-32666.

One parameter, the plume scaling factor (FCTR), alters the plume shape. This is accomplished by using the plume scaling factor as a

multiplier for the similarity parameter, M_b/γ, in the Herron plume correlation. (M_b is the Mach number along the plume boundary, and γ is the ratio of specific heats.) Altering the plume scaling influences the plume impingement angle and, hence, the resulting shock strength.

A plume scaling factor of 1.2 resulted in model predictions that agreed well with the experimental data for small nozzle spacing as shown in Figure III-5. However, for tests with larger nozzle spacing, the model predictions became less accurate when a constant scaling factor, as shown in Figure III-6, was used. Decreasing the plume scaling factor to 0.9 improved the accuracy for large nozzle spacing (Figure III-7). A correlation between plume scaling factor and nozzle spacing, as shown in Figure III-8, can be inferred, but the validity of applying it to other dual throat geometries needs to be determined.

The second parameter, the Nash factor (N), is used in the recompression criteria relating the pressure behind the plume attachment shock to the recirculation pressure. This parameter adjusted the stagnation pressure loss to match the cold-flow data. While the plume scaling factor shifts the base pressure versus bleed flow curve up or down, the Nash factor changes the actual shape of the curve (Figure III-9). A Nash factor of 0.4 was found to result in model predictions that agreed well with the cold-flow data.

As shown in Figure III-5, the bleed flowrate for the "blow-off" condition matches the cold-flow data to within 1/2%, but the base pressure prediction becomes asymptotic after 3.5% bleed. At 3.5%, the plume impingement results in a 3% loss in stagnation pressure according to the oblique shock calculations. The Nash "recompression criteria" indicate the actual stagnation pressure loss to be approximately 0.4 of the 3%. So the situation that exists is that increasing the bleed flowrate from 3.5% to 5.5% results in a small change in stagnation pressure loss and in the corresponding base pressure.

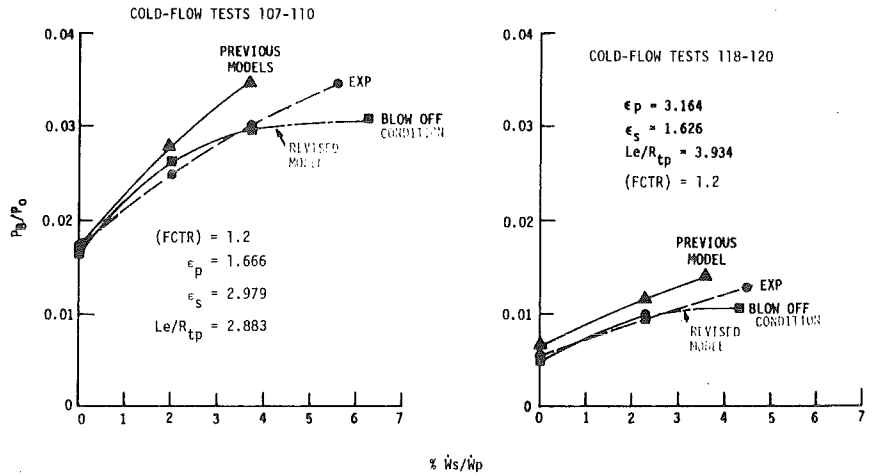

Figure III-5. Model Improvements Allowed More Accurate Predictions for Smaller Nozzle Spacing

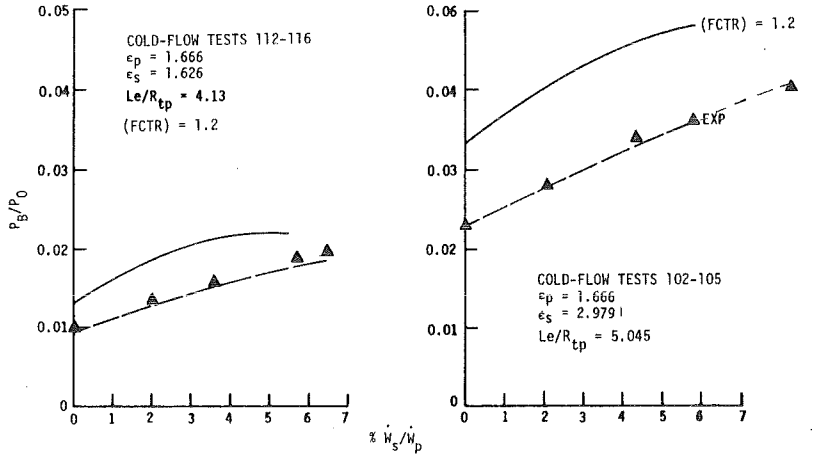

Figure III-6. Model Predictions became less Accurate with Increasing Nozzle Spacing

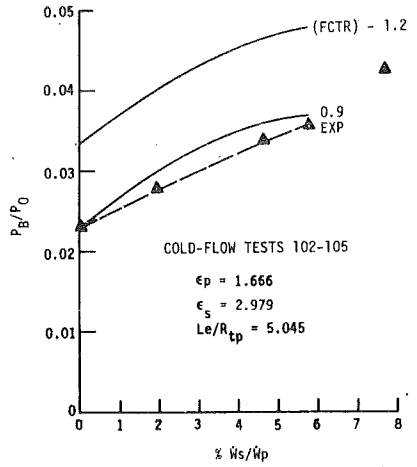

Figure III-7. Model Accuracy Improved by Changing Plume Scaling Factor

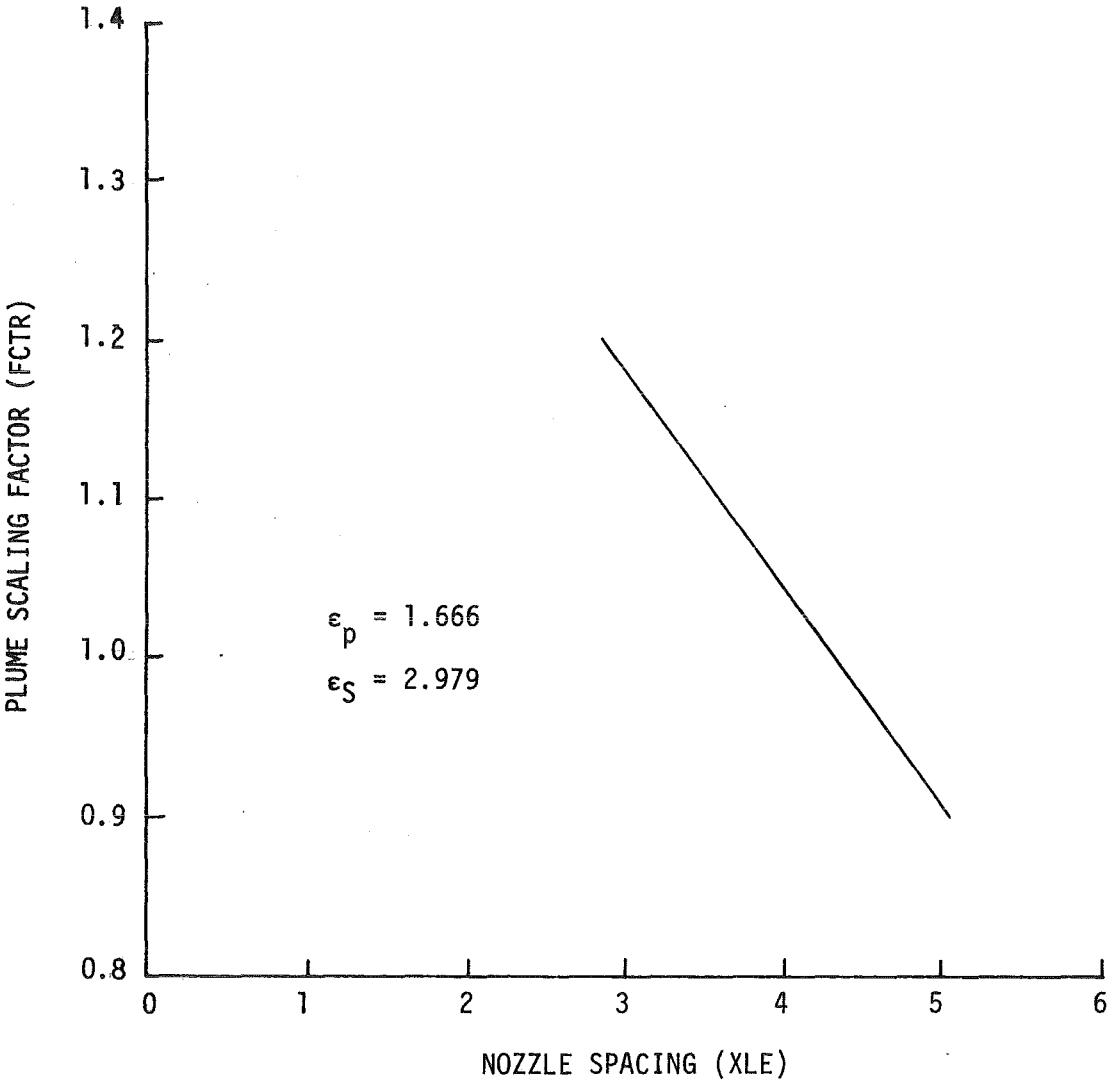

Figure III-8. Nozzle Spacing Influence on Plume Scaling Factor

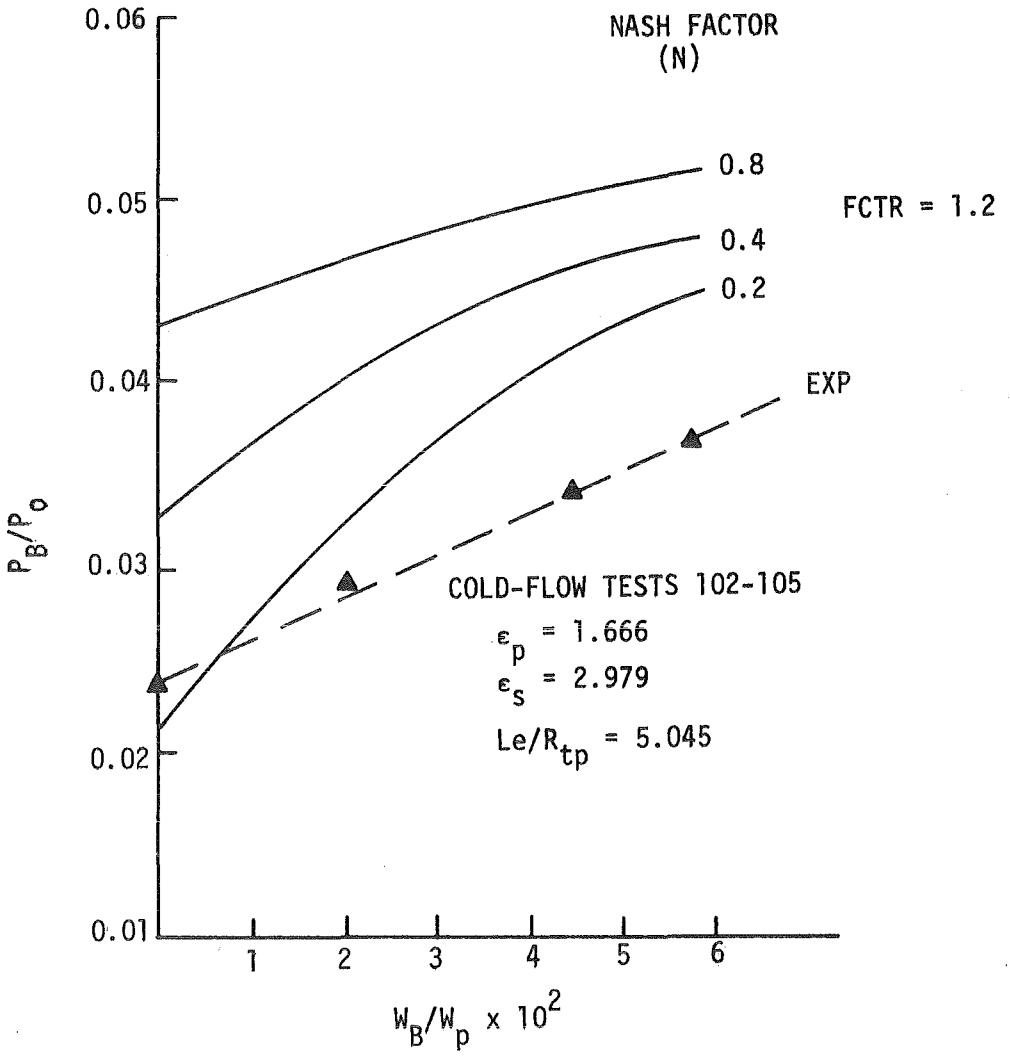

Figure III-9. Base Pressure versus Bleed Flow

The third empirical factor is the jet spreading parameter (sigma), which is used in the shear layer calculations and defines the rate at which the shear layer jets spread. Presently, the bleed flow model uses a correlation developed by Korst which states that the spreading parameter is a function of plume boundary Mach number. From the derivation of the shear layer calculations presented in Section III,B,1, it can be seen that the jet spreading parameter will influence the mass fraction Y_{pr} and recirculation temperature T_r/T_o. Calibration to the cold-flow data was not possible since the recirculation temperature was not measured during cold or hot-fire testing.

4. Parametric Analysis

A parametric analysis was performed to investigate the effects of varying bleed flow thermodynamic properties and primary nozzle geometry on bleed flow requirements. Changes were made in molecular weight (MW) and specific heat (C_p) for both primary and bleed flows, bleed flow to primary flow stagnation temperature ratio, nozzle axial spacing, primary nozzle area ratio, primary nozzle size and contour.

Table III-II lists the effects of bleed flow thermodynamic properties on bleed flow requirements. The nozzle configuration simulated was that used for the dual throat cold-flow tests (NAS 8-32666). Varying the ratio of specific heats (γ_B) for the bleed flow appears to have little effect on the required bleed flowrate. Variations in bleed flow molecular weight and stagnation temperature appear to have significant effects on bleed flow requirements. Decreasing the molecular weight of the bleed gas results in a lower required flowrate, whereas a decrease in stagnation temperature results in an increase in the required bleed flow. An increase in the primary flow gamma (γ_p) will also result in requiring less bleed flow to turn the plume for a shock-free attachment.

TABLE III-II

EFFECT OF BLEED FLOW PROPERTIES ON REQUIRED BLEED FLOWRATE

γ_P	γ_B	MW_P	MW_B	T_{OB}/T_{O_p}	$\% \frac{Ws}{W_P}$	P_B/P_{O_p}
1.23	1.40	20	29	1.0	11.93	.0483
1.23	1.15	20	29	1.0	11.54	.0483
1.23	1.40	20	29	0.5	15.22	.0483
1.23	1.40	20	15	1.0	8.60	.0483
1.40	1.23	29	20	1.0	4.95	.0310

γ_P - Primary Nozzle Flow Ratio of Specific Heat

γ_B - Bleed Flow Ratio of Specific Heat

MW_P - Molecular Weight Primary Nozzle

MW_B - Molecular Weight Bleed Flow

T_{OB}/T_{O_p} - Ratio of Stagnation Temperatures

$\% W_s/W_p$ - Bleed Flowrate

P_B/P_{Op} - Bleed Flow Pressure Ratio

NOTE: Configuration Simulated was Dual Throat Cold-Flow Hardware

III, B, Aerodynamic Bleed Flow Model (cont.)

The effect of geometric design parameters on bleed flow requirements was investigated by single parameter variations about a baseline configuration. A baseline configuration was generated from the operating specifications presented in the final report of the Dual-Fuel, Dual Throat Engine Preliminary Analysis (NAS 8-32967). Table III-III lists the main geometric design parameters for this design, and Figure III-10 shows the baseline geometry and plume contours for various bleed flowrates. For the baseline design, the bleed flow model calculated that a 5.94% bleed flowrate was needed for the plume to attach shock-free to the secondary nozzle, i.e., the blowoff condition. Reducing the bleed flow from the blowoff condition to approximately 3% showed that the resulting plume boundary pressure, plume contour, and shock strength were practically the same in the blowoff condition.

The results of varying the nozzle spacing are presented in Table III-IV. Figure III-11 shows the configurations used and the resulting plume contours for 0% bleed flow. For this case, the plume attachment point moves further upstream as the nozzle spacing increases. The plume boundary pressure also increases with increased nozzle spacing, resulting in a decreased slope of the plume at the attachment point. Further, as the nozzle spacing increases, the bleed flow requirement for flow attachment at the secondary throat also increases. The net effect of these trends is that the total flow angle decreases with increased nozzle spacing, resulting in reduced shock strength.

Table III-V lists the bleed flow requirements for varying the primary nozzle area ratio. As the primary nozzle area ratio increases, the bleed flow requirement decreases. For 0% bleed flow, increasing the primary nozzle area ratio causes the plume attachment point to move upstream and the plume boundary pressure to decrease. The decrease in plume boundary pressure

TABLE III-III

DUAL THROAT BASELINE GEOMETRY

Mode I Sea Level Thrust - 600,000 lbF
Mode I to Mode II Thrust Ratio - 3.2

SECONDARY NOZZLE:

Chamber Pressure	2800 psia
Mixture Ratio	2.8
Area Ratio	45.6
Contraction Ratio	2.5
Throat Radius	6.41 in.
Percent Mode I Thrust	70%
Inlet Radius	6.41 in.
Upstream Throat Radius	6.41 in.
Downstream Throat Radius	3.25 in.
Nozzle Length	123.7 in.

PRIMARY NOZZLE:

Chamber Pressure	4000 psia
Mixture Ratio	7.0
Area Ratio	2.7
Contraction Ratio	2.5
Throat Radius	2.90 in.
Percent Mode I Thrust	30%
Inlet Radius	2.90 in.
Upstream Throat Radius	2.90 in.
Downstream Throat Radius	1.80 in.
Nozzle Length	6.3 in.
Nozzle Spacing	2.75 in.

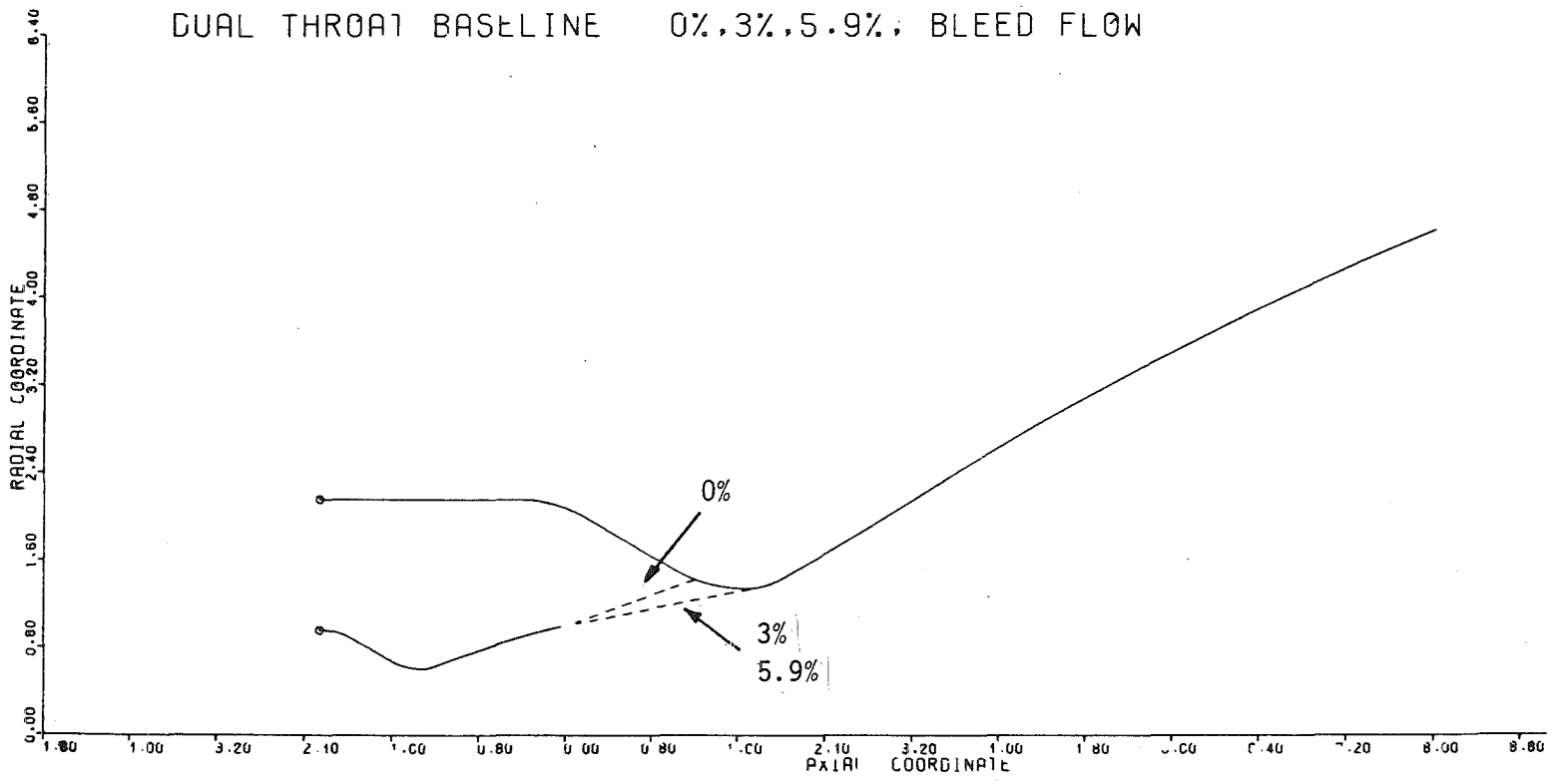

Figure III-10. Dual Throat Baseline Configuration

TABLE III-IV

VARIATION IN NOZZLE SPACING

XLE	W_s/W_p	P_B/P_0	M_b	α_{Plume}	δ_{Flow}	Θ_{Wall}	$\delta_{S.L.}$
2.0	0	.02782	2.81	26.0°	43°	-17°	.10763
	3.84	.05745	-	-	-	-	-
2.753	0	.04285	2.60	19.5	39.7	-20°	.15506
	3.0	.07023	2.35	11.5	10.32	1.18	.21629
	5.3	.071689	2.34	11.2	1.1	10.1	.22967
	5.94	.07170	-	-	-	-	-
3.5	0	.05530	2.47	15.4	37.8	-22.4	.20673
	3.0	.07793	2.29	9.8	14.7	-4.9	.25875
	8.18	.08215	-	-	-	-	-
4.0	0	.06239	2.41	13.4	36.8	-23.4	.24294
	3.0	.08187	2.27	9.0	17.0	-8.0	.28907
*	8.0	.08765	2.23	7.9	2.4	5.5	.32214
*	9.76	.08768	2.23	-	-	-	-
*	$P_B/P_0 > P_e/P_c$ Validity of Results Questionable						

M_{E_p} = 2.25 P_{cp} = 4000 psia

P_c/P_c = .08389 R_{tp} = 2.90

ε_p = 2.707

F Ratio = 3.2

XLE - Spacing Between Primary Nozzle Exit and Secondary Nozzle Throat

W_s/W_p - Bleed Flowrate

P_B/P_0 - Plume Boundary to Chamber Pressure Ratio

M_b - Mach Number Along Plume Boundary

α_{Plume} - Plume Angle at Attachment Point

δ_{Flow} - Total Flow Turning Angle

Θ_{Wall} - Wall Angle At Attachment Point

$\delta_{S.L.}$ - Shear Layer Thickness

ε_p - Primary Nozzle Area Ratio

R_{tp} - Primary Nozzle Throat Radius

F Ratio - Mode I to Mode II Thrust Ratio

P_e/P_o - Pressure Ratio for Primary Nozzle

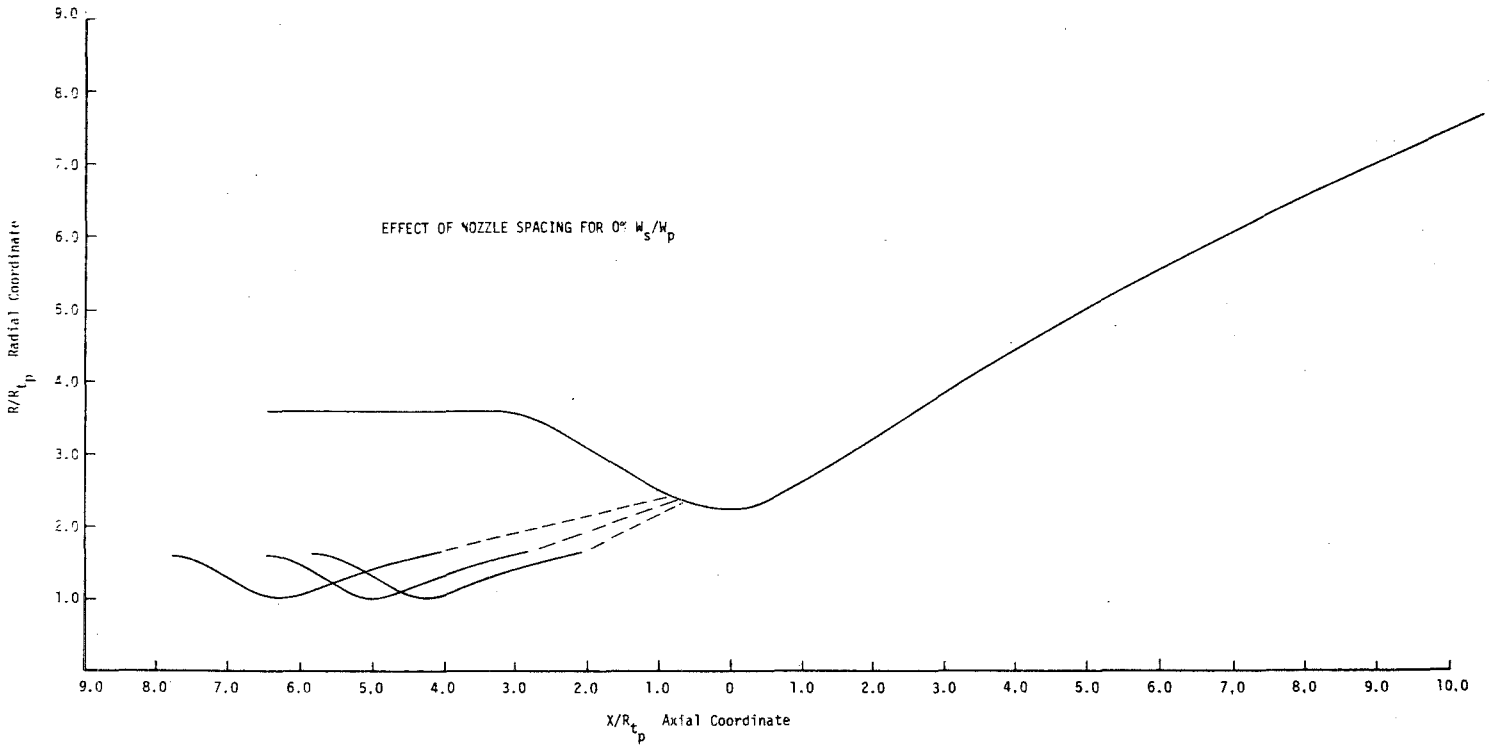

Figure III-11. Effect of Nozzle Spacing for 0% W_s/W_p

TABLE III-V

VARIATION IN PRIMARY NOZZLE AREA RATIO

ε_p	W_s/W_p	P_B/P_0	M_b	α_{Plume}	δ_{Flow}	Θ_{Wall}	$\delta_{S.L.}$
1.62	0	.06569	2.38	23.6	36.4	-12.8	.24237
	3.0	.09087	2.21	18.4	14.4	4.0	.29991
	8.17	.09428	-	-	-	-	-
		M_{E_p} = 1.83		P_e/P_o = .18098			
2.707	0	.04285	2.60	19.5	39.7	-20.2	.15506
	3.0	.07023	2.35	11.5	10.3	1.18	.21629
	5.3	.07169	2.34	11.2	1.1	10.1	.22967
	5.94	.07170	-	-	-	-	-
		M_{E_p} = 2.25		P_e/P_o = .08389			
4.06	0	.03929	2.64	13.8	40.4	-26.7	.10816
	3.0	.07045	2.35	4.4	8.8	-4.3	.16162
	5.55	.07246	-	-	-	-	-
		M_{E_p} = 2.54		P_e/P_o = .04782			
	XLE = 2.753			P_{cp} = 4000			
	R_{tp} = 2.90			F Ratio = 3.2			

XLE - Spacing Between Primary Nozzle Exit and Secondary Nozzle Throat

W_s/W_p - Bleed Flowrate

P_B/P_0 - Plume Boundary to Chamber Pressure Ratio

M_b - Mach Number Along Plume Boundary

α_{Plume} - Plume Angle at Attachment Point

δ_{Flow} - Total Flow Turning Angle

Θ_{Wall} - Wall Angle at Attachment Point

$\delta_{S.L.}$ - Shear Layer Thickness

ε_p - Primary Nozzle Area Ratio

R_{tp} - Primary Nozzle Throat Radius

F Ratio - Mode I to Mode II Thrust Ratio

P_e/P_o - Pressure Ratio for Primary Nozzle

is due to the decreasing nozzle exit pressure from the increase in nozzle area ratio. Figure III-12 shows the resulting plume contours for 0% bleed flow.

Changing the primary nozzle size was accomplished by keeping the same primary nozzle area ratio but changing the throat area. A change in throat area corresponds to a change in the Mode I to Mode II thrust ratio. Table III-VI lists the change in bleed flow requirements for change in throat radius. As the throat radius increases, decreasing thrust ratio, the bleed flow requirement increases slightly. For the 0% bleed flow case, the plume attachment point moves upstream, and the plume boundary pressure increases with increasing throat radius. Figure III-13 shows the plume contours for the 0% bleed flow case.

The effect of primary expansion nozzle contour was evaluated by comparing aerodynamic model predictions for the baseline Bell contour nozzle with an exit angle of 16° to results calculated for a 10° conical nozzle. The low exit angle conical nozzle is predicted to require less bleed flow (4.5% vs 5.9%) which subsequently results in a lower base pressure ratio (0.0717 to 0.05489). These decreased values are due to the change of nozzle exit angle which, when combined with the Prandtl-Meyer expansion angle at the nozzle lip, results in a smaller plume expansion angle. Having a plume boundary with a shallow angle requires less bleed flow and a smaller base pressure to turn the plume and allow it to attach tangentially to the secondary nozzle wall.

In summary, the dual throat aerodynamic bleed flow model developed during NAS 8-32666 has been updated to include a procedure for predicting the base pressure generated in Mode II operation with zero bleed flow and provide for dissimilar exhaust gases to be used for the primary and bleed flows. These changes have enhanced the analysis capability of the Mode II

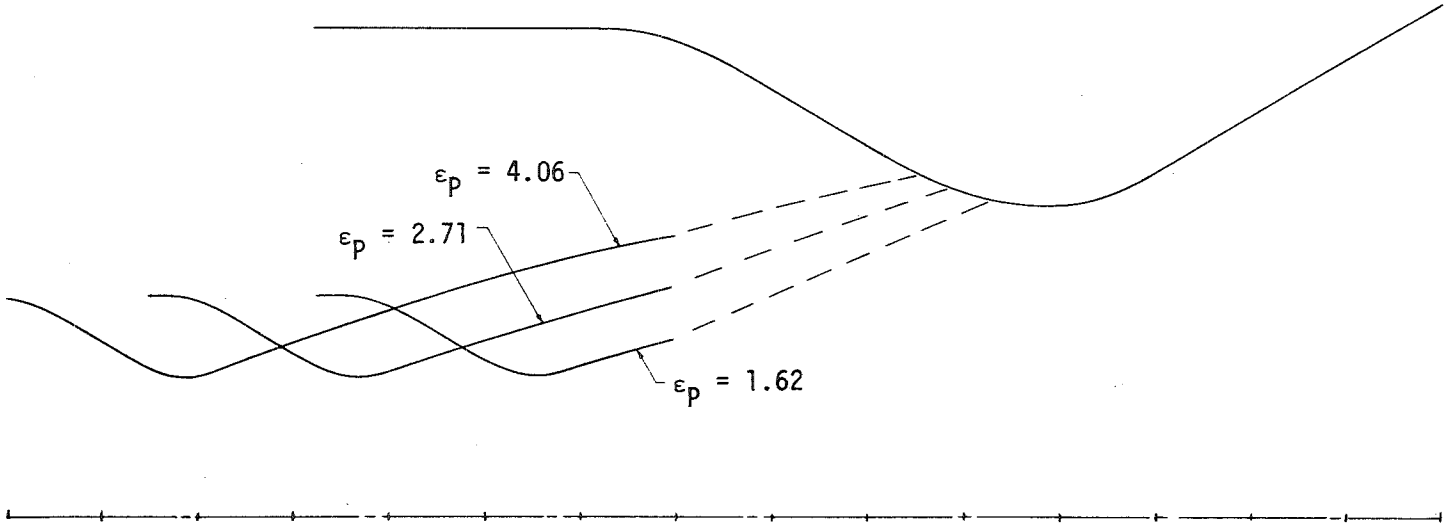

Figure III-12. Effect of Varying Primary Nozzle Area Ratio on Plume Attachment for 0% W_s/W_p

TABLE III-VI

VARIATION IN PRIMARY NOZZLE SIZE

R_{tp}	W_s/W_p	P_B/P_0	M_b	α_{Plume}	δ_{Flow}	Θ_{Wall}	$\delta_{S.L.}$	F Ratio
*4.29	0	.13476	2.0	.988°	29.87°	-28.9	.16368	1.5
*	5.492	.14353	-	-	-	-	-	-
3.48	0	.07470	2.32	10.5	35.3	-24.8	.15444	2.25
	6.643	.11117	-	-	-	-	-	-
2.90	0	.04285	2.60	19.5	39.7	-20.2	1556	3.2
	3.0	.07023	2.35	11.5	10.3	1.18	.21629	
	5.3	.071689	2.34	11.2	1.1	10.1	.22967	
	5.94	.07170	-	-	-	-	-	-
2.44	o	.02378	2.89	28.2	44.3	-16.1°	.16234	4.5
	5.311	.04603	-	-	-	-	-	-

M_{Ep} = 2.25 P_{cp} = 4000 psia

P_e/P_c = .08389 XLE = 2.753

ε_p = 2.707

*P_B/P_0 > P_e/P_o Validity of Result Questionable.

XLE - Spacing Between Primary Nozzle Exit and Secondary Nozzle Throat

W_s/W_p - Bleed Flowrate

P_B/P_0 - Plume Boundary to Chamber Pressure Ratio

M_b - Mach Number Along Plume Boundary

α_{Plume} - Plume Angle at Attachment Point

δ_{Flow} - Total Flow Turning Angle

Θ_{Wall} - Wall Angle at Attach Point

$\delta_{S.L.}$ - Shear Layer Thickness

ε_p - Primary Nozzle Area Ratio

R_{tp} - Primary Nozzle Throat Radius

F Ratio - Mode I to Mode II Thrust Ratio

P_e/P_o - Pressure Ratio for Primary Nozzle

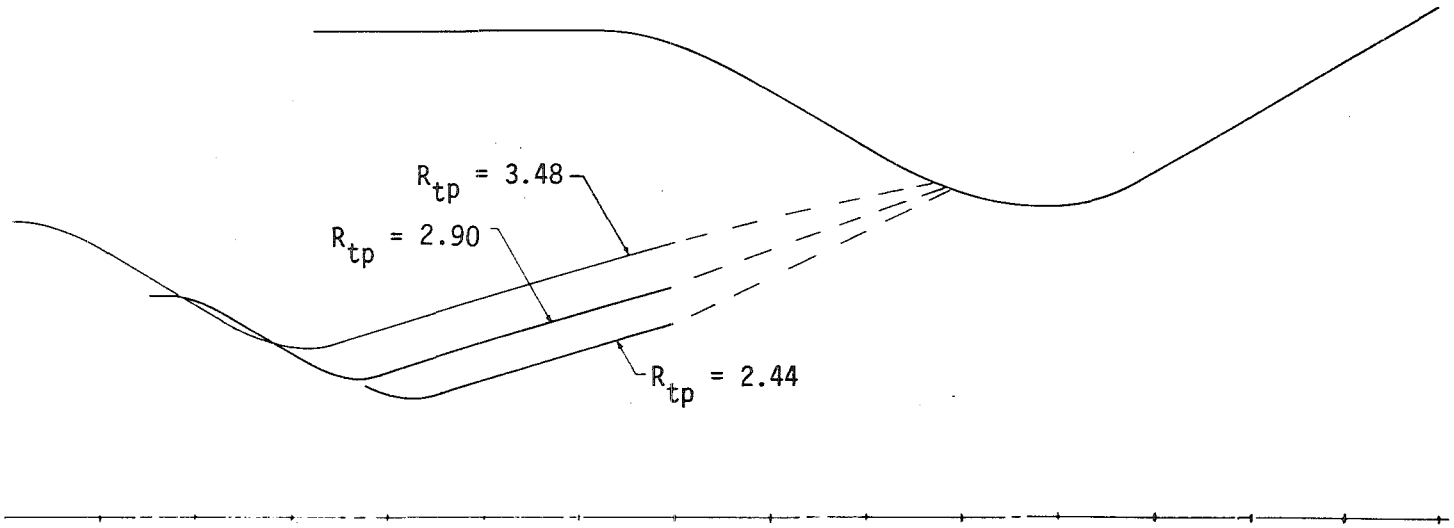

Figure III-13. Effect of Varying Primary Nozzle Size on Plume Attachment for 0% W_s/W_p. ε = 2.71

dual throat operation and provide a design tool to permit tradeoffs of various geometric and operating parameters.

The improved model has been used to evaluate bleed flow requirements as a function of both bleed flow properties and geometric design parameters. These results are summarized in Table III-VII. This model, together with other dual-throat design and analysis improvements, has also been utilized to assess changes in predicted performance of the dual-throat concept as discussed in later sections of this report. The bleed flow model, with suitable modifications, also provided the basis for prediction of the base flow region of the dual expander concept as described in Section V of this report.

C. MODE II BOUNDARY LAYER LOSS VERIFICATION

1. Previous Simplified Approach

During Contract NAS 8-32666, the Mode II boundary layer loss was obtained by using the turbulent boundary layer chart procedures outlined in Appendix B of CPIA No. 178 with some additional considerations to the aerodynamics associated with Mode II operation. The primary assumptions for this calculation are that the boundary thrust decrement is additive and proportional to the momentum thickness. The boundary layer loss was obtained by using the TBL chart procedures for a conventional Rao nozzle having an area ratio defined by the point of plume attachment and the primary throat. A ratio of the shear layer momentum thickness (at the point of attachment given by the aerodynamic bleed flow program) to the momentum thickness given by the TBL chart procedures was used to proportion the conventional nozzle boundary layer loss to approximate the actual thrust layer loss obtained for the nozzle from the attachment point to the secondary nozzle exit, yielding the total Mode II boundary layer loss. This procedure is outlined in Figure III-14.

TABLE III-VII

BLEED FLOW THERMODYNAMIC PROPERTIES EFFECTS

PROPERTY	EFFECT ON BLEED FLOW REQUIREMENT
Bleed Flow γ_B	Not Significant
Temperature Ratio $\left(\frac{T_{OB}}{T_{OP}}\right)$	Increases with Decreasing $\left(\frac{T_{OB}}{T_{OP}}\right)$
MW Bleed Flow	Decreases with Decreasing MW_B

GEOMETRIC PARAMETER EFFECTS

PROPERTY	EFFECT ON BLEED FLOW REQUIREMENT
Nozzle Spacing (XLE)	Decreases with Decreasing XLE
Primary Nozzle Area Ratio (ϵ_p)	Increases with Decreasing ϵ_p
Primary Nozzle Size (R_{tp})	Decreases with Decreasing R_{tp}
Primary Lip Angle (THE_p)	Decreases with Decreasing THE_p

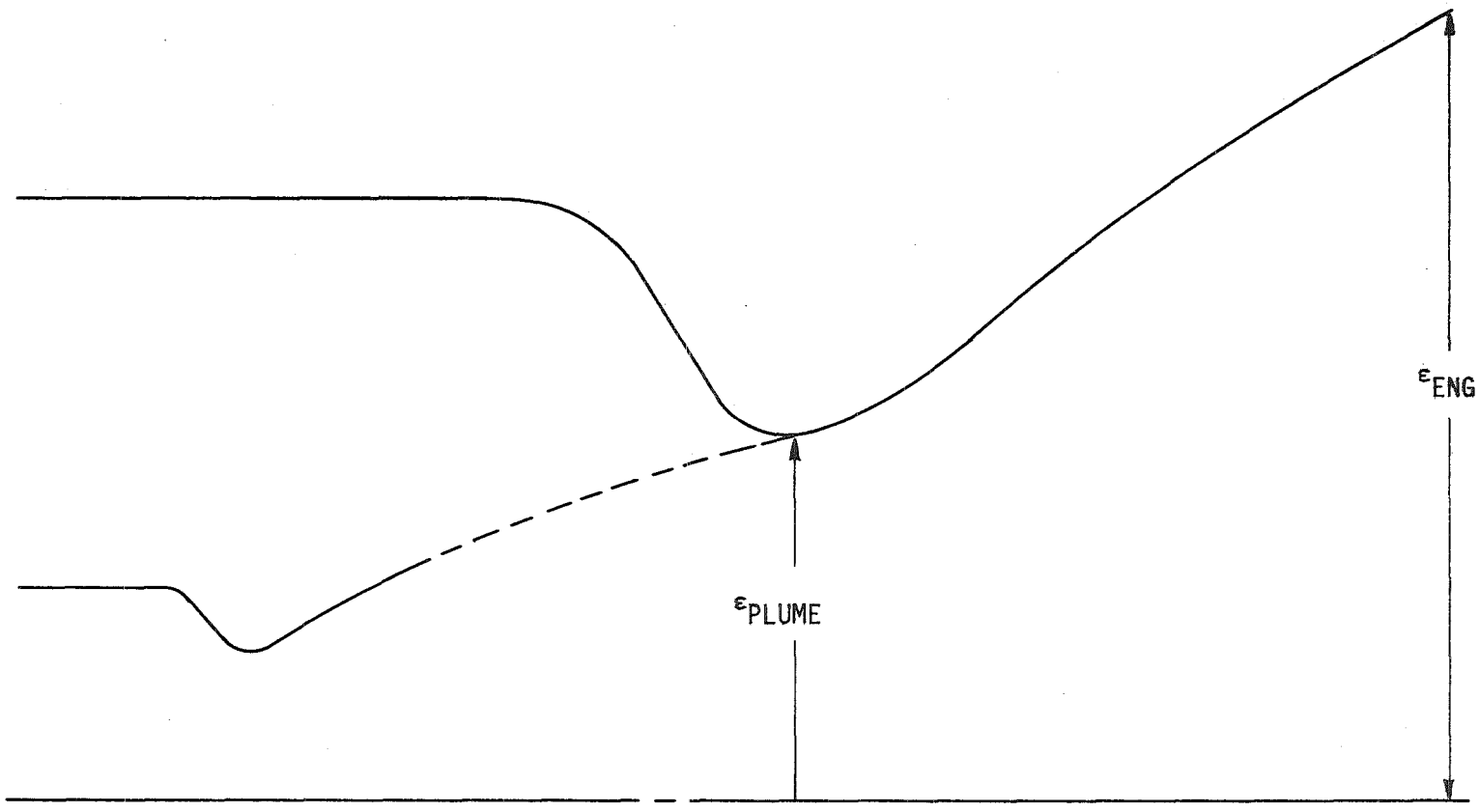

$$\text{MODE II } \Delta I_{SP_{B.L.}} = \left(\frac{\theta_{BLEED}}{\theta_{CONV}}\right)_{\varepsilon_{PLUME}} \Delta I_{SP_{\varepsilon_{PLUME}}} + \left(\Delta I_{SP_{\varepsilon_{ENG}}} - \Delta I_{SP_{\varepsilon_{PLUME}}}\right)$$

NAS 8-32666 BOUNDARY LAYER LOSS METHODOLOGY θ - MOMENTUM THICKNESS

Figure III-14. NAS 8-32666 Boundary Layer Loss Methodology

These calculations were made by assuming an adiabatic wall to simplify the calculation of loss due to heat extraction from the boundary as well as the gain due to the addition of this heat to the incoming regenerative coolant fuel.

2. BLIMP Analysis

The BLIMP computer program was used to provide a rigorous analysis of the boundary layer loss during Mode II operation for comparison to the simplified approach described above. BLIMP was successfully run using the Kendall and binary diffusion options for the Mode II dual throat baseline configuration with full bleed flow. These options are consistent with the standardized JANNAF performance methodology. To accomplish this, it was necessary to modify the aerodynamic bleed flow model to generate additional points used in the spline fit to describe the effective Mode II "nozzle contour" and to calculate the momentum thickness at the plume attachment point, including the contribution due to the bleed flow. Also, the TDK program was modified to accept the increased spline fit size needed to calculate the pressure profile to be used in BLIMP.

The BLIMP run was started at the plume attachment point (Station 1) and continued throughout the secondary nozzle. The BLIMP input parameter S(1), which represents the length of a flat plate required to generate the desired momentum thickness, was varied until the momentum thickness at Station 1 equaled the momentum thickness calculated by the bleed flow program. In this manner, the conditions for the first calculation station within the BLIMP solution are representative (at least in terms of momentum deficit) of the conditions calculated for the shear layer using the bleed flow model. In other words, the BLIMP analysis was started with initial boundary layer profiles which are representative of the boundary layer growth within the primary nozzle and shear layer, including the effects of bleed flow addition.

III, C, Mode II Boundary Layer Loss Verification (cont.)

Starting with these initial conditions, the BLIMP computer program calculated the additional boundary layer growth in the secondary nozzle downstream of the plume attachment to the nozzle exit. Standard BLIMP parameters at the final station were then used to calculate the net boundary layer loss, as shown in Table III-VIII.

Table III-VIII also shows a comparison between the boundary layer loss calculated from the BLIMP analysis and that determined by using the simplified procedure from NAS 8-32666. As can be seen, the net loss based on the BLIMP results is more than twice as great as the loss calculated by using the simplified procedure. Since the BLIMP solution is by far the more rigorous procedure, it is considered the best available current estimate for Mode II boundary layer losses. It should be noted, however, that even the net boundary layer loss from the BLIMP solution includes the performance loss resulting from the addition of the bleed flow.

As a result of the poor comparison between the simplified and rigorous boundary layer loss procedures, a new simplified procedure was developed in order to provide loss estimates close to those calculated from the BLIMP procedure without extensive and detailed analysis. While the revised procedure still uses the TBL chart as a basis for the loss calculation, it scales the results to account for shear layer effects in a different manner than the previous method.

Briefly, the TBL chart method is used to calculate the momentum thickness for a conventional nozzle expansion from the primary nozzle to the plume attachment point. The momentum thickness calculated from the shear model is then divided by this conventional momentum thickness to define a parameter, RTHETA, which is used in the simplified procedure to account for upstream influences on the boundary layer. Thus,

TABLE III-VIII

COMPARISON OF BOUNDARY LAYER LOSS CALCULATIONS

Mode II Baseline Configuration (See Table III-III)
% Bleed Flow = 5.3

Boundary Layer Performance Parameters	BOUNDARY LAYER ANALYSIS TECHNIQUE		
	BLIMP	NAS 8-32666 Simplified Procedure	Revised Procedure
Total Flowrate (lbm/sec)	483.3	483.3	483.3
Gross Thrust Loss (lbF)	8095	3335	7974
Gross Isp Loss (sec)	16.8	6.9(1)	16.5(2)
Total Heat Loss (Btu/sec)	37,050	0	N/A
Isp Gain From Regen Heat (sec)	3.3	0	3.4(3)
Net BLL (sec)	13.5	6.9	13.1

(1) Based on TW/TS = 1.0 RTHETA = 1.00

(2) Based on TW/TS = 0.2 RTHETA = 2.22

(3) Based on Difference Between Boundary Layer Loss for TW/TS = 0.2 & TW/TS = 1.0

$\frac{T_W}{T_S}$ = $\frac{\text{Wall Temperature}}{\text{Stagnation Temperature}}$

III, C, Mode II Boundary Layer Loss Verification (cont.)

$$\text{RTHETA} = \left[\theta_{\text{shear}}/\theta_{\text{TBL}}\right]_{\substack{\text{model} \\ \text{chart}}} \quad \text{Plume attach point}$$

Previously defined trends, such as those shown in Figure III-15, are used to estimate the change in the RTHETA value for further expansion in the secondary nozzle section. This final RTHETA value (i.e., at the secondary nozzle exit) is used to ratio the momentum thickness calculated for a conventional nozzle expansion from the primary nozzle throat to the secondary nozzle exit, i.e.,

$$\theta_{\text{Exit}} = \theta_{\text{Exit, TBL}} \times \text{RTHETA}$$

The boundary layer calculations are made by using the actual wall temperature conditions. In the event of regenerative cooling, the new approach also takes into account the increase in the Isp_{ODE} due to the increased propellant enthalpy transferred to the regenerative coolant.

This approach was incorporated into a computer program called DT*BLLOSS. The inputs required for the program are 1) characteristic velocity (C_p^*), 2) chamber pressure (P_{cp}), 3) throat radius (R_{tp}), 4) ratio of specific heats (γ_p), 5) Mode II area ratio (ε_{eng}), 6) ODE Isp at ε_{eng}, 7) area ratio at plume attachment point (ε_{PLM}), and 8) momentum thickness (θ_{Bleed}) at the plume attachment point. The first six parameters are obtained from ALRC's Dual Throat Geometry and Performance Prediction Program (FD 0169). The last two parameters come from the Aerodynamic Bleed Flow Program (FD 0170).

The results of this "revised procedure" for the baseline case are compared to both the BLIMP rigorous and previous simplified cases in Table III-VIII. As noted, the new procedure provides loss predictions which are similar to the BLIMP calculations. The impact of this new procedure on the

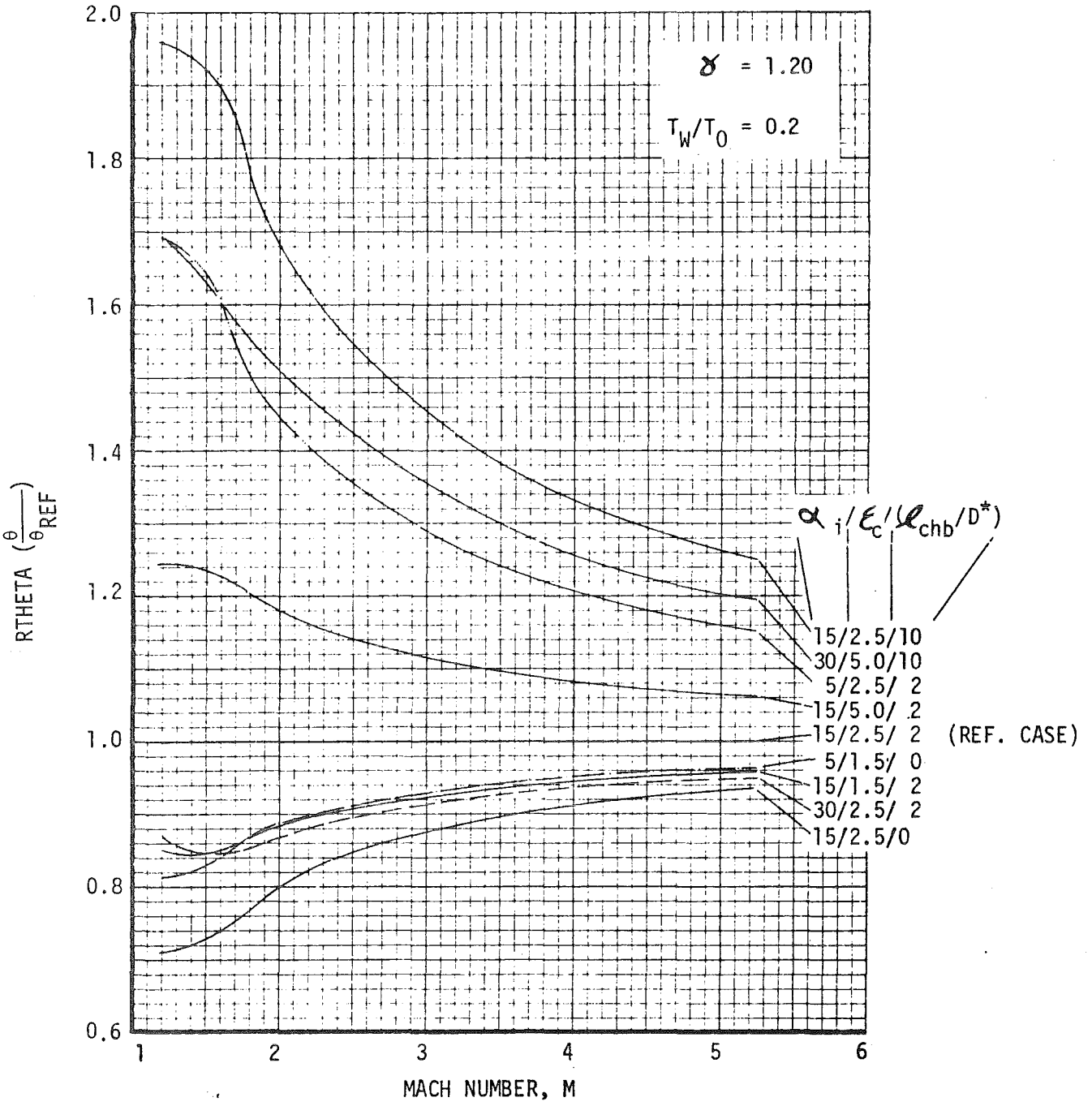

Figure III-15. Effect of Nozzle Inlet Conditions on the Momentum Thickness for a Cooled Nozzle Wall

performance predictions for Mode II dual throat operation is identified quantitatively in Section III,F of this report.

D. SHOCK MODEL

The objective of this subtask was to develop a method for obtaining two-dimensional axially symmetric flow field solutions that include the effects of shocks to estimate shock effects on performance and thermal operating characteristics. Mode II operation at design conditions will necessarily contain shock waves, the effect of which may be negligible at low area ratios but which are significant at high area Mode II conditions.

Since shock wave development in a nozzle is fundamentally a two-dimensional problem, a two-dimensional computer analysis must be used to predict the effect of shocks on performance. The computer code selected for this purpose is the VNAP code (Ref. 4). It has been modified for use in calculating both the flow field within the dual throat nozzle during Mode II operation and the resulting performance.

The VNAP program was selected for performing the dual throat nozzle calculations because it is the only computer code readily available that is capable of treating supersonic nozzle flow with imbedded shocks in a general manner. It is capable of calculating viscous as well as inviscid steady and unsteady internal flow. The approach used is to solve the Navier-Stokes equations for two-dimensional, time-dependent, compressible flow. The fluid is assumed to be a perfect gas. An explicit artificial viscosity is used for the shock calculations. The steady-state solution is obtained as the asymptotic solution for large time. The nozzle walls are transformed to a rectangular grid so that the resulting partial differential equations can be solved by using the second-order MacCormack finite-difference scheme.

III, D, Shock Model (cont.)

Modifications to VNAP were required to add a thrust calculation for obtaining thrust chamber performance and converting the plotting subroutines for use with the Cal-Comp plotter. Three cases were investigated:

(1) A shock-free nozzle configuration. Output from this case was then compared with output from TDK to verify and calibrate the accuracy of the VNAP code.

(2) A baseline design configuration where bleed flow is used to control the plume attachment.

(3) A baseline design configuration with zero bleed flow. Output from this case was used to define the freestream boundary conditions after the shock.

Previously, VNAP had been applied mainly to transonic analyses. This study was the first time that the program was used to investigate supersonic flow fields such as those occurring in large area ratio nozzles. Systematic errors were expected because of the large solution grid used in the finite-difference approach.

To determine the magnitude of these errors, VNAP was used to analyze the flow field for a conventional shock-free nozzle with the same Mode II area ratio and envelope as that of the dual-throat baseline. A comparison of the performance calculated by VNAP with that calculated by TDK for the conventional nozzle provided a performance correction factor which presumably could be applied to the VNAP solutions obtained with shock flow. The results of this calibration are as follows:

$$Isp_{VNAP} = 484.2 \text{ sec}$$

$$Isp_{TDK} = 473.5$$

$$f_{Isp\ corr} = \frac{473.5}{484.2} = .978$$

III, D, Shock Model (cont.)

Therefore, it appears that the VNAP calculation results in a performance which is approximately 2% greater than an accurate method of characteristic solution (TDK) and that the .978 correction factor should be utilized for the two additional VNAP cases which contain flow shocks.

Plots were generated showing velocity, Mach number, pressure, temperature, and density profiles to help visualize the flow field situation. Examples of these plots for the conventional nozzle analysis are shown in Figures III-16 through III-21. To help facilitate the computer storage requirement, the nozzle's flow fields were arbitrarily divided into two segments, referred to as upstream and downstream on the referenced figures.

The VNAP simulation of the dual throat baseline Mode II configuration predicted a nozzle performance of 480.2 seconds. This was corrected to 469.6 seconds by using the correction factor obtained from the conventional nozzle simulation. The resulting Mode II nozzle divergence efficiency was found to be 0.988, compared to a conventional nozzle efficiency of .996. Thus, the divergence efficiency of the dual throat Mode II expansion is approximately 0.8% less than that of a conventional nozzle expanding to the same area ratio. This is only 0.3% greater than the value used during NAS 8-32666.

Plots of the flow field (Figures III-22 to III-27) show a right running shock wave forming in the nozzle due to the compression caused by the highly contoured secondary nozzle wall. This shock structure, however, never reaches the downstream secondary wall and thus has only a slight influence on performance and heat transfer.

The VNAP program provided a means for determining the gas-side boundary conditions used in the thermal analysis of the secondary throat

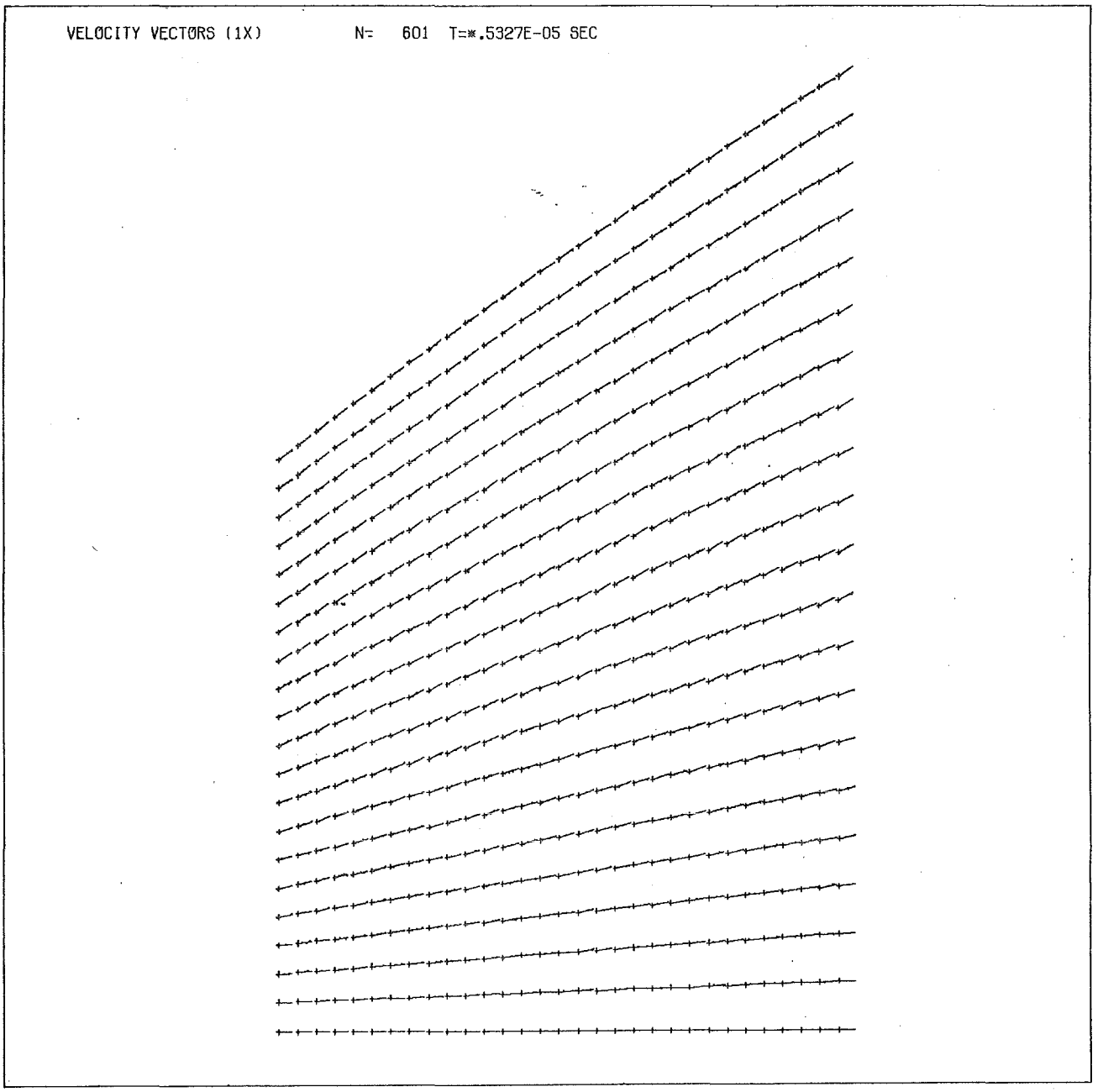

Figure III-16. Conventional Nozzle Upstream Velocity Vector Plot

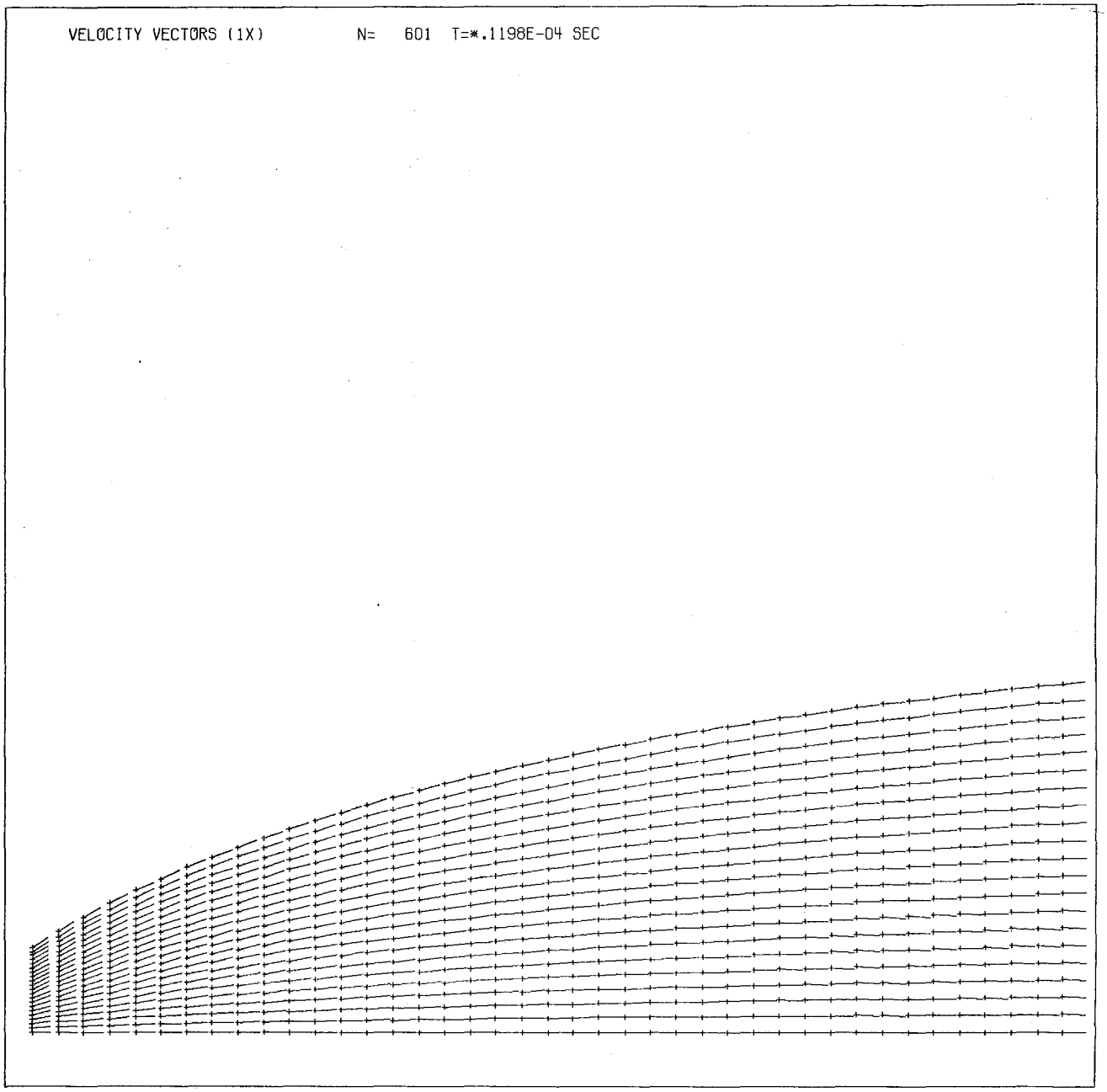

Figure III-17. Conventional Nozzle Downstream Velocity Vector Plot

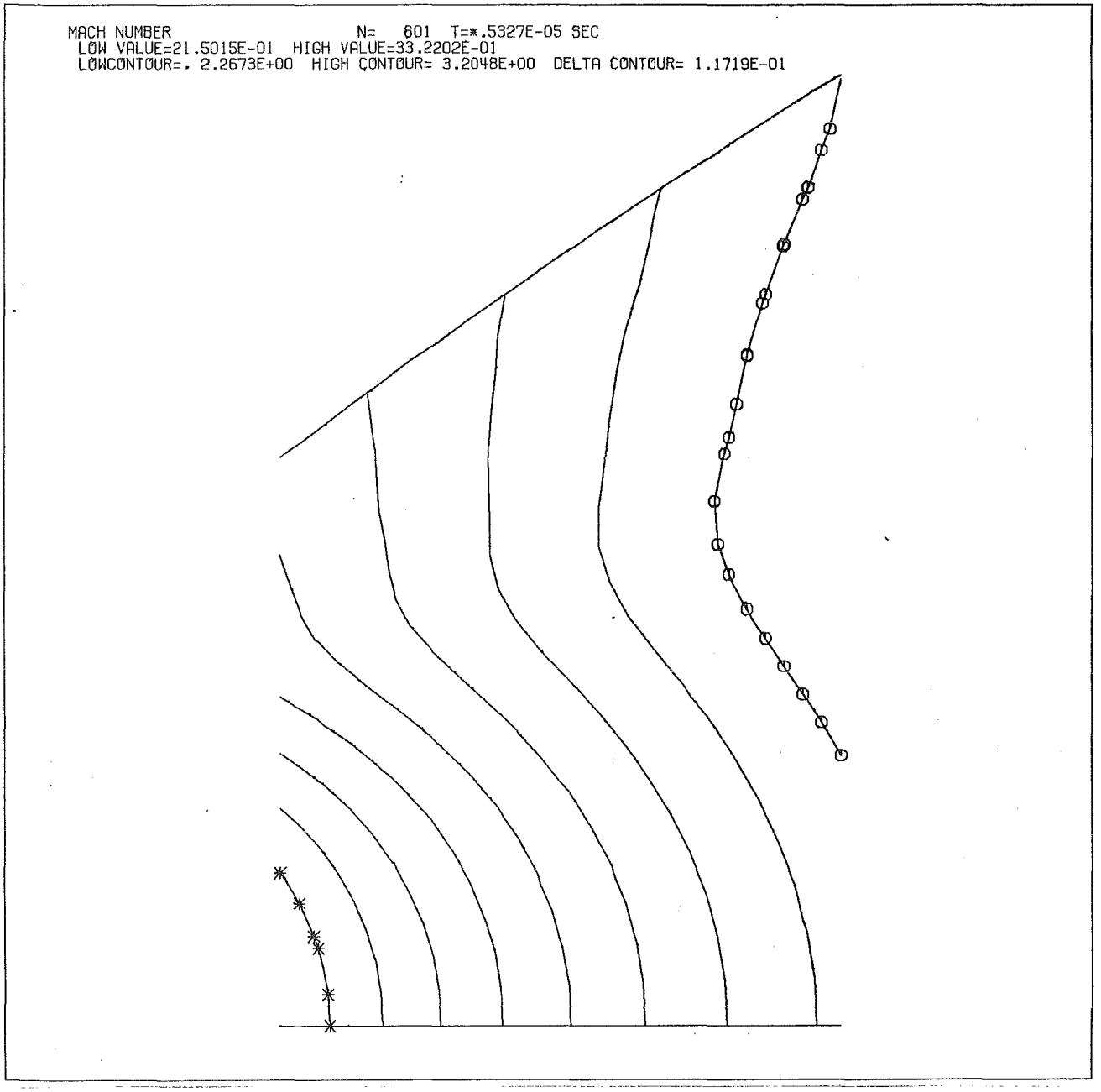
MACH NUMBER N= 601 T=*.5327E-05 SEC
LOW VALUE=21.5015E-01 HIGH VALUE=33.2202E-01
LOWCONTOUR=. 2.2673E+00 HIGH CONTOUR= 3.2048E+00 DELTA CONTOUR= 1.1719E-01

Figure III-18. Conventional Nozzle Upstream Mach Number Plot

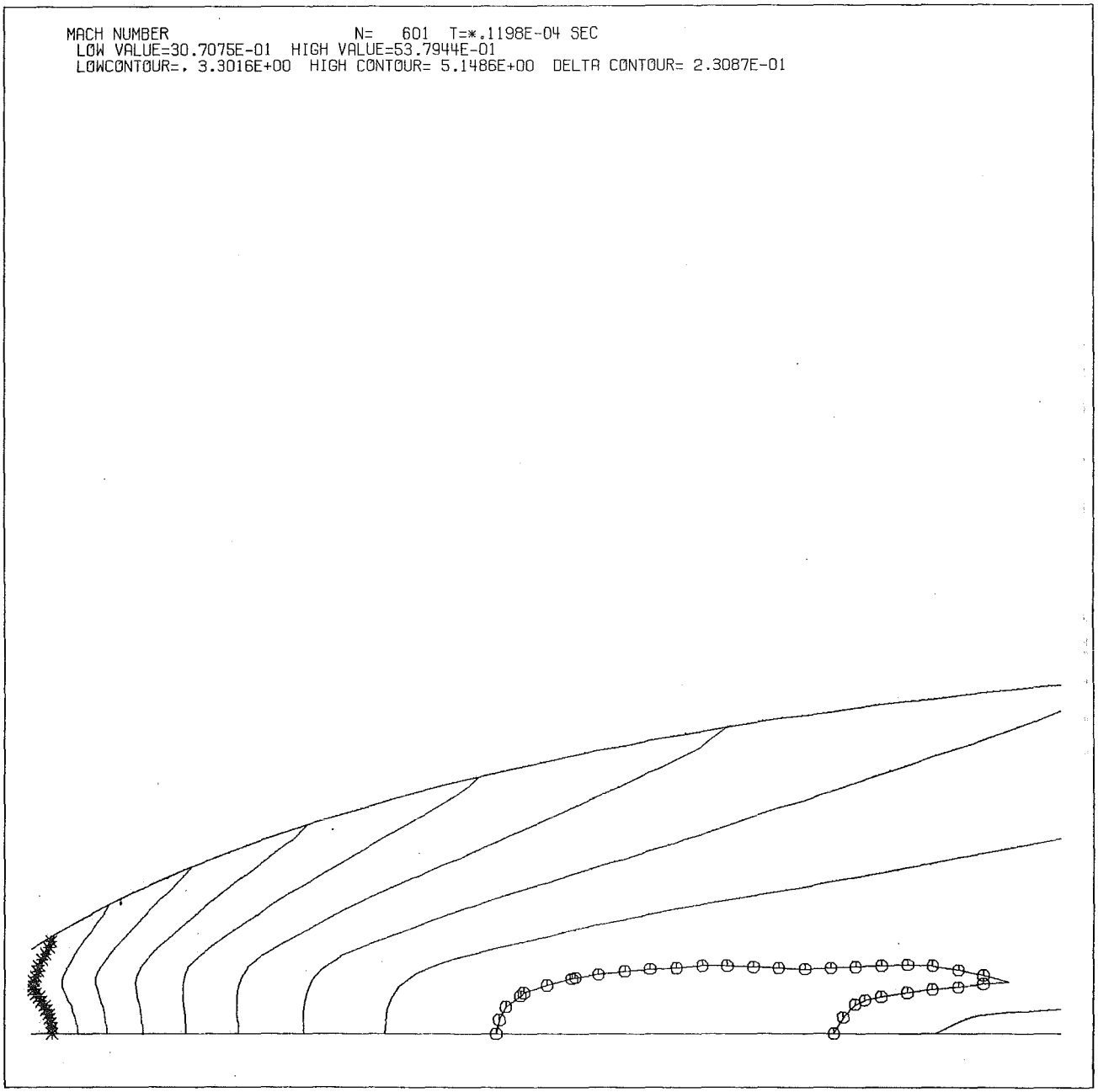
MACH NUMBER N= 601 T=*.1198E-04 SEC
LOW VALUE=30.7075E-01 HIGH VALUE=53.7944E-01
LOWCONTOUR=, 3.3016E+00 HIGH CONTOUR= 5.1486E+00 DELTA CONTOUR= 2.3087E-01

Figure III-19. Conventional Nozzle Downstream Mach Number Plot

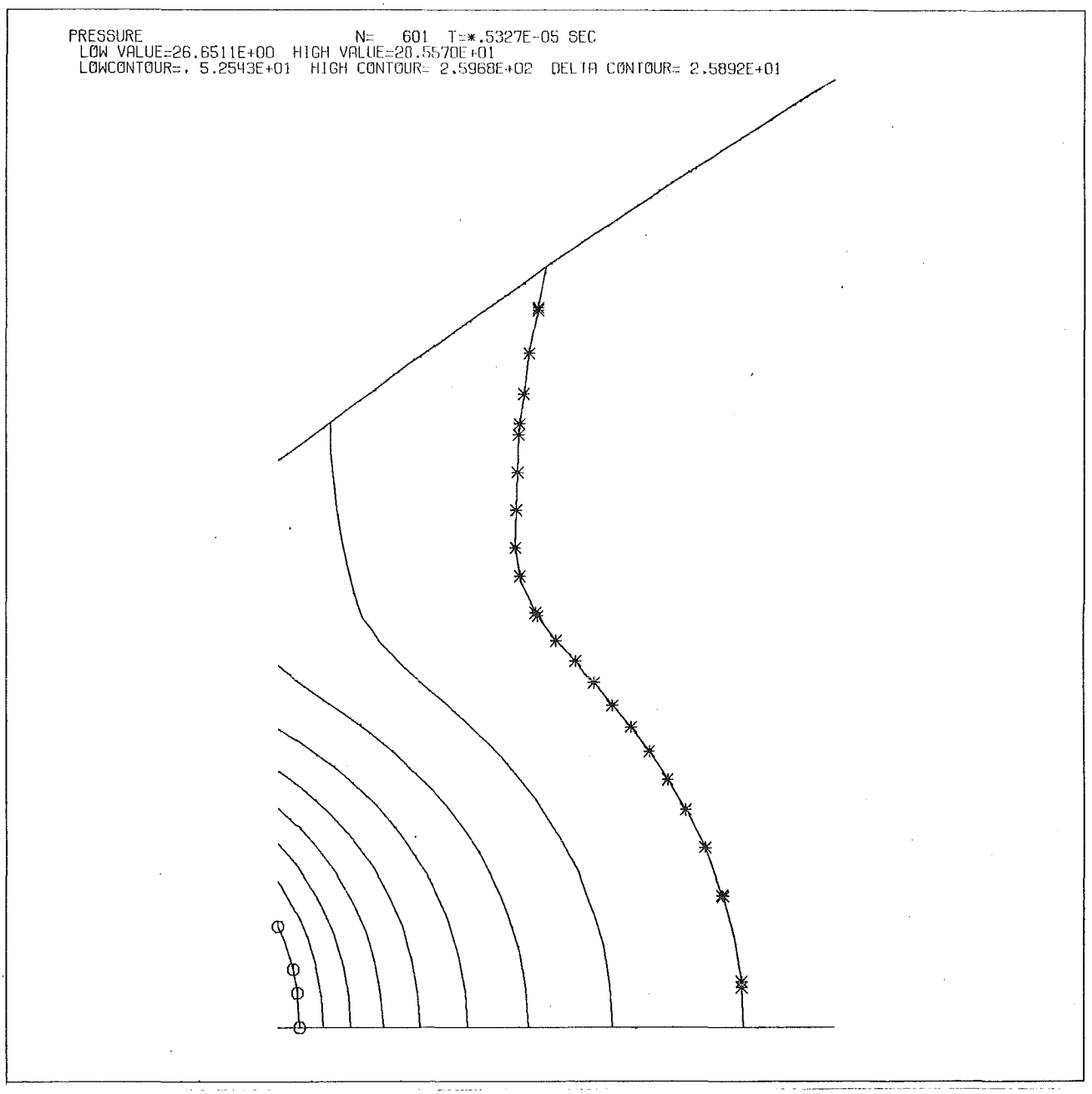
PRESSURE N= 601 T=*.5327E-05 SEC
LOW VALUE=26.6511E+00 HIGH VALUE=20.5570E+01
LOWCONTOUR=, 5.2543E+01 HIGH CONTOUR= 2.5968E+02 DELTA CONTOUR= 2.5892E+01

Figure III-20. Conventional Nozzle Upstream Pressure Plot

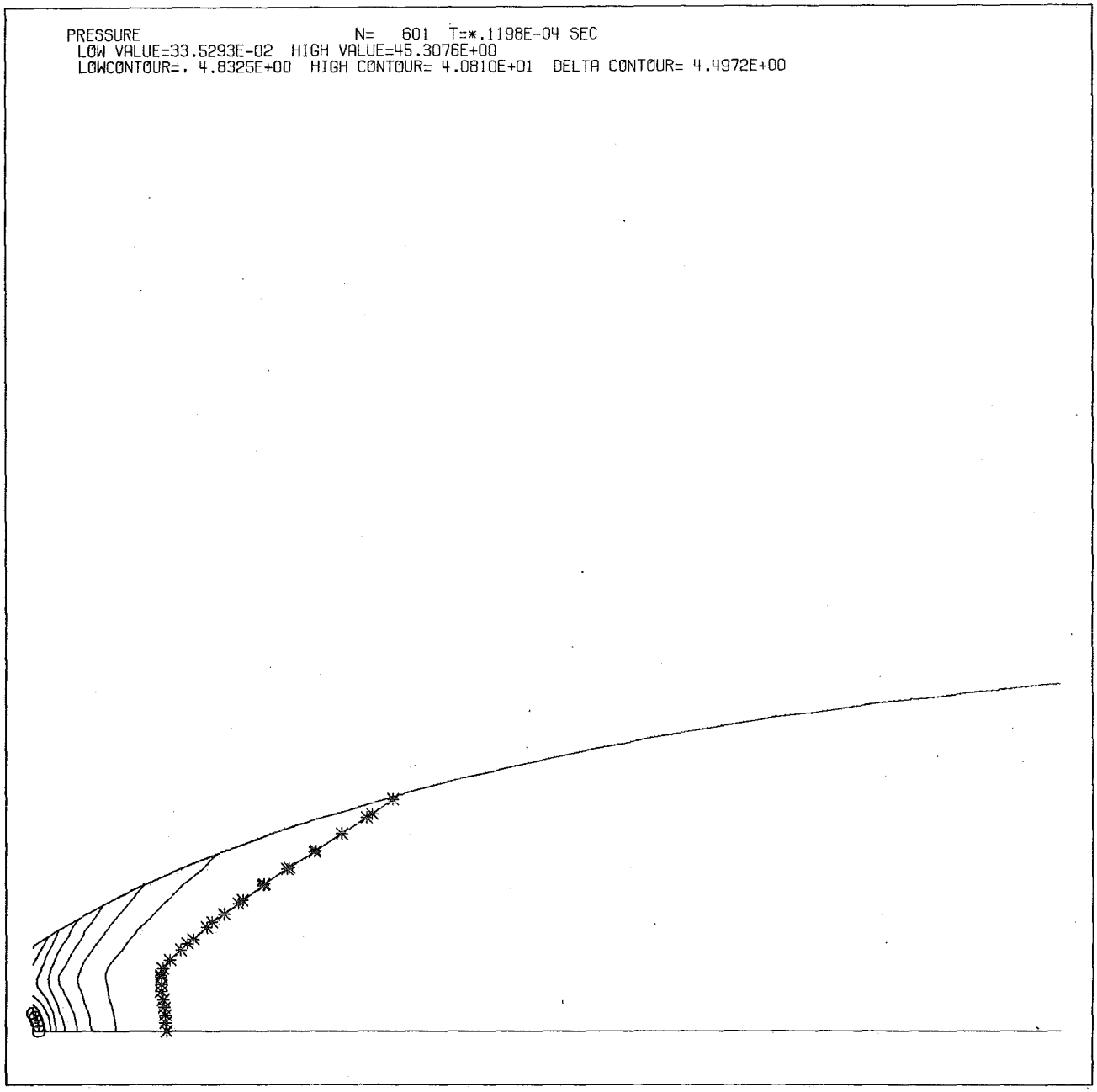
PRESSURE N= 601 T=*.1198E-04 SEC
LOW VALUE=33.5293E-02 HIGH VALUE=45.3076E+00
LOWCONTOUR=. 4.8325E+00 HIGH CONTOUR= 4.0810E+01 DELTA CONTOUR= 4.4972E+00

Figure III-21. Conventional Nozzle Downstream Pressure Plot

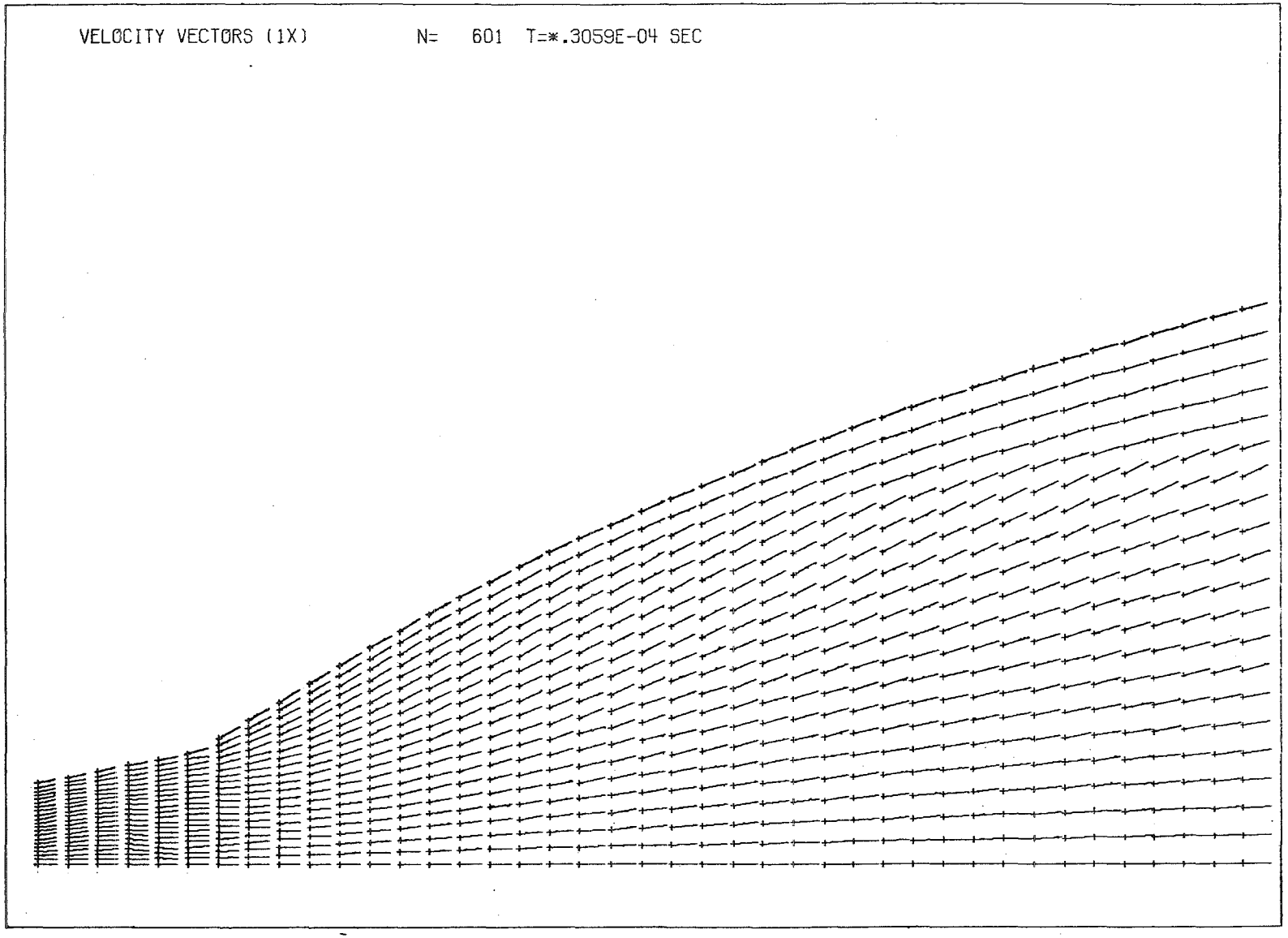

Figure III-22. Dual Throat Baseline Upstream Velocity Vector Plot

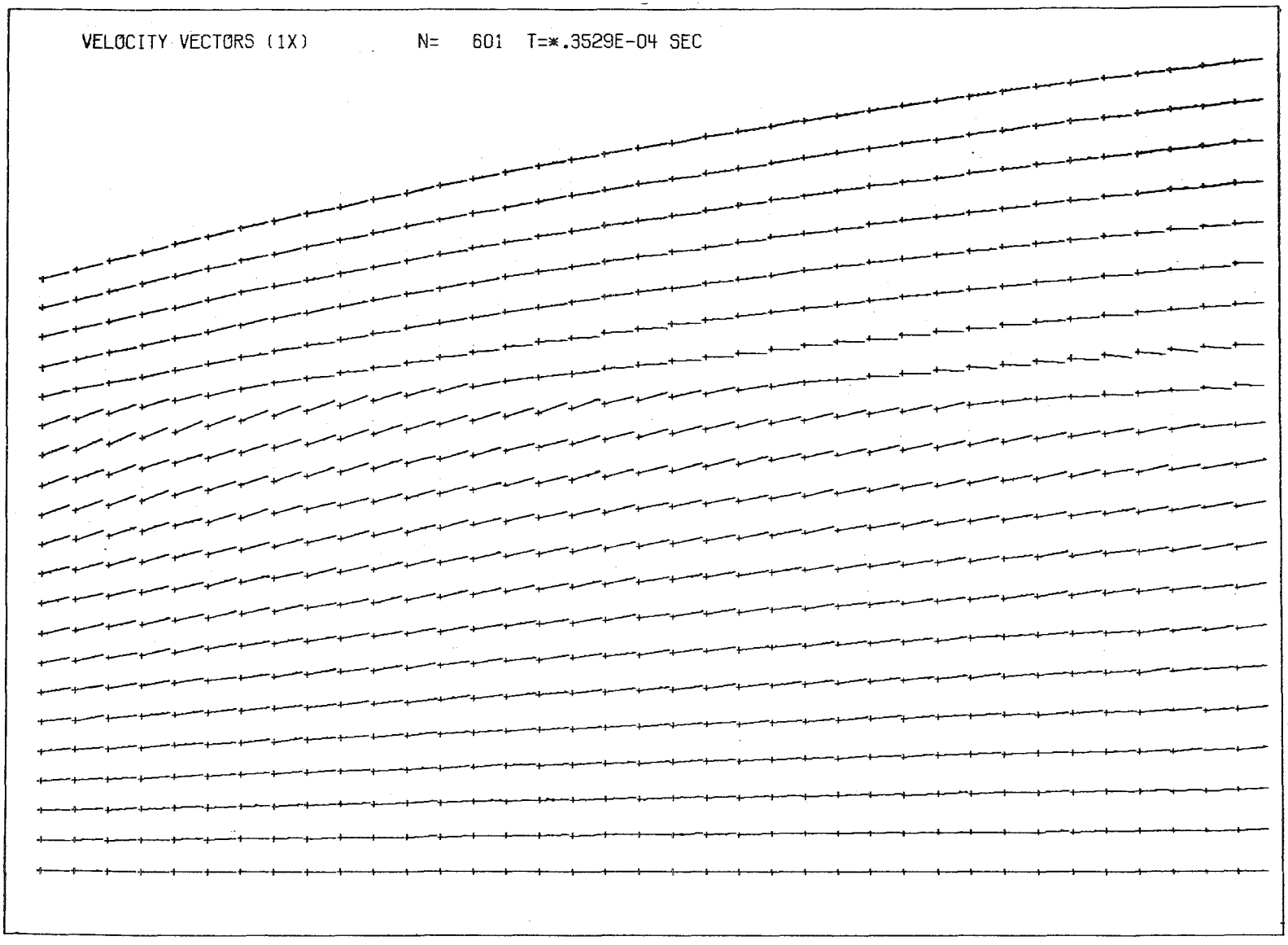

Figure III-23. Dual Throat Baseline Downstream Velocity Vector Plot

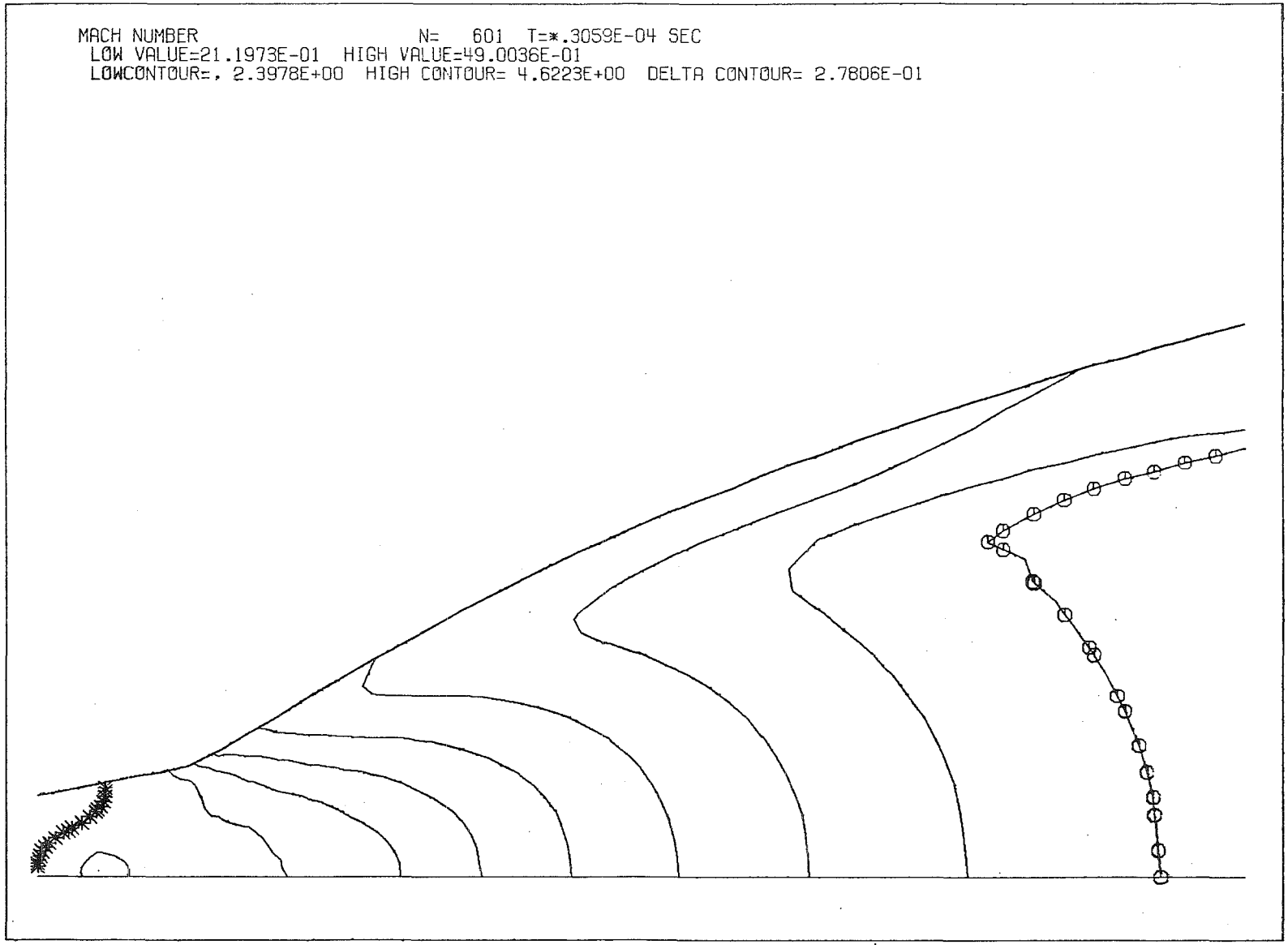
MACH NUMBER N= 601 T=*.3059E-04 SEC
LOW VALUE=21.1973E-01 HIGH VALUE=49.0036E-01
LOWCONTOUR=, 2.3978E+00 HIGH CONTOUR= 4.6223E+00 DELTA CONTOUR= 2.7806E-01

Figure III-24. Dual Throat Baseline Upstream Mach Number Plot

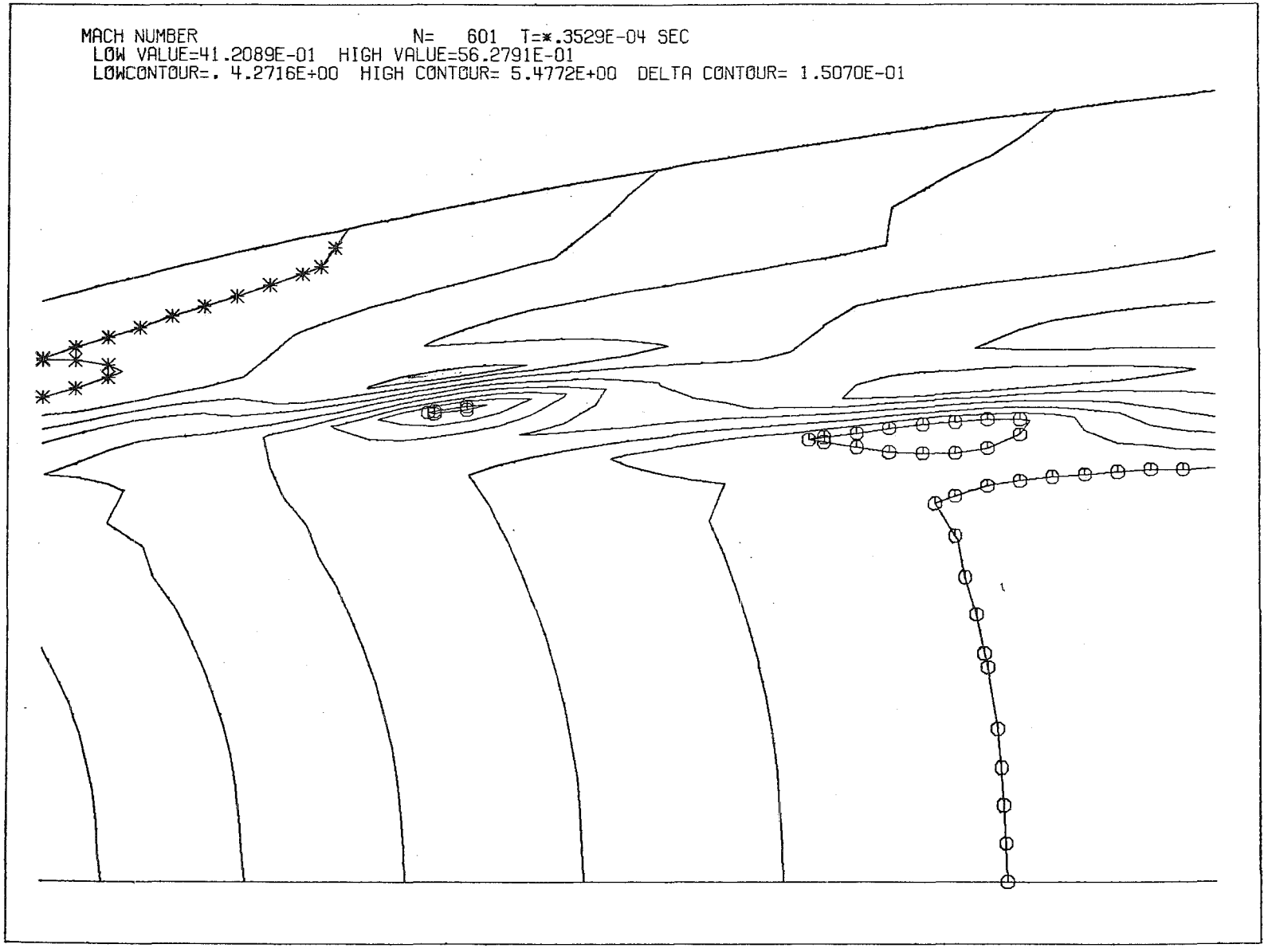
MACH NUMBER N= 601 T=*.3529E-04 SEC
LOW VALUE=41.2089E-01 HIGH VALUE=56.2791E-01
LOWCONTOUR=. 4.2716E+00 HIGH CONTOUR= 5.4772E+00 DELTA CONTOUR= 1.5070E-01

Figure III-25. Dual Throat Baseline Downstream Mach Number Plot

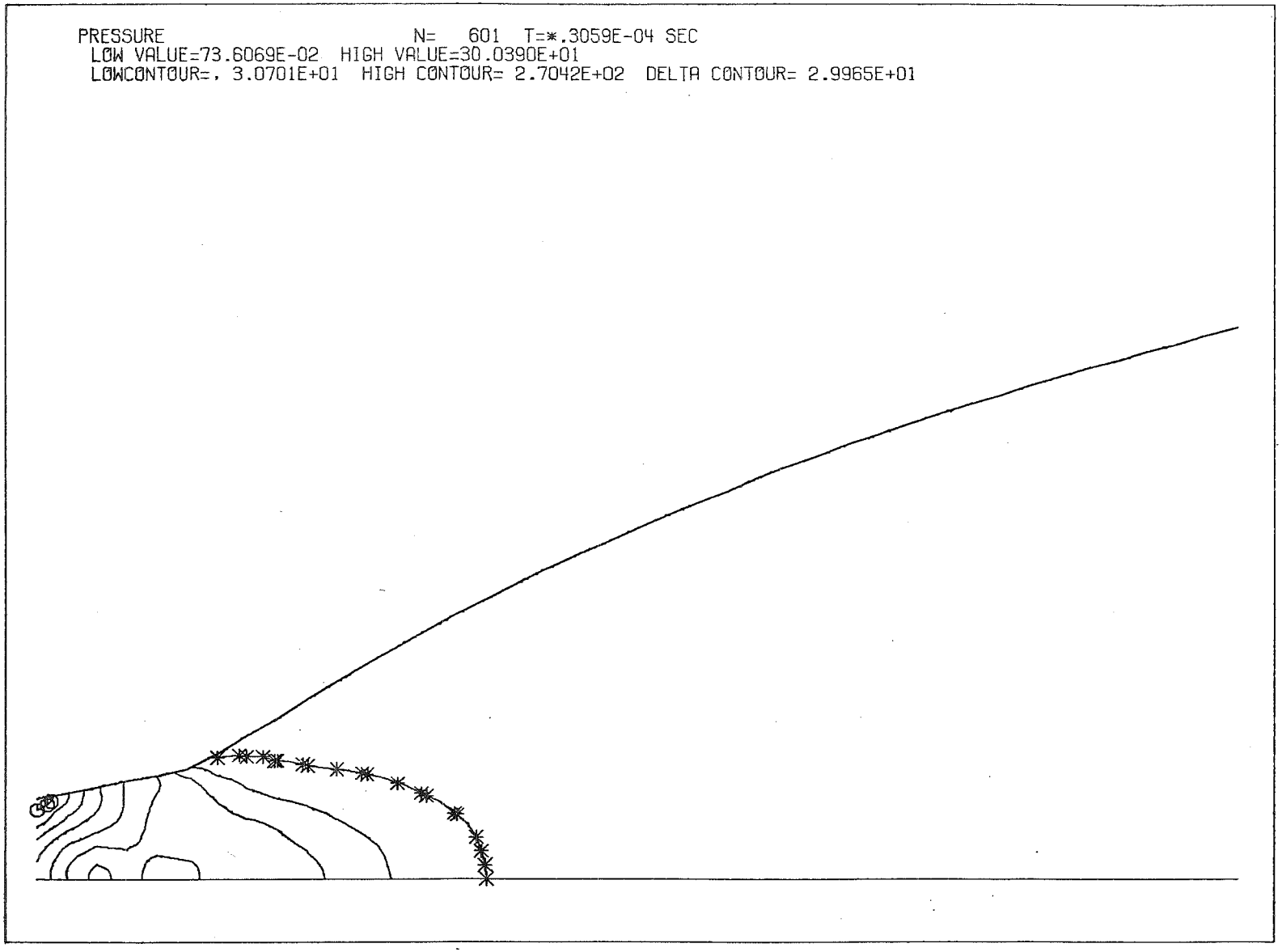
PRESSURE N= 601 T=*.3059E-04 SEC
LOW VALUE=73.6069E-02 HIGH VALUE=30.0390E+01
LOWCONTOUR=. 3.0701E+01 HIGH CONTOUR= 2.7042E+02 DELTA CONTOUR= 2.9965E+01

Figure III-26. Dual Throat Baseline Upstream Pressure Plot

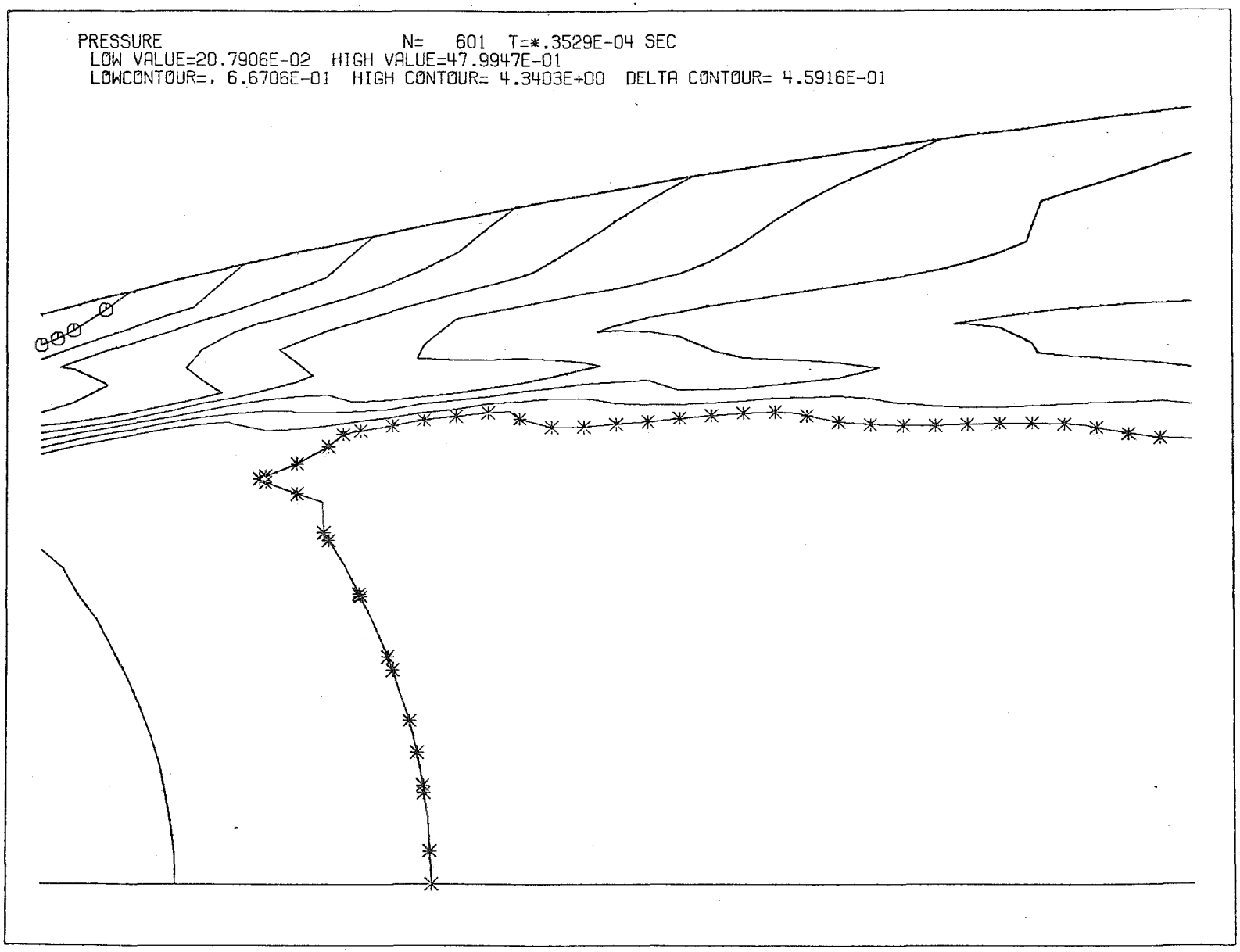
PRESSURE N= 601 T=*.3529E-04 SEC
LOW VALUE=20.7906E-02 HIGH VALUE=47.9947E-01
LOWCONTOUR=, 6.6706E-01 HIGH CONTOUR= 4.3403E+00 DELTA CONTOUR= 4.5916E-01

Figure III-27. Dual Throat Baseline Downstream Pressure Plot

region for the case having zero bleed flow (the case expected to be the most adverse Mode II operating condition). Pressures and mass velocities were obtained at different axial locations and used as boundary conditions for the design thermal analysis (discussed in Section IV).

The flow field plots (Figures III-28 through III-30) show the formation of the plume attachment shock. The plots are indicative of a weak shock formation. This can also be seen in the wall pressure profile shown in Figure III-31. The static pressure rise is approximately 15% larger than the value calculated by the aerodynamic bleed flow model, but it is approximately 45% of what would be expected with a discrete shock. This value appears to be consistent with the Nash factor value of 0.4 chosen during calibration of the bleed flow model, as described in Section III,B,2.

E. SECONDARY NOZZLE CONTOUR OPTIMIZATION

During Mode I operation, the dual throat nozzle operates as a conventional nozzle. The secondary nozzle contour is designed by using the optimization technique developed by G. V. R. Rao. This technique, which is derived from the calculus of variations and employs the method of characteristics, is used in ALRC's nozzle design program (FD 0002) and will calculate contours to provide maximum thrust for a specified length and/or area ratio. The Rao method is applicable when, together with an initial wall contour, a shock-free supersonic data line is given across the nozzle. In ALRC's program, this initial data line is automatically provided by using the modified Hall method to approximate the solution of the transonic flow equations in the nozzle throat region. In general, however, the method can be applied to any supersonic approach flow that is shock-free. This fact has been utilized in the study presented here to provide the design computer program with the capability of designing optimum nozzle contours for dual throat thrusters. The method used to design nozzles for Mode II operation is described below.

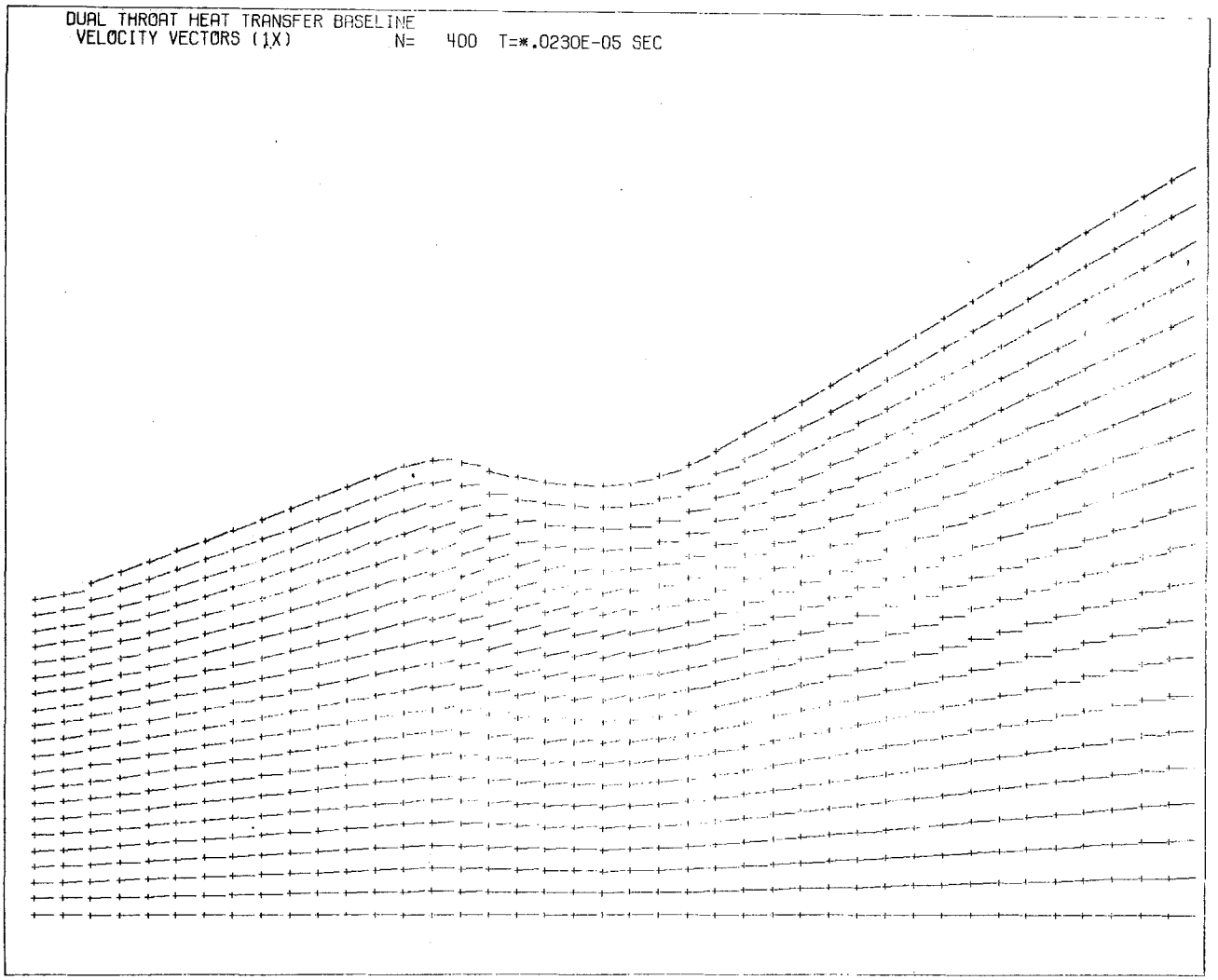

Figure III-28. Dual Throat Baseline Zero Bleed Flow Velocity Vector Plot

O - HIGH VALUE

* - LOW VALUE

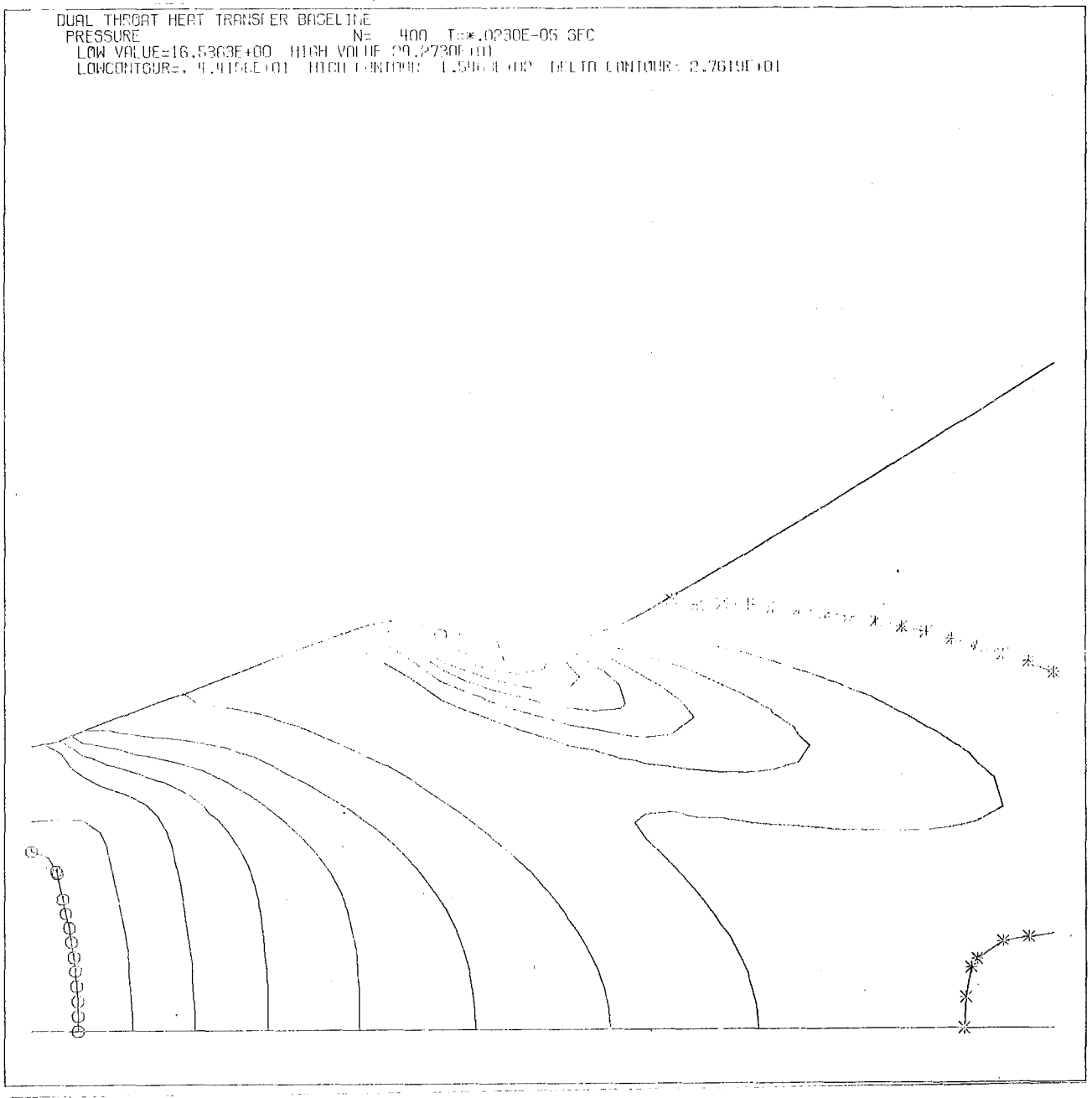
DUAL THROAT HEAT TRANSFER BASELINE
PRESSURE
N= 400 T=*.0230E-05 SEC
LOW VALUE=16.5363E+00 HIGH VALUE=29.2730E+00
LOWCONTOUR=, 4.4156E+01 HIGH CONTOUR= 1.5961E+02 DELTA CONTOUR= 2.7619E+01

Figure III-29. Dual Throat Baseline Zero Bleed Flow Pressure Profile

O - HIGH VALUE CONTOUR

* - LOW VALUE CONTOUR

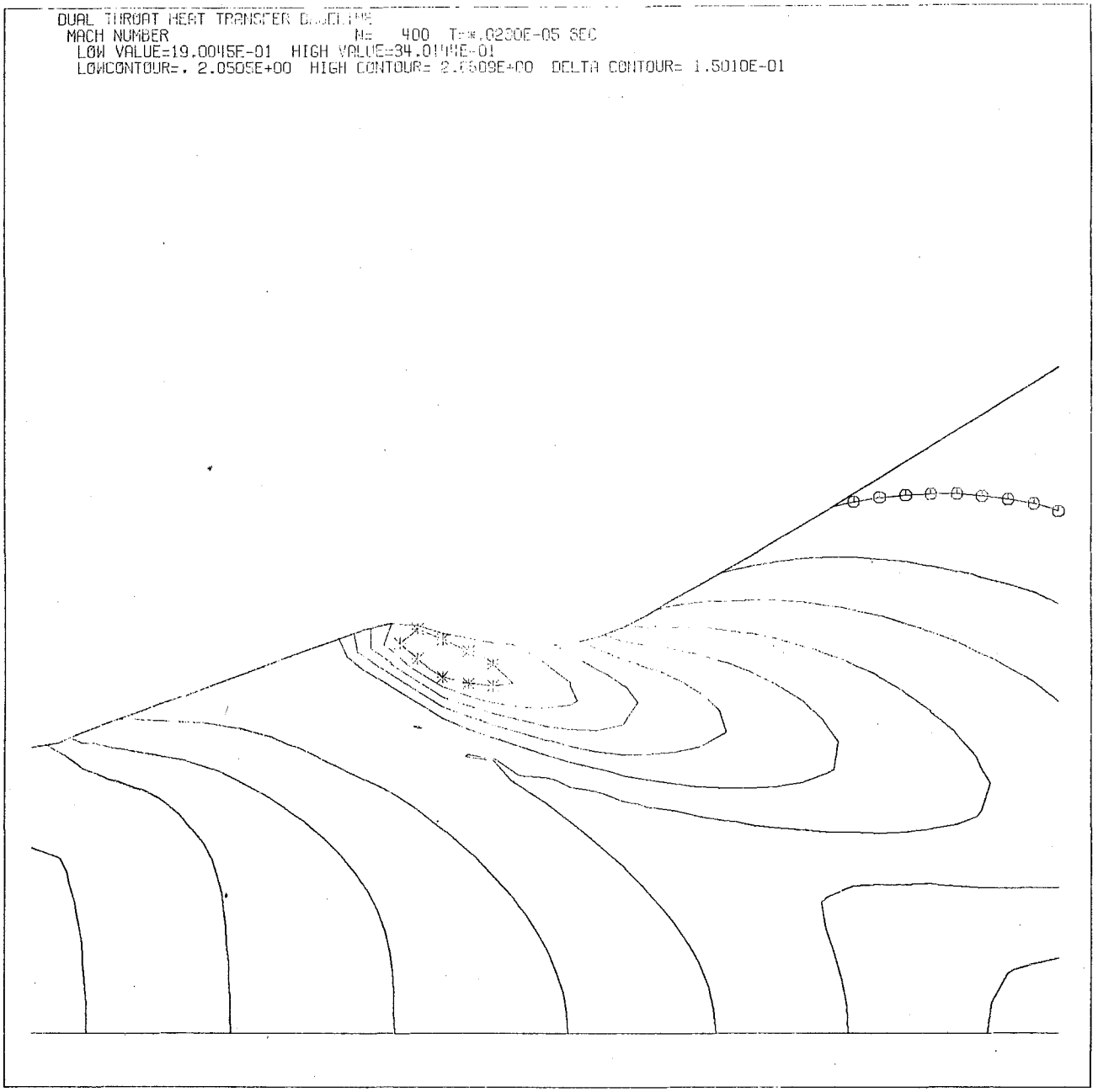

Figure III-30. Dual Throat Baseline Zero Bleed Flow Mach Number Profile

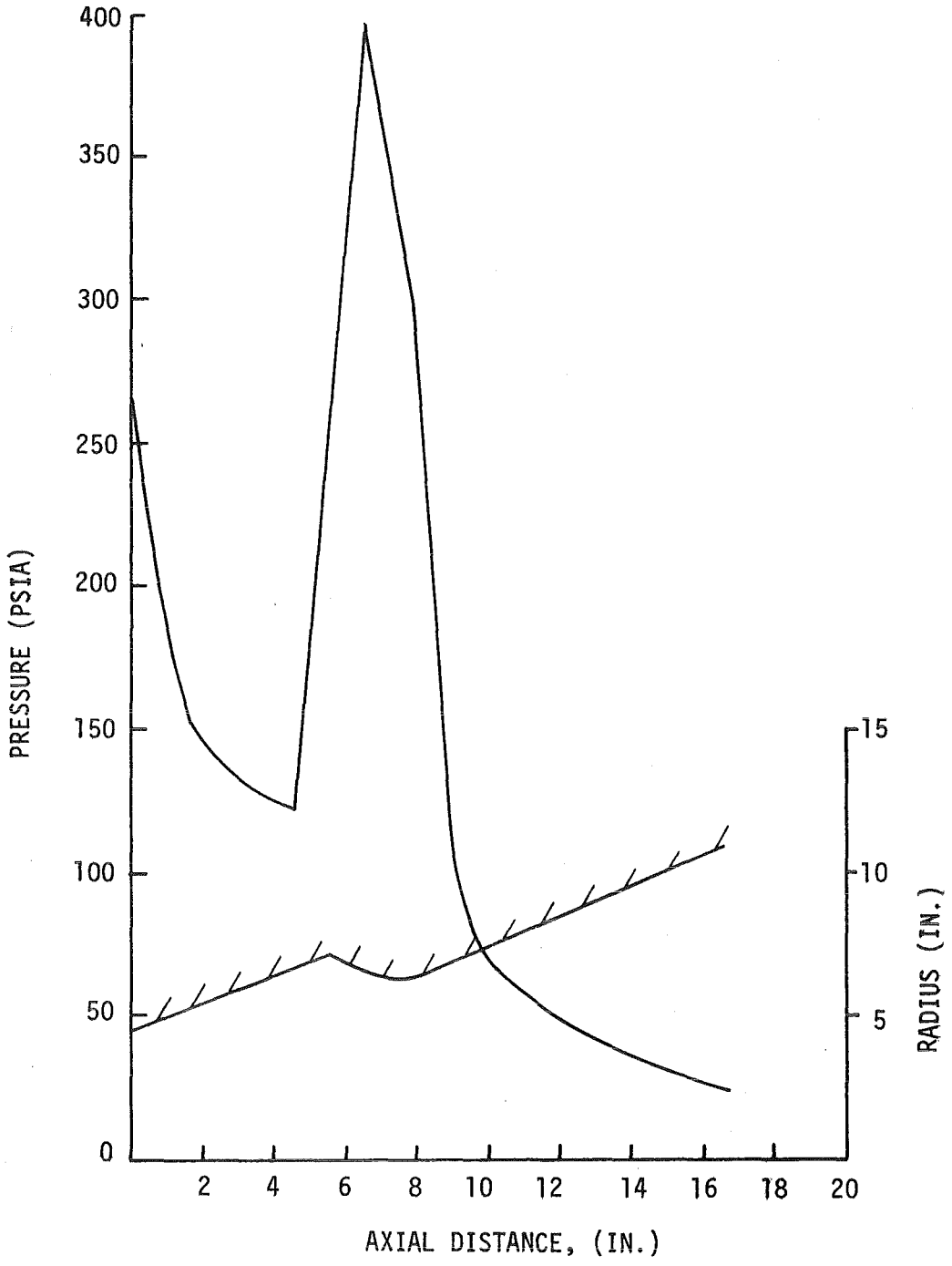

Figure III-31. Dual Throat Baseline Zero Bleed Flow Wall Pressure Profile

III, E, Secondary Nozzle Contour Optimization (cont.)

1. Design Method

The aerodynamic model presented in Section III,B can be used to design a dual-throat thruster assembly which, by use of bleed flow, operates with a plume shape and attachment position such that the flow field is nearly shock-free. Once the approach flow is specified up to the plume attachment position, the Rao procedure can be used to calculate an optimal contour for the exterior wall downstream of the attachment position. This wall contour is typically quite long because the thruster mission requires a high expansion ratio.

The design computer program has been modified to allow an optimum nozzle contour to be calculated where the approach flow is determined by an input nozzle contour. This feature of the program is called the "Extended Nozzle Wall Option." The steps used to implement this option are as follows:

First, the wall geometry subroutines of the TDK method of characteristics program were transferred to the ALRC program and checked out. These are subroutines WALL, CUBIC, and XSLP. The maximum number of points allowed for inputting the nozzle wall using the spline fit option (IWALL = 4) was increased from 20 to 40. This same modification was also made to the aerodynamic model computer program.

Next, subroutines WALL1 and WALL2 were revised to allow the circular arc portion of the wall contour to be centered at a predetermined position. Previously it had been necessary to position the circular arc at the nozzle throat and center it at (1, 0). A new wall point MOC subroutine, called WALLPT, was also written and checked out.

III, E, Secondary Nozzle Contour Optimization (cont.)

A logic subroutine, called RRC, was written to construct a nozzle flow field for a given nozzle wall geometry (i.e., as constructed by subroutine WALL) using Right Running Characteristics (RRC's). The flow field constructed (shown in Figure III-32), is bounded as follows:

(a) The upstream boundary is the initial data line RRC.

(b) The upper boundary is the nozzle wall contour.

(c) The lower boundary is the flow axis.

(d) The downstream boundary is the RRC extending from the wall end point.

Finally, the main program, FD002, and the logic program, LOGIC, were modified to accept the above. The program was checked out for the baseline case for the dual throat nozzle. That is, an optimum nozzle contour of fixed length and area ratio was designed for the secondary nozzle wall, assuming the approach flow to be that given by the primary nozzle and plume (aerodynamic wall) with 5.3% bleed flow.

2. Optimization Analysis Results

A parametric analysis was performed to investigate the effect of optimizing the secondary nozzle contour for either Mode I or Mode II. Table III-IX and Figure III-33 show the results of this analysis, including a comparison of the Mode II nozzle contours according to the following parameters:

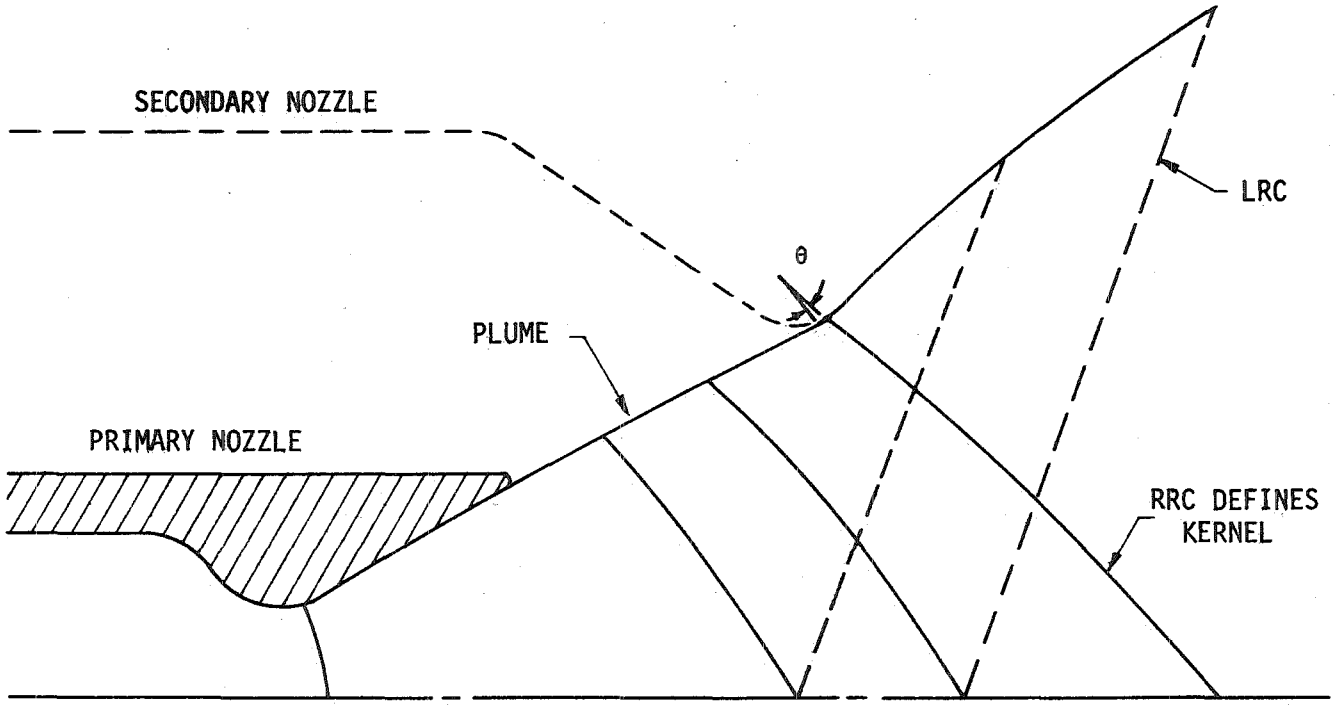

Figure III-32. Secondary Nozzle Optimization Program Procedure

III, E, Secondary Nozzle Contour Optimization (cont.)

Contour (1) is a conventional Bell nozzle with an expansion ratio of 222:1. The chamber throat and exit point of this nozzle are those of the primary nozzle of the dual throat baseline contour.

Contour (2) results from optimizing the secondary nozzle for Mode I operation. The plume attaches to a secondary nozzle contour designed for an 46:1 area ratio in Mode I operation.

Contour (3) has been designed in terms of "Extended Nozzle Wall Option" discussed in this section. The approach flow passes through the dual throat primary nozzle and the plume expansion, subsequently attaching at the secondary nozzle throat. Contour (3) is the optimal contour given this approach flow. This nozzle has an expansion ratio of 222:1.

Contours (1) and (3) have the same throat and exit point, but, as can be seen from Figure III-33, they are very different in shape. Contours (2) and (3) have different throat locations but the same exit point. Contour (2) is designed to yield maximum thrust during Mode I operation. Contour (3) is designed to yield maximum thrust during Mode II operation. As can be seen from Figure III-33, Contour (3) has less curvature than Contour (2) in order to turn the high Mach number approach flow isentropically. The net performance effect of the two optimization options is shown in Table III-IX.

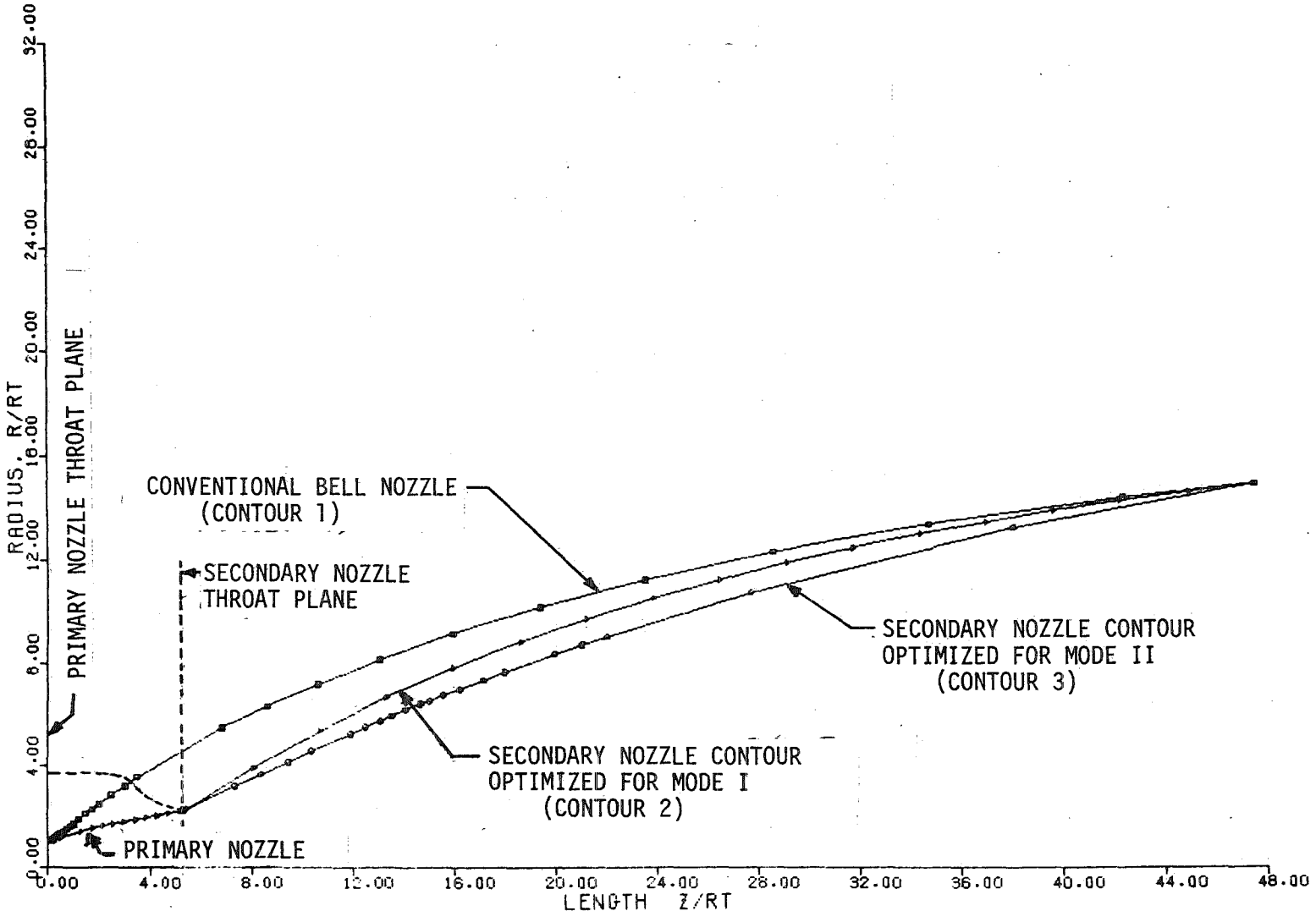

Figure III-33. Dual Throat Secondary Nozzle Contour Comparison

TABLE III-IX

COMPARISON OF NOZZLE DIVERGENCE EFFICIENCIES FOR TWO TYPES OF OPTIMUM NOZZLE CONTOURS

Operating Mode:	Mode I ε= 45:1		Mode II ε= 222:1	
Secondary Nozzle Optimizied For:	MODE I (Contour 2)	MODE II (Contour 3)	MODE I (Contour 2)	MODE II (Contour 3)
η_{DIV}	.991	.988	.982	.985

Source: TDE Option TDK Program

The absolute values of the divergence efficiencies shown in Table III-IX are somewhat questionable because of the simplified treatment of the flow recompression used in the TDE analysis. The relative efficiency values appear to be valid, however. Therefore, optimizing the secondary nozzle contour for Mode I or Mode II will only slightly change the performance.

F. DUAL THROAT PERFORMANCE

Many of the model improvements described previously have a direct impact on the performance prediction methodology for dual throat engines. Improvements in the aerodynamic model have resulted in less restrictive calculational assumptions, tying it directly to the shear model and overall boundary layer model via the evaluation of the momentum thickness at the plume attachment point. Results of detailed two-dimensional flow analyses (VNAP and TDE) have further verified the fluid conditions within the dual throat thruster and the resulting performance efficiencies.

III, F, Dual Throat Performance (cont.)

Presented within this section are the results of an assessment in the changes in the predicted dual throat performance based on the use of the improved aerodynamic model and updated simplified performance model. First, an analysis of the baseline design condition for Mode II is presented and compared to a conventional gas-generator cycle engine. Secondly, the performance of a limited set of parametric cases calculated during NAS 8-32967 is compared to values calculated by using the updated simplified performance model.

1. Baseline Design Performance

The baseline operating point, shown in Table III-X, is the same as that recommended in Contract NAS 8-32967. For this design condition, a bleed flowrate of 5.3% is predicted to be required for shock-free (zero pressure loss) plume attachment. However, the bleed flow can be reduced to 3.5% with only a small loss in total pressure ($\sim$1%), and thus this test condition was selected as a reasonable design tradeoff for this comparison.

The calculated specific impulse for Mode II operation is shown in Table III-XI and compared to a conventional gas-generator cycle engine operating at the same condition. The results of this comparison show that the performance of the dual throat engine in Mode II is approximately 6 seconds (1-1/4%) lower than that of the conventional engine. As noted, most of this difference in performance is attributed to the less efficient expansion process of the dual throat engine in Mode II which results in a greater divergence efficiency. This performance penalty must, of course, be traded off with other dual throat advantages as a result of its unique capabilities.

2. Comparison of Simplified Performance Parametrics

The effect of the previously described model improvements on performance parametric trends was briefly investigated by using the updated

TABLE III-X

DUAL THROAT BASELINE OPERATING POINT

MODE I SEA LEVEL THRUST 2.669 MN (600K lbF)
MODE I TO MODE II THRUST RATIO 3.2

PRIMARY NOZZLE

CHAMBER PRESSURE	27.58 MPa (4000 psia)
MIXTURE RATIO	7.0
PROPELLANT	LOX/LH_2

SECONDARY NOZZLE

CHAMBER PRESSURE	19.31 MPa (2800 psia)
MIXTURE RATIO	2.8
PROPELLANT	LOX/RP-1

TABLE III-XI

COMPARISON OF THE DUAL THROAT AND CONVENTIONAL GAS-GENERATOR ENGINE CONCEPTS

PROPELLANTS:	LO_2/LH_2
MIXTURE RATIO:	6.0 (Overall)
CHAMBER PRESSURE:	27.58 MPa (4000 psia)
AREA RATIO:	222:1
THRUST (VAC):	956 KN (215K lbF)
TOTAL FLOWRATE:	215.6 Kg/sec (475 lbm/sec)

DUAL THROAT - MODE II		CONVENTIONAL GG CYCLE	
BLEED FLOW	= 3.5%	GG FLOW	= 3.5%
PRIMARY O/F	= 7.0	TCA O/F	= 7.0
$I_{SP\ ODE}$	= 480.4 sec.	$I_{SP\ ODE}$	= 480.4 sec.
η_{DIV}	= .988	η_{DIV}	= .996
η_{ERE}	= .990	η_{ERE}	= .990
η_{KIN}	= .999	η_{KIN}	= .999
$\Delta I_{SP\ BL}$	= 13.4 sec.	$\Delta I_{SP\ BL}$	= 5.7 sec.
$I_{SP\ TCA}$	= 456.2 sec.	$I_{SP\ TCA}$	= 467.5 sec.
$I_{SP\ ENG}$	= 456.2 sec.	$I_{SP\ ENG}$	= 462.2 sec.

dual throat simplified model. The results for five parametric cases examined during NAS 8-32967 were compared with the present model predictions for both Mode I and II operation. These cases were used to investigate the effects of chamber pressure and thrust ratio ($F_{vac,\ Mode\ 1}/F_{vac,\ Mode\ 2}$) on engine performance.

In Mode I, the vacuum specific impulse predictions and trends are essentially unchanged from the previously reported results. However, because the calculational technique was changed to require equal streamtube static pressure at the secondary throat during Mode I operation, a significant difference in the sea level specific impulse trend with thrust ratio was noted. This is illustrated in Figure III-34. The current model predicts less variation in the sea level specific impulse at the extremes of the thrust ratio. Note that at the baseline thrust ratio of 3.2, the present model predicts a sea level specific impulse which is approximately 6 sec greater than the previous model predictions. Engine geometry trends with thrust ratio were also impacted, as noted in Figure III-35. The secondary throat size, rather than increase as previously predicted, is now expected to actually decrease slightly with thrust ratio (while holding sea level thrust constant).

In all cases, the Mode II specific impulse is lower with use of the updated performance model because of larger boundary layer and divergence losses. The magnitude of this difference varies from case to case, but is generally 1 to 2% less. While the magnitude of the Mode II performance is less than previously predicted, the certainty of the prediction is much greater as a result of the work completed during this study. In addition, as noted, the Mode II performance predicted for the recommended baseline is only 1-1/4% less than that of a conventional gas-generator engine, and thus the previous simplified model predictions appear optimistic in this light.

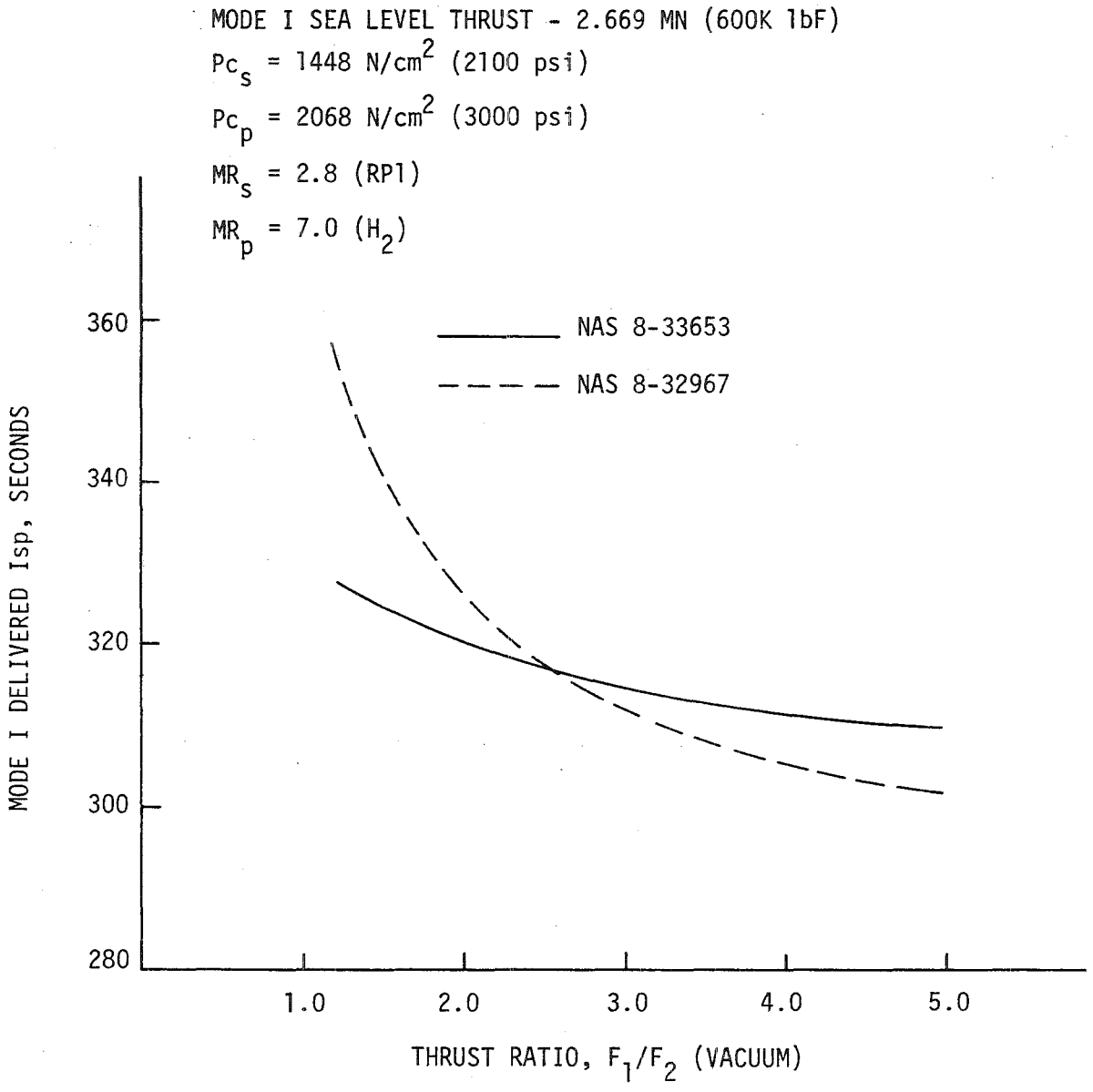

Figure III-34. Mode I Delivered I_{sp} versus Thrust Ratio

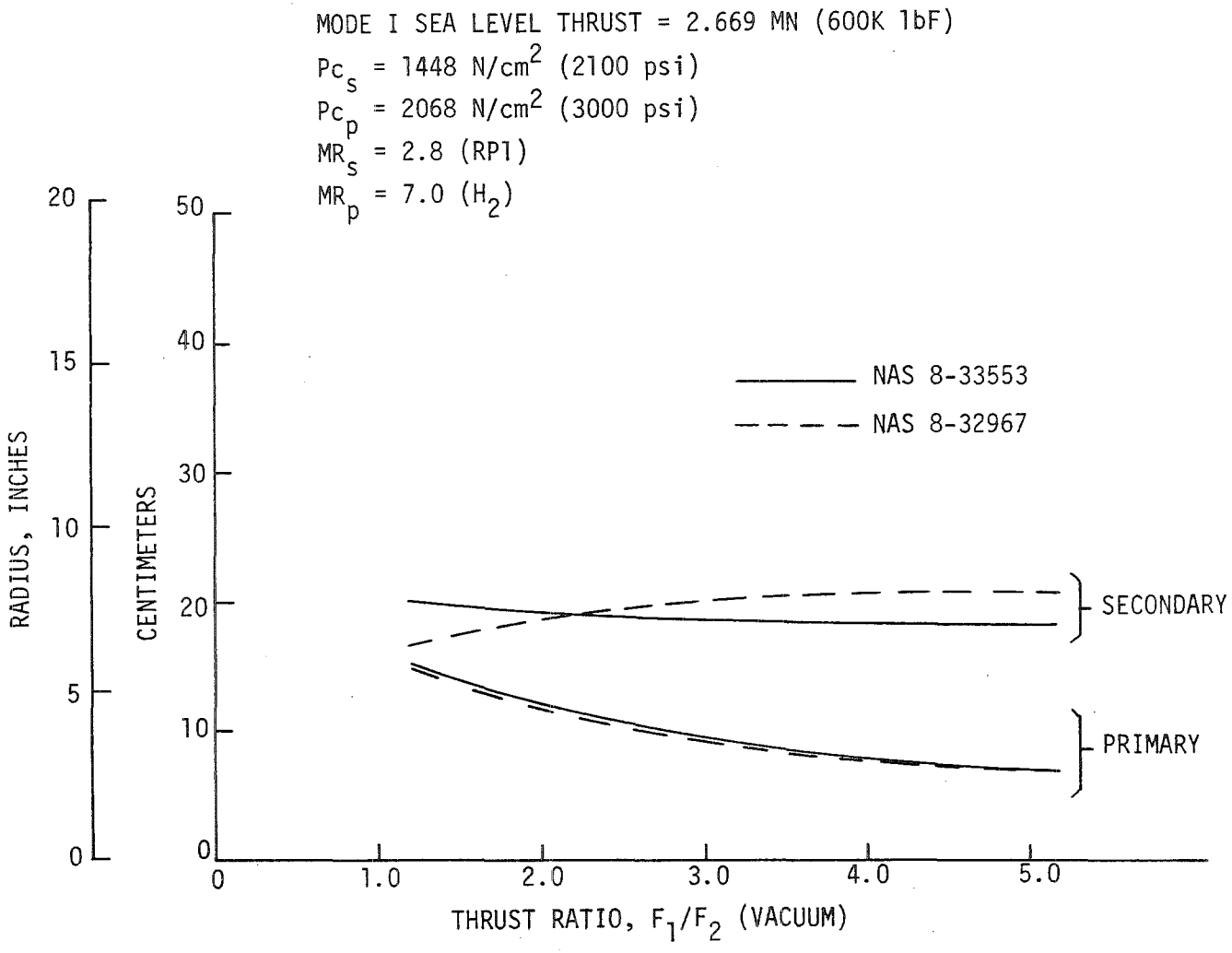

Figure III-35. Dual Throat Engine Throat Radius as a Function of Thrust Ratio

G. RECOMMENDATIONS

1. Design Approach

The previous methodology determines primary nozzle area ratio by the following correlation:

$$\varepsilon_p = \frac{A_{t_s}}{A_{t_p}} \quad \frac{1}{EPPM}$$

where EPPM is an empirical factor. A value of EPPM = 1.8 was chosen on the basis of the cold-flow test results from NAS 8-32666. Nozzle spacing was chosen to be 0.8, the length of the conical portion of the secondary convergence section.

The primary nozzle area ratio and axial spacing between the primary and secondary throats should be chosen to ensure that the secondary flow is choked at the secondary throat, rather than at the primary lip, by allowing enough flow area on the secondary side of the primary nozzle lip. This design approach requires small primary nozzle area ratios and large nozzle spacing. Secondly, the nozzle spacing chosen must result in the ambient pressure at the primary nozzle lip being low enough to cause the primary flow to be choked. This implies that the nozzle spacing should be small. Analyses of bleed flowrate trends for Mode II indicate that bleed flow requirements decrease with increasing primary nozzle area ratio and decreasing nozzle spacing. These trends are shown in Figure III-36. The primary nozzle area ratio and nozzle spacing chosen must be a compromise of all these requirements.

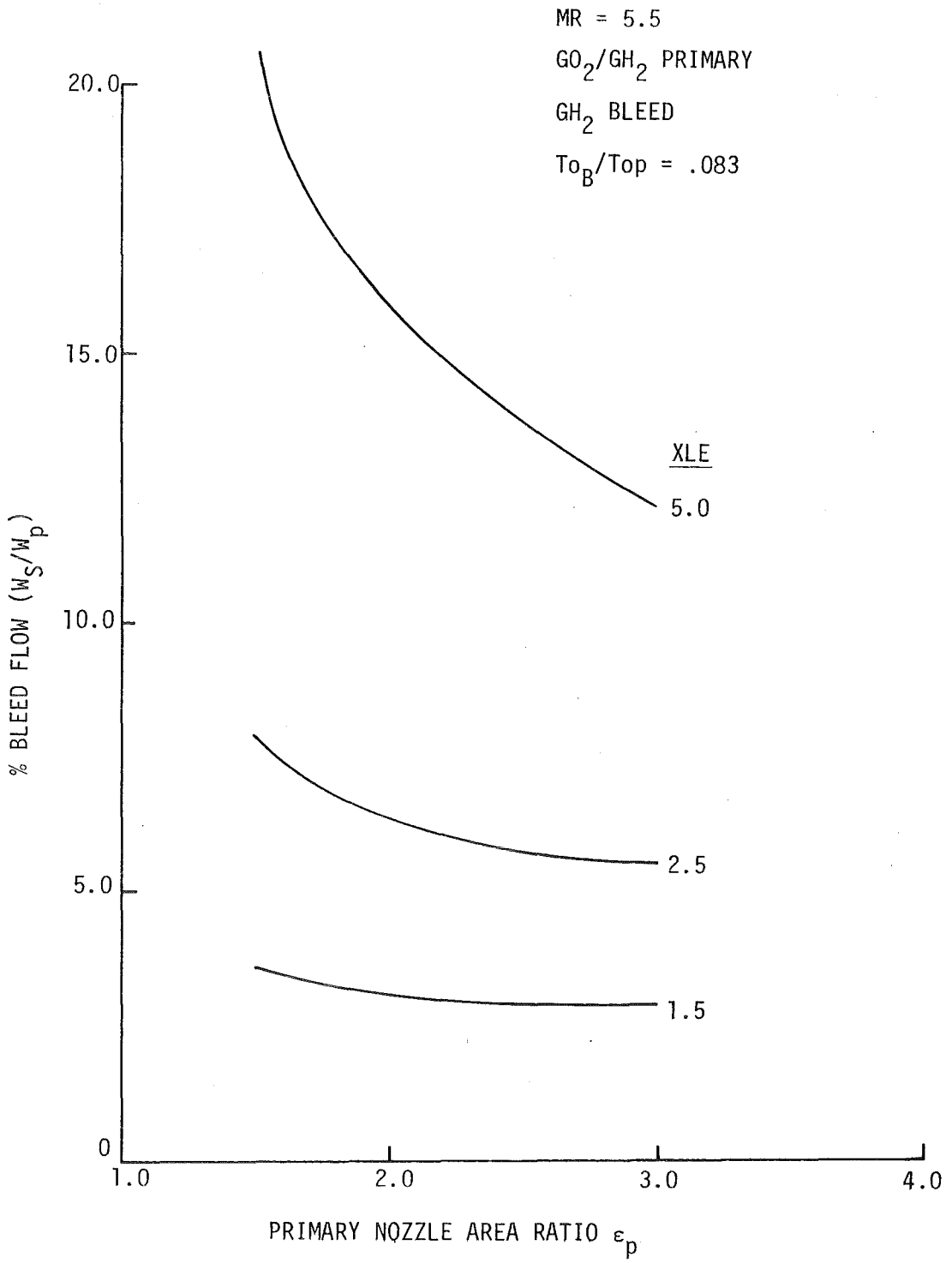

Figure III-36. Percent Bleed Flow versus Primary Nozzle Area Ratio

III, G, Recommendations (cont.)

2. Test Programs

The aerodynamic bleed flow model has three empirical parameters (identified in Section III,B). Two of these parameters have been calibrated: the plume scaling factor and the NASH factor, using cold-flow and NASA/MSFC test data. The third parameter, the spreading factor, still needs to be calibrated. This parameter will influence the value of the mass fraction of primary flow entrained in the recirculation region and the resulting recirculation temperature calculated. This may impact the cooling requirements in the plume attachment region. A test design is required that allows thermal data acquisition in these regions. This may be done either through a calorimetric convergence section or placement of thermocouples.

3. Model Improvements

The aerodynamic bleed flow model computer program currently determines the plume boundary shape by using a correlation of the form suggested by Herron. The intersection of the plume boundary and the secondary nozzle wall is determined and, together with the slope of these two surfaces, used to calculate recompression criteria for the shear layer. Because a correlation is used, the plume boundary is limited in range and is necessarily somewhat inaccurate. The effect of specific heat ratio is grossly simplified. The point of intersection and the slope of the plume and wall at the intersection are also in error. The error in streamline slope change, i.e., the deflection angle of the plume streamline, can be more than 20%.

Figure III-37a shows isobars calculated by the MOC for a cold-flow nozzle configuration. The streamline shape was calculated by the correlation discussed above. The plume streamline should be constant pressure, but is actually correct to within only about 15%. (The isobar labeled

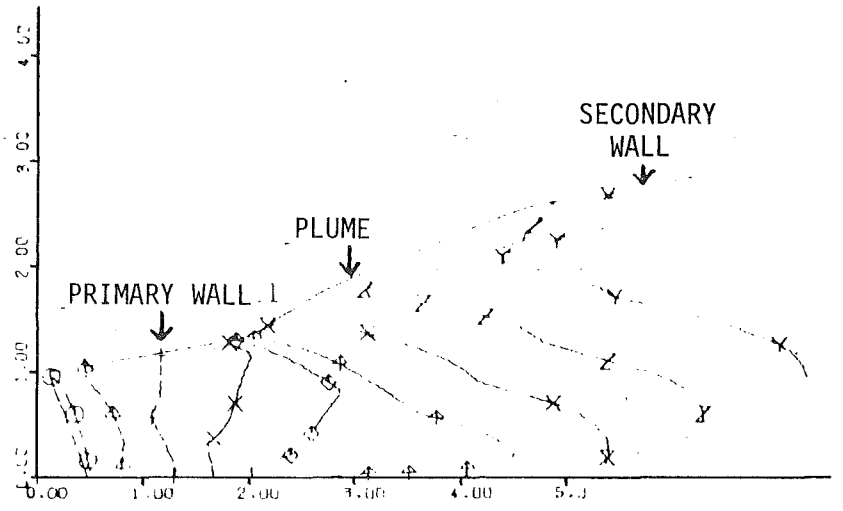

a. ISOBARS

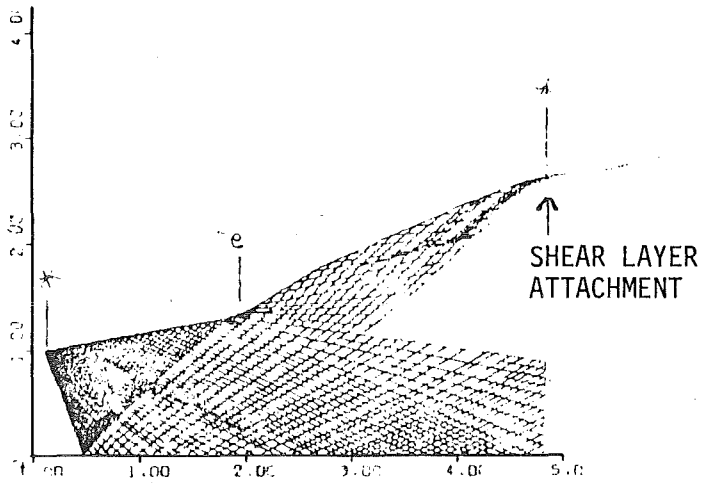

b. CHARACTERISTICS

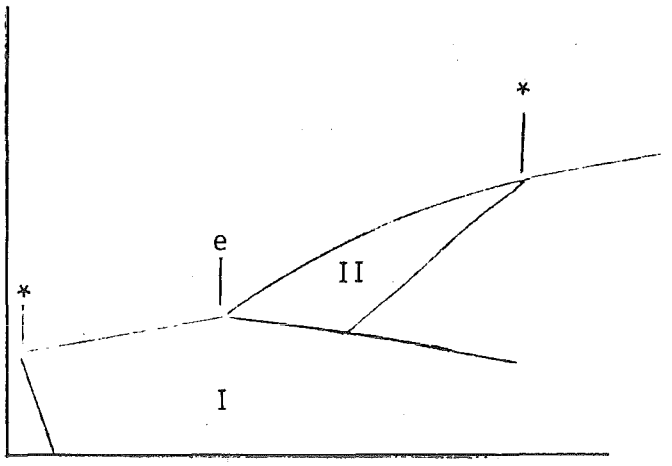

c. REGIONS

Figure III-37. Isobars, Characteristic Lines and Flow Field Regions

X approximately follows the plume streamline.) Figure III-37b shows characteristic lines calculated by the MOC interior to the nozzle and plume boundary streamlines. In Figure III-37c, the flow field has been divided into two regions that are separated by the RRC that comes down from the primary nozzle lip. Region I, upstream of this RRC, is independent of the plume shape. Region I can be calculated by using the TDK Program and then input to the Bleed Flow program.

Next, Region II can be calculated and used to replace the plume correlation. It is defined as follows:

Upstream boundary:	RCC ending Region I
Left-hand corner:	Prandtl-Meyer fan expanded to the base pressure
Upper boundary:	Constant pressure boundary (= base pressure)
Downstream boundary:	LRC from the upstream boundary to the plume attachment point on the secondary nozzle

It would be necessary to calculate Region II using the MOD within the inner search procedure of the Bleed Flow program, i.e., directly replace the plume correlation with a MOC calculation. As can be seen from Figure III-37b, however, it is not necessary to calculate many points (only perhaps 300). The advantage would be that the MOC solution will be highly accurate. Thus, it is recommended that the aerodynamic model be modified to incorporate a MOC calcualtion for the plume boundary.

IV. DUAL EXPANDER ANALYSIS

A. PRELIMINARY GEOMETRIC ANALYSIS

This study was the first effort in technically analyzing the dual expander nozzle concept. The analysis determined the dependence of performance, throat area, nozzle and steamtube area ratios, mass flow, and nozzle length with the variation in Mode I sea level thrust, thrust ratio (Mode I/Mode II), primary and secondary chamber pressures, chamber pressure ratio (P_{cs}/P_{cp}), and nozzle exit pressure. The parametric range analyzed was as follows:

Thrust	2.22 - 8.90 MN	(5×10^5 - 2×10^6 lbF)
Thrust Ratio	1.0 - 5.0	
Chamber Pressure	6.89 - 55.16 MPa	(1000 - 8000 psia)
Pc Ratio	0.25 - 1.0	
Exit Pressure	34.5 - 101 KPa	(5.0 - 14.7 psia)

To ensure a valid comparison with the dual throat analysis, LOX/RP-1 was chosen as the primary nozzle propellant, and LOX/LH_2 was chosen for the secondary nozzle. Mixture ratios used were 2.8 and 7.0 for the primary and secondary chambers, respectively.

Table IV-I lists the parametric values used for each case. The resulting performance, area ratios, throat areas, flowrates, and efficiencies are listed in Table IV-II.

Mode I performance calculations were based on the simplified JANNAF methodology and were similar to the streamtube approach used during the Dual Throat Geometry Program (FD 0169). Mode II performance was determined by applying the simplified JANNAF methodology to a Bell nozzle having the same throat area, area ratio, and length as the secondary nozzle during Mode II operation. The procedures were programmed into a Dual Expander Preliminary Geometry and Performance Prediction Program.

TABLE IV-I

DUAL EXPANDER CASES ANALYZED

CASE	SEA LEVEL THRUST MN (lbF)	THRUST RATIO	P_{CP} MPa (psia)	P_{CS} MPa (psia)	P_{EXIT} KPa (psia)	P_{CS}/P_{CP}
1	2.67 (6×10^5)	2.37	41.37 (6000)	20.68 (3000)	34.5 (5.0)	.5
2	2.67 (6×10^5)	2.37	41.37 (6000)	10.34 (1500)	34.5 (5.0)	.25
3	2.67 (6×10^5)	2.37	41.37 (6000)	31.03 (4500)	34.5 (5.0)	.75
4	2.67 (6×10^5)	2.37	41.37 (6000)	41.37 (6000)	34.5 (5.0)	1.0
5	2.67 (6×10^5)	1.25	41.37 (6000)	20.68 (3000)	34.5 (5.0)	.5
6	2.67 (6×10^5)	3.50	41.37 (6000)	20.68 (3000)	34.5 (5.0)	.5
7	2.67 (6×10^5)	4.50	41.37 (6000)	20.68 (3000)	34.5 (5.0)	.5
8	2.67 (6×10^5)	5.0	41.37 (6000)	20.68 (3000)	34.5 (5.0)	.5
9	2.67 (6×10^5)	2.37	13.79 (2000)	6.89 (1000)	34.5 (5.0)	.5
10	2.67 (6×10^5)	2.37	27.58 (4000)	13.79 (2000)	34.5 (5.0)	.5
11	2.67 (6×10^5)	2.37	55.16 (8000)	27.58 (4000)	34.5 (5.0)	.5
12	2.22 (5×10^5)	2.37	41.37 (6000)	20.68 (3000)	34.5 (5.0)	.5
13	4.44 (1×10^6)	2.37	41.37 (6000)	20.68 (3000)	34.5 (5.0)	.5
14	6.67 (1.5×10^6)	2.37	41.37 (6000)	20.68 (3000)	34.5 (5.0)	.5
15	8.90 (2.0×10^6)	2.37	41.37 (6000)	20.68 (3000)	34.5 (5.0)	.5
16	2.67 (6×10^5)	2.37	41.37 (6000)	20.68 (3000)	68.9 (10.0)	.5
17	2.67 (6×10^5)	2.39	41.37 (6000)	20.68 (3000)	101 (14.7)	.5
18	2.67 (6×10^5)	1.0	-	20.68 (3000)	34.5 (5.0)	-

TABLE IV-II

PARAMETRIC ANALYSIS RESULTS

CASE	THRUST SPLIT	MODE 1														MODE 2			
		F1 VAC	ISP_D VAC	ISP_D S.L.	ε_I	A_{tp}	A_{ts}	$A_{t_{noz}}$	WPF	WPOX	W_{TP}	WSF	WSOX	W_{TS}	$\eta_{OVERALL}$	F2 VAC	ISP_D	ε_{II}	$\eta_{OVERALL}$
1	59.3/40.7	676440	390.4	346.3	63.2	34.13	48.2	82.33	290.4	813.2	1103.6	78.6	550.3	628.9	.9669	285533	454	107.9	.9737
2	59.3/40.7	683403	386.2	339.1	42.4	34.53	99.42	133.95	293.8	822.7	1116.5	81.6	571.3	652.9	.9676	288306	441.6	57.1	.9743
3	59.4/40.6	673341	391.9	349.2	75.9	34.02	31.72	65.74	289.5	810.5	1100	77.3	541.1	618.4	.9649	284192	459.6	157.3	.9725
4	59.4/40.6	671416	392.9	351.2	84.5	33.94	23.57	57.51	288.8	808.7	1097.5	76.4	534.8	611.2	.9638	283209	463.4	206.1	.9718
5	20.2/79.8	682766	422.4		52.8	11.71	94.9	106.61	99.67	279.1	378.77	154.7	108.3	1237.7		549583	444.0	59.4	
6	72.9/27.1	674274	380.4	338.5	68.3	41.82	32.21	74.03	355.9	996.4	1352.3	52.5	367.5	420	.9653	192676	458.5	156.9	.9714
7	79.2/20.8	673266	376.0	335.1	71.0	45.37	24.82	70.19	386.0	1080.9	1466.9	40.5	283.4	323.9	.9647	149604	461.9	200.8	.9709
8	81.3/18.7	672933	374.5	333.9	72.0	46.58	22.31	68.89	396.3	1109.7	1506	36.4	254.7	291.1	.9644	134593	462.4	222.4	.9692
9	59.7/40.3	702529	370.5	316.4	26.2	111.37	154.84	266.21	319.9	895.7	1215.6	85.1	595.6	680.70	.9635	296 336	435.3	45.0	.9722
10	59.4/40.6	684471	383.8	336.4	45.4	52.53	73.98	126.31	299.4	838.3	1137.7	80.7	565.2	645.9	.9658	288 803	447.1	77.7	.9726
11	59.2/40.8	671761	394.6	352.4	80.1	25.20	35.72	60.92	285.0	797.9	1082.9	77.5	542.3	619.8	.9667	283 410	457.3	136.7	.9725
12	59.3/40.7	563712	390.4	346.2	63.2	28.45	40.18	68.63	242.1	677.8	919.90	65.5	458.7	524.2	.9667	237950	453.9	107.9	.9735
13	59.3/40.7	1127339	390.6	346.5	63.2	56.87	80.28	137.15	483.9	1354.9	1838.8	130.9	916.6	1047.5	.9673	475857	454.3	107.9	.9742
14	59.3/40.7	1690938	390.7	346.6	63.2	85.28	120.27	205.65	725.7	2031.8	2757.5	196.3	1374.2	1570.5	.9677	713750	454.5	107.9	.9747
15	59.3/40.7	2254520	390.8	346.7	63.2	113.69	160.44	274.13	967.4	2708.6	3676	261.7	1831.6	2093.3	.9679	951634	454.6	107.9	.9748
16	59.5/40.5	643040	380.4	355.0	36.5	33.39	46.81	80.20	284.1	795.5	1079.6	76.3	534.4	610.7	.9684	271292	444.2	62.5	.9739
17	59.6/40.4	631733	374.4	355.6	27.0	33.38	46.62	80.00	284.0	795.1	1079.1	76.0	532.2	608.2	.9692	266506	438.2	46.3	.9731
18	0/100	686078	441.0	385.6	49.1	-	119.25	-	-	-	-	194.5	1361.4	1555.9	.9736	686078	441	49.1	.9768

Thrust Split - $\frac{\text{Mode I Primary Thrust}}{\text{Mode I Secondary Thrust}}$

F1VAC - Total Mode I Vacuum Thrust

Isp_D - Delivered Specific Impulse Vacuum (Vac) and Sea Level (S.L.)

ε_I - Total Mode I Area Ratio

A_t - Throat Area P-Primary S-Secondary Noz - Total

WPF - Primary Fuel Flowrate

WPOX - Primary Oxidizer Flowrate

WTP - Primary Total Flowrate

WSF - Secondary Fuel Flowrate

WSOX - Secondary Ox Flowrate

WTS - Secondary Total Flowrate

η - $\frac{Isp_D}{Isp_{CDE}}$

F2VAC - Mode II Thrust

IV, A, Preliminary Geometric Analysis (cont.)

Figures IV-1 through IV-3 show the dependence of engine performance and area ratio on thrust split. Decreasing Mode I performance as thrust ratio increases is due to the increased contribution of the lower-performing primary flow to the overall performance. The Mode II delivered Isp increases with thrust ratio because the Mode II area ratio is increased. This increase in area ratio occurs because the secondary throat decreases with respect to the nozzle exit area as the thrust ratio increases.

The Mode I area ratio increases with thrust split because of increases in primary throat area with thrust split. From geometry, the Mode I area ratio can be defined as:

$$\varepsilon_I = \frac{\varepsilon_p A_{tp}/A_{ts} + \varepsilon_S}{(A_{tp}/A_{ts} + 1)}$$

The primary (ε_p) and secondary (ε_S) streamtube area ratios are constant for a given ratio of specific heats (γ) and pressure ratio (P_e/P_c). Therefore, increasing A_{tp} results in a larger ε_I.

Figures IV-4 and IV-5 show the effect of variation in thrust on specific impulse and throat area. Throat area will increase with increasing thrust, but the specific impulse will essentially be unchanged.

Figures IV-6 through IV-8 show the effects of chamber pressure on throat area, area ratio, and specific impulse. Increasing chamber pressure or chamber pressure ratio results in decreasing throat areas and increasing area ratio, in turn resulting in an increase in specific impulse.

Figures IV-9 and IV-10 show how decreasing nozzle exit pressure will result in increasing nozzle area ratio and specific impulse.

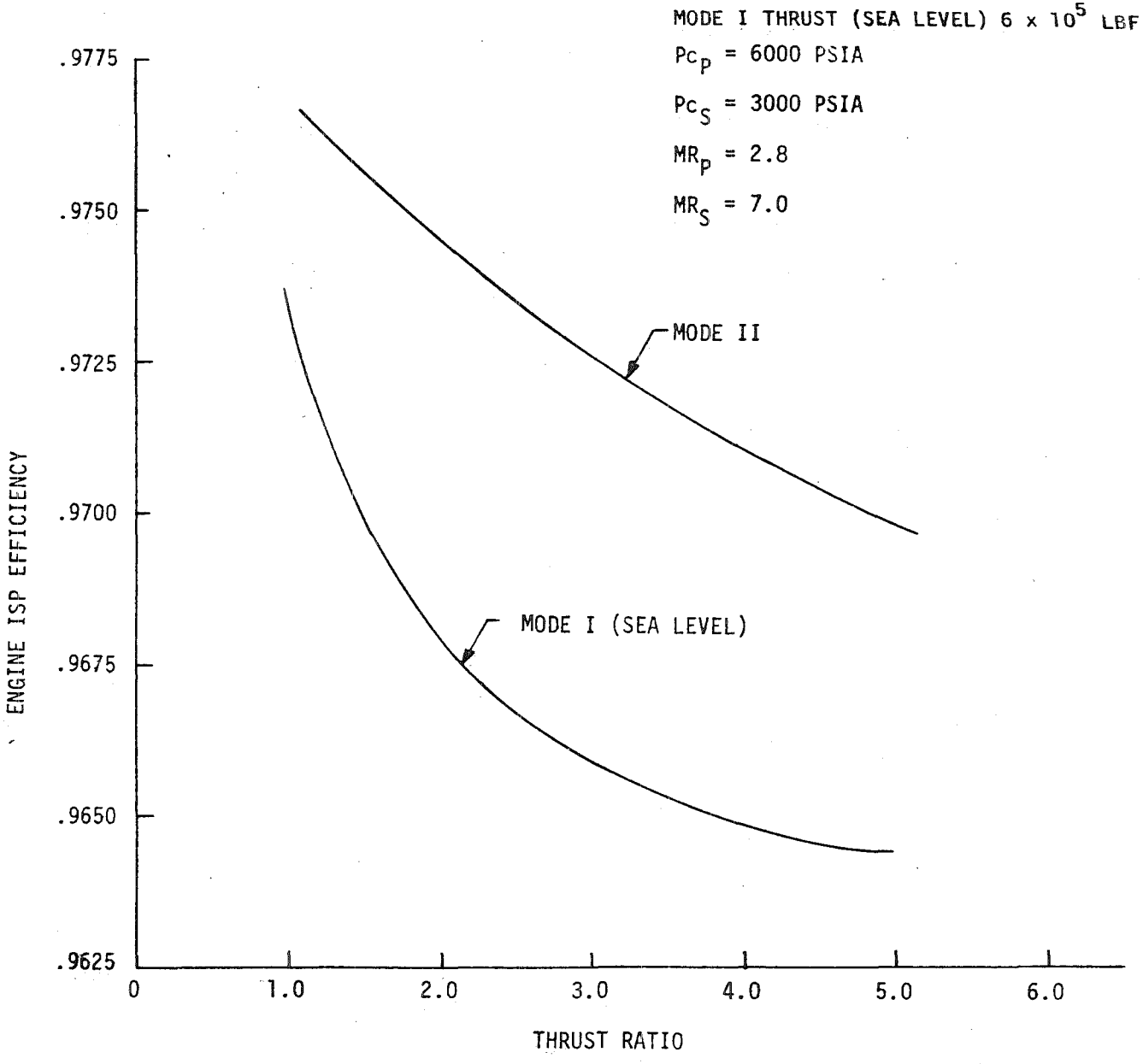

Figure IV-1. Engine Efficiency versus Thrust Ratio

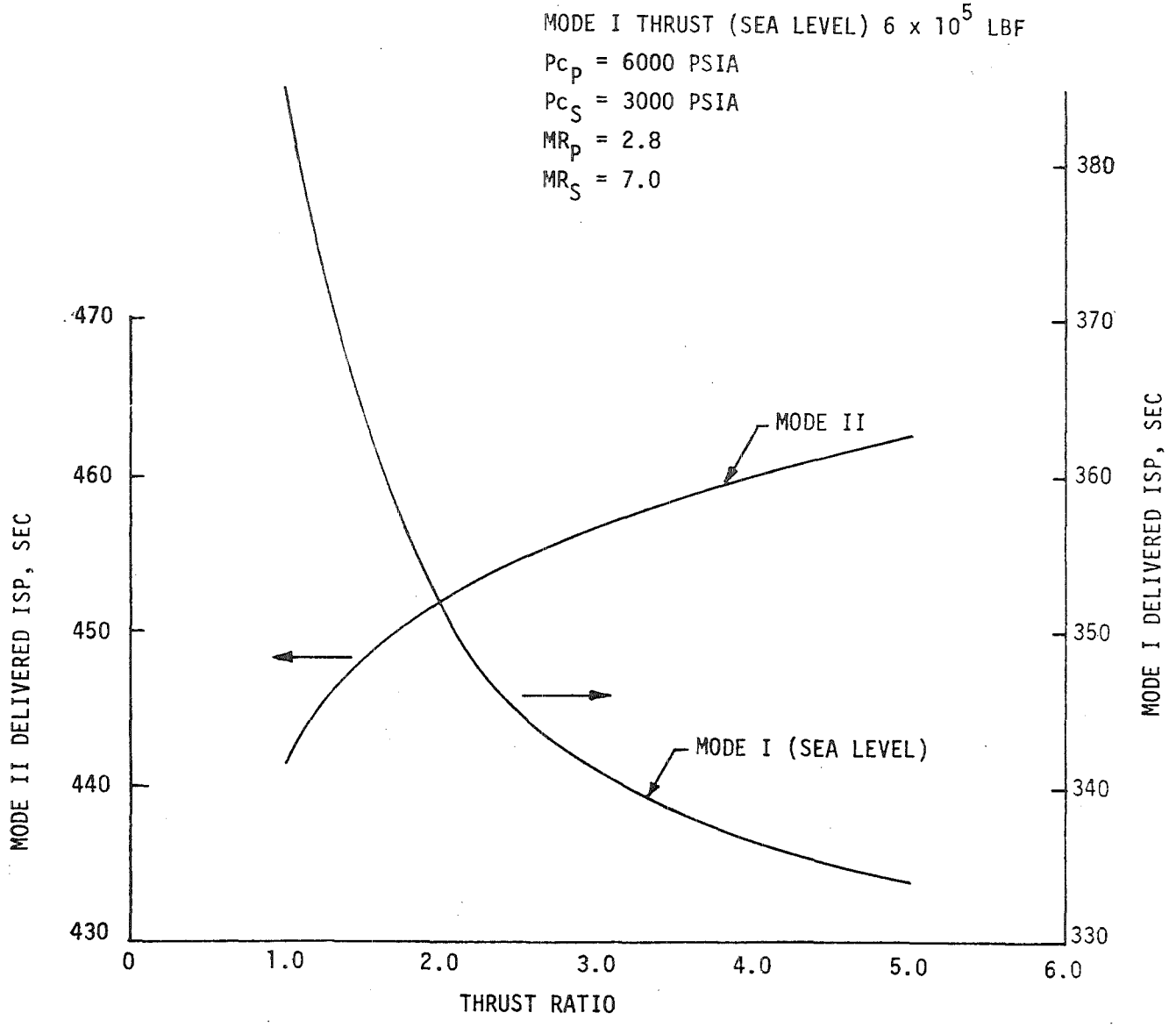

Figure IV-2. Engine I_{sp} versus Thrust Ratio

MODE I $THRUST_{S.L.}$ = 6×10^5 LBF

MR_P = 2.8 Pc_P = 6000 PSIA

MR_S = 7.0 Pc_S = 3000 PSIA

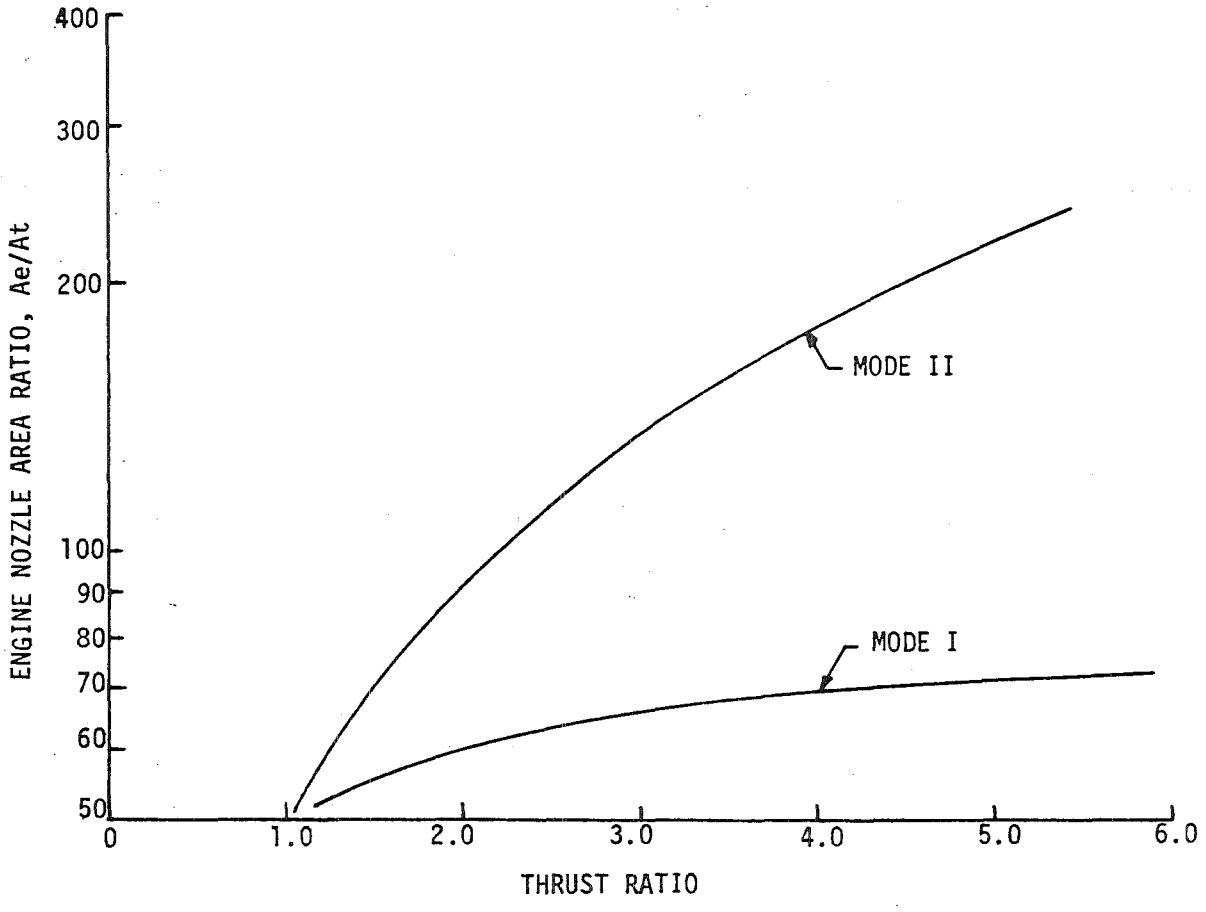

Figure IV-3. Engine Area Ratio versus Thrust Ratio

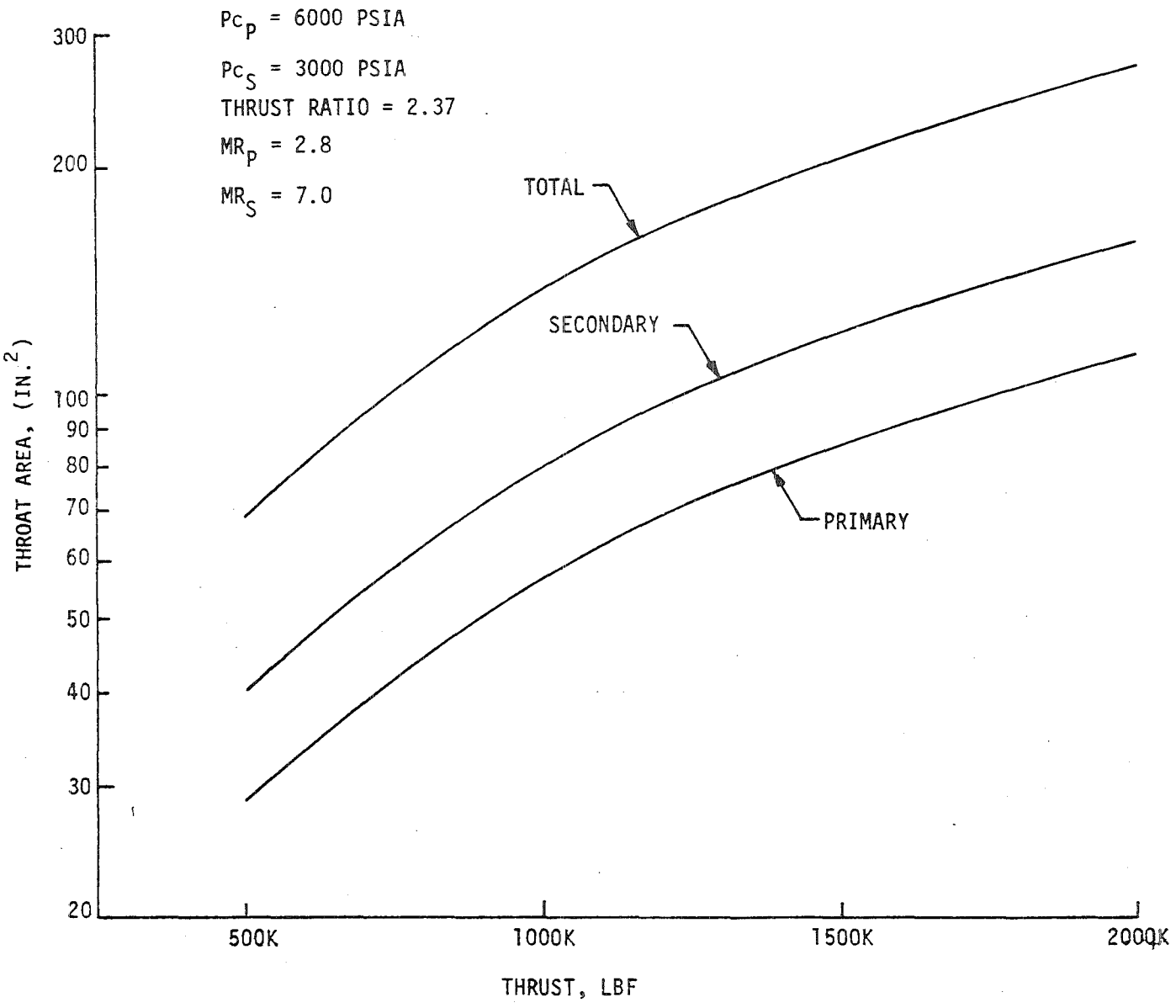

Figure IV-4. Throat Area versus Thrust

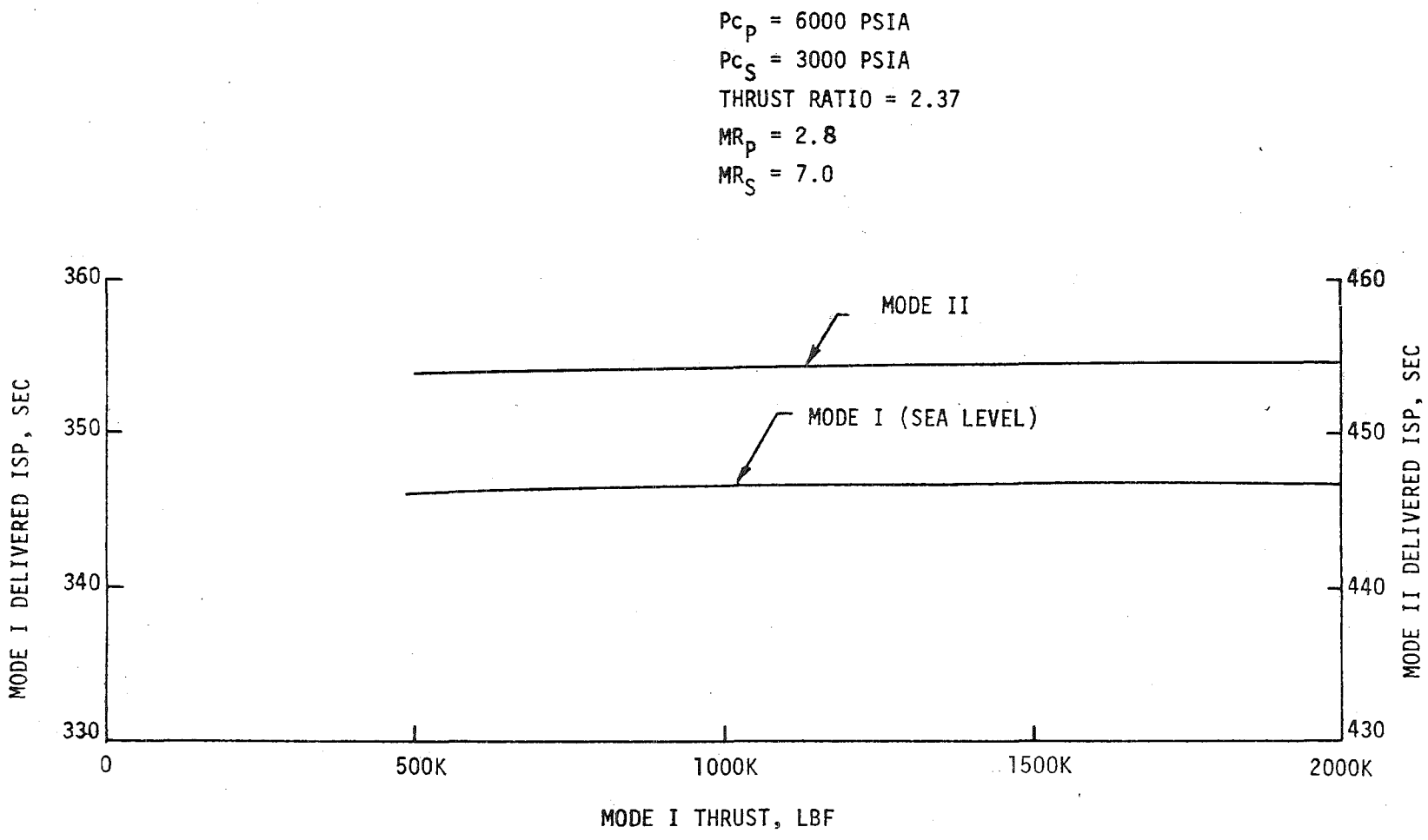

Figure IV-5. Engine I_{sp} versus Thrust

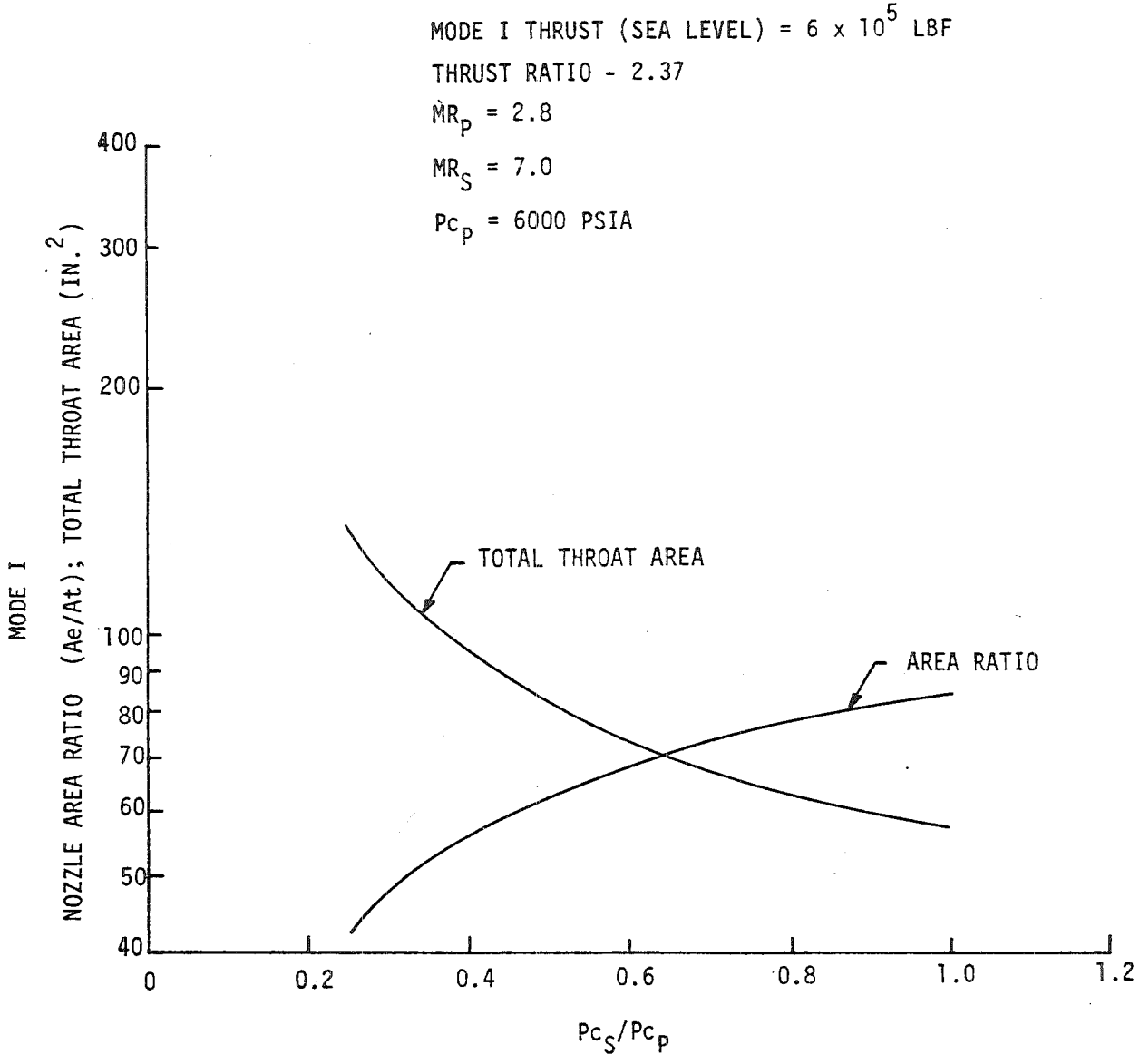

Figure IV-6. Mode I Nozzle Size versus Chamber Pressure Ratio

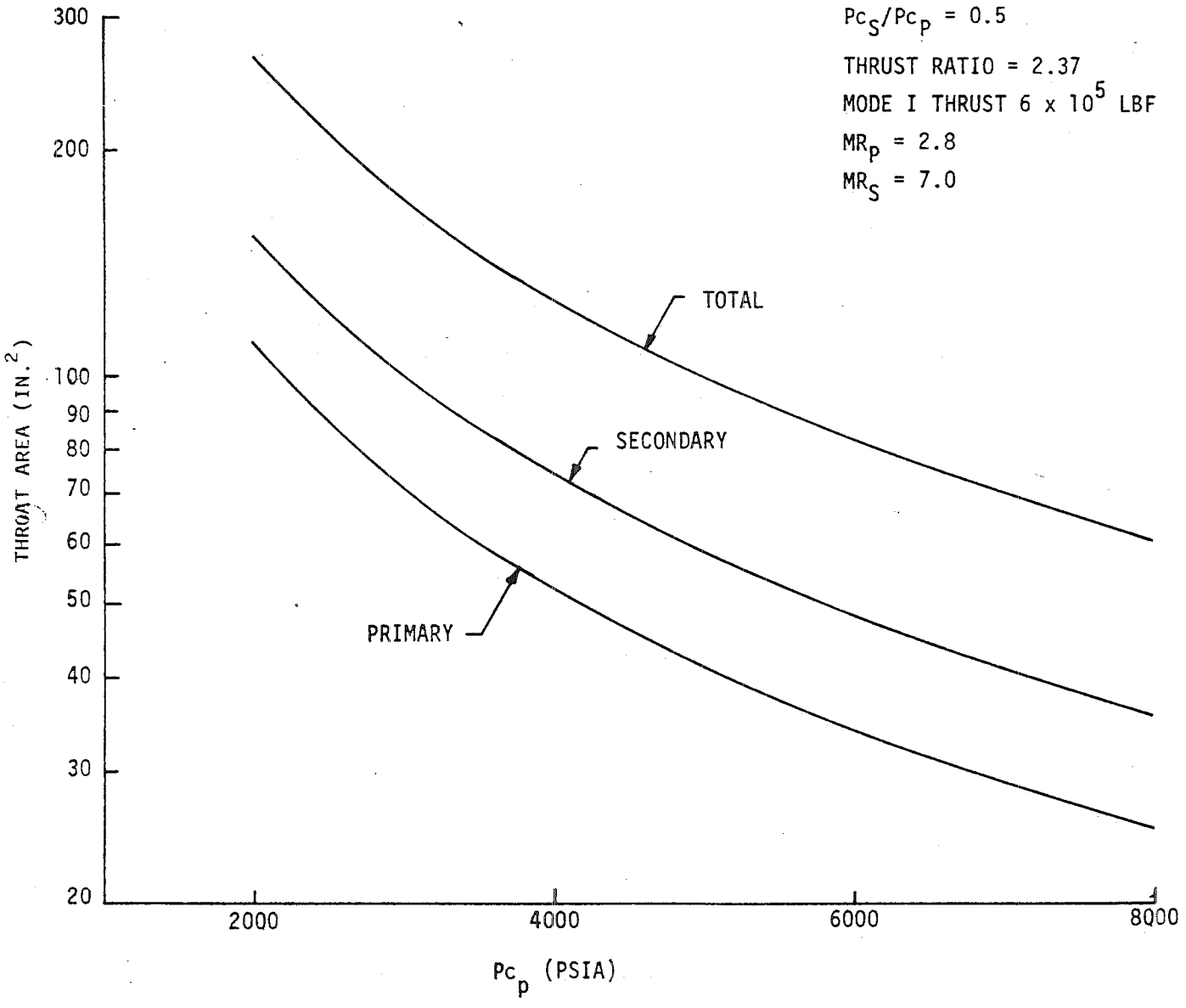

Figure IV-7. Throat Area versus Chamber Pressure

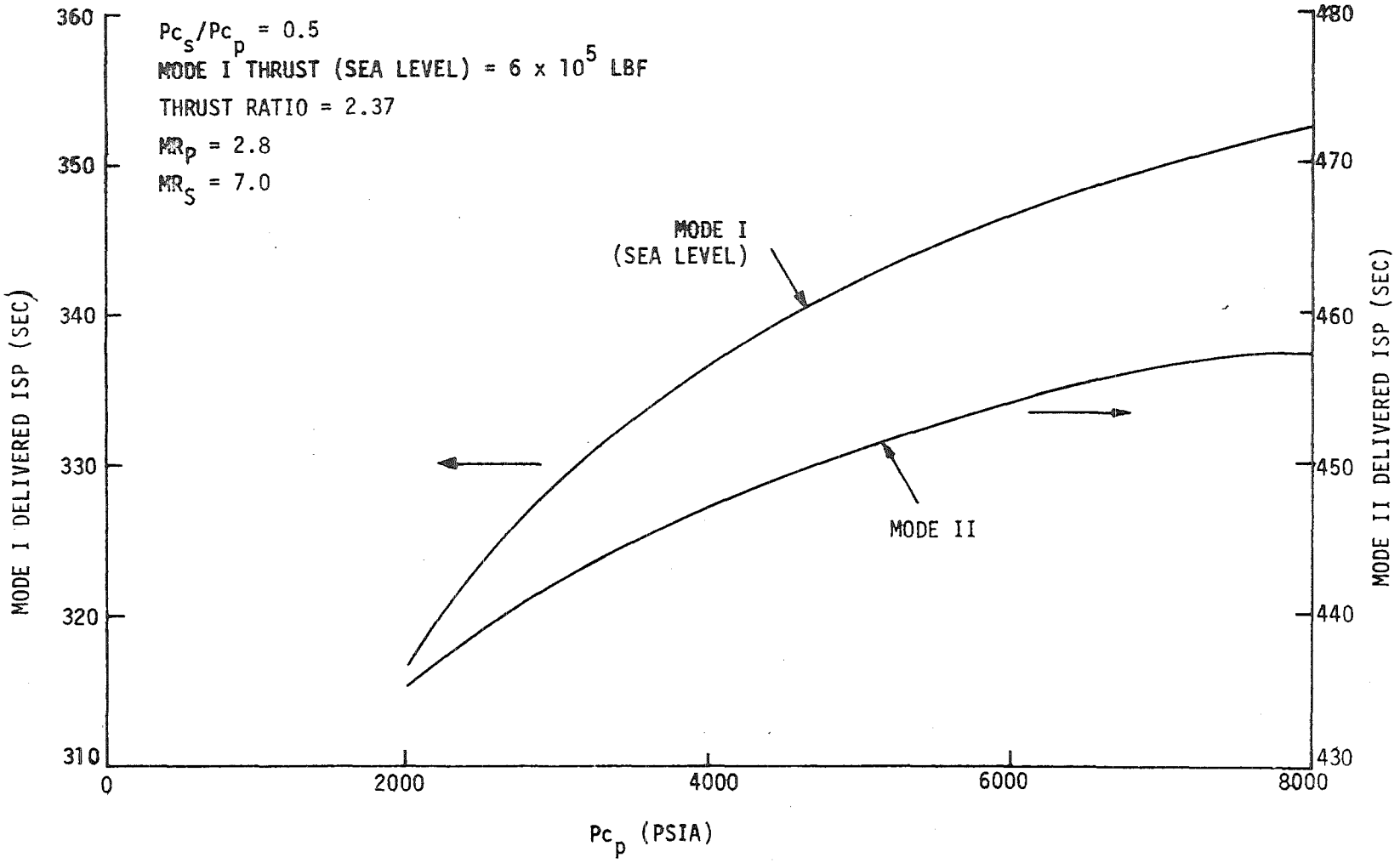

Figure IV-8. Engine I_{sp} versus Chamber Pressure

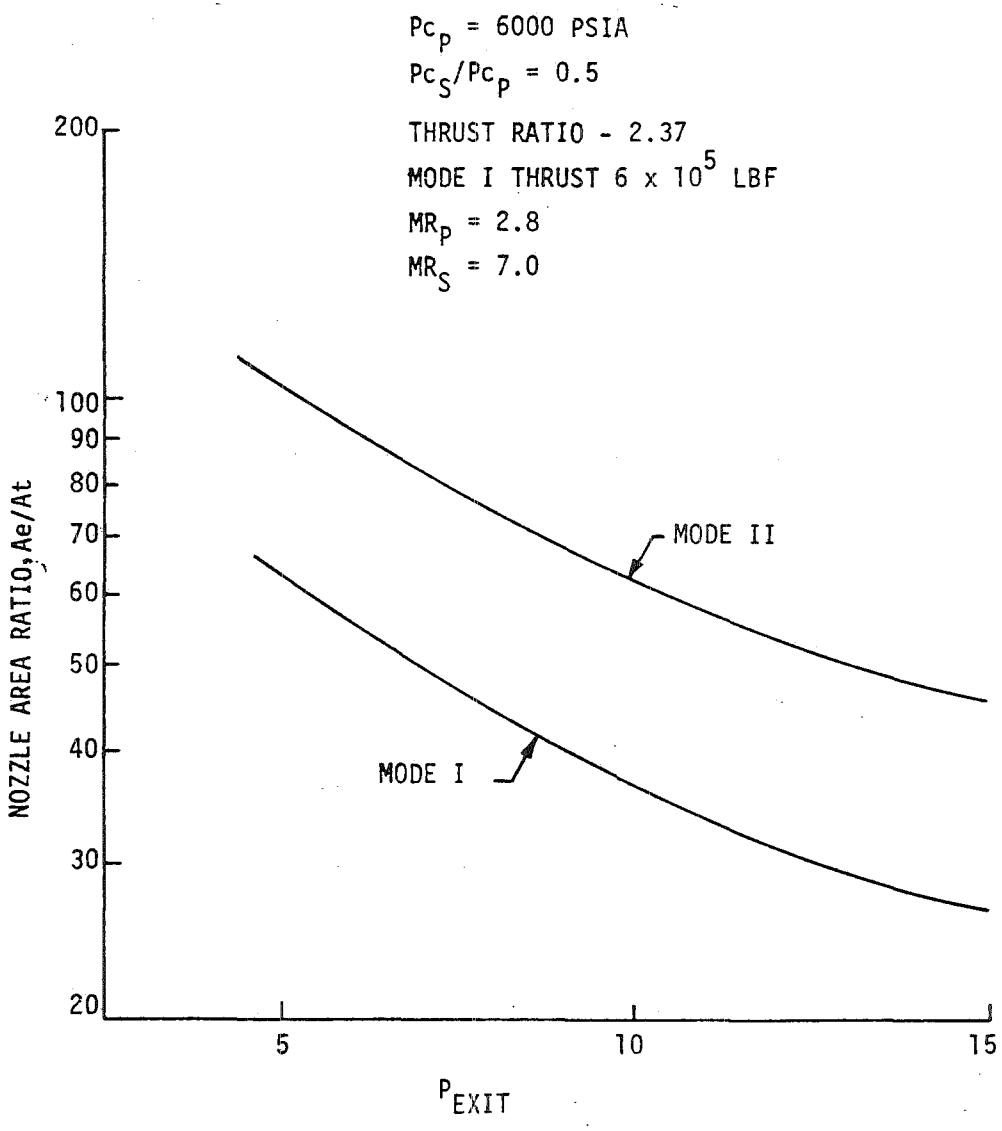

Figure IV-9. Nozzle Area Ratio versus Exit Pressure

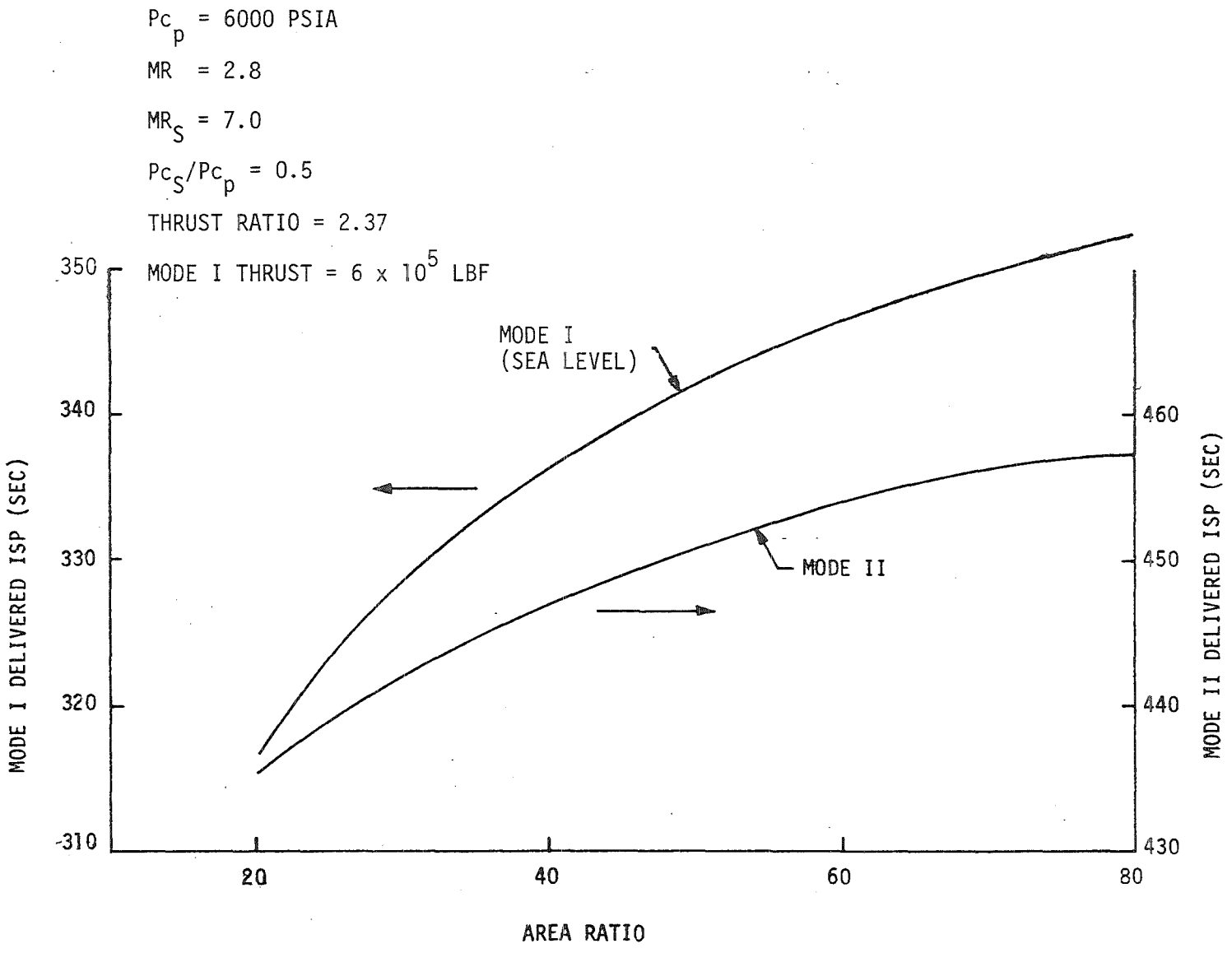

Figure IV-10. Engine I_{sp} versus Area Ratio

IV, A, Preliminary Geometric Analysis (cont.)

The previously listed geometric parameters were used in determining the dual-expander nozzle design. The primary nozzle contour was found by truncating a bell nozzle optimized for the primary flow field area ratio to some specified length or area ratio. An annular nozzle with a conical internal expansion section was positioned such that the flow angle and static pressure at the exit of the internal expansion section matched the flow angle and static pressure at the primary nozzle exit.

These steps are part of the procedure developed for designing the dual-expander nozzle. The nomenclature for this procedure is shown in Figure IV-11. Derivation of the equations is given in Appendix B.

The design procedure is as follows:

1. Calculate the overall engine area ratio, primary and secondary flows streamtube area ratios, throat areas, and equivalent nozzle lengths for a given set of operating conditions.

2. Generate a Rao nozzle contour for the primary nozzle by using the calculated streamtube area ratio and nozzle length. Truncate this contour to the desired area ratio value. The primary nozzle exit radius (R_{E_p}), flow angle (θ_L), and 2-D pressure are now known.

3. Once the secondary nozzle chamber pressure and the desired exit pressure are known, calculate the required conical section area ratio. A conical section is used because the 2-D to 1-D Mach number ratio will be close to one. The conical section exit area (A_{E_c}) can now be calculated for the secondary flow.

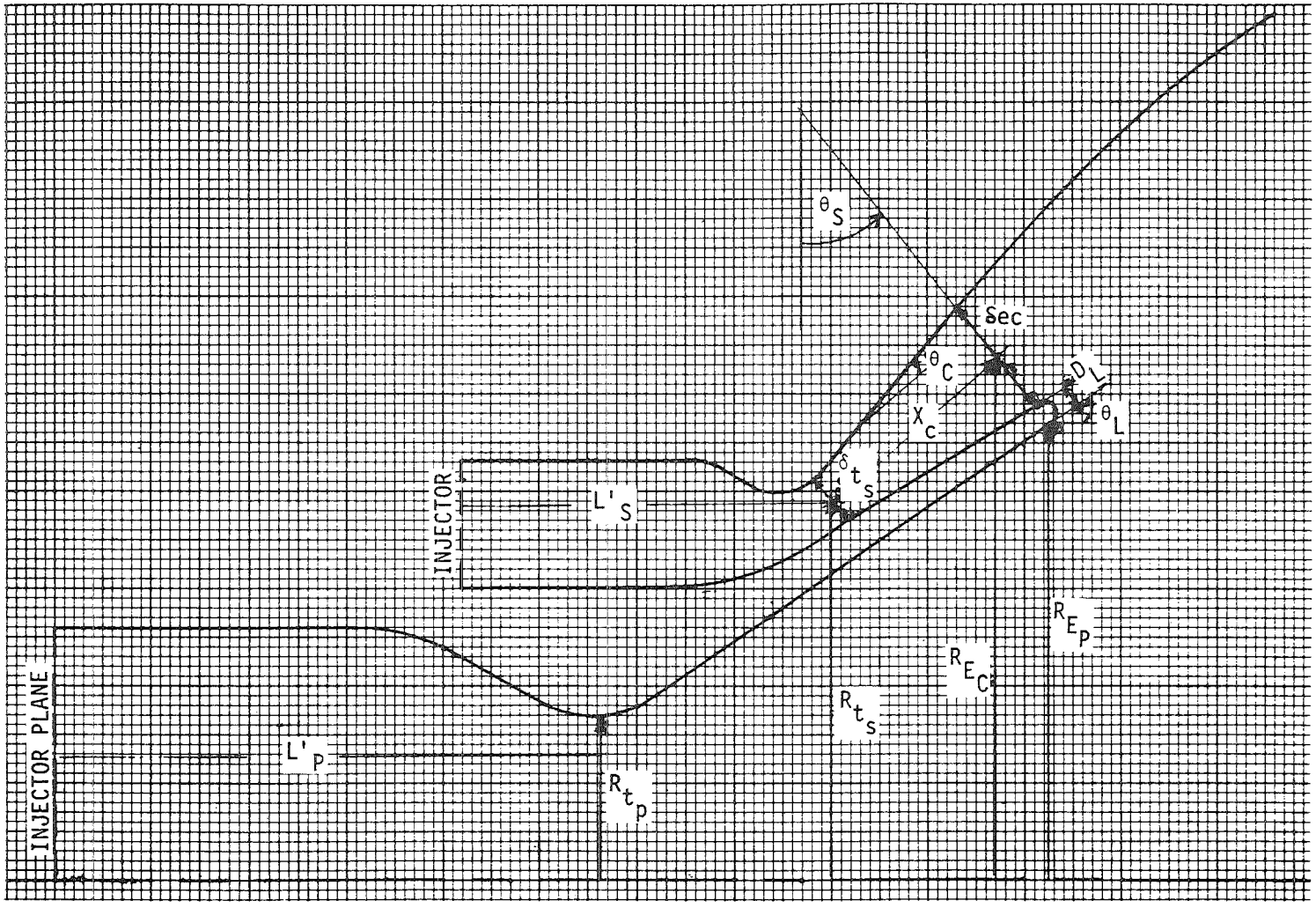

Figure IV-11. Dual Expander Nomenclature

IV, A, Preliminary Geometric Analysis (cont.)

4. Pick a value for either the gap (Δ_{E_c}) or the radius (R_{E_c}) at the conical section exit and solve for the other value by using Equation 1.

$$A_{E_c} = 2\pi \quad \delta_{E_c} \quad R_{E_c} \tag{1}$$

5. Choose an inner lip thickness (D_L) and calculate the secondary flow inclination angle (θ_s) from Equation 2.

$$\text{Cos } \theta_s = \frac{2 (R_{E_c} - R_{E_p} - D_L \text{ Cos } \theta_L)}{\delta E_c} \tag{2}$$

6. The exit geometry for the conical section is now known. The conical half-angle can also be found by

$$\theta_c = \theta_s - \theta_L$$

The next step is to find the proper secondary nozzle throat radius (R_{t_s}) and gap (δ_{t_s}) that occur for the inclination angle, θ_s, and secondary nozzle throat area (A_{t_s}) calculated in Step 1.

7. The secondary nozzle throat radius (R_{t_s}) is calculated from Equation 4.

$$Rt_s^2 \left[2 \sec \theta_s \left(1 - \frac{\sin \theta L}{\sin \theta_s \cos \theta_c}\right)\right] - Rt_s \left[2 \sec \theta_s \left(RE_p + D_L \cos \theta_L - \frac{RE_c \sin \theta_L}{\sin \theta_s \cos \theta_c}\right)\right]$$

$$- \frac{A_{t_s}}{2\pi} = 0 \tag{4}$$

Equation (4) is of the form

$$ax^2 + bx + c = 0$$

IV, A, Preliminary Geometric Analysis (cont.)

$$R_{t_s} = \frac{-b \pm \sqrt{b^2 - 4ac}}{2a}$$

$$a = 2 \sec \theta_s \left(1 - \frac{\sin \theta_L}{\sin \theta_s \cos \theta_c}\right)$$

$$b = -2 \sec \theta_s \left(R_{E_p} + D_L \cos \theta_L - \frac{R_{E_c} \sin \theta_L}{\sin \theta_s \cos \theta_c}\right)$$

$$c = \frac{-A_{t_s}}{2\pi}$$

8. Once R_{t_s} is known, the throat gap (δ_{t_s}) can be found by using Equation 5:

$$A_{t_s} = 2\pi S_{t_s} R_{t_s} \tag{5}$$

The length of the conical section (X_c) is found by the following equation:

$$X_c = \frac{R_{E_c} - R_{t_s}}{\text{Sin } \theta_s} \tag{6}$$

9. The remainder of the secondary nozzle contour is approximated with a third-order parabola:

$$R = A + BX + CX^2 + DX^3$$

The constants A, B, C, D are determined by specifying the coordinates and angle of the outer conical section wall and specifying the coordinates and angle at the overall nozzle exit. The exit radius is found from Step 1, and

the exit angle is assumed to be the same as calculated for the complete primary nozzle contour.

Equations (1) through (6) show that once the exit radius (R_{E_C}) and gap (δ_{E_C}) are picked, there is only one set of values, θ_s, R_{t_s}, δ_{t_s}, X_c, that will satisfy these equations and result in a symmetrical conical nozzle section. Table IV-III lists different values of R_{E_C}, δ_{E_C}, and D_L and their influence on throat gap and location, throat orientation, and length of the conical section. For a constant lip thickness, increasing the exit radius results in decreasing the exit gap, the throat orientation angle, and the distance of the secondary throat from the central axis. The secondary throat gap and the length of the conical section both increase with increasing R_{E_C}. Increasing the lip thickness for a given R_{E_C} and δ_{E_C} causes the secondary throat inclination angle to increase and moves the throat further from the central axis. Both the throat gap and conical section length get smaller.

B. DUAL-EXPANDER AERODYNAMIC BLEED FLOW MODEL

1. Model Development

An aerodynamic model has been developed for Mode II operation and is presented in this section. This model differs from the dual-throat thruster Mode II aerodynamic model in several respects. First, the input geometry for the dual expander aerodynamic model is very simple. It is only necessary to specify the throat area, A_{t_s}, and lip angle, θ_L. The plume model is also very simple. The flow at the exit of the annular nozzle is assumed to be one-dimensional in a cross section normal to the nozzle lip. The flow is assumed to follow a Prandtl-Meyer expansion around the nozzle lip until an angle is reached such that the pressure of the base region is achieved. The plume boundary is taken to be a straight line inclined at this angle.

TABLE IV-III

DUAL EXPANDER GEOMETRIC INFLUENCES

D_L	R_{E_C}	δ_{E_C}	θ_S	θ_C	R_{t_s}	δ_{t_s}	X_C
0.5	10.	3.2986	81.2	50.2	8.9978	0.8526	1.014
0.5	10.5	3.1416	61.4	30.4	8.8027	0.8715	1.933
0.5	10.75	3.0685	49.3	18.3	8.2898	0.9254	3.245
0.5	10.85	3.0402	43.6	12.6	7.695	0.9969	4.575
0.5	11.0	2.9988	33.4	2.4	3.9776	1.9286	12.76
0.5	10.75	3.0685	49.3	18.3	8.2898	0.9254	3.2451
0.75	10.75	3.0685	59.1	28.1	8.9741	0.8548	2.0697
1.0	10.75	3.0685	68.1	37.1	9.4266	0.8138	1.4263
0.5	11.0	2.988	33.4	2.4	3.9776	1.9286	12.76
0.75	11.0	2.988	46.2	15.2	8.2536	0.9294	3.8051
1.0	11.0	2.988	56.7	25.7	9.1272	0.8405	2.2407

$\epsilon_{p_{TRUNC}} = 8.0$

$\epsilon_C = 4.3$

$A_{E_C} = 207.26 \text{ in.}^2$

$A_{t_s} = 48.2 \text{ in.}^2$

$R_{Ep} = 9.32 \text{ in.}$

$\theta_L = 31°$

IV, B, Dual-Expander Aerodynamic Bleed Flow Model (cont.)

The shear layer is superimposed on the plume boundary. With one exception, the assumptions made in formulating the shear layer model are the same as those used for the dual throat (described in Section III). The exception is that the shear layer is assumed to have axial symmetry. Assuming axial rather than planer symmetry significantly complicates the formulation; however, as discussed in Section III, this assumption is necessary for the dual expander because of the proximity of the shear layer to the flow axis. In Reference 18, Mueller has presented an analysis for an axisymmetric shear layer for a gas with constant properties. The analysis presented here allows for the addition of bleed flow into the base recirculation region. As was the case with the dual throat aerodynamic bleed flow model, the bleed flow gas can have properties different from those of the primary stream. The dual expander shear model is illustrated in Figures IV-12 and IV-13. Figure IV-12 shows the shear layer developing along the jet boundary until a position is reached where the shear layer is turned and transformed into a wake. The position at which the shear layer is turned is called the "neck." Turning the flow abruptly at the neck results in a recompression shock (shown in Figure IV-12). The distance from the exit of the interior nozzle to the neck, z_3, is shown in Figure IV-13. The streamline deflection angle at the neck, θ_3, and the trailing wake radius, r_w, are also shown in Figure IV-13. The calculational procedure is illustrated in Figure IV-14. As was the case for the dual throat aerodynamic bleed flow model, the problem requires solving three nonlinear simulateous equations for three unknowns. The three unknown quantities are P_b/P_{op}, H_r/H_{op} and Y_{pr}. The three equations are (A), (B), and (C) in Figure IV-14. These equations are:

$$\dot{W}_s/\dot{W}_p - \frac{\pi z_3^2}{A_p \cos \theta_3} M_p \left(\frac{P_b}{P_{op}}\right)\left(\frac{\gamma_p+1}{2}\right)^{\frac{\gamma_p+1}{2(\gamma_p-1)}} \left[1 - C_b^2\right]^{-1/2}$$

$$* \left[- A \left(I_1 (\eta_j) - I_1 (\eta_d) + (J_1 (\eta_j) - J_1 (\eta_d)\right] = 0 \qquad (A)$$

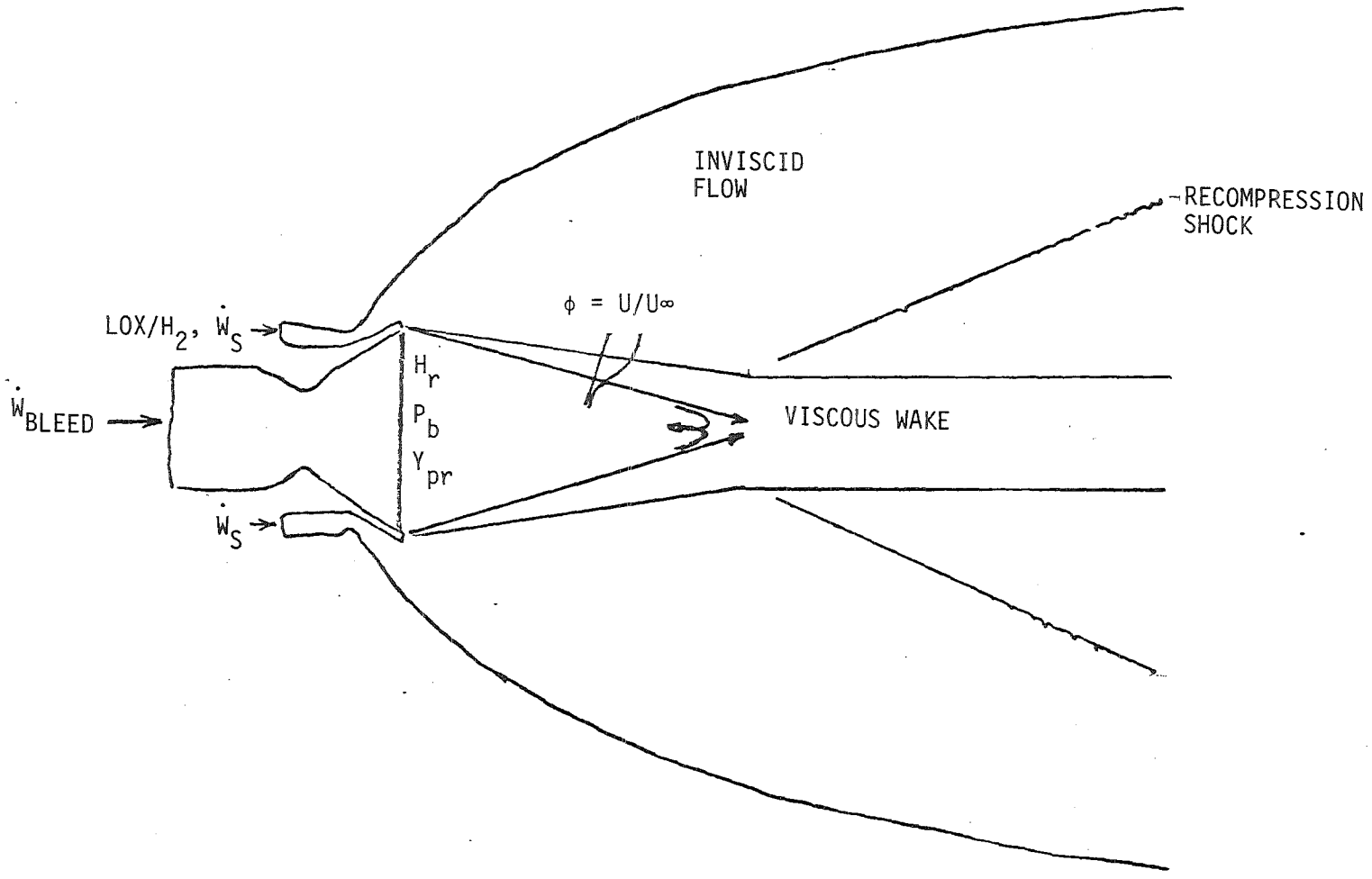

Figure IV-12. Dual Expander Shear Layer Model

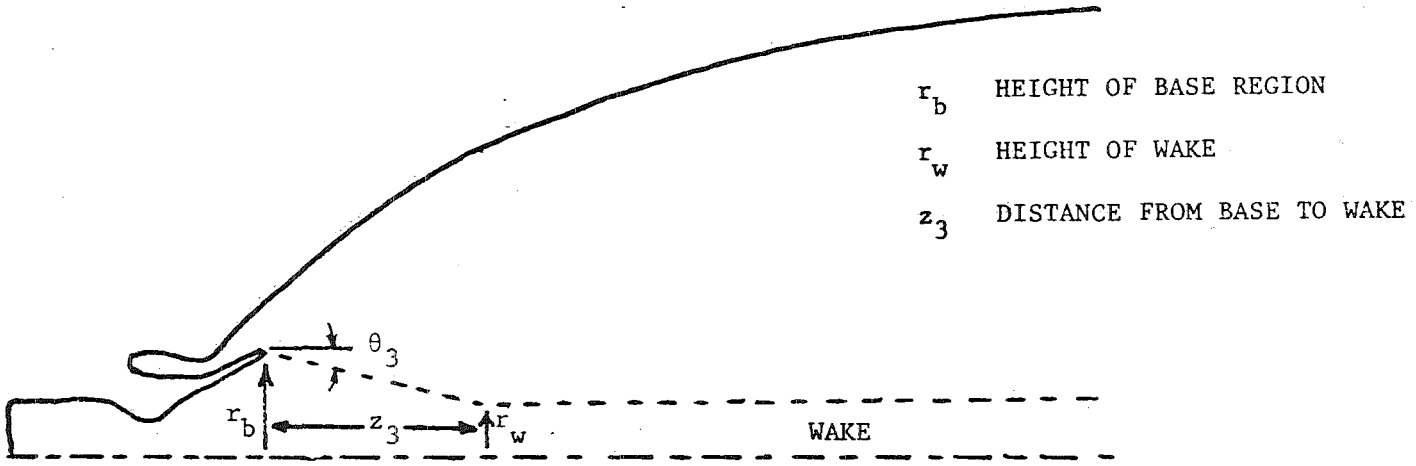

Figure IV-13. Dual Expander Aerodynamic Model Geometry

INPUT:

GAS PROPERTIES;

C_P, M_W, AND H_O FOR BOTH STREAMS

P_O FOR OUTER STREAM

MACH NO.

RECOMPRESSION FACTOR, N

% BLEED.

GEOMETRY;

R^*, θ_B, R_W, R_B, A_P

ESTIMATES

P_B/P_O , H_R/H_O , Y_{PR}

METHOD:

NEWTON'S METHOD, GIVEN ABOVE ESTIMATES FIND CONVERGED VALUES THAT SATISFY CONDITION OF

(A) CONTINUITY FOR TOTAL FLOW

(B) ENERGY CONSERVATION

(C) CONTINUITY OF BASE FLOW COMPOSTION

SPECIAL CASE: 0% BLEED.

OUTPUT:

P_B/P_O , H_R/H_O , Y

CONSTANT PRESSURE BOUNDARY SHAPE

Figure IV-14. Calculational Procedure for the Dual Expander Aerodynamic Model

IV, B, Dual-Expander Aerodynamic Bleed Flow Model (cont.)

$$\frac{H_{os}}{H_{op}} - \left\{\frac{H_r}{H_{op}} + \left[\frac{H_r}{H_{op}} - 1\right] \alpha\right\} = 0 \qquad (B)$$

$$Y_{pr} - \frac{\alpha}{1+\alpha} = 0 \qquad (C)$$

where:

$$\alpha = \frac{-A \quad (I_3 (\eta_d) + J_3 (\eta_d)}{-A \quad (I_1 (\eta_j) - I_1 (\eta_d) + J_1 (\eta_j) - J_1 (\eta_d)}$$

and

$$A = \frac{J_3 (3) - \left[J_1 (3) - J_1 (\eta_d)\right]}{I_3 (e) - \left[I_1 (3) - I_1 (\eta_d)\right]}$$

In the above equations, the integrals I_1, I_3, J_1, and J_3 are

$$I_1 (\eta) = \int_{-3}^{\eta} \frac{\rho}{\rho_b} \phi \, d\eta$$

$$I_3 (\eta) = \int_{-3}^{\eta} \frac{\rho}{\rho_b} \phi^2 \, d\eta$$

$$J_1 (\eta) = \int_{-3}^{\eta} \frac{\rho}{\rho_b} \phi\eta \, d\eta$$

and

$$J_3 (\eta) = \int_{-3}^{\eta} \frac{\rho}{\rho_b} \phi^2 \eta \, d\eta$$

IV, B, Dual-Expander Aerodynamic Bleed Flow Model (cont.)

An input manual for the dual expander aerodynamic bleed flow model is presented in Appendix C.

2. Model Calibration

The dual expander base flow model contains the following three parameters that must be determined from experimental data:

σ = The jet spreading parameter

N = The Nash recompression factor

k = A proportionality factor relating the radius of the trailing wake to the shear layer velocity thickness

The approach taken in selecting each of these parameters is discussed below. Note that all of the data used is for air (γ = 1.4) without bleed flow.

σ, the Jet Spreading Parameter

The classical jet spreading expression measured by Korst (Ref. 6) for air was used, i.e.,

$$\sigma = 12 + 2.758M_b$$

For incompressible flow (M_b = 0), this expression gives the well-known result that

$$\sigma_o = 12.$$

Many alternate expressions for σ are available in the literature (see Ref. 7, 11, 18).

IV, B, Dual-Expander Aerodynamic Bleed Flow Model (cont.)

N, the Nash Recompression Factor

The data presented by Mueller (Ref. 18) was used to determine N. This data is for the flow of air past a cylinder. Measured values of base pressure ratio vs the Mach number of the approach flow are presented in Figure IV-15.* The theory predicts that base pressure depends only weakly on the trailing wake radius ratio. Measured values of the trailing wake radius ratio are shown in Figure IV-16.

The computer model was calibrated by inputting the flow conditions that correspond to the experimental conditions and by inputting the trailing wake radius from Figure IV-16. It was found that

$$N = .4$$

gave the best fit to the data. This is consistent with the treatment used in the dual throat aerodynamic model computer program. It should be noted that Mueller (Ref. 18) used a value of N = 1 (i.e., the full value from the shock) and a different expression for a σ (i.e., an expression that gives values that are greater than those given by the Korst expression).

K, Shear Layer/Wake Proportionality Factor

For the case of air without bleed flow, the trailing wake radius ratio can be obtained from Figure IV-16. In order to obtain a similar result for situations with bleed flow and with gases other than air, the following assumption was made.

*Figures IV-15 and IV-16 are from Reference 18.

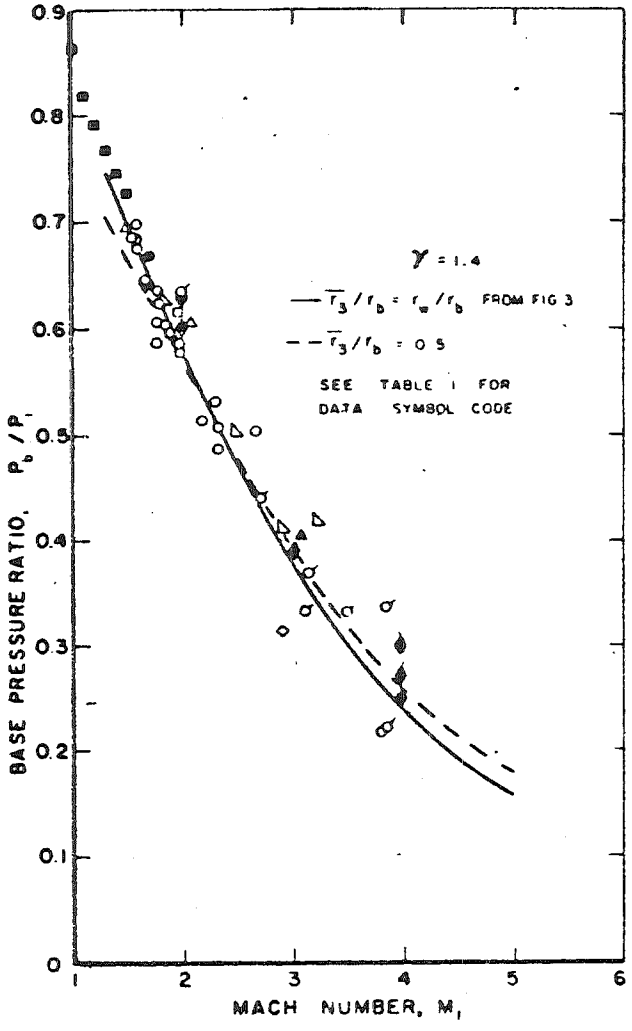

Figure IV-15. Axisymmetric Supersonic Base Pressure From Modified Conical Pressure Rise Method

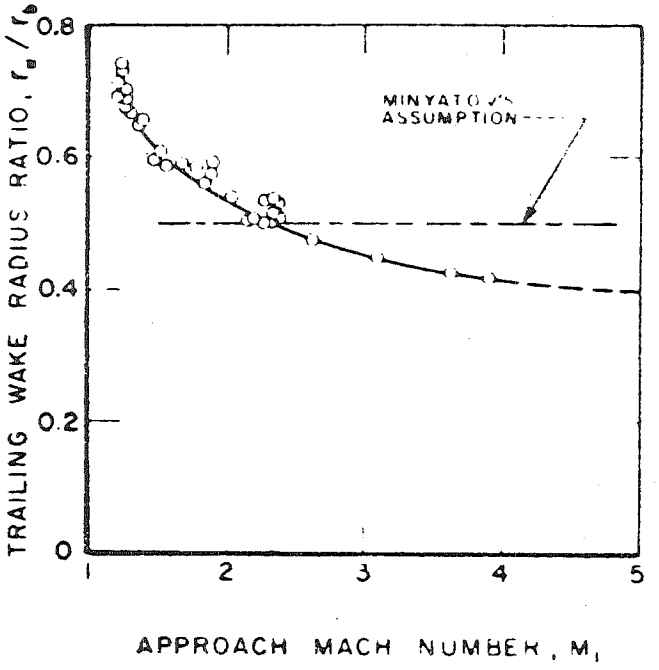

Figure IV-16. Trailing Wake Radius versus Mach Number for $\delta = 1.4$

IV, B, Dual-Expander Aerodynamic Bleed Flow Model (cont.)

It was assumed that the radius of the trailing wake is proportional to the velocity thickness of the shear layer at the neck, δ. Since this value is proportional to

$$(x/r_b)/\sigma$$

where x/r_b is the nondimensional shear layer length, it follows that

$$r_w/r_b = k\,(x/r_b)\sigma$$

where

K is the proportionality constant.

It was found that

$$K = 4$$

i.e., this approximate value was consistently calculated when

$$\sigma = 12 + 2.758M_b$$

$$N = .4$$

and the cases shown in Figure IV-16 were calculated.

C. DUAL EXPANDER FLOW FIELD ANALYSIS

Performance calculations were carried out for both Mode I and Mode II operation. In order to carry out these calculations, it was convenient to divide the dual expander flow field into regions that could be analyzed separately. These regions, numbered I through V, are shown in Figures IV-17a and IV-17b.

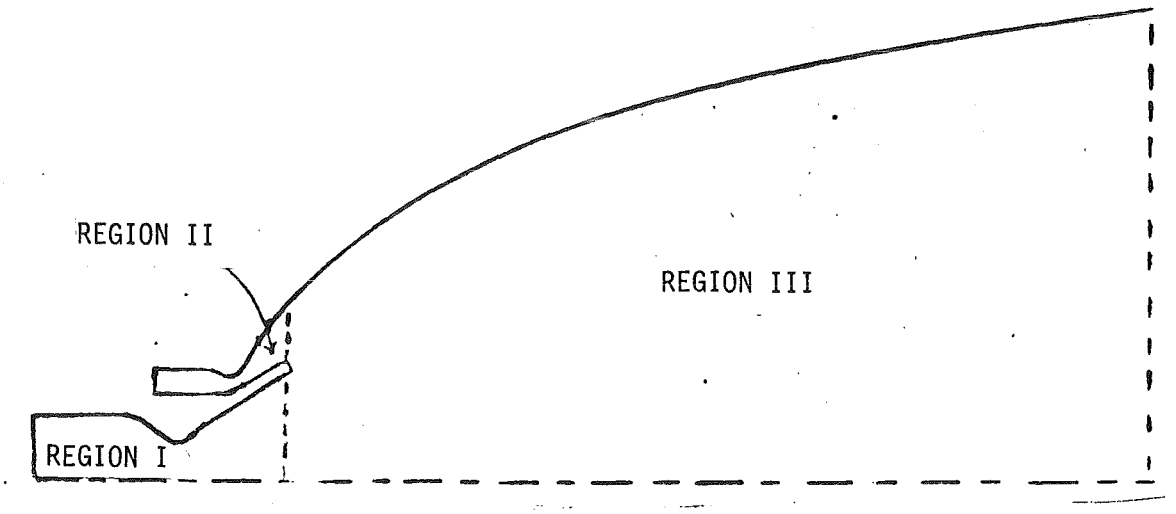

a. DUAL EXPANDER MODE I OPERATION
BOTH ENGINES ON

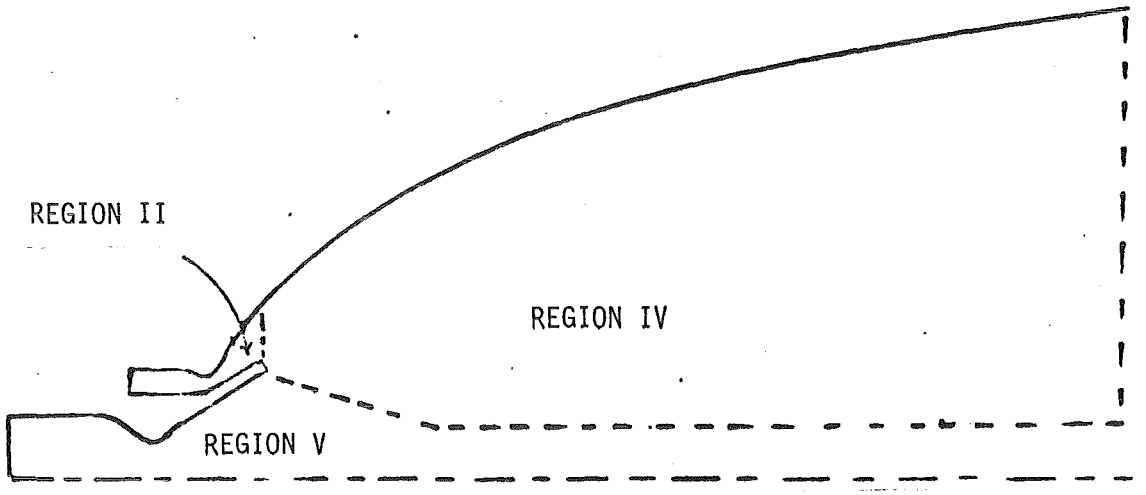

b. DUAL EXPANDER MODE II OPERATION
OUTER ENGINE ON, INNER ENGINE OFF

Figure IV-17. Dual Expander Modes I and II Operation

IV, C, Dual Expander Flow Field Analysis (cont.)

Region I is the flow field inside the interior thruster during Mode I operation. The downstream boundary of Region I is the exit plane of the primary thruster. Region I can be conveniently, accurately, and inexpensively calculated by using the TDK computer program (Ref. 3).

Region II is the flow field inside the annular thruster. This flow field is the same during both Mode I and Mode II operation. The downstream boundary of Region II is the exit plane of the annular thruster. Region II can be calculated by using the VNAP computer program (Ref. 4) that was discussed in Section III. VNAP is particularly well suited to calculating the transonic flow field in an annular nozzle. The VNAP calculations are somewhat lengthy and require dividing Region II into subregions in order to obtain sufficient accuracy.

Region III is the dual expander flow field during Mode I operation (both engines on) that is downstream from Regions I and II. In order to minimize shock losses, the engine is designed to operate so that the static pressures in Regions I and II are equal at the point where these two flow streams come together. This point is the origin of a contact discontinuity, or slip line, between the two streams. The TDK program has been modified to calculate the flow field in Region III. In order to use the option, it is necessary to input flow conditions along the exit planes of Regions I and II. The two flow streams that comprise Region III are allowed to have different values of stagnation pressure, specific heat ratio, and molecular weight.

Region IV is the inviscid portion of the flow field that occurs downstream of Region II during Mode II operation (inner thruster off, outer thruster on). The interior boundary of Region IV is determined by the shape of the viscous-inviscid boundary of the base recirculation flow and wake. Region IV can contain shock waves. The VNAP computer program (Ref. 4) has

been used to calculate the flow field in this region so that the effect of shock waves can be included. In order to maintain accuracy, it is necessary to divide Region IV into subregions.

Region V is the base flow recirculation and wake region that is calculated by the dual expander aerodynamic model described in the previous section.

A prototype design for the dual-expander thruster was generated by using the procedure defined in Section IV,A, and performance calculations were carried out by analyzing the five flow regions described above. These calculations are described in the following subsections.

1. Calculations for Mode II Operation

Calculating the dual expander performance for Mode II operation requires calculating Regions V, II, and IV that were shown in Figure IV-17b. Results obtained for each region are discussed below. The purpose of these calculations was to determine the influence of primary nozzle truncation and/or the introduction of bleed flow. In order to isolate these influences, it was necessary to keep the same secondary nozzle contour and vary the primary nozzle exit area only.

Region V

Region V was calculated for the prototype engine for three bleed flow values and for three truncation positions for the dividing wall. Results from these nine cases are presented in Table IV-IV, labeled as Cases 2 through 10.* The bleed flow values used were zero bleed, "moderate" bleed, and "maximum" bleed.

*Case 1 was used as a sample case for VNAP for program checkout prior to completing Cases 2 through 10.

TABLE IV-IV

BASE FLOW STUDY, SUMMARY OF RESULTS

Case No.	R_B cm	R_B in.	θ_3 °	Z_3/R_b	r_w/r_b	% Bleed	M_p	θ_s	Truncation
1	24.97	(9.83)	21.°	1.3	.5	N/A	N/A	N/A	Minimum
2	25.18	(9.913)	14.64°	2.296	.4	0%	2.79	23.4°	Minimum
3	25.18	(9.913)	8.62°	3.300	.5	.05%	2.79	19.2°	Minimum
4	N/A	N/A	N/A	N/A	N/A	N/A	2.79	N/A	Minimum
5	22.47	(8.8446)	12.80°	2.203	.5	0%	2.19	25.2°	Moderate
6	22.47	(8.8446)	7.02°	3.249	.6	.25%	2.19	21.7°	Moderate
7	22.47	(8.8446)	4.92°	3.487	.7	.5%	2.19	20.7°	Moderate
8	19.93	(7.8474)	10.38°	2.730	.5	0%	1.016	34.2°	Maximum
9	19.93	(7.8474)	6.17°	2.775	.7	1%	1.016	32.4°	Maximum
10	19.93	(7.8474)	3.53°	3.240	.8	3%	1.016	35.3°	Maximum

IV, C, Dual Expander Flow Field Analysis (cont.)

The aerodynamic model is a small bleed flow model. If the bleed flowrate becomes too large, it will lead to the following: the base pressure region will not close; there will be no recirculation, the model will no longer be applicable. "Maximum" bleed was defined as an amount just short of causing this condition. "Moderate" bleed flow was taken as half of the "maximum" bleed flow value.

"Minimum" truncation corresponds to arbitrarily choosing to truncate the primary nozzle to a geometric area ratio of 8:1. "Maximum" wall truncation was obtained by truncating the dividing wall just downstream of the Mach one position on the annular nozzle side of the wall. The "moderate" wall truncation position was taken as halfway between "maximum" and "minimum" truncation.

The parameters tabulated in Table IV-IV were illustrated in Figure IV-13. Inputs to the dual expander aerodynamic model that differ in each case are 1) the exit radius of the interior nozzle, r_b, 2) the Mach number of the approach flow at the end and upper side of the dividing wall, M_p, and 3) % bleed for inner engine. The approach flow angle is 31°. The operating conditions for these cases are listed in Table IV-V.

TABLE IV-V

MODE II OPERATING CONDITIONS

	Outer Nozzle	Bleed to Inner Nozzle
Flow	LOX/LH_2	GG
Mixture Ratio	7.0	.72
γ	1.18	1.389
C_p	.81371 cal/gm °K	2.04454 cal/gm °K
Molecular Weight	16.	3.467
Total Temperature	3778°K (6800°R)	712°K (1281°R)
Total Pressure	20.68 MPa (3000 psia)	N/A
Throat Area	281 cm^2 (43.5 $in.^2$)	N/A

IV, C, Dual Expander Flow Field Analysis (cont.)

The geometry of the shear layer and wake as calculated by the dual expander aerodynamic model is defined by the parameters θ_3, z_3/r_b, and r_w/r_b. Calculated values for these parameters are listed in Table IV-IV. Also listed is the value of the shock angle, θ_s, corresponding to a deflection angle of θ_3.

The approach Mach number at the three truncation positions was input from the VNAP results for Region II. The shear layer and wake shape calculated for Region V was used to define the lower boundary for Region IV. The Region II and IV calculations are discussed below.

Region II

Figure IV-18 shows an enlargement of Regions I and II. The upper wall of Region II is steep, having a maximum wall angle of 67°. To obtain accuracy, Region II was divided into an upstream subregion and a downstream subregion, and these were calculated separately by using VNAP.

Mach number contours calculated for the upstream subregion are shown in Figure IV-19. Inlet conditions for this subregion were prescribed to be one-dimensional parallel flow along a vertical cross section at the extreme left of Figure IV-19. The calculations show that, along the lower wall, the flow is turned inward abruptly while subsonic (M = .4). Along the upper wall, the nozzle throat, a circular arc with a small radius of curvature, causes the flow to be choked. The mass flowrate through the nozzle is found to be only about 91% of the one-dimensional flow value. At the exit of this subregion, the flow is found to be supersonic, and, therefore, independent of the conditions downstream.

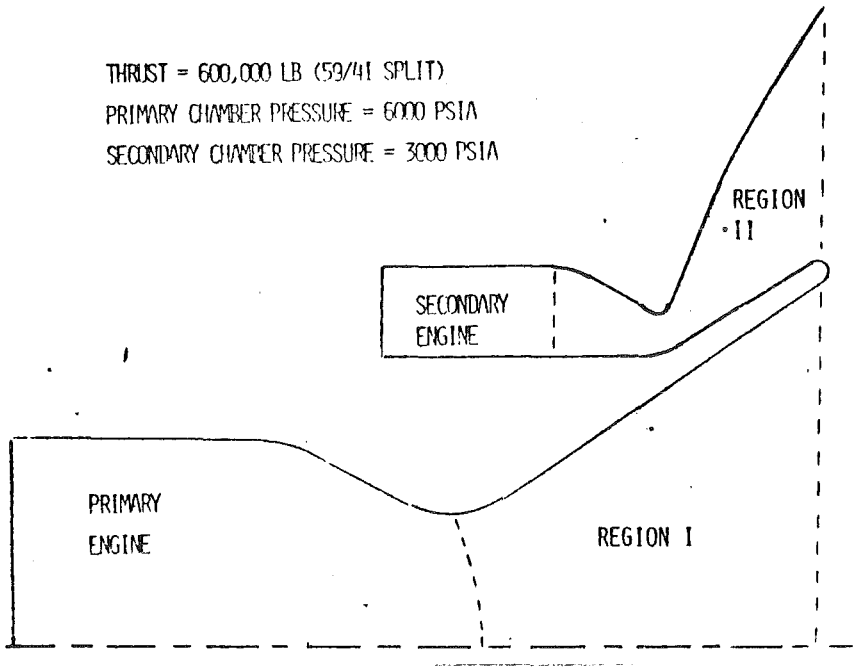

Figure IV-18. Dual Expander Thrust Chamber Geometry

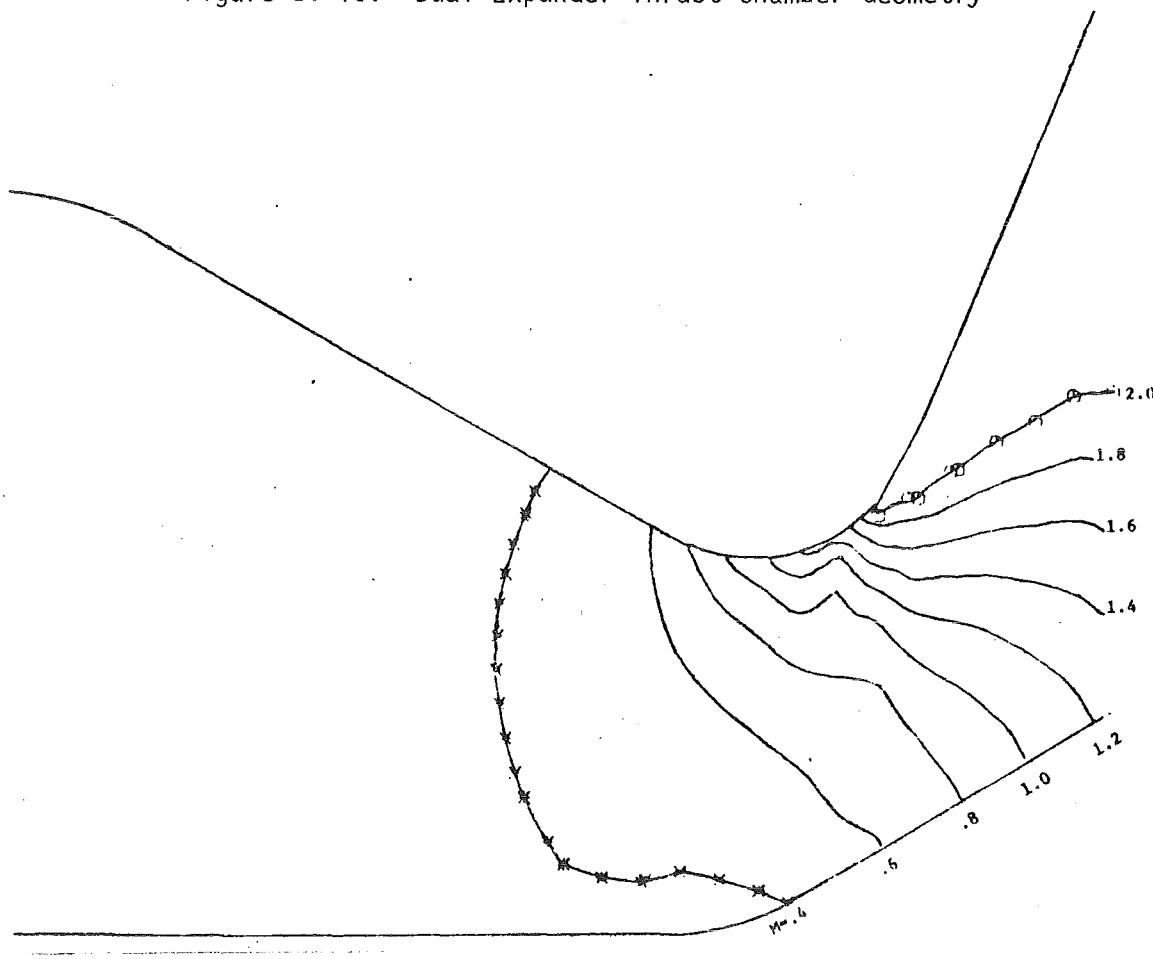

Figure IV-19. Annular Nozzle Throat Section Mach No. Contours

IV, C, Dual Expander Flow Field Analysis (cont.)

Mach number contours calculated for the downstream subregion of Region II are shown in Figure IV-20. Inlet conditions for this subregion are the exit conditions of the upstream subregion.* An interesting feature of this plot is that the flow near the lower wall is found to expand like a one-dimensional flow. This tends to validate the design approach of using a conical section in the annular portion of the secondary nozzle so that the pressure may be determined by using one-dimensional calculations. As was discussed previously, it is important to be able to estimate this pressure value when designing the nozzle. It can also be seen from Figure IV-20 that the flow is being compressed by the upper wall. Downstream, this compression develops into a shock.

The Region II calculations are used to supply inlet conditions to Region IV and also to the Region III, Mode I, calculations.

Region IV

Inlet line conditions for Region IV were supplied by selecing the appropriate flow cross section from the VNAP results for Region II. The upper wall boundary was determined by using the design approach described in Section IV,A. The lower boundary was defined by the parameters θ_3, z_3/r_b, and r_w/r_b.

Region IV was divided into an upstream subregion and a downstream subregion. The following 5 plots were prepared for each case:

*Each region is actually overlapped to increase the accuracy. The last line or two calculated by VNAP is not accurate because of the outflow boundary condition that must be imposed by the method to close the problem. (See Ref. 4.) Thus, the VNAP calculations have been overlapped and the last two lines were discarded.

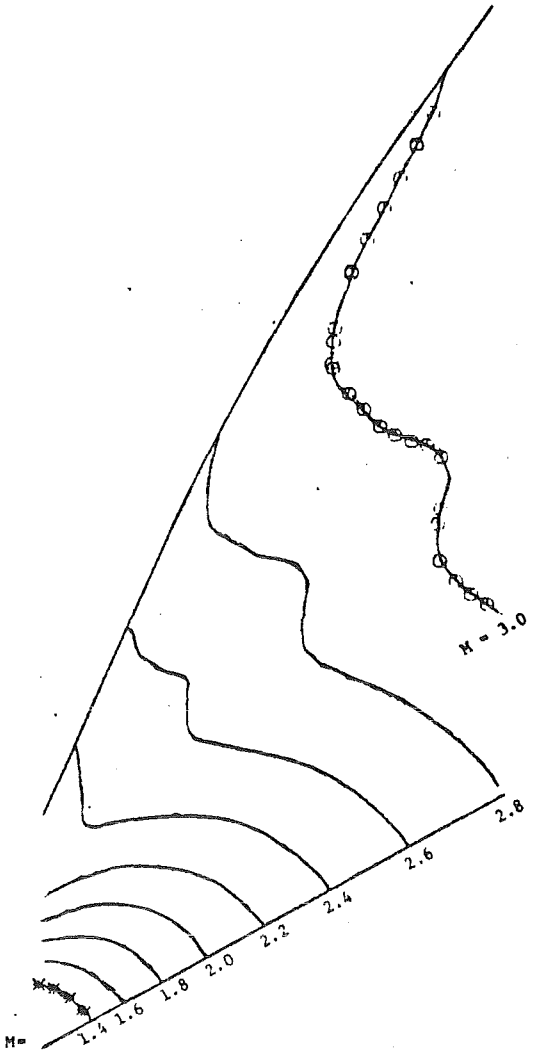

Figure IV-20. Annular Nozzle Downstream Section Mach No. Contours

(1) velocity field, (2) pressure, (3) density, (4) temperature, and (5) Mach number contours. Only the Mach number contours are discussed in this report. Mach number contours for these subregions are presented in Figures IV-21 and IV-22 for case 2, i.e., zero bleed and no truncation. Thus, Figures IV-19, -20, -21, and -22 show the entire Mode II flow field predicted for the baseline nozzle contour and zero bleed flow.

The lower boundary in Figure IV-21 is the shear layer. The lower left-hand corner in the figure shows the Prandtl-Meyer expansion fan at the lower lip of the annular nozzle where the flow turns through 45.64°. The finite-difference method used by VNAP cannot accurately calculate this expansion fan because the Mach number gradients are too great for the relatively coarse mesh spacing required by VNAP. Thus, this expansion fan is a source of error in the VNAP calculations.

The lower boundary of Figure IV-22 is the shear layer and wake. A compression shock is induced at the corner where the flow is deflected through an angle of 14.64°. This deflection angle corresponds to a shock angle of 23.4°. Figure IV-22 clearly shows this "neck" shock; however, the shock angle appears to be less than 23.4°. VNAP predicts that the neck shock will exit the nozzle far from the upper wall.

A shock can also be seen in the upper half of Figure IV-22. This shock is induced by compression of the flow by the upper wall.

Results

Results of the Mode II performance predictions are summarized in Table IV-VI.

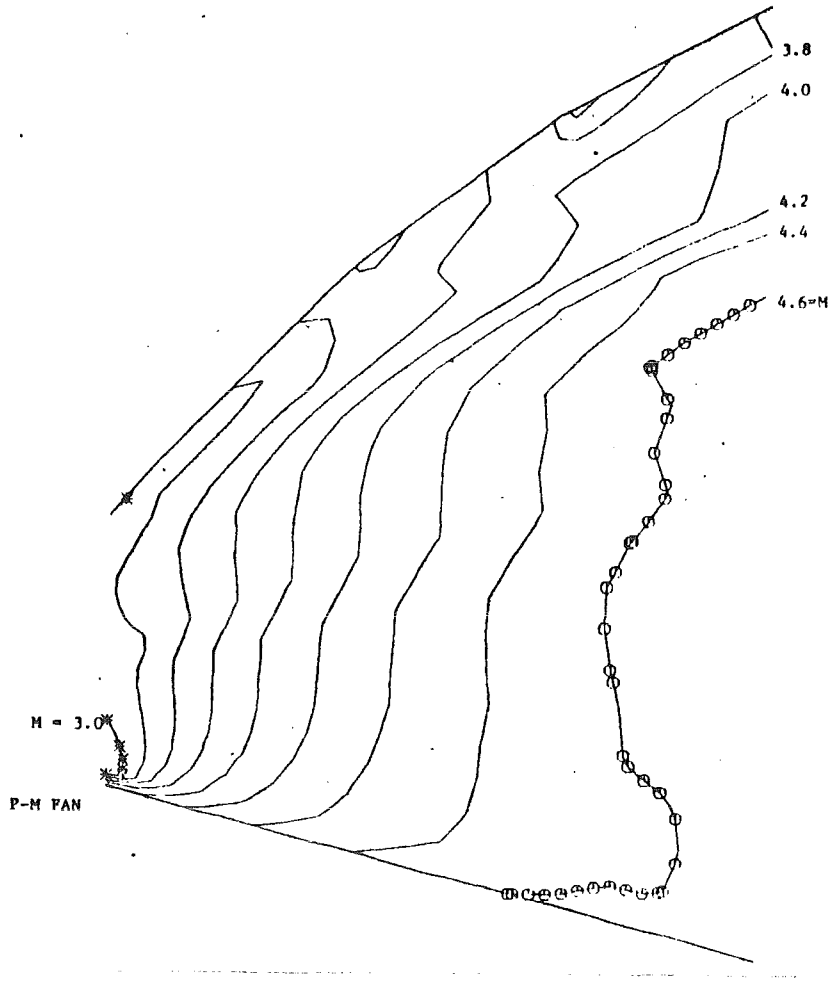

Figure IV-21. Region IV Upstream Mach No. Contours, Case 2, Zero Truncation, 0% Bleed

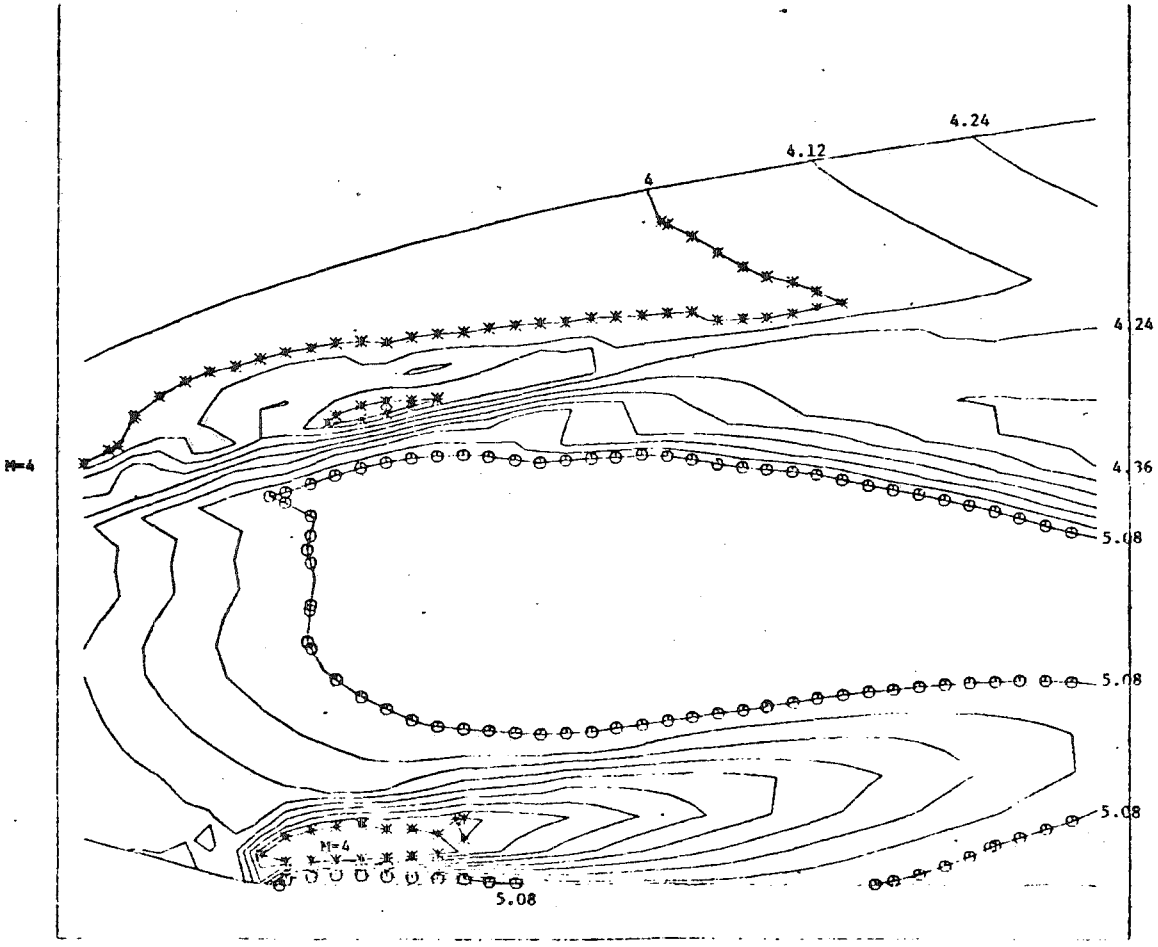

Figure IV-22. Region IV Downstream Mach No. Contours, Case 2, Zero Truncation, 0% Bleed

TABLE IV-VI

SUMMARY OF RESULTS, MODE II PERFORMANCE PREDICTION

CASE	TRUNCATION	BASE PRESSURE MPa	BASE PRESSURE (psia)	% BLEED $W_B/W_S \times 10^2$	$\dot{m}$ INITIAL LINE Kg/sec	$\dot{m}$ INITIAL LINE (lbm/sec)	F INITIAL LINE KN	F INITIAL LINE (K lbF)	$\dot{m}$ EXIT LINE Kg/sec	$\dot{m}$ EXIT LINE (lb/sec)	F_1 EXIT LINE MN	F_1 EXIT LINE (K lbF)	F_2 EXIT LINE MN	F_2 EXIT LINE (K lbF)	I_{SP_1}* sec	I_{SP_2}** sec
2	Min.	.0183	(2.65)	0	262.7	(578.7)	704.7	(158.4)	260.0	(573.2)	1.089	(244.8)	1.107	(248.9)	423.1	434.2
3	Min.	.0322	(4.67)	.05	262.7	(578.7)	704.7	(158.4)	270.8	(597.1)	1.154	(259.6)	1.151	(258.8)	448.6	433.4
4	Min.	.0684	(9.92)	$\approx$ .07	262.7	(578.7)	704.7	(158.4)	260.7	(574.7)	1.132	(254.5)	1.111	(249.4)	439.8	434.1
5	Mod.	.123	(17.89)	0	263.1	(579.7)	665.4	(149.6)	282.5	(622.9)	1.212	(272.4)	1.198	(269.3)	469.9	432.3
6	Mod.	.191	(27.7)	.25	263.1	(579.7)	665.4	(149.6)	279.6	(616.5)	1.215	(273.2)	1.191	(267.7)	471.2	434.1
7	Mod.	.222	(32.2)	.5	263.1	(579.7)	665.4	(149.6)	282.0	(621.7)	1.222	(274.6)	1.198	(269.3)	473.7	433.2
8	Max.	1.727	(250.5)	0	259.5	(571.7)	672.9	(151.3)	382.2	(842.7)	1.675	(376.6)	1.631	(366.6)	658.7	435.0
9	Max.	2.14	(310.4)	1	259.5	(571.7)	672.9	(151.3)	374.3	(825.2)	1.678	(377.2)	1.598	(359.3)	659.8	435.4
10	Max.	2.437	(353.5)	3	259.5	(571.7)	672.9	(151.3)	377.3	(831.8)	1.678	(377.3)	1.604	(360.6)	659.9	433.5

* $(Isp)_1 = F_1/\dot{m}_{\substack{\text{initial}\\\text{line}}}$

** $(Isp)_2 = F_2/\dot{m}_{\substack{\text{exit}\\\text{line}}}$

IV, C, Dual Expander Flow Field Analysis (cont.)

For cases 2, 3, and 4, where the wall dividing the upper and lower nozzles were as shown in Figure IV-18, the approach Mach number was found to be 2.79. With zero bleed flow, the predicted Prandtl-Meyer turning angle at the nozzle lip was 31 + 14.64 = 45.64°. This turn gives a Mach number of 4.62 for the shear layer boundary. For a Mach number this high, very little bleed flow is required to open the wake. The aerodynamic model predicted a trailing wake radius ratio approaching one for a bleed flow of only .07%. The values of base pressure predicted for cases 2, 3, and 4 are shown in column one of Table IV-VI, and are found to be quite low. For cases 5, 6, and 7, which have moderate wall truncation, and cases 8, 9, and 10, which have maximum wall truncation, the approach Mach numbers are 2.19 and 1.016, respectively. Consequently, the predicted values of base pressure and bleed flow required to open the wake are larger than for the zero truncation cases.

The remainder of Table IV-VI summarizes the value of mass flow, thrust, and specific impulse that were predicted by VNAP. Mass flowrate and thrust were calculated by using two different methods:

1) Initial Line Method

$\dot{m}_{\text{initial line}}$ = Integral across the VNAP start line of Figure IV-21.

F_1 = Integral of axial momentum + pressure across the VNAP start line of Figure IV-21, + integral of axial pressure along both the upper and lower boundaries

IV, C, Dual Expander Flow Field Analysis (cont.)

2) Exit Line Method

$\dot{m}_{\text{exit line}}$ = Integral across the VNAP line at the end of the nozzle

F_2 = Integral of axial momentum + pressure across the VNAP line at the end of the nozzle

Two different values of specific impulse were calculated by using the above quantities:

$$(I_{SP})_1 = F_1/\dot{m}_{\text{initial line}}$$

$$(I_{SP})_2 = F_2/\dot{m}_{\text{exit line}}$$

Referring to Table IV-VI, it can be seen that there is substantial error growth in both the mass flow and thrust calculations, especially for cases 8, 9, and 10. This is primarily because of the inability of VNAP to properly calculate the large gradient region in the vicinity of the Prandtl-Meyer expansion fan. These gradients are especially large in the last three cases because of the low Mach number (1.016) of the flow upstream of the fan. Nearly all of the observed error growth occurs in this region, i.e., in calculating the first several VNAP solution lines. The Initial Line Method cannot be used to predict the specific impulse, because a thrust calculation with error growth should not be ratioed to a mass flow value with no error growth. The Exit Line Method, however, seems to give a consistent prediction of specific impulse for all 9 cases. This is because the mass flow and thrust integrals are very similar and experience nearly the same error growth. All nine cases are found to yield a specific impulse of 434 $\pm$ 1.5 seconds. Correcting these values by using the VNAP correction factor (.978) obtained during the dual throat analysis, the Mode II divergence efficiency was found to be 100% $\pm$ .2%.

IV, C, Dual Expander Flow Field Analysis (cont.)

Although the results for Mode II operation obtained with VNAP appear to be qualitatively correct, it is clear that a more accurate method must be used to predict the nozzle performance and that a cold-flow test program is needed to verify these results.

2. Performance Calculations For Mode I Operation

Calculating the dual expander performance for Mode I operation required calculating Regions I, II, and III shown in Figure IV-17a. Results obtained for each region are discussed below.

Regions I and II

Results of the Region II calculations were available from the Mode II analysis. Region II results were discussed in the preceding subsection and are applicable to both modes of operation. Next, Region I was calculated by using the TDK computer program, with operating conditions for the inner nozzle as shown below in Table IV-VII.

TABLE IV-VII
MODE I OPERATING CONDITIONS

	Outer Nozzle	Inner Nozzle
Flow	LOX/LH_2	LOX/RP-1
Mixture Ratio	7.0	2.8
γ	1.18	1.199
C_p	.8137 cal/gm°K	.44985 cal/gm°K
Molecular Weight	16.	26.6
Total Temperature	3778°K (6800°R)	3972°K (7150°R)
Total Pressure	20.68 MPa (3000 psia)	41.37 MPa (6000 psia)
Throat Area	280.6 cm^2 (43.5 $in.^2$)	220.6 cm^2 (34.2 $in.^2$)

IV, C, Dual Expander Flow Field Analysis (cont.)

It was intended to adjust the chamber pressure of the inner nozzle so that the calculated exit pressure would match the VNAP exit pressure. However, a satisfactory match was obtained on the first attempt. Pressures calculated along the dividing wall for Regions I and II are shown in Figure IV-23. Pressures at the downstream end of the wall are nearly equal, about 105 psia on both sides. It is important to match the static pressures at the end of the wall to avoid forming a strong shock wave at the position where the two flow streams come together.

Figure IV-23 demonstrates that a large, negative pressure gradient occurs along the upper wall and that a much lower gradient occurs along the lower wall. Thus, if the wall is truncated, a large difference in static pressure will result at the end of the wall. For example, at the "moderate" truncation position, the upper and lower wall pressures are found to be 1970 (286) and 979 (142) KPa (psia), respectively. For "maximum" truncation, the values are 11606 (1683) and 1248 (181) KPa (psia). In order to match the pressures at the lip for these truncations and still operate at the desired chamber pressure requires a complete redesign of the nozzle.

Region III

Region III, shown in Figure IV-17a, is the dual expander flow field during Mode I operation (both engines on) that is downstream from Regions I and II. The TDK program has been modified to calculate Region III. Previously, TDK would calculate the flow field only if the difference between the streamtube and stagnation pressure was within 10% of each other. For the dual expander this difference is 20%.

Region III is divided into an inner region and an outer region. The inner region is composed of exhaust gases from the LOX/RP-1

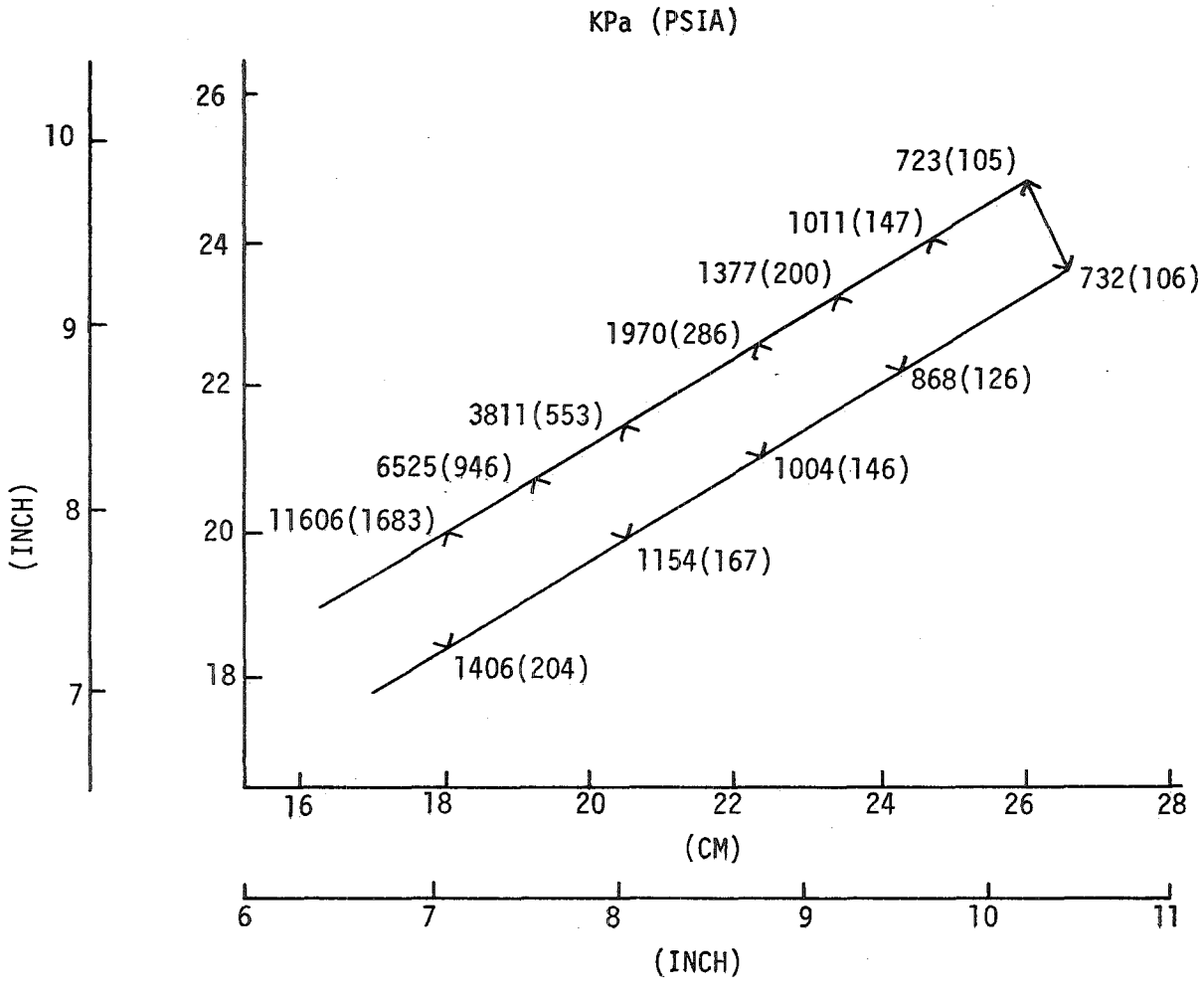

Figure IV-23. Inner and Outer Wall Pressures (Predicted)

propellants at a mixture ratio of 2.8. The outer region is composed of exhaust gases from the LOX/LH_2 propellants at a mixture ratio of 7.0. Operating conditions for the two engines are as shown in Table IV-VII.

Inputs along the start line for the inner region were input from the exit plant of the TDK calculation for Region I. Inputs along the start line for the outer region were input from the last vertical line of the VNAP calculation of Region II. Values input are pressure, density, flow angle, and velocity at each point. The two regions are divided by a slip line, i.e., a double valued streamline with equal values of pressure and flow angle, but different values of velocity, density, Mach number, and temperature on each side.

The TDK calculations were made by removing the thickness of the dividing wall and then correcting the TDK calculations for mass flow and thrust. This calculation showed the divergence efficiency to be .995, matching the simplified prediction.

D. RECOMMENDATIONS

1. Mode II Performance Prediction Program

After careful analysis of the existing Mode II performance prediction methods for the flow field of the dual expander propulsion concept, it is now felt that a method of characteristics analysis and computer program capable of more precise prediction techniques is needed. A sketch illustrating the geometry and the major features of the flow field is presented in Figure IV-24. In view of the complexity of this flow field, a finite-difference method that smears Prandtl-Meyer expansions and oblique shock waves, such as the VNAP program, is considered inadequate to fully determine the potential performance of the dual expander concept.

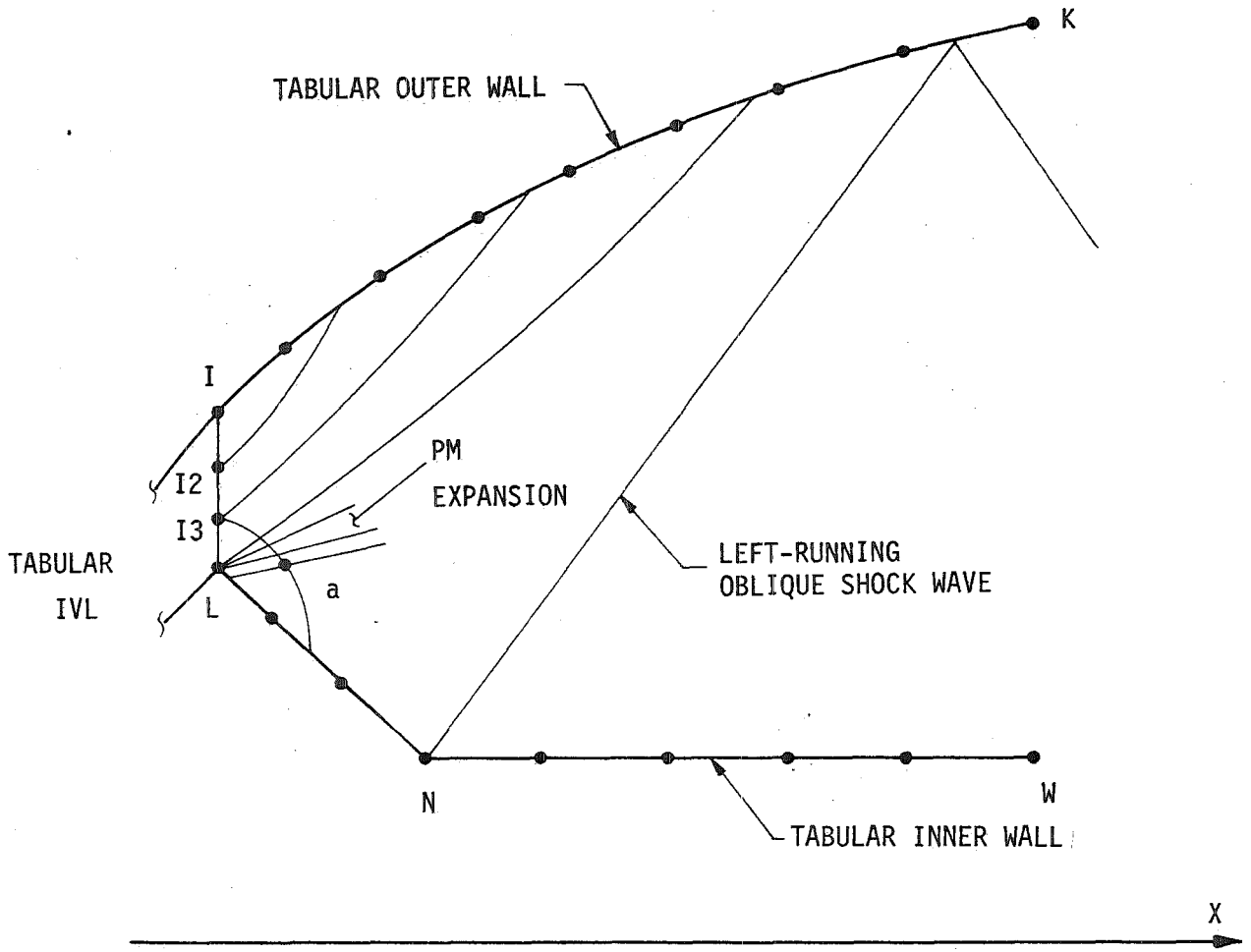

Figure IV-24. Dual Expander Geometry and Flow Field Model

The general features of the proposed flow model are presented, along with a discussion of the overall numerical algorithm. The program would be less complex, faster and cheaper to run than VNAP. Such advantages allow the program to be run parametrically to determine an optimum Mode II design. The possibility also exists to expand the program to analyze dual throat Mode II operation.

2. Flow Model

The flow model should be developed for steady axisymmetric flow. The flow should be allowed to be rotational to account for the entropy gradient created by the oblique shock wave emanating from the inner wall. The gas would be assumed to have constant specific heats and molecular weight. The supersonic initial value line (IVL) would be input to the analysis in tabular form. Both the outer wall and inner wall would be input in tabular form. A Prandtl-Meyer expansion would emanate from point L on the inner wall. A discrete left-turning obliquie shock wave would emanate from point N on the inner wall and be reflected from the outer wall if it intersects that wall.

All unit processes for calculating the flow field would be based on the method of characteristics. The interior point unit process would be constructed by following the two Mach lines. Outer and inner wall unit processes would follow the appropriate Mach line and the streamline (i.e., the wall itself).

3. Overall Numerical Algorithm

The overall logic would follow left-running Mach lines. The first left-running line would emanate from the second point on the initial-valve line (IVL) below the outer wall, point I2. That Mach line would be

extended through the flow field until it intersects the outer wall. Subsequent left-running Mach lines would emanate from the remaining points on the IVL, in decreasing order, until the Mach line from point L has been extended to the outer wall. Left-running Mach lines would then be generated through the Prandtl-Meyer expansion fan at point L until the required amount of flow turning at point L has been achieved. Each of these left-running Mach lines would be extended across the flow field to the outer wall. A right-running Mach line would then be extended from the second point on the last left-running Mach line of the expansion fan, point A, to the inner wall. A left-running Mach line would be extended from that wall point across the flow field until it intersects the outer wall. This procedure would be repeated until the left-running Mach line emanating from point N on the inner wall has been extended across the flow field. A left-running oblique shock wave would then be generated at point N and extended across the flow field. This shock wave would either intersect the outer wall or pass beyond the nozzle exit. If it intersects the outer wall, a shock reflection unit process would be employed to determine the flow properties across the reflected shock wave. Left-running Mach lines would be extended from points on the inner wall downstream of point N until a left-running Mach line passes beyond point K on the outer wall (the exit lip point). If the inner wall is a constant radius section, the solution is complete. If not, the solution would be continued until the flow field is determined on the inner wall at point W. The nozzle thrust would then be determined by calculating the momentum flux and pressure thrust across the tabular initial-value line, line IL, and adding to it the integral of the pressure forces along the outer wall.

V. PRELIMINARY HEAT TRANSFER ANALYSIS

The objective of Task IV was to conduct a preliminary thermal analysis for both the dual throat and dual expander configurations. The dual throat studies represent a continuation and refinement of the work initiated in Ref. 2. Vehicle studies following that effort resulted in a change in the baseline design point: primary and secondary chamber pressures, respectively, were increased from 20.68/14.48 MPa (3000/2100 psia), to 27.58/19.31 MPa (4000/2800 psia), and the Mode I secondary (LOX/RP-1) thrust was increased from 60 to 70 percent of the total. Both changes make chamber cooling more difficult and result in a baseline design point not explicitly considered in the parametric studies of Ref. 2. A new baseline design was developed which included special emphasis on the lip region formed by the termination of the primary chamber and on the effect of primary chamber plume impingement in the secondary throat region during Mode II operation. New parametric design studies investigated the effects of independent changes in chamber pressure and Mode I thrust split.

Previous thermal analysis of the dual expander concept was limited to a very preliminary IR&D study (Ref. 21) which indicated problems in apportioning the limited hydrogen coolant flow among the three heated surfaces. Three candidate baseline designs were investigated in the present study: (1) regenerative cooling with hydrogen only; (2) regenerative cooling with hydrogen and oxygen; (3) a transpiration-regenerative cooling combination with hydrogen. A special study of the supersonic lip region formed by the termination of the primary chamber was also included in the baseline design effort, conducted for a primary chamber pressure of 41.37 MPa (6000 psia) (LOX/RP-1), secondary chamber pressure of 20.68 MPa (3000 psia) (LOX/H_2), and a Mode I primary thrust equal to 59 percent of the 698 MN (600K lbF) total. Parametric studies investigated the effects of changes in thrust, thrust split, and both chamber pressures for the first cooling concept noted above.

V, Preliminary Heat Transfer Anlaysis (cont.)

A. SPECIAL STUDIES

1. Lip Regions

One of the heat transfer problem areas unique to the dual throat and dual expander concepts is the lip formed by the termination of the primary chamber. During Mode I operation, the primary and secondary chamber flows create a wake region behind this lip. Therefore, a special study of the lip regions was conducted to identify the boundary conditions established by the wake flow and the design problems associated with regenerative cooling of a corner heated on both sides.

Wake region heat transfer data in the literature are primarily for supersonic flow over axisymmetric bodies, with the sidewall boundary layer thickness small in relationship to the base diameter. The concept of interest to us incorporates what is, essentially, a plane surface with a relatively thick boundary layer and subsonic flows for the dual throat and supersonic flows for the dual expander. Because of these differences, a conservative design approach has been adopted, using the literature data as a guide. The latter indicate that heat fluxes at the center of the wake region are typically 80-90 percent of the sidewall heat flux immediately upstream of the wake region (see Refs. 22 and 23), but that a significant reduction in heat flux is observed as it moves away from the center of the wake toward the sidewall (Refs. 22-24). Figure V-1 shows the radial heat flux variation observed in Ref. 22; Ref. 24 indicates a greater reduction, with the local base heat flux being proportional to $(1 - r/R_B)^{1.2}$ for $r/R_B \leq 0.8$.

Preliminary mechanical design studies indicate that a conventional rectangular channel construction, as illustrated in Figures V-2 and V-3 for the dual throat and dual expander, respectively, can be utilized in the lip regions. Therefore, the emphasis in the present study was on the lip

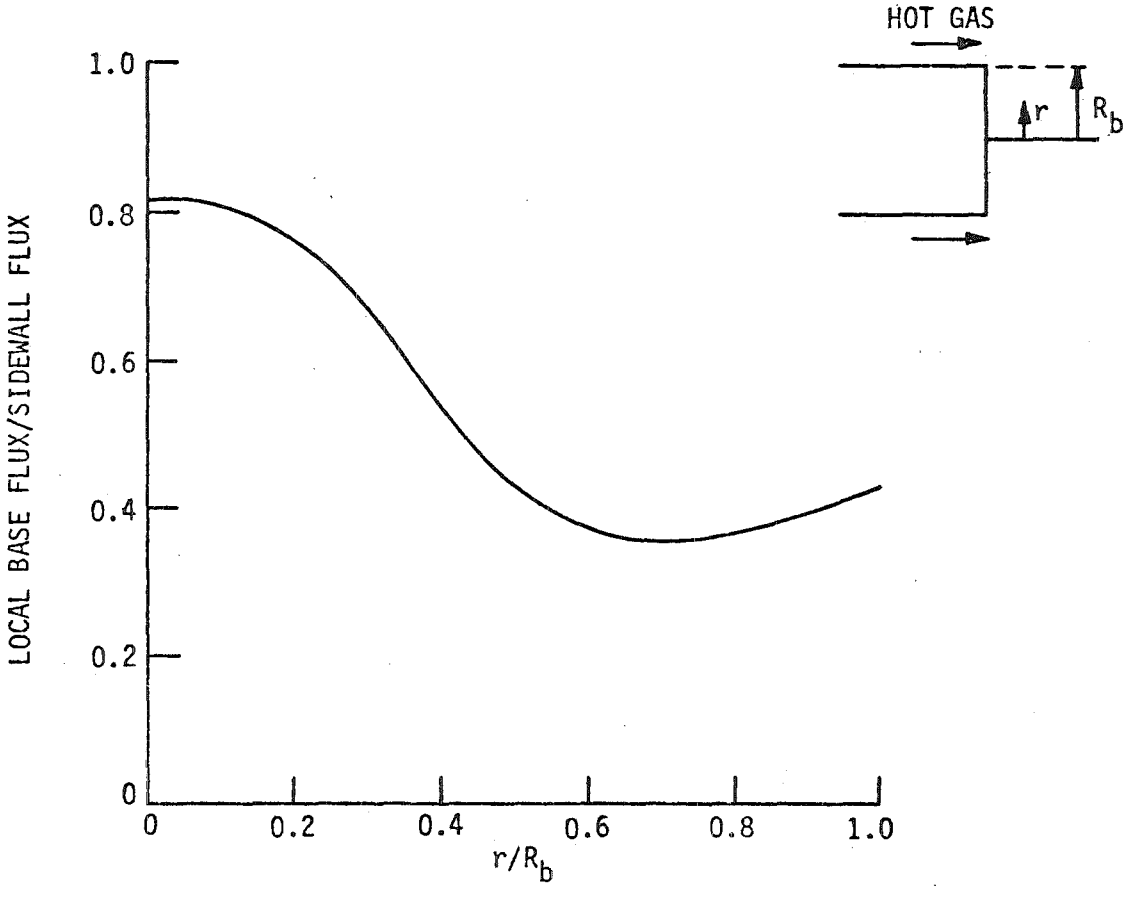

Figure V-1. Typical Lip Region Heat Flux Variation

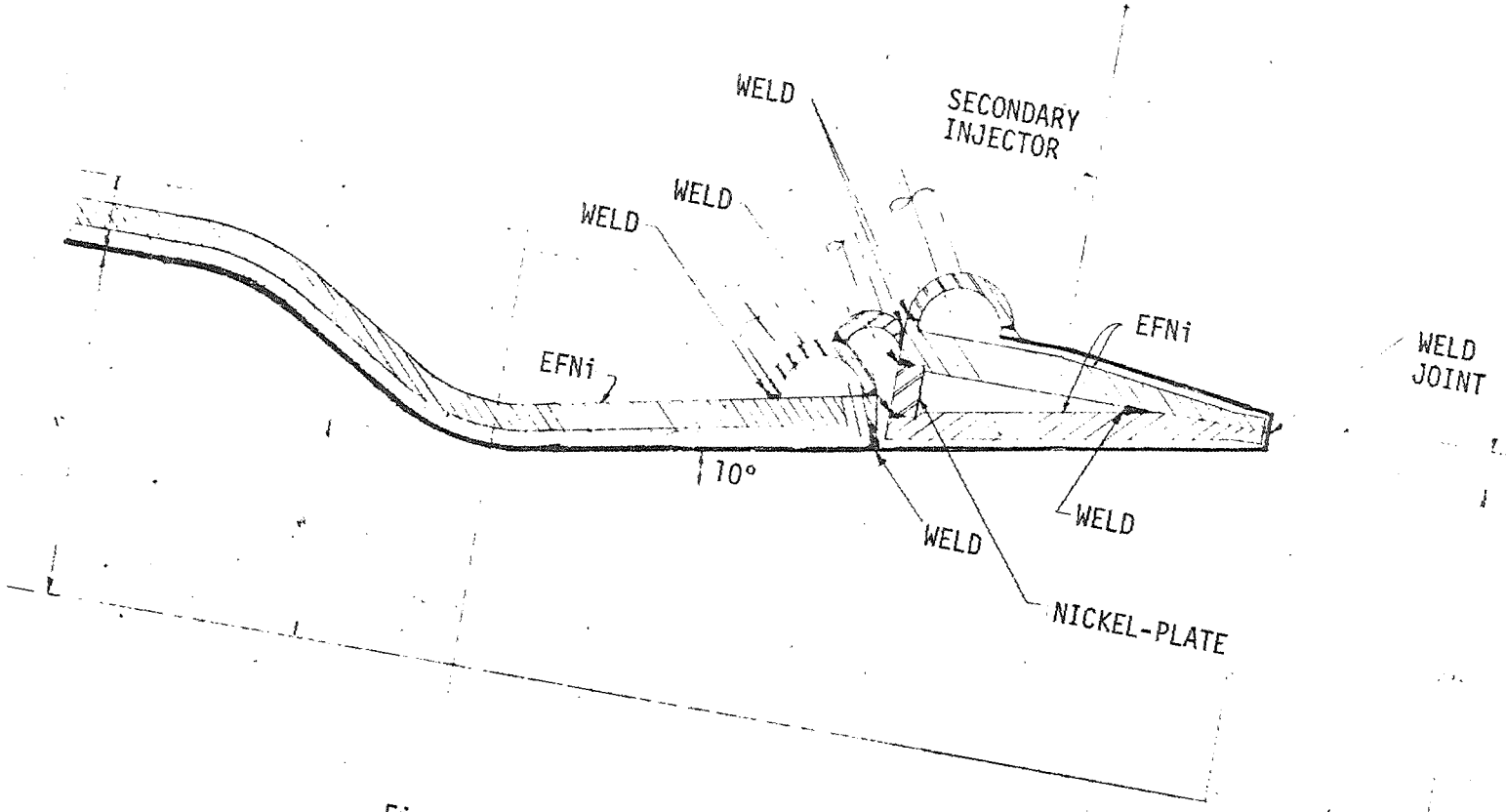

Figure V-2. Dual Throat Lip Region Design

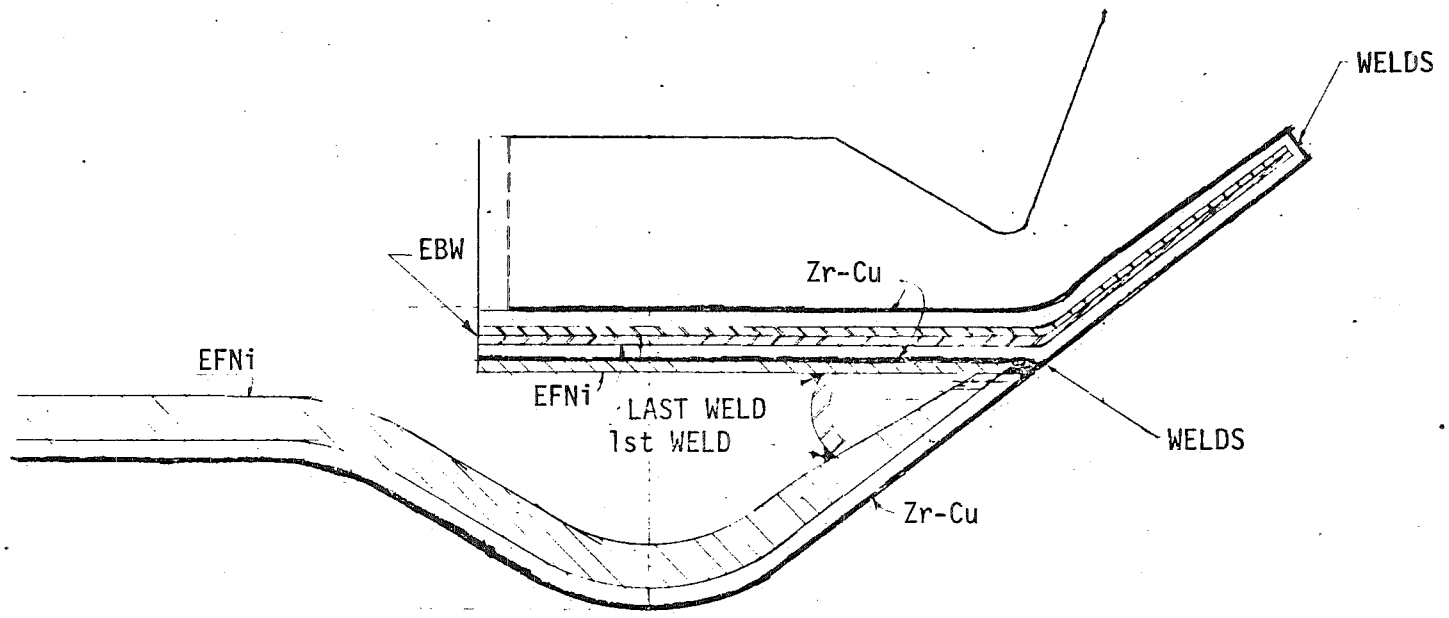

Figure V-3. Dual Expander Design

region corners, where a severe cooling problem occurs since, at a land centerline, heat input from two surfaces must be conducted in three directions to reach cooled surfaces. A three-dimensional SINDA model of such a corner was developed and is shown in Figure V-4. The model does not include any part of the electroformed nickel closure and thus is limited to that part of the corner adjacent to the coolant channels. Since the electroformed nickel can be relatively thin in the lip region, the corner model covers a significant fraction of the lip half-thickness. Therefore, the procedure used in the present study to provide a conservative design relative to the boundary conditions of Figure V-1 was as follows:

(1) Apply a uniform heat transfer coefficient over the end wall equal to 80 percent of the sidewall coefficient.

(2) Set the lip channel depth equal to the sidewall channel depth (symmetrical corner model), thereby accommodating an even higher heat flux at the center of the lip.

It should be noted that the sidewall boundary layer was assumed to be unaffected by the throat region shock structure. In addition, the coolant heat transfer coefficients were considered to be unaffected by the turn at the lip corner; the actual enhancement due to curvature was omitted to compensate for the lack of a channel corner radius and increased wall thickness in the wall conduction model.

The corner model was used to define the lip region channel depth required for each baseline design to limit the corner temperature to approximately 756°K (900°F). Figure V-5 shows a typical gas-side wall temperature distribution over a land centerline in the vicinity of a lip corner for the dual throat concept; temperatures over the channel centerline are only slightly lower.

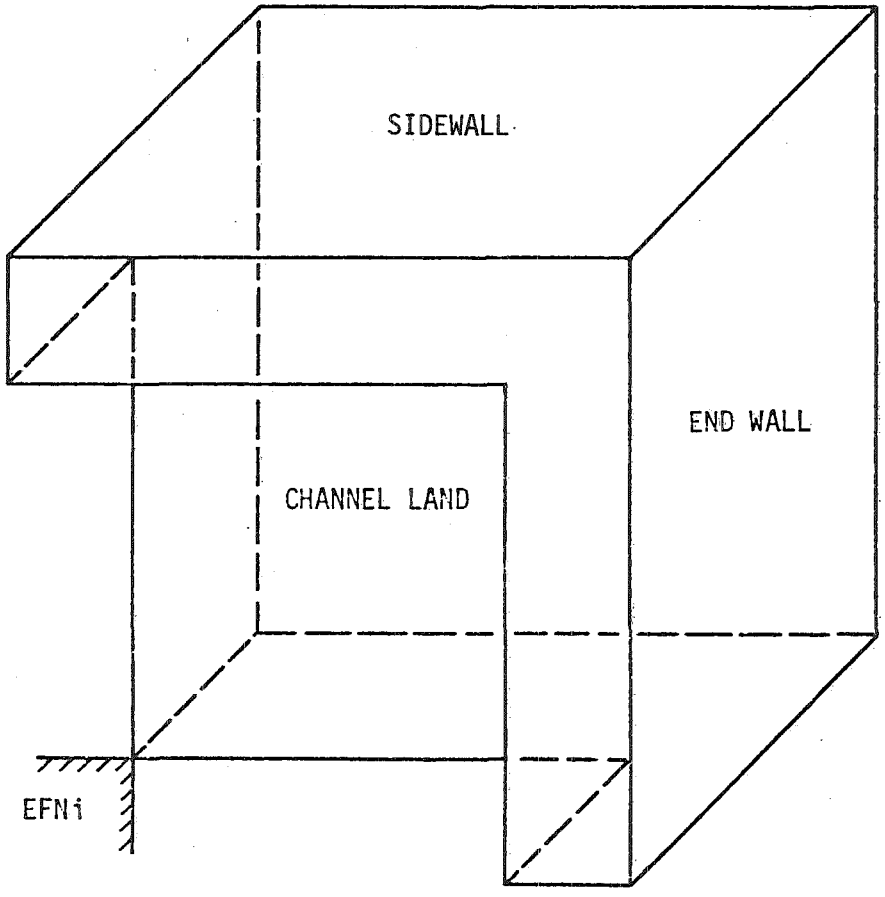

Figure V-4. Lip Region 3-D Thermal Model

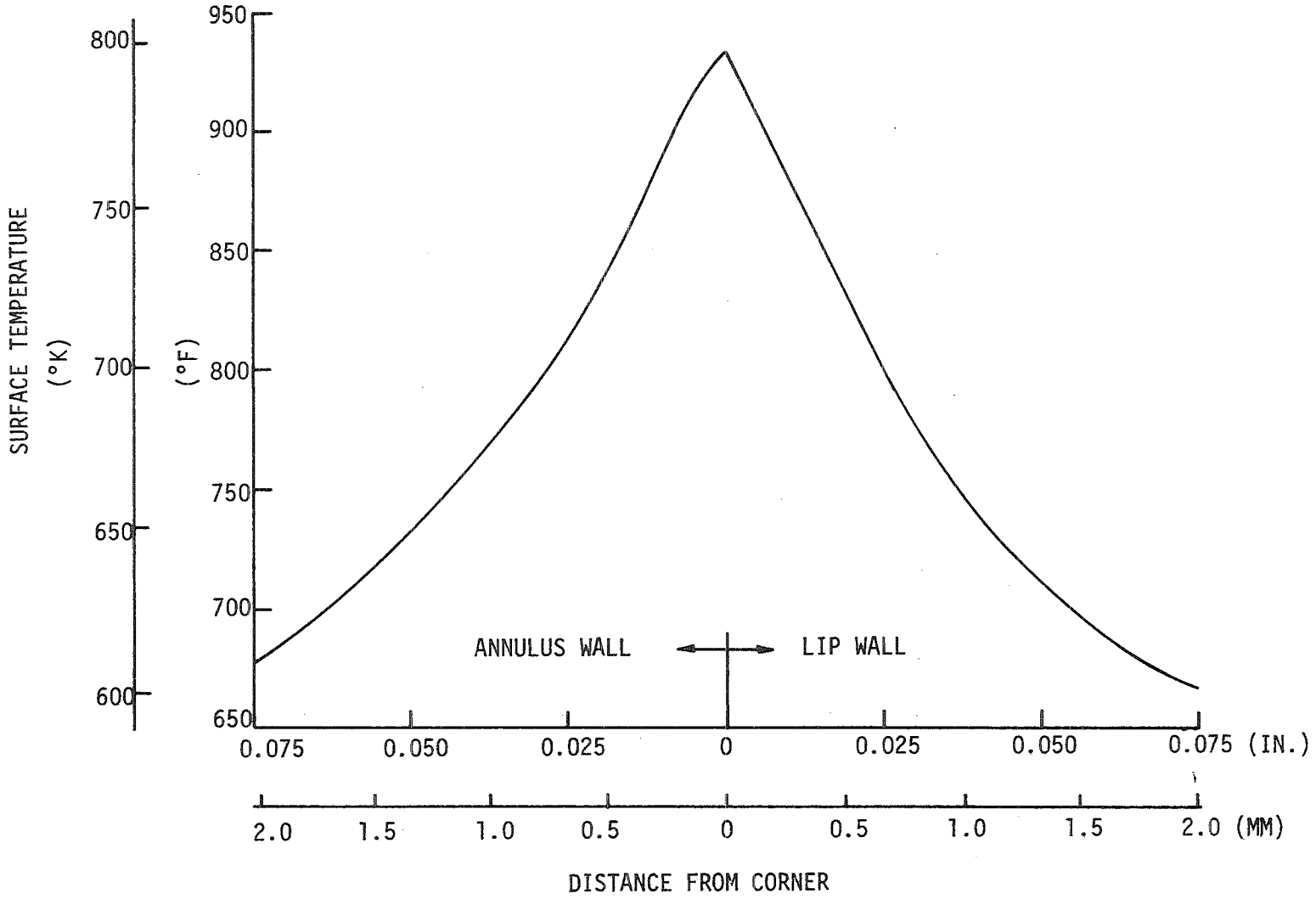

Figure V-5. Dual Throat Lip Region Wall Temperatures

In order to provide lip region channel depths for the parametric design studies, we used a simple one-dimensional conduction model with an effective wall conductance and coolant surface area defined from results of the three-dimensional SINDA model. The validity of this model was demonstrated by successfully predicting a dual throat baseline design, using a dual expander design to define the one-dimensional model parameters. In all cases, the total pressure drop for the two lip region corners was taken as three velocity heads. Results from the 3D baseline and 1D parametric models are presented in subsequent sections as part of the overall results for each concept.

2. Secondary Throat Analysis for Dual Throat Mode II

During normal Mode II operation of the dual throat concept, the secondary chamber bleed flow causes the primary chamber plume to attach to the secondary wall downstream of the throat such that the plume flow is nearly parallel to the wall. In this case, throat heat fluxes are expected to be well below those during Mode I operation. Of interest herein is the possibility of bleed flow failure and impingement of the primary plume upstream of the secondary throat, with resultant heat fluxes that might be more severe than Mode I values.

A number of studies of rocket exhaust plume impingement on adjacent vehicle structures were found in the literature (Refs. 25-27). Analyses and correlation of these data split the problem into strong and weak shock regions, with the former treated as a stagnation point region as far as heat transfer is concerned. However, because of the effect on the plume boundary of the back pressure in the secondary chamber, formation of a strong shock region was not considered likely in the present problem. Therefore, the VNAP program was used to define the inviscid flow field for zero bleed flow. This program provides an exact inviscid solution, and its use for the nominal

bleed flow case was already planned as part of Task I. A boundary layer analysis based on the edge conditions determined by VNAP was used to define the heat transfer to the secondary wall.

Figure V-6 shows the Mode II pressure and mass velocity profiles at the secondary wall from VNAP for the baseline design with zero bleed flow. The maximum pressure and mass velocity due to the plume impingement occurs 4.3 cm (1.7 in.) upstream of the throat. The freestream velocity, shown in Figure V-7, is essentially constant in the region of interest, i.e., from the attachment point through the zone of maximum heating. This feature of the inviscid flow was used to advantage herein, since it greatly simplifies the integral momentum equation for the boundary layer. For constant velocity, this equation becomes

$$\frac{d\theta}{dx} + \frac{1}{\rho_e} \frac{d\rho_e}{dx} \theta = C_f/2$$

This form of the momentum equation was solved by using the Van Driest skin friction law for compressible flow based on the Von Karman turbulent mixing length (Ref. 28):

$$Re_\theta = 0.191 \frac{\mu_w}{\mu_e} \exp\left(0.4 \xi \sqrt{\frac{2}{C_f} \frac{T_e}{T_w}}\right)$$

in which ξ is a function of Mach number and wall temperature ratio. The Mach number and freestream static temperature distributions from VNAP are nearly uniform. A design wall temperature of 811°K (1460°R), consistent with the Mode I design studies described later, was used.

The momentum thickness at the attachment point must be specified to start the above boundary layer analysis. Two cases were considered. In one case, the momentum thickness of the plume shear layer defined by the

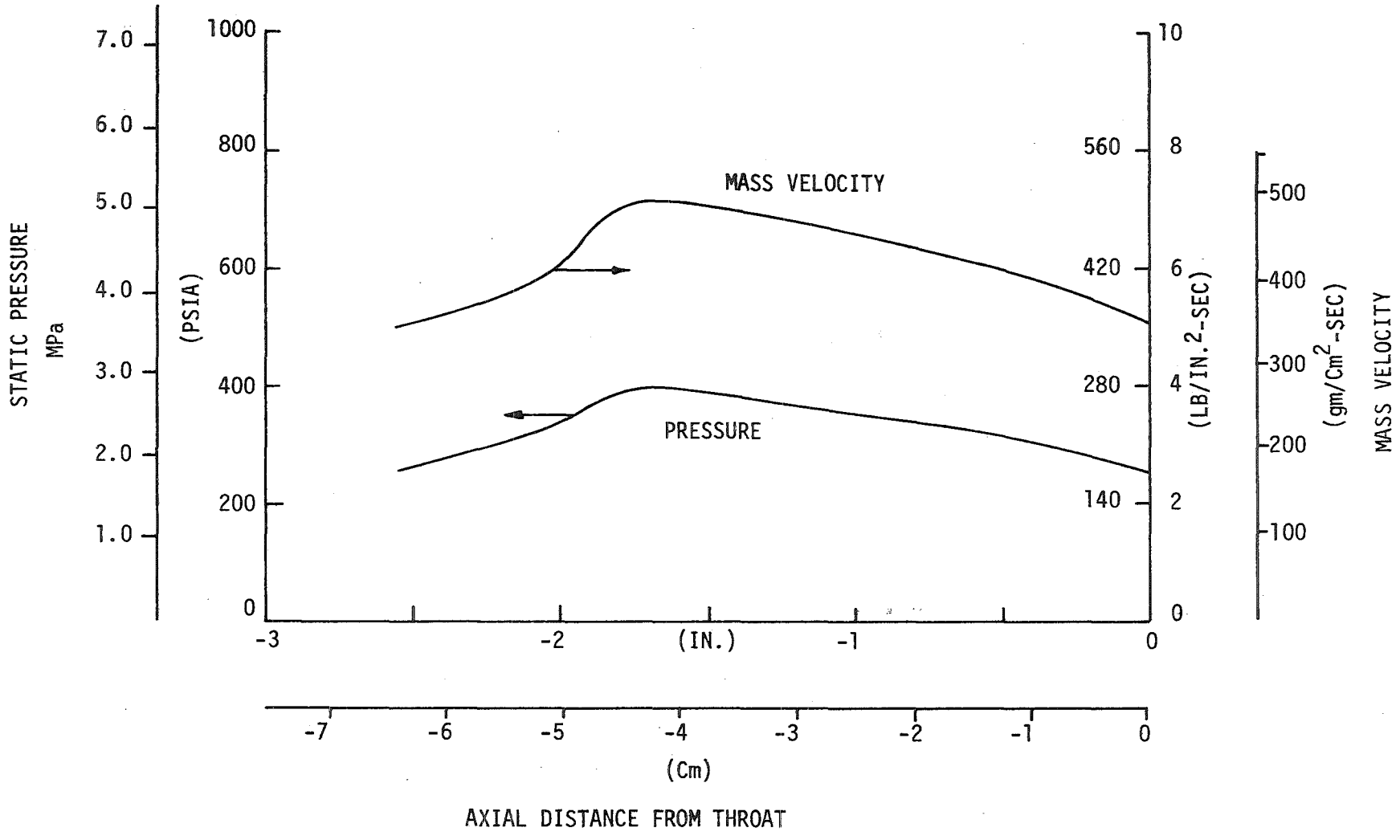

Figure V-6. Primary Plume Impingement in Secondary Throat Region with No Bleed Flow

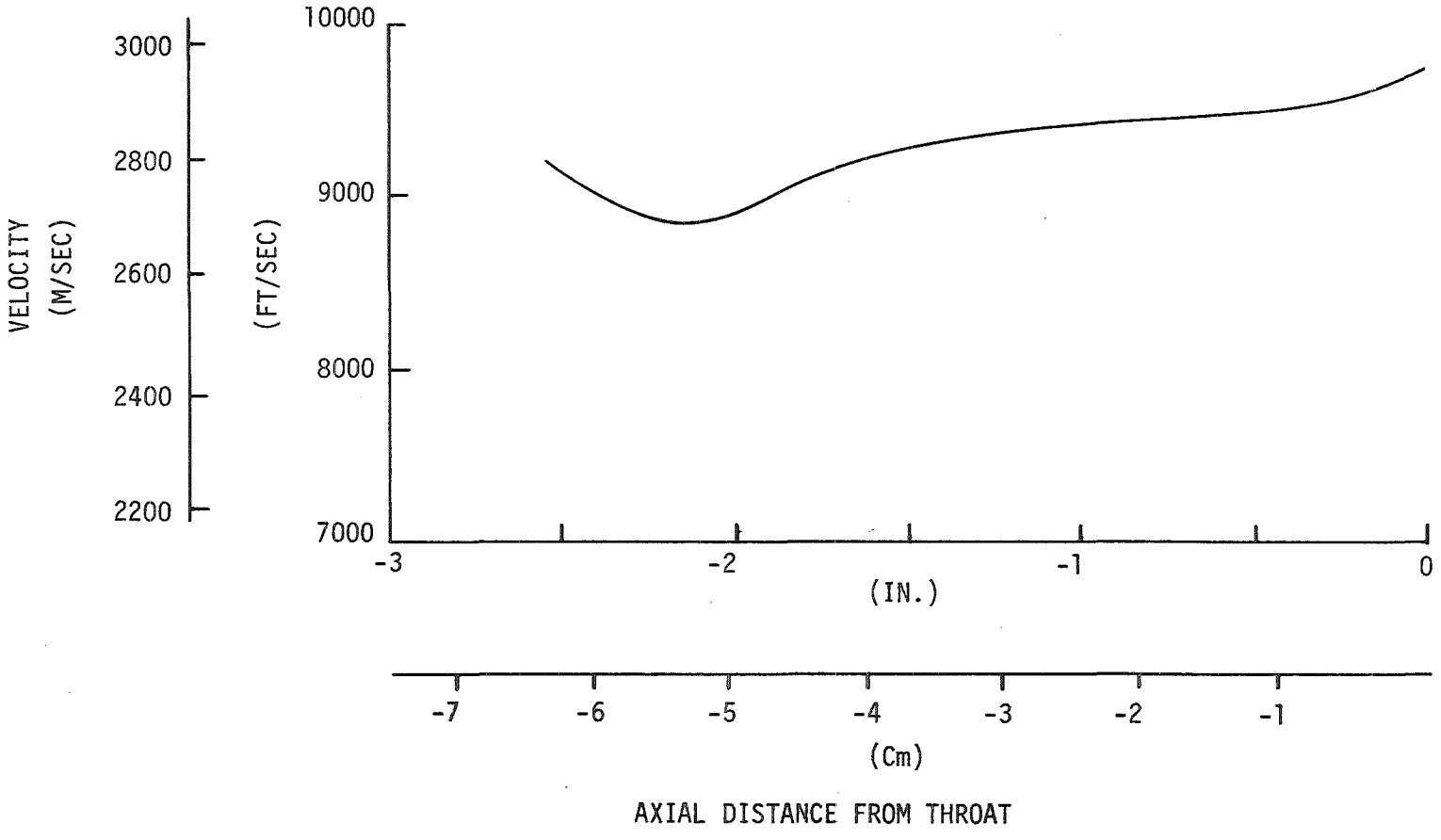

Figure V-7. Freestream Velocity Distribution Mode II Secondary Throat Region with No Bleed Flow

Task I bleed flow aerodynamic model was used. This approach assumes that the shear layer is not disturbed by its interaction with the wall. In the second case, the shear layer was assumed to be nearly destroyed by its interaction with the wall, such that the initial momentum thickness for the wall boundary layer is very small. Results reported for this case are for an initial thickness of .0254 mm (0.001 in.), compared with a shear layer momentum thickness of .861 mm (0.0339 in.). Further reductions in initial momentum thickness have little effect on the Stanton number at the location of the maximum freestream mass velocity. Therefore, these two cases are considered to bound the actual interaction of the shear layer with the wall.

Stanton numbers were defined from the skin friction coefficient, using a Reynolds analogy factor of 1.25. This value is a compromise between the value of 1.19, calculated from the theory of Ref. 28 for a turbulent Prandtl number of 0.9, and the value of 1.32 defined by the Colburn factor $Pr^{-2/3}$. Results from the boundary layer analysis are summarized below for the location of maximum freestream mass velocity:

	Initial Momentum Thickness, mm (in.)	
	.861 (0.0339)*	.0254 (.001)
θ,	.0247	.00244
$Re_\theta \times 10^{-4}$	3.35	.331
St	.00179	.00263
hg, KW/m^2-°K ($Btu/in.^2$-sec-°F)	30.32 (.0103)	44.45 (.0151)
Heat Flux, MW/m^2 ($Btu/in.^2$-sec)	86.1 (52.7)	126.3 (77.3)

*Defined by plume shear layer

These results compare with a maximum Mode I heat transfer coefficient of 28.38 KW/m^2-°K (0.00964 $Btu/in.^2$-sec-°F) and heat flux

of 85.46 MW/m^2 (52.3 $Btu/in.^2$-sec) in the secondary throat region. Thus, when the initial momentum thickness for the zero bleed flow boundary layer is equal to that from the plume shear layer, the maximum Mode I and Mode II heat fluxes are essentially equal. A similar result for Mode II is obtained by scaling the maximum heat flux from the Task I BLIMP run for nominal bleed flow according to the local VNAP wall pressures (a procedure suggested by various flow reattachment data):

$$\phi_{\text{no bleed}} = \phi_{\substack{\text{nom. bleed} \\ \text{BLIMP}}} \left(\frac{P_{\text{no bleed}}}{P_{\substack{\text{nom. bleed} \\ \text{VNAP}}}} \right)$$

$$= 14.2 \left(\frac{397}{98.9} \right) = 57 \text{ Btu/in.}^2\text{-sec } (93.14 \text{ MW/m}^2)$$

The nominal bleed flow BLIMP was started with an initial momentum thickness from the corresponding plume shear layer (D streamline) since the plume flow is very nearly parallel to the wall. When the initial momentum thickness for the zero bleed flow boundary layer is very small, the maximum Mode II heat flux is almost 50% higher than that for Mode I. The ability of the secondary chamber cooling system to accommodate this higher heat flux is discussed in Section V,C,1.

B. CHANNEL DESIGN PROCEDURES

Two computer programs for regenerative cooling were used for the present studies: one with the dual throat geometric details built in, the other for the dual expander. These programs were derived from the SCALER program for conventional geometry which was developed specifically for parametric design studies. With these programs, it is economically feasible to generate a relatively large number of parametric design points and still obtain a detailed, multi-station analysis of a rectangular channel at each design point. The chamber geometry and the local gas-side heat transfer

coefficients and coolant heat loads are scaled from reference input to other thrusts and chamber pressures. At each station, the programs iterate to determine the channel depth required to satisfy a gas-side wall temperature limit, which can be specified as a function of closeout wall temperature consistent with cycle life and creep criteria (Figure V-8). The only simplifying assumption is that gas-side wall temperature differences between the reference input and scaled cases have a negligible effect on gas-side heat transfer coefficients and heat loads. Normally, gas-side wall temperature limits are well known in advance so that local reference gas-side heat transfer analyses can be run at appropriate wall temperatures.

Two-dimensional conduction effects in rectangular channels, as well as the spatial variations of the coolant heat transfer coefficient, are approximated as shown in Figure V-9. The hot wall adjacent to the channel, the entire land, and that part of the external wall adjacent to the channel are represented as fins; that part of the external wall adjacent to the land is assumed to be isothermal. A simple resistance network represents the hot wall adjacent to the land and connects the hot-wall fin to the land fin. Different coolant heat transfer coefficients are associated with each fin. That for the hot wall is based on the average of the centerline (TWL2) and corner (TCORN) wall temperatures, while the coefficient for the external wall is based on its centerline wall temperature (TBS). The land coefficient is merely a weighted average of the other two. In this way, it has been possible to simulate the wall temperatures predicted by the SINDA network analyses very closely.

Channel geometry constraints imposed in the present study due to fabrication and flow distribution considerations were as follows:

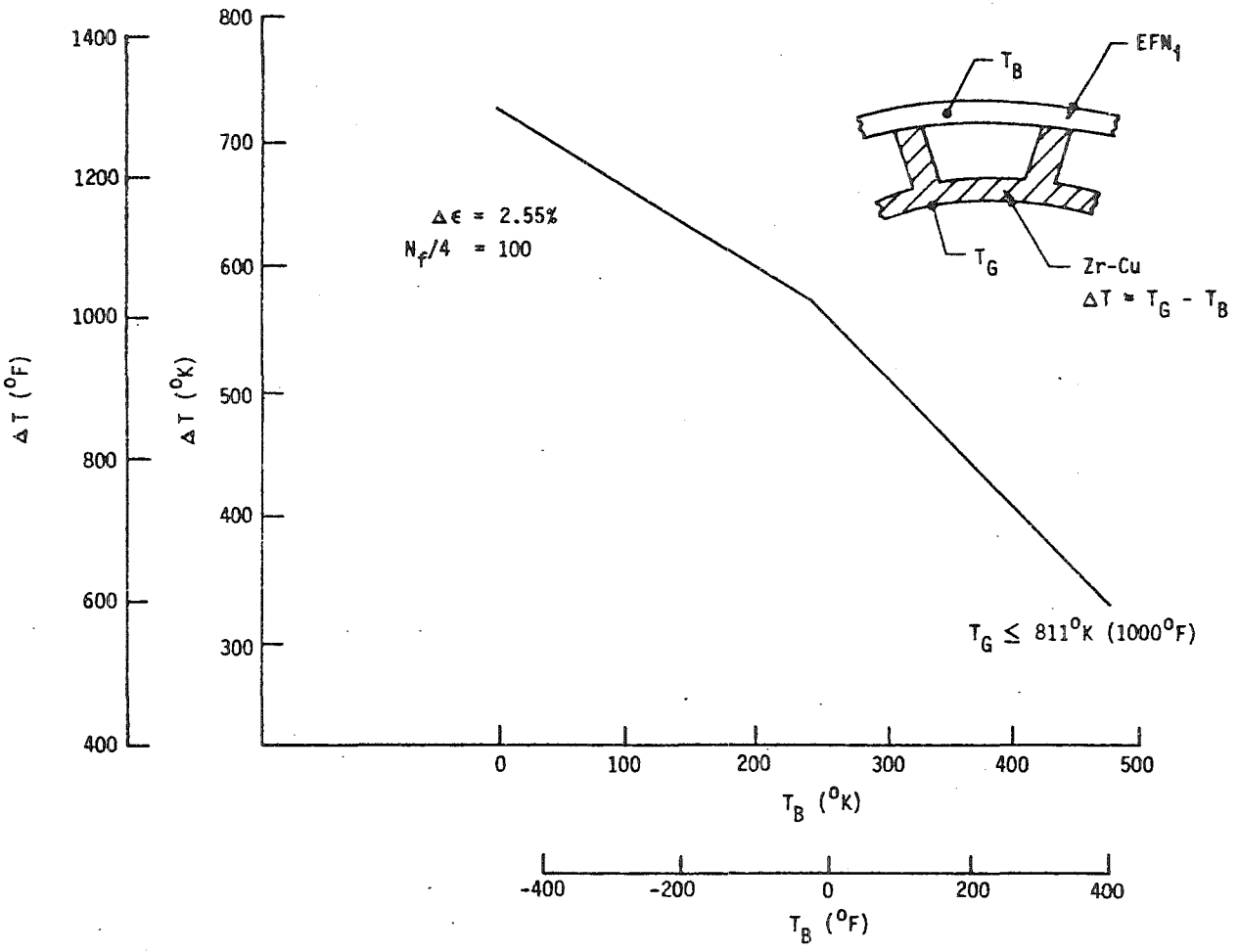

Figure V-8. Cycle Life/Creep Wall Temperature Criteria

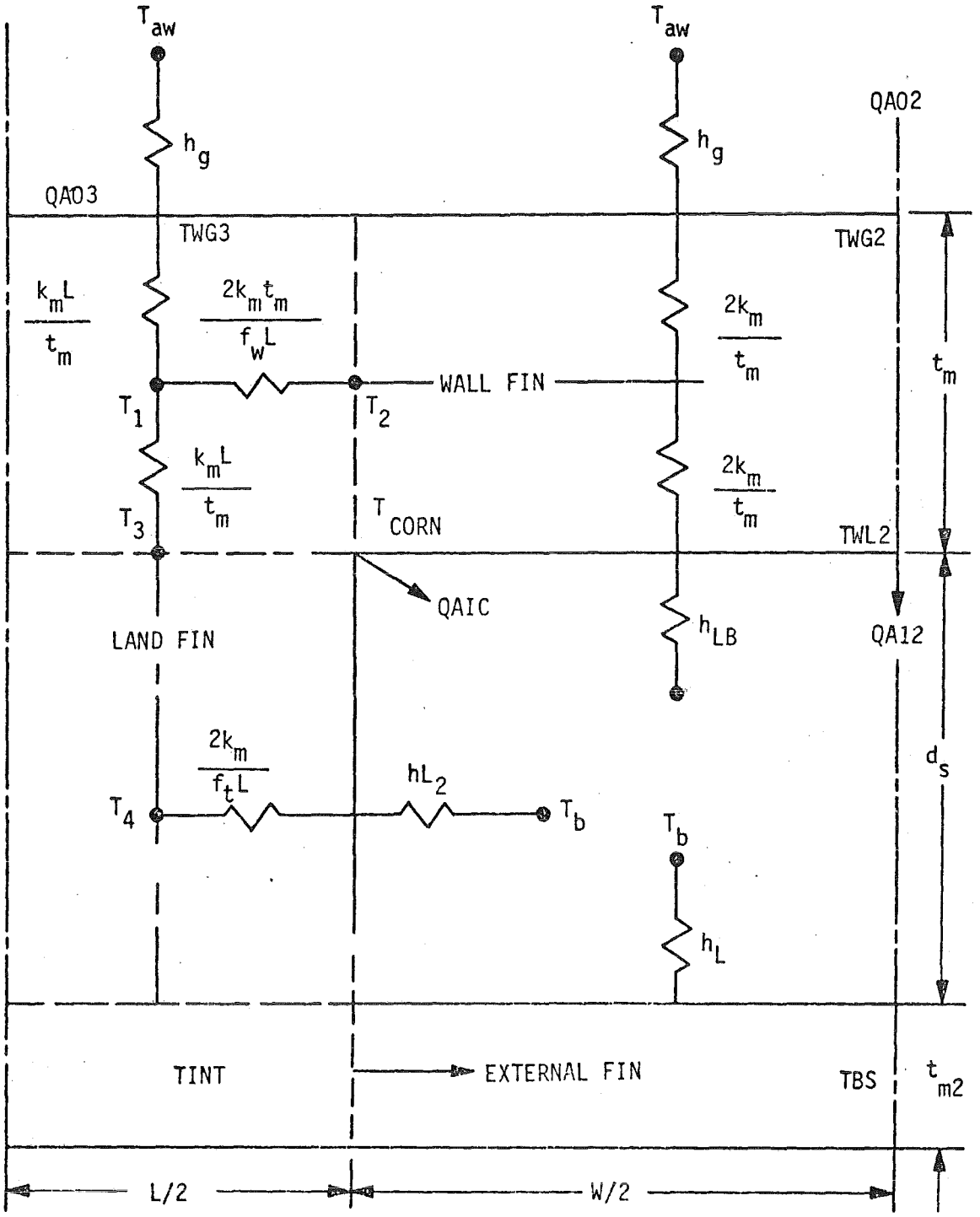

Figure V-9. Schematic of Wall Conduction Model

V, B, Channel Design Procedures (cont.)

Minimum wall thickness, mm (in.)	.635 (.025)
Minimum land width, mm (in.)	1.016 (.040)
Minimum channel width, mm (in.)	1.016 (.040)
Minimum channel depth, mm (in.)	.889 (.035)
Maximum channel depth/width	5:1

Wall thicknesses were also required to satisfy the strength criteria of Figure V-10. The number of coolant channels was determined by utilizing the above minimum dimensions for both the land and channel widths at either the throat or the location in a circuit of the minimum radius.

Channel layouts were limited to combinations of regions with constant channel width or constant land width (straddle milling). Increases in flow area relative to the throat beyond those possible with channel depth increases were accomplished by constant land width regions or by step changes in channel width. At the pressure levels associated with the present baseline designs, only very small increases in channel width .102-.127 mmg (.004 - .005 in.) above the 1.016 mm (0.040 in.) minimum were possible without increasing the wall thickness above .635 mm (0.025 in.). Details of the channel layouts for each concept are presented in subsequent sections.

C. DUAL THROAT

1. Baseline Design

As shown schematically in Figure V-11, three parallel cooling circuits are used in all dual throat designs presented herein. A separate circuit is included for the inner annulus, lip region, and part of the primary nozzle; in previous dual throat analyses (Ref. 20), these regions were included in the primary chamber circuit. Since the primary chamber dictates

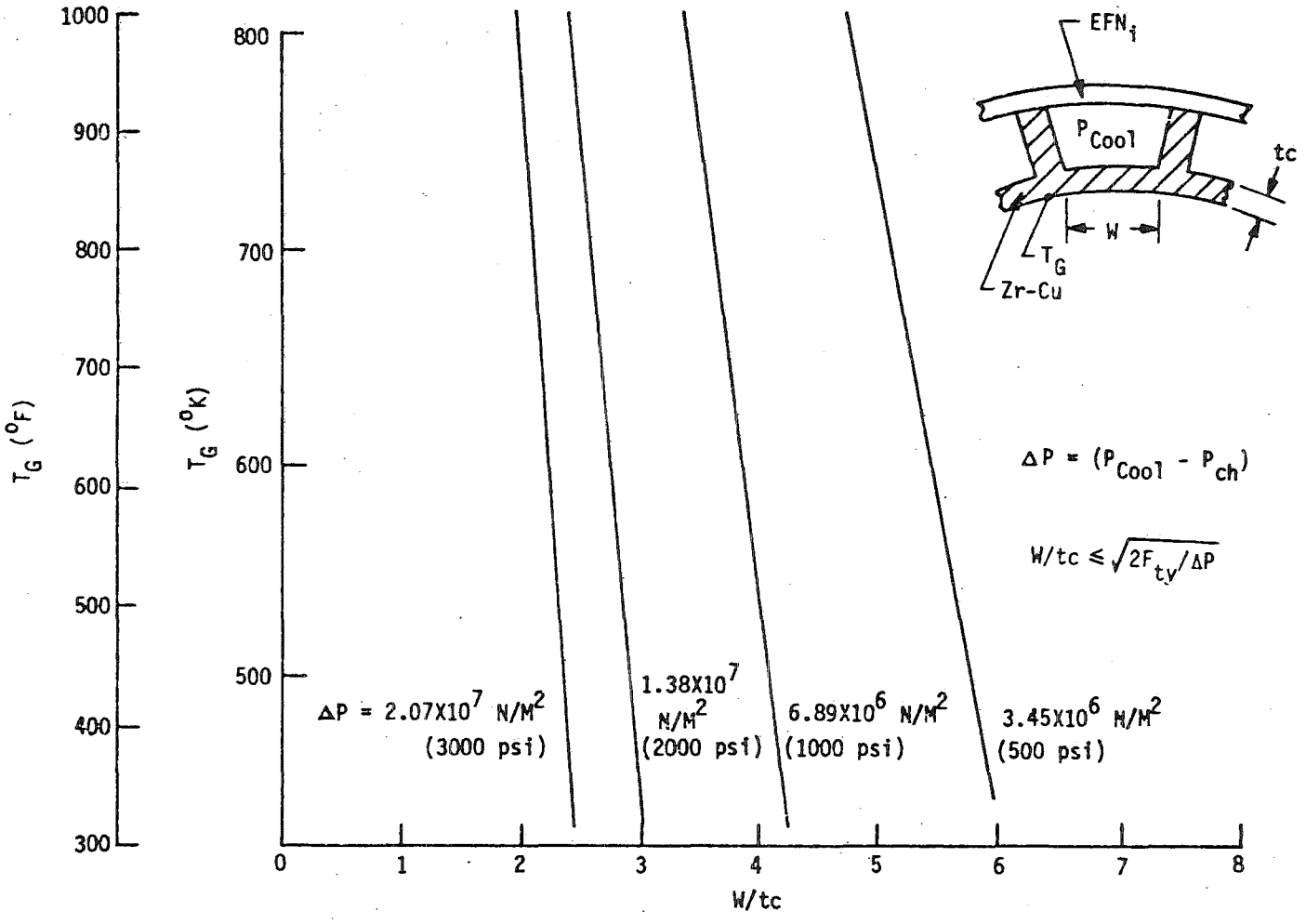

Figure V-10. Zr-Cu Chamber Wall Strength Criteria

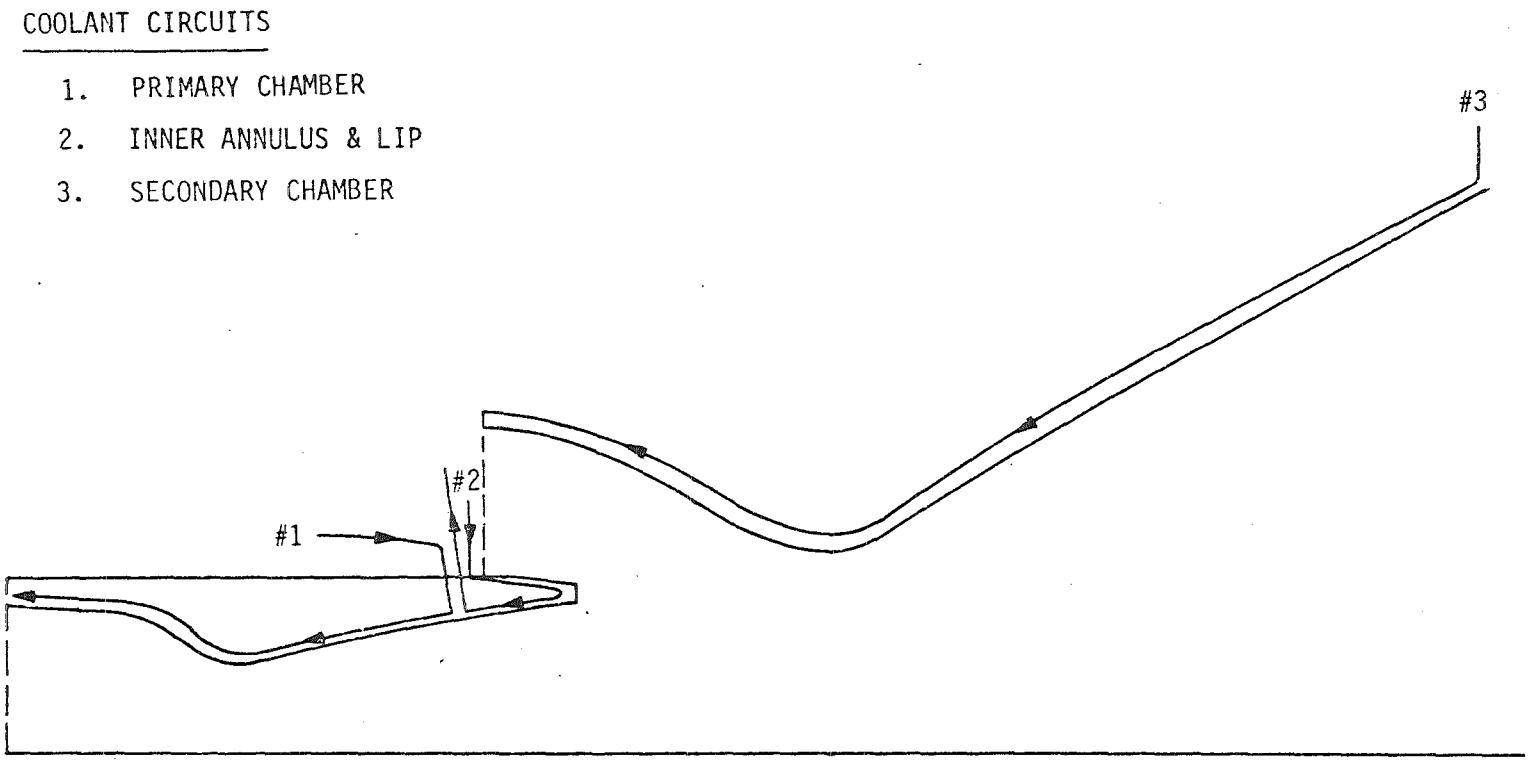

Figure V-11. Dual Throat Coolant Flow Schematic

the overall system pressure drop, use of a separate circuit to accommodate the pressure drop required for lip cooling significantly reduces the overall pressure drop. The primary nozzle area ratio, ε_I, at the interface between these circuits was a parameter in the baseline design study; a maximum value of 1.92 is possible from a mechanical design standpoint. Note that the secondary circuit extends to an area ratio of 7.8, after which an oxygen-cooled tube bundle would be used for the remainder of the secondary nozzle. A parametric design study of such a tube bundle was presented in Ref. 2.

Channel layout details for the baseline design are given in Table V-I. The primary circuit utilizes straddle milling in part of the convergent section in order to increase the channel width from the throat values. In order to avoid the channel aspect ratio limit in the barrel, it was necessary to increase the channel width above that consistent with the strength criteria for the minimum wall thickness. Therefore, the barrel wall thickness was increased to .762 mm (0.030 in.). In the secondary circuit, the minimum wall thickness of .635 mm (0.025 in.) was used in the barrel, which limited the channel width to 1.143 mm (0.045 in.), i.e., only .127 mm (0.005 in.) greater than the throat channel width. In order to increase the flow area away from the throat region more rapidly than provided for by straddle milling, a step change in width occurs in the convergent section. This barrel design was not optimized for Mode I, since throat cooling in Mode II dictates most of the circuit pressure drop and since the total pressure drop does not appear to be a problem. The throat land width is maintained in the first part of the secondary nozzle, with the wall thickness increasing to 1.270 mm (0.050 in.) to accommodate the increased channel widths. A channel width consistent with the strength criteria for the 1.270 mm (0.050 in.) wall thickness is maintained in the second part of the secondary nozzle. A uniform channel width of 1.016 mm (0.040 in.) was maintained in the lip circuit. This is necessary in the primary nozzle segment of the circuit in order to provide the

TABLE V-I

BASELINE CHANNEL LAYOUT SUMMARY (SI UNITS)

		DUAL THROAT			DUAL EXPANDER			
		Primary	Secondary	Lip	Primary	Secondary	Inner Annulus	Primary Nozzle
Barrel								
Channel Width (W)		1.346	1.143		1.118	1.016	1.118	
Land Width (L)		1.854	2.108		2.083	1.295	1.346	
Wall Thickness (t)		.762	.635		.635	.635	.635	
Convergent Section	(1) L =	1.854	Step W	W=1.016	Step W	W=1.016	W=1.118	
	(2) W =	1.016						
Throat or Min. Radius								
Channel Width		1.016	1.016	1.016	1.016	1.016	1.118	1.016
Land Width		1.016	1.016	1.016	1.016	1.016	1.575	1.016
Wall Thickness		.635	.635	.635	.635	.635	.635	.635
Nozzle	W =	1.016	(1) L=1.016 (2) W=2.007 t=1.270	W=1.016	L=1.016	L=1.016	W=1.118	W=1.016

TABLE V-I (cont.)

BASELINE CHANNEL LAYOUT SUMMARY (ENGLISH UNITS)

	DUAL THROAT			DUAL EXPANDER			
	Primary	Secondary	Lip	Primary	Secondary	Inner Annulus	Primary Nozzle
Barrel							
Channel Width (W), in.	.053	.045		.044	.040	.044	
Land Width (L), in.	.073	.083		.082	.051	.053	
Wall Thickness (t), in.	.030	.025		.025	.025	.025	
Convergent Section	(1) L = .073 (2) W = .040	Step W	W = .040	Step W	W = .040	W = .044	
Throat or Min. Radius							
Channel Width, in.	.040	.040	.040	.040	.040	.044	.040
Land Width, in.	.040	.040	.040	.040	.040	.062	.040
Wall Thickness, in.	.025	.025	.025	.025	.025	.025	.025
Nozzle	W = .040	(1) L = .040 (2) W = .079 t = .050	W=.040	L=.040	L = .040	W = .044	W = .040

most effective channel geometry in the lip region. However, the inner annulus segment could be straddle-milled, which would provide a small reduction in circuit pressure drop.

Figure V-12 shows the pressure drops required for the primary circuit for two inlet area ratios as a function of the fraction of the hydrogen flow used in the circuit. Each point on these curves represents a different channel depth profile, as defined by the cycle life criterion of Figure V-8 and the maximum depth/width ratio of 5. As the hydrogen flow fraction initially increases, the local channel depth increases for a fixed coolant velocity; however, the increased depth results in a larger effective coolant surface area, thereby reducing the required coolant velocity and allowing an even greater channel depth. The reduced velocity and increased hydraulic diameter result in a significant decrease in required pressure drop. However, as the coolant flow continues to increase, substantial portions of the chamber reach the channel aspect ratio limit resulting in a pressure drop increase. Figure V-12 indicates that reducing the inlet area ratio of the primary circuit reduces its pressure drop; the coolant Mach number, which exceeds 0.30 for higher area ratios, is also reduced. In addition, the hydrogen flow fraction at the minimum pressure drop decreases slightly as the inlet area ratio is reduced, thereby providing more flow for the other circuits.

Figure V-12 also includes the required pressure drop characteristics for the secondary circuit for Mode I operation. A hydrogen flow fraction of 0.30 was selected for the secondary circuit in order to provide a large pressure drop margin for redesign of the throat region for Mode II operation with a bleed flow malfunction. The Mode II secondary throat analysis discussed previously (Section V,A,2) indicated that local heat fluxes in the primary plume impingement region may be as much as 50% higher than for Mode I.

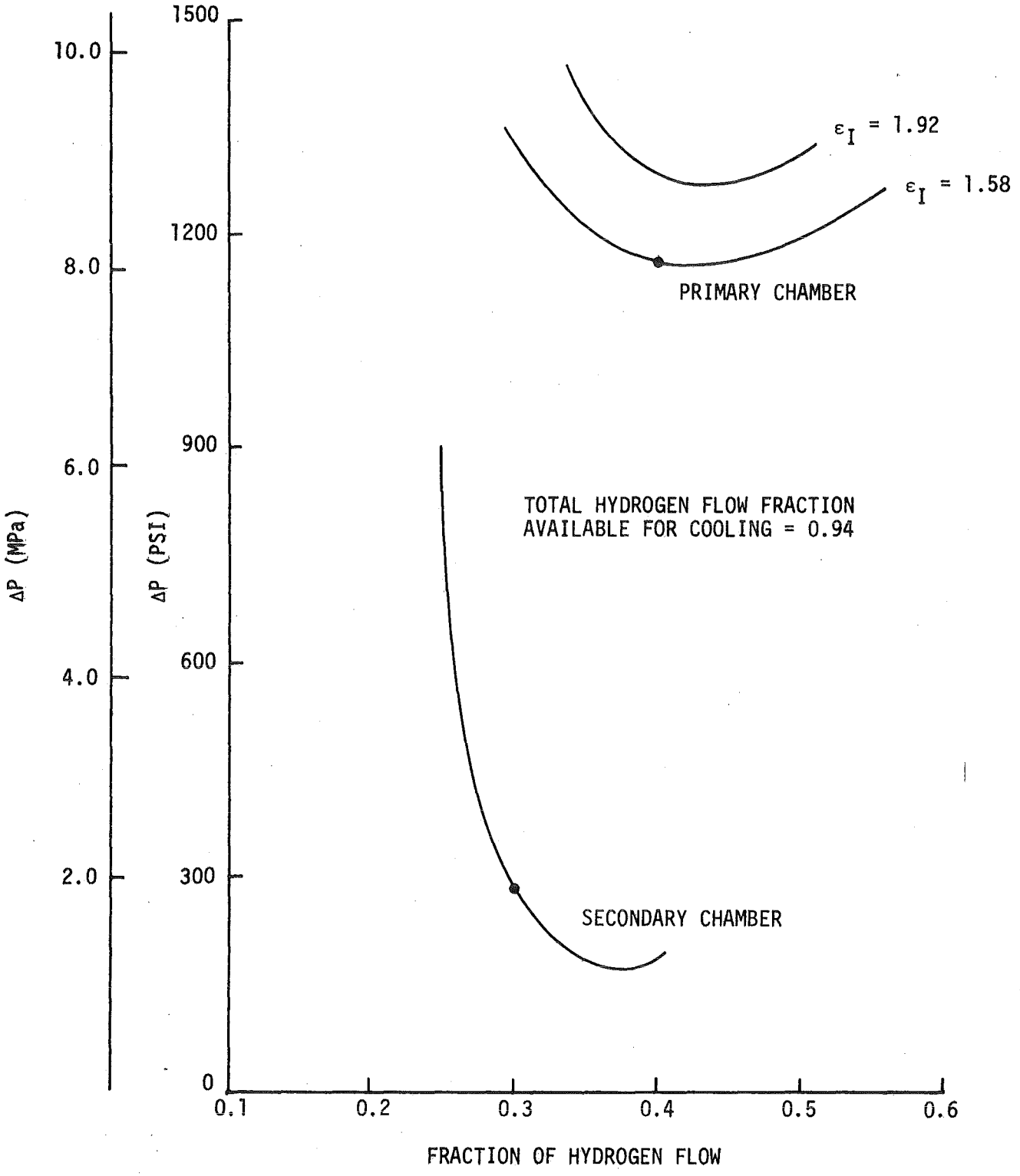

Figure V-12. Dual Throat Baseline Cooling Circuit Pressure Drop Characterisitcs

V, C, Dual Throat (cont.)

A composite design with revised channel depths in the Mode II impingement region was developed for the worst-case boundary condition of Section V,A,2; Figure V-13 compares the Mode I and II heat flux profiles. The pressure drop for the composite design during Mode I operation is 4.45 MPa (645 psi), which is well below the primary circuit pressure drop of Figure V-12. A detailed design of the lip region circuit was completed for an interface area ratio of 1.58, assuming a primary circuit flow fraction equal to the optimum value of 0.40. In all cases, the total hydrogen flow fraction available for cooling was assumed to be 0.94, based on the gas generator/staged combustion mixed cycle studies of Ref. 2. Therefore, the flow fraction available for the lip region circuit was 0.24. Table V-II summarizes the baseline designs for all three cooling circuits. Since the lip circuit pressure drop is well below that of the primary circuit, it is apparent that further reduction in the interface area ratio is desirable in order to minimize the cooling system pressure drop.

2. Parametric Study

Chamber pressure and thrust split were varied independently in the dual throat parametric study. Primary chamber pressure* was varied from 20.68 to 34.47 MPa (3000 to 5000 psia) at the baseline thrust split. However, at 34.47 MPa (5000 psia), the coolant Mach number was impractical; therefore, the highest pressure for which results are reported is 31.06 MPa (4500 psia). Mode I thrust from the secondary propellants was varied from 60 to 80% at the baseline chamber pressures. The design procedure in each case was similar to that for the baseline, except that composite secondary designs including the effects of Mode II were not generated. Primary and secondary circuit designs for Mode I were defined as a function of hydrogen flow

*Secondary chamber pressure was always 70% of the primary, as defined by aerodynamic considerations.

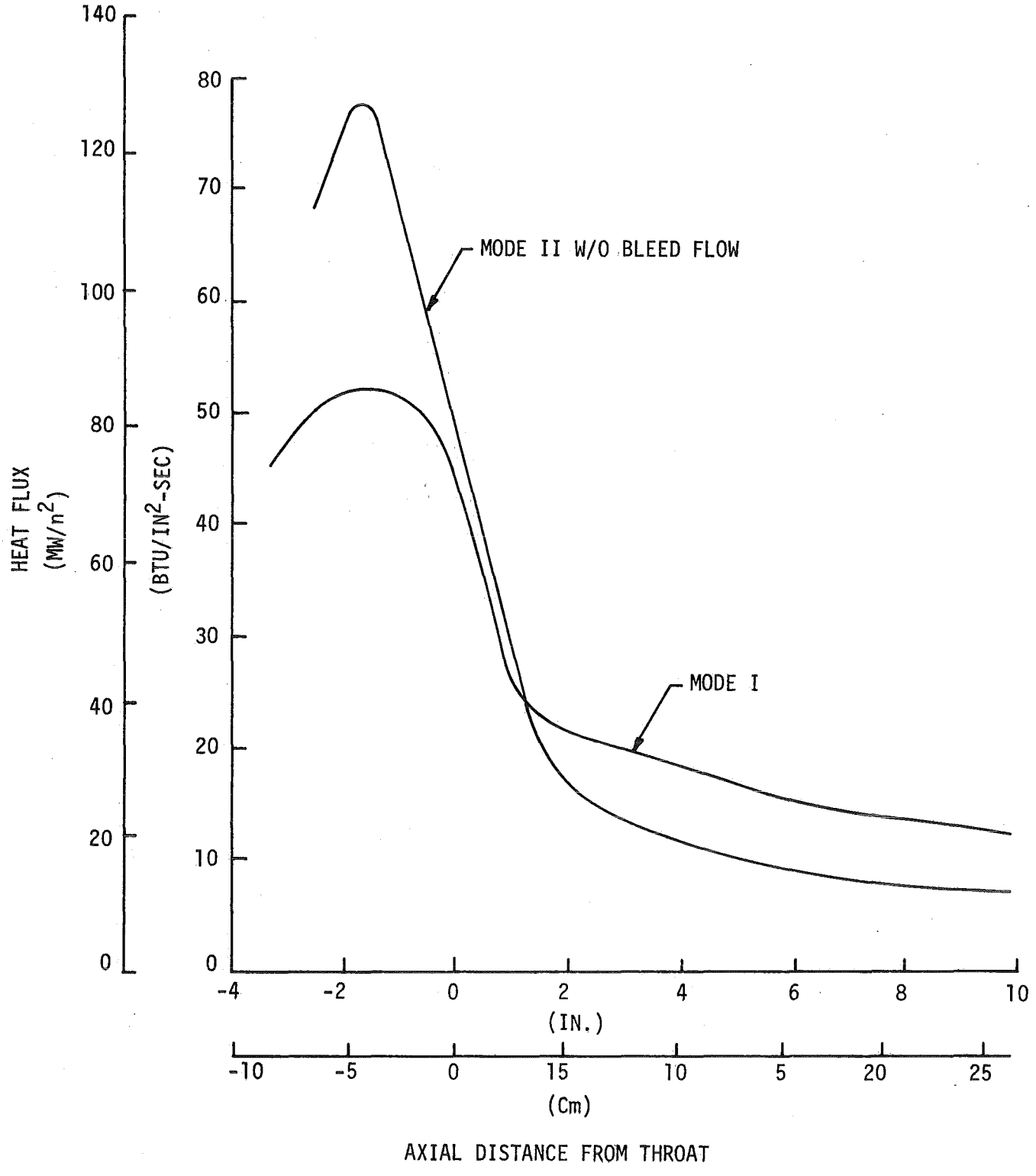

Figure V-13. Comparison of Secondary Throat Region Heat Fluxes

TABLE V-II

DUAL THROAT BASELINE COOLING CIRCUITS

INTERFACE AREA RATIO = 1.58

Circuit	Hydrogen Flow Fraction	Pressure Drop MPa (Psi)	ΔT_b °K (°F)	Max. Mach No.	Minimum Channel Depth, mm (in.)
Primary	0.40	8.07 (1170)	115 (207)	0.29	2.184 (.086)
Inner Annulus	0.24	4.41 (640)	112 (202)		
Annulus		.483 (70)	36 (64)	0.04	5.080 (.200)
Lip		2.69 (390)	5 (9)	0.11	2.032 (.080)
Primary Nozzle		1.24 (180)	72 (129)	0.12	3.200 (.126)
Secondary (Composite)	0.30	4.45 (645)	363 (654)	0.31	1.118 (0.044)

fraction, as shown previously in Figure V-12 for the baseline. The secondary circuit flow fraction was selected to provide a large pressure drop margin relative to the minimum primary circuit pressure drop; this margin is available to provide smaller channel depths in the Mode II impingement region. The remaining coolant flow was divided between the primary and lip region circuits, with the primary flow selected to give the minimum pressure drop whenever possible. For the higher thrust split and chamber pressure cases, it was necessary to select a primary flow less than optimum, resulting in a pressure drop up to 11% higher than minimum. Due to the time required to design the lip region circuit, the flow split between the primary and lip circuits was not optimized by balancing the required pressure drops.

The parametric designs are summarized in Table V-III. Figures V-14 and V-15 show the coolant pressure drop and Mach number as a function of primary chamber pressure and thrust split, respectively. At the highest pressure and thrust split, the coolant Mach number has reached 0.37; therefore, further increases in these parameters are not practical with the present channel layout.

D. DUAL EXPANDER

1. Baseline Designs

As shown in Figure V-16, the initial design considered was a hydrogen regeneratively cooled system with three parallel cooling circuits. Note that these circuits are conceptually the same as for the dual throat designs. Although the lip region cooling problem is less severe for the dual expander, the inner annulus circuit is much longer and includes a throat region.

TABLE V-III

DUAL THROAT PARAMETRIC DESIGN SUMMARY

Primary Pc MPa (psia)	Mode I Thrust Split	Circuit	Hydrogen Flow Fraction	Pressure Drop MPa (Psi)	ΔT_b °K (°F)	Max. Mach No.	Minimum Channel Depth, mm (in.)
27.58 (4000)	60/40	P	.40	7.060 (1024)	94 (169)	.24	2.591 (.102)
		L	.24	4.116 (597)	77 (139)	.14	3.048 (.120)
		S	.30	1.372 (199)	26 (466)	.09	4.089 (.161)
	75/25	P	.35	9.384 (1361)	149 (268)	.33	1.753 (.069)
		L	.24	4.585 (665)	127 (229)	.12	1.600 (.063)
		S	.35	2.289 (332)	382 (688)	.12	2.896 (.114)
	80/20	P	.35	10.85 (1574)	166 (299)	.37	1.575 (.062)
		L	.20	5.578 (809)	168 (303)	.15	1.016 (.040)
		S	.40	2.682 (389)	402 (724)	.13	2.540 (.100)
20.68 (3000)	70/30	P	.30	3.220 (467)	146 (262)	.20	2.692 (.106)
		L	.30	2.020 (293)	97 (175)	.08	3.429 (.135)
		S	.30	1.145 (166)	373 (672)	.09	4.216 (.166)
31.06 (4500)		P	.40	13.12 (1903)	119 (215)	.37	1.778 (.070)
		L	.24	6.709 (973)	109 (197)	.14	1.600 (.063)
		S	.30	3.330 (483)	364 (656)	.13	2.388 (.094)

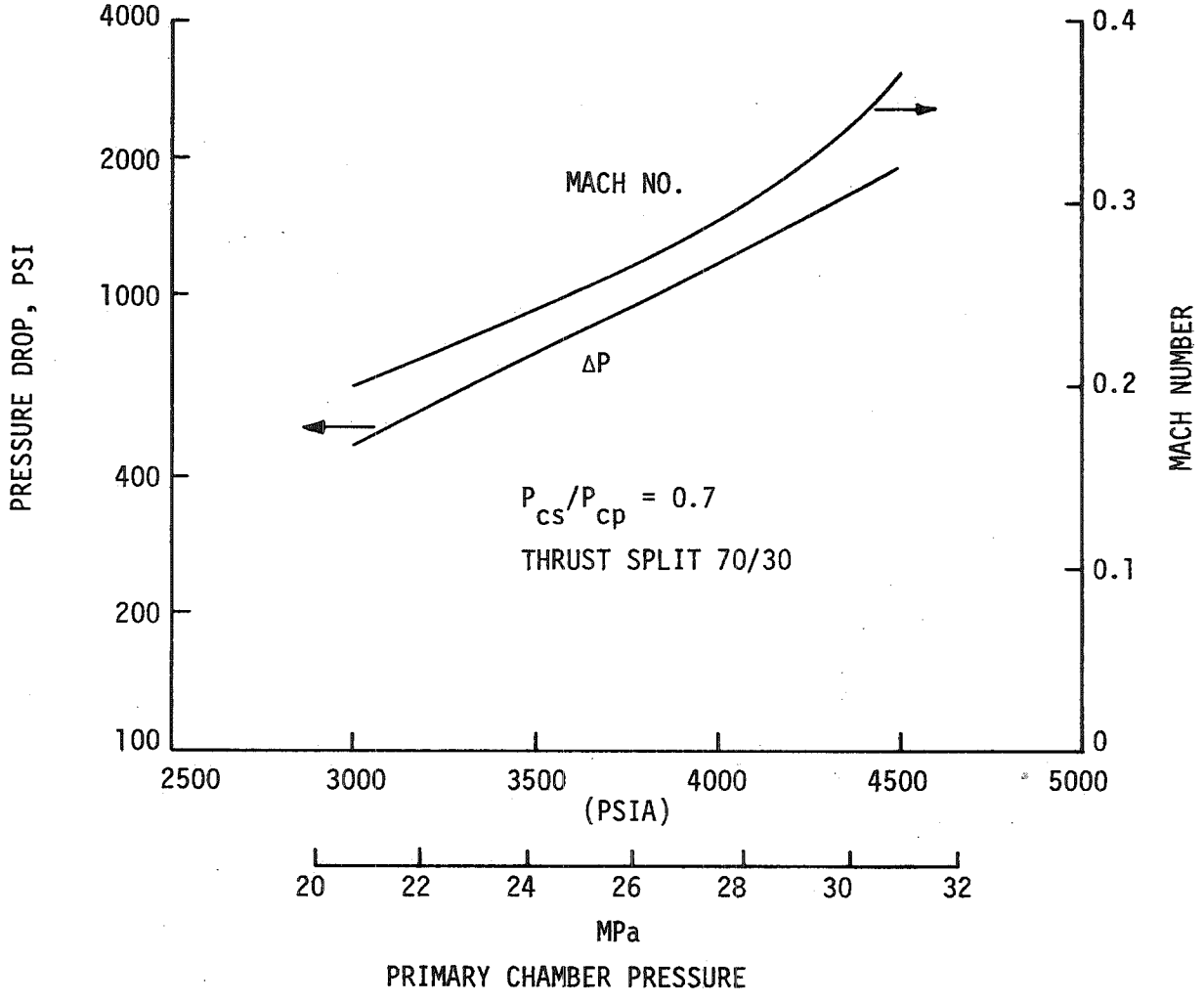

Figure V-14. Dual Throat Parameter Study Effect of Chamber Pressure on Coolant Pressure Drop and Mach Number

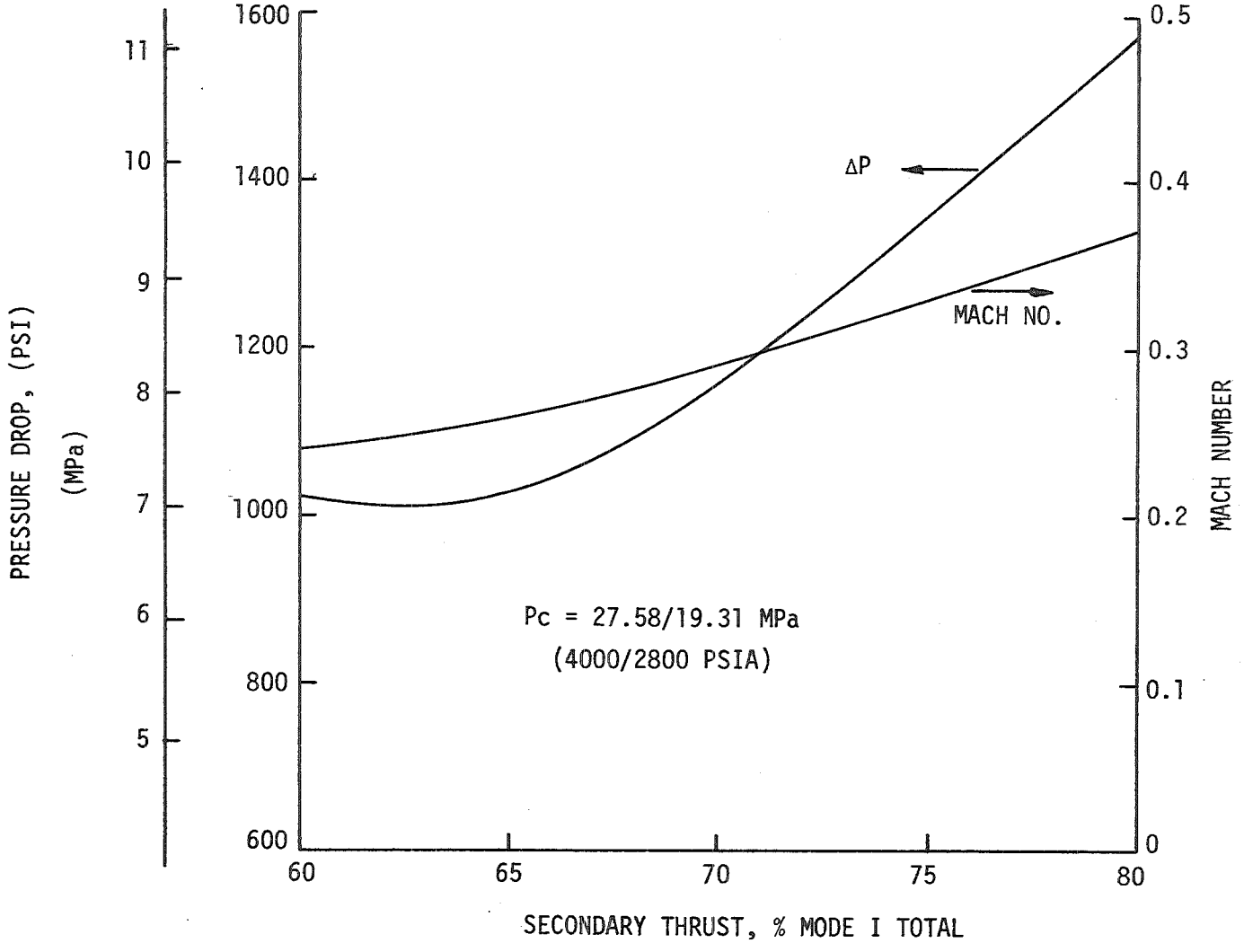

Figure V-15. Dual Throat Parameter Study Effect of Thrust Split on Coolant Pressure Drop and Mach Number

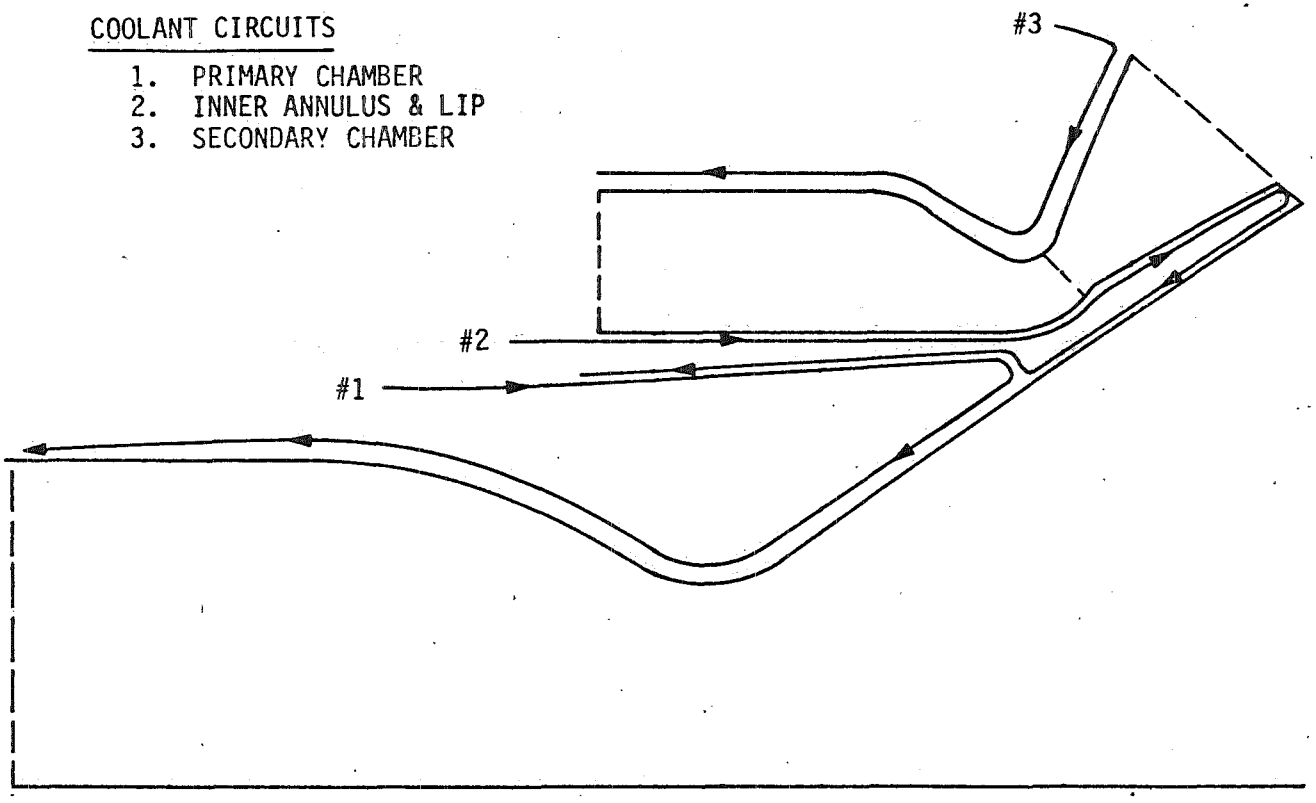

Figure V-16. Dual Expander Coolant Flow Schematic

V, D, Dual Expander (cont.)

Channel layout details for the baseline design are included in Table V-I. The primary circuit layout is similar to the dual throat secondary circuit. Channel aspect ratios in the barrel are within the design limit, so there was no motivation for increasing the wall thickness to provide a wider channel. A uniform channel width of 1.016 mm (0.040 in.) was maintained in the barrel and convergent sections of the secondary circuit because of the small channel depths required. A uniform channel width was also used over the entire inner annulus surface. It was found that a 1.118 mm (0.044 in.) width provided a lower pressure drop than the minimum allowable width of 1.016 mm (0.040 in.). The latter value was maintained in the primary nozzle section of the inner annulus circuit. This section defined the number of channels in the circuit and is shown separately in Table V-I.

Two area ratios were considered for the interface between the primary circuit inlet and the inner annulus circuit outlet: 2.34, which represents the maximum from a mechanical design standpoint, and 1.66. Figure V-17 shows the primary circuit pressure drop characteristics for these two interface area ratios, along with the secondary circuit characteristics. The coolant flow fraction for the latter is set at 0.24 by the minimum channel depth constraint. Inner annulus flow requirements for Mach number control, the remaining hydrogen flow fractions available for the primary circuit, and the corresponding primary circuit pressure drops from Figure V-17 are as follows:

Interface Area Ratio	Inner Annulus Flow Fraction	Primary Flow Fraction	Primary ΔP, MPa (psi)
2.34	0.35	0.35	11.86 (1720)
1.66	0.40	0.30	12.86 (1860)

The reduced flow available for the primary circuit with the lower interface area ratio offsets the reduced length and increases the primary circuit

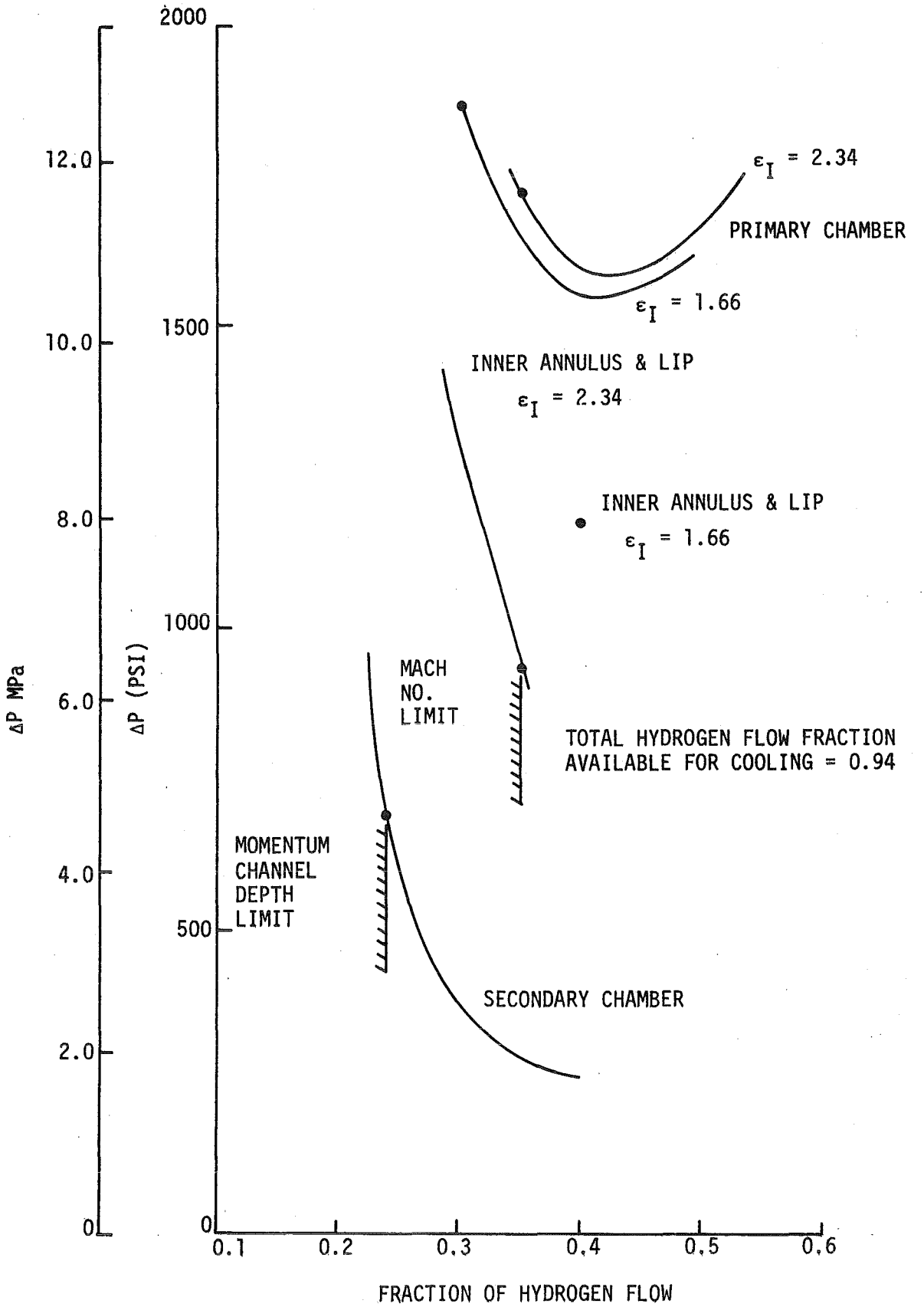

Figure V-17. Dual Expander Baseline Cooling Circuit Pressure Drop Characteristics

pressure drop. In both cases, the inner annulus flow required for coolant Mach number control forces the primary flow to be less than optimum. Table V-IV summarizes the circuit designs for an interface area ratio of 2.34. In view of the Mach numbers in the primary and inner annulus circuits and the channel depth in the secondary circuit, it is clear that cooling limitations have been reached in both the primary and secondary chambers. The secondary/primary chamber pressure ratio was selected in anticipation of such a result. However, a slightly lower ratio would have allowed the primary circuit pressure drop to be optimized.

Figure V-17 indicates that the hydrogen pressure drop can be reduced to 10.69 MPa (1550 psi) by increasing the primary circuit flow fraction to 0.40 with an interface area ratio of 1.66. This can be accomplished by using oxygen to cool the secondary circuit. Table V-V summarizes such a design; it should be noted that the secondary circuit channel design has not been optimized for oxygen cooling.

Figure V-18 shows the effect of transpiration cooling the throat region of the primary chamber for an interface area ratio of 1.66. The upstream end of the transpiration region was varied, with the downstream end fixed at area ratio 1.44, which is 3.74 cm (1.47 in.) aft of the throat. Since the secondary chamber was assumed to be hydrogen cooled, only 30% of the total hydrogen flow was available for the two primary cooling circuits. Consequently, the significant coolant flow fractions required for the longer transpiration sections severely limit the available regenerative cooling flow and result in increased pressure drops. The minimum regenerative pressure drop in this case is about 11.03 MPa (1600 psi), which is higher than the optimum value of Figure V-17 that can be achieved by oxygen cooling of the secondary.

TABLE V-IV

DUAL EXPANDER BASELINE COOLING CIRCUITS

INTERFACE AREA RATIO = 2.34

Circuit	Hydrogen Flow Fraction	Pressure Drop MPa (Psi)	ΔT_b °K (°F)	Max. Mach No.	Minimum Channel Depth, mm (in.)
Primary	0.35	11.86 (1720)	157 (282)	0.30	2.159 (.085)
Inner Annulus	0.35	6.45 (935)	182 (328)		
Annulus		4.48 (650)	161 (289)	0.29	1.321 (.052)
Lip		.93 (135)	1.7 (3)	0.09	5.08 (.200)
Primary Nozzle		1.03 (150)	20 (36)	0.10	5.08 (.200)
Secondary	0.24	4.76 (690)	237 (427)	0.27	9.14 (.036)

TABLE V-V

DUAL EXPANDER BASELINE WITH OXYGEN-COOLED SECONDARY

INTERFACE AREA RATIO = 1.66

Circuit	Coolant Flow Fraction	Pressure Drop MPa (Psi)	ΔT_b °K (°F)	Max. Mach No.	Minimum Channel Depth, mm (in.)
Primary	0.40 H_2	10.69 (1550)	132 (237)	0.28	2.39 (.094)
Inner Annulus	0.40 H_2	8.0 (1160)	166 (299)		
Annulus		4.62 (670)	141 (254)	0.29	1.65 (.065)
Lip		1.48 (215)	1.7 (3)	0.11	5.08 (.200)
Primary Nozzle		1.90 (275)	23 (42)	0.12	5.08 (.200)
Secondary	0.60 O_2	10.0 (1450)	136 (244)	0.23	2.79 (.110)

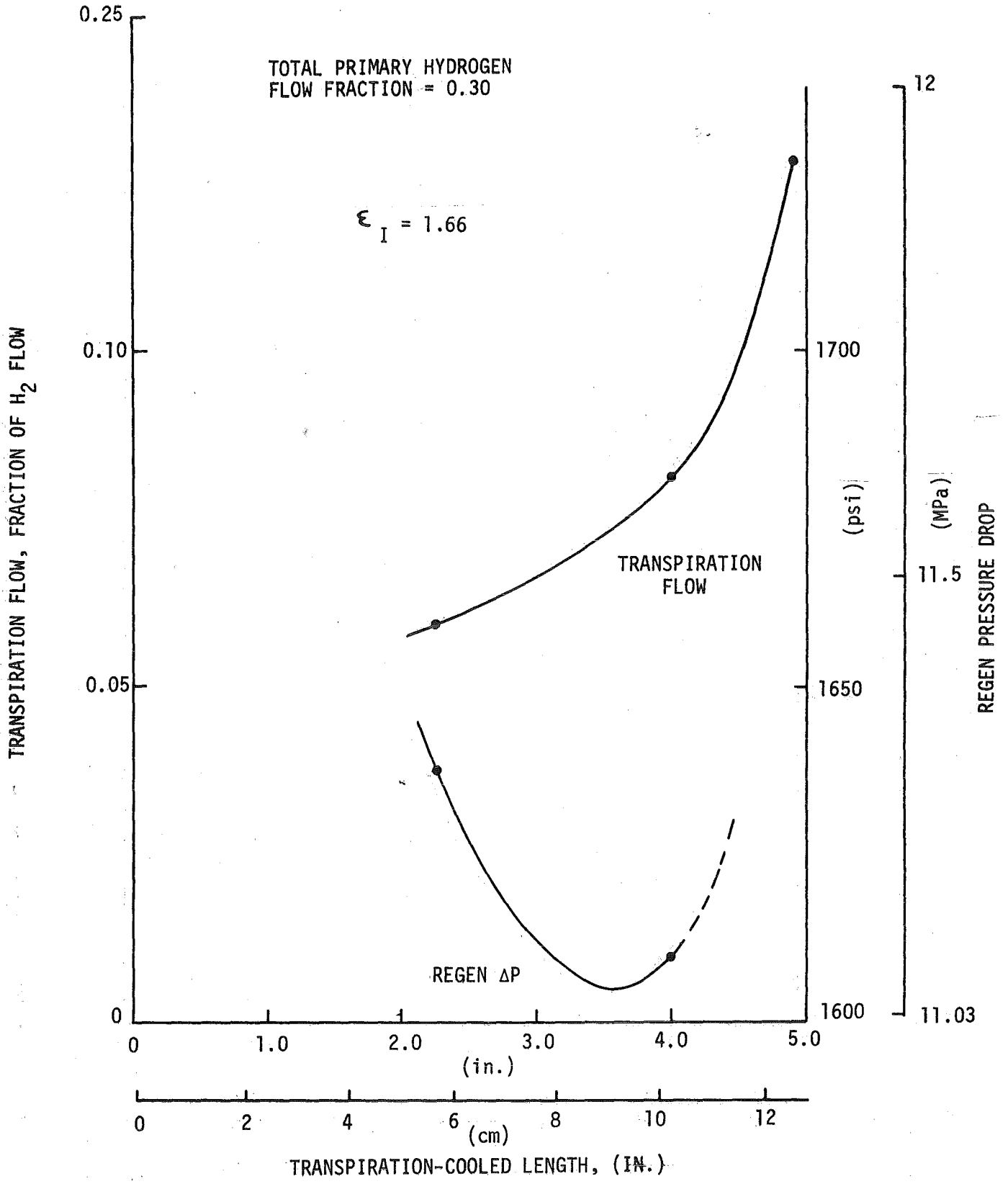

Figure V-18. Dual Expander Transpiration Cooling

V, D, Dual Expander (cont.)

2. Parametric Study

The dual expander parametric study was based on the hydrogen regeneratively cooled concept of Table V-IV. Independent variations of thrust and Mode I thrust split at the baseline chamber pressures were investigated, along with various chamber pressure combinations at the baseline thrust and thrust split. Table V-VI indicates the design points attempted and identifies those for which chamber designs could not be obtained; characteristics of the successful designs are summarized in Table V-VII.

In all cases with increased chamber pressures or Mode I thrust split relative to the baseline, designs could not be obtained due to insufficient hydrogen flow for the cooling of three circuits. A reduction in secondary chamber pressure to 10.34 MPa (1500 psia) with the primary chamber pressure unchanged resulted in convergence failure due to large pressure drops in the primary circuit. The latter results from the reduction in coolant inlet pressure associated with the reduction in secondary chamber pressure. From the baseline and parametric results, it appears that the present baseline design point is near the optimum chamber pressure ratio and is very close to the chamber pressure vs thrust split characteristic which represents a practical cooling limit. Future parametric studies should define additional points on such a characteristic and consider smaller chamber pressure increments to optimize the pressure ratio.

E. SUMMARY OF RESULTS

A satisfactory dual throat baseline design was obtained by using three parallel cooling circuits. The primary circuit coolant flows from area ratio 1.58 in the primary nozzle to the primary injector; this circuit defines the system pressure drop, so its coolant flow fraction is selected to provide the minimum pressure drop. A separate circuit cools the inner annulus

TABLE V-VI

DUAL EXPANDER PARAMETRIC STUDY DESIGN POINTS

Thrust MN	Thrust (10^6 lbF)	Mode I Thrust Split	Primary Pc MPa (psia)	Secondary Pc MPa (psia)	Result
2.67	(0.6)	59/41	41.37 (6000)	10.34 (1500)	Convergence Failure - Primary
				24.82 (3600)	Insufficient Coolant
			27.58 (4000)	13.79 (2000)	Successful Design
			48.26 (7000)	24.13 (3500)	Convergence Failure - Inner Annulus
		44/56	41.37 (6000)	20.68 (3000)	Successful Design
		68/32			Insufficient Coolant
4.44	(1.0)	59.41			Successful Design
6.67	(1.5)				Successful Design

TABLE V-VII

DUAL EXPANDER PARAMETRIC DESIGN SUMMARY

Chamber Pressure MPa (psia)	Total Thrust MN (10^6 lbF)	Mode I Thrust Split	Circuit	Hydrogen Flow Fraction	Pressure Drop MPa (Psi)	ΔT_b °K (°F)	Max. Mach No.	Minimum Channel Depth, mm (in.)
27.58/13.79 (4000/2000)	2.67 (0.6)	59/41	P	.25	3.96 (574)	219 (394)	.22	2.82 (.111)
			IA	.35	2.70 (391)	174 (314)	.18	2.14 (0.84)
			S	.30	.641 (93)	172 (309)	.09	3.10 (.122)
41.37/20.68 (6000/3000)	2.67 (0.6)	44/56	P	.25	11.30 (1639)	118 (213)	.28	2.03 (.080)
			IA	.25	7.67 (1112)	153 (276)	.21	2.13 (.084)
			S	.25	1.41 (204)	146 (263)	.11	2.95 (.116)
	4.44 (1.0)	59/41	P	.40	10.42 (1511)	122 (220)	.30	2.87 (.113)
			IA	.30	5.96 (865)	182 (327)	.25	1.52 (.060)
			S	.24	2.0 (290)	194 (350)	.15	1.80 (.071)
	6.67 (1.5)		P	.30	10.45 (1515)	147 (264)	.29	2.87 (.113)
			IA	.30	7.36 (1068)	167 (300)	.22	1.98 (.078)
			S	.25	1.613 (234)	165 (297)	.11	2.82 (.111)

surface, the lip region, and the rest of the primary nozzle. The majority of the channel pressure drop in this circuit is required for the lip region, for which a three-dimensional SINDA model was developed. A counterflow circuit cools the outer surface of the secondary chamber. This circuit is a composite design considering both Mode I and Mode II operation; the channel design over a short region upstream of the secondary throat is defined by the primary plume impingement associated with a bleed flow malfunction in Mode II. An exact solution for the inviscid plume impingement problem was obtained with the VNAP program. This solution provided edge conditions for an integral boundary layer analysis which defined the wall heat transfer. The initial momentum thickness for the boundary layer analysis was varied in order to bound the problem, with the channel design based on the worst case; the maximum heat flux ranged from essentially the Mode I value to almost 50% higher.

Table V-II summarizes individual cooling circuit characteristics for the dual throat baseline design. Although the fuel system pressure drop of 8.00 MPa (1160 psi) is set by the primary circuit, the coolant Mach number is slightly higher in the secondary circuit when the latter is designed to accommodate the maximum postulated Mode II heat flux with no bleed flow. Parametric study results indicate that it is the coolant Mach number rather than pressure drop which limits increases in chamber pressure and Mode I thrust split. Increasing the chamber pressures to 31.02/21.72 MPa (4500/3150 psia) or the thrust split to 80/20 results in a primary circuit Mach number of 0.37.

The dual expander designs are cooled with three parallel circuits similar to those of the dual throat. However, the inner annulus circuit is now a major circuit in terms of length and heat load, and it includes a throat region. Regenerative cooling of the baseline design point with hydrogen only is difficult. Coolant flows in the secondary and inner annulus circuits must

V, E, Summary of Results (cont.)

be selected to avoid minimum channel depth and Mach number limits, respectively, and the remaining flow available for the primary is less than optimum. As a result, the system pressure drop of 11.86 MPa (1720 psi) is .896 MPa (130 psi) above the minimum primary circuit value. Using oxygen to cool the secondary circuit and reducing the interface area ratio between the primary circuit inlet and the inner annulus circuit outlet allows the hydrogen pressure drop to be reduced to 10.69 MPa (1550 psi). These designs are sumamrized in Tables V-IV and V-V. Transpiration cooling the throat region of the primary chamber was not effective since the hydrogen flow fractions required for transpiration cooling, coupled with the flow requirements of the other circuits, severely limit the flow available for regeneratively cooling the remainder of the primary circuit and result in relatively high pressure drops.

Parametric study designs could not be obtained with increased chamber pressures or increased Mode I thrust split, or with the secondary chamber pressure reduced to 10.34 MPa (1500 psia). The latter results from the high primary chamber pressure drop associated with reduced coolant inlet pressure. These results, along with the baseline design details, indicate the baseline design point is near the optimum chamber pressure ratio and is very close to the chamber pressure vs thrust split characteristic which represents a practical cooling limit.

VI. HOT-FIRE DATA ANALYSIS

A. PRE-TEST ANALYSIS

The overall objective of this task was to provide support for the hot-fire testing of the dual throat hardware by NASA/MSFC. ALRC's first objective was to review the MSFC's test plan and provide whatever consultation might be necessary during testing. Secondly, ALRC would review the hot-fire data and interpret test results by using the aerodynamic model and previous cold-flow data. Test data would also be used to correlate dual throat nozzle Mode II performance. Thirdly, corrections to the aerodynamic model believed advisable were to be incorporated into the model, and further model improvements were to be recommended.

The hardware tested was the same as that used during cold-flow testing (NAS 8-32666), (Ref. 1). For these tests, the small primary nozzle (ε_p = 1.72) and the large secondary nozzle (ε_s = 3.0) were used. A layout of the test hardware is shown in Figure VI-1. The proposed test plan called for testing to be conducted at three different nozzle spacings, using GH_2 as the bleed gas. Recommendations were made by ALRC for testing to be done with various bleed flow gas compositions and temperatures to verify the improvements made to the aerodynamic bleed flow model to simulate such conditions. Funding and time limitations did not permit testing a survey of bleed flow gases, although one series of tests, at the larger nozzle spacing, was performed with GN_2 as the bleed gas. The tests conducted are summarized in Table VI-I.

The improved aerodynamic bleed flow model was used to define the "blowoff" condition to provide a safe first test operation. The predicted trend in bleed flowrate versus nozzle spacing is shown in Figure VI-2, for both a GH_2 and a GN_2 bleed. A significant influence of bleed flow properties on operating characteristics was predicted. These predictions indicated that one and one-half to two times the bleed flow would be

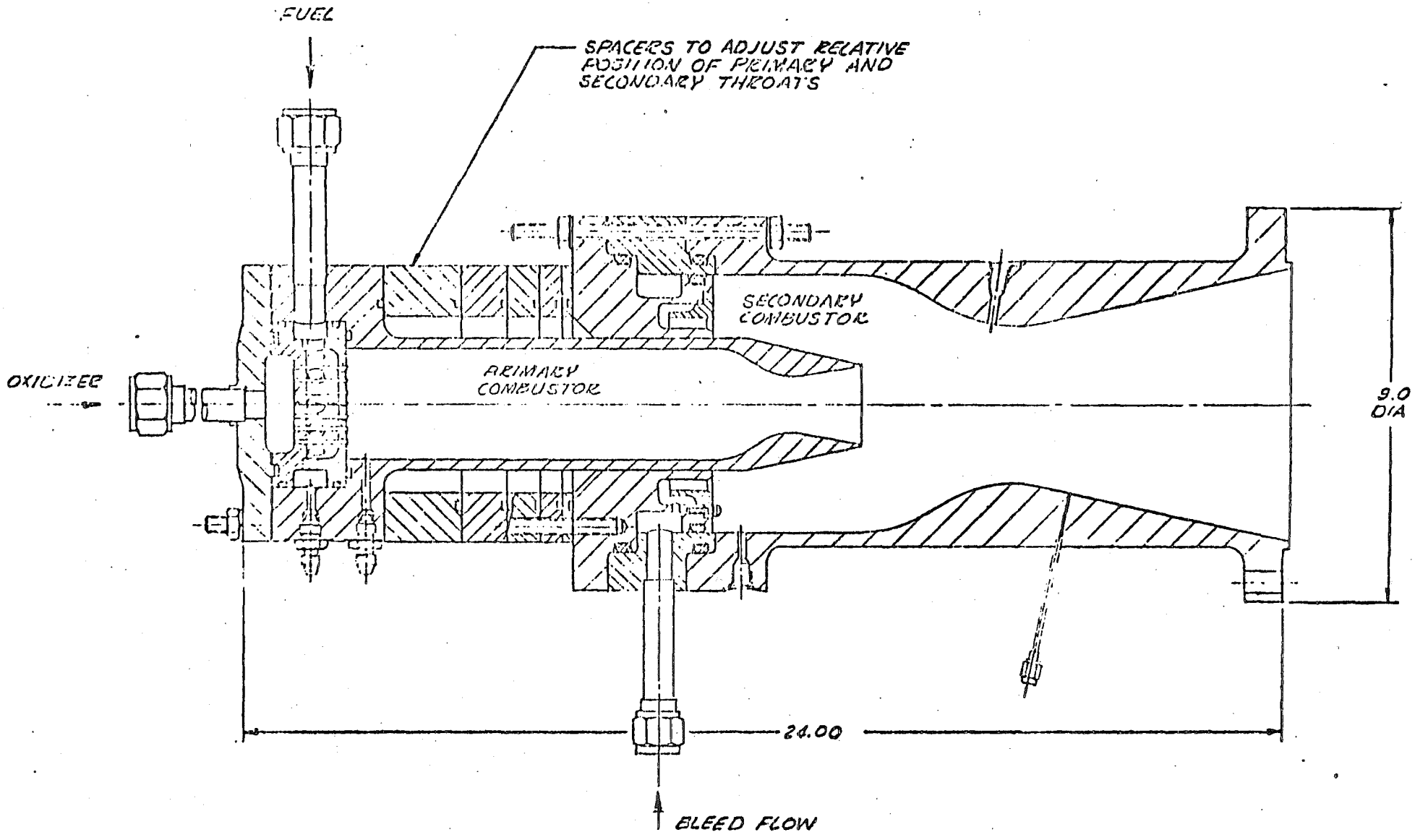

Figure VI-1. Existing Dual Throat Test Article

TABLE VI-I

DUAL THROAT THRUSTER

MSFC IN-HOUSE TEST SUMMARY

TEST NO.	LE RTP	BLEED GAS	BLEEDFLOW W_S/W_P, %	°/F	Pc, PSIA	DURATION, SEC
8	5.062	GH_2	8.9	.74	442	10
9	↓	↓	7.5	.77	455	10
10	↓	↓	5.5	.74	440	10
11	↓	↓	3.4	.79	455	10
12	↓	↓	1.3	.80	454	10
13	↓	↓	0	.79	455	10
14	5.062	GN_2	14.5	.76	440	5
15	↓	↓	11.4	.81	458	5
16	↓	↓	8.6	.79	451	5
17	(NO TEST)	↓	—	—	—	—
18	↓	↓	5.2	.83	460	5
19	(NO TEST)	↓	—	—	—	—
20	↓	↓	2.6	.78	454	5
21	↓	↓	0	.81	464	5
22	2.997	GH_2	8.5	.81	451	5
23	↓	↓	7.2	.84	459	5
24	↓	↓	4.5	.80	452	5
25	↓	↓	3.4	.82	459	5
26	(NO TEST)	↓	—	—	—	—
27	↓	↓	1.4	.78	451	5
28	↓	↓	0	.80	457	5
29	3.979	GH_2	8.9	.79	452	5
30	↓	↓	7.3	.79	450	5
31	(NO TEST)	↓	—	—	—	—
32	↓	↓	3.5	.79	450	5
33	↓	↓	1.5	.81	448	5
34	↓	↓	0	.80	450	5

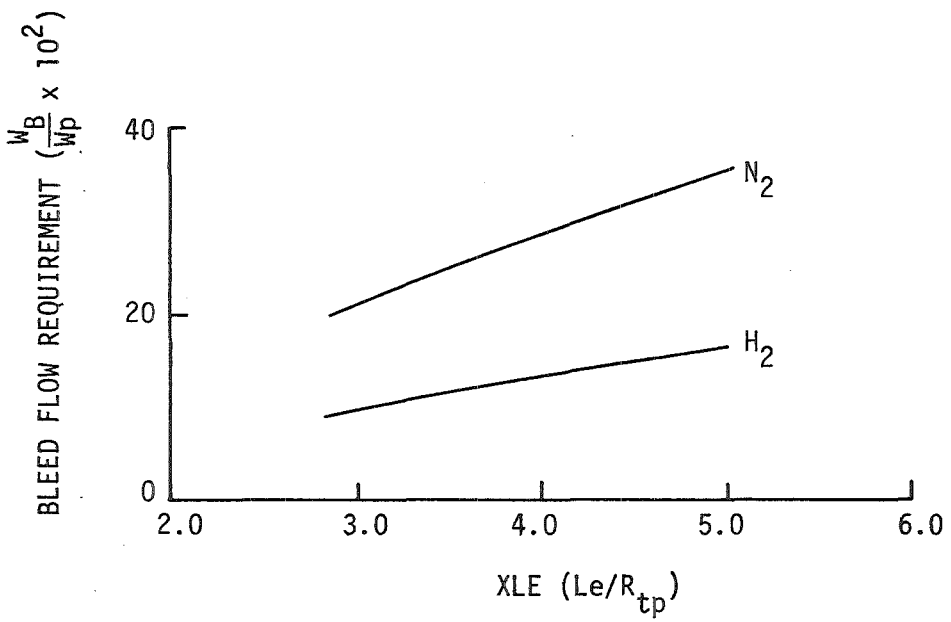

- DEFINED BLOW-OFF CONDITION TO PROVIDE SAFE 1ST TEST OPERATION
- PREDICTED SIGNIFICANT INFLUENCE OF BLEED FLOW PROPERTIES ON OPERATING CHARACTERISTICS

Figure VI-2. Predicted Trend in Bleed Flowrates versus Nozzle Spacing

required when using GN_2 as opposed to using GH_2. This difference is due to the influence that GN_2 has on the shear layer mixing equations with its larger molecular weight and smaller specific heat (C_p). One item of concern was the large bleed flowrates predicted using GN_2 and for the large nozzle spacing using GH_2. The assumptions used in developing the bleed flow model were expected to limit the model's validity and applicability to small bleed flows of approximately 10% or less. As noted in Section III, significant reductions in bleed flow from the blowoff condition can be made without measurably inducing a loss in total pressure.

B. TEST RESULTS

1. Data Evaluation

Wall pressure profiles for the various test configurations are shown in Figures VI-3 through VI-5 for various nozzle spacings and in Figure VI-6 for N_2 bleed flow. In general, the pressure data are reasonable and similar to the previous cold-flow test results (Ref. 1). A comparison of the hot-fire and cold-flow pressure profiles is shown in Figure VI-7 for the large nozzle spacing (L_e/R_{tp} = 5.06) with GN_2 bleed. The plume impingement point is shown to move toward the secondary throat with increasing bleed flow, as was seen in cold-flow testing. Also, the plume impingement shock strength is decreased with bleed flow, which is consistent with the cold-flow data and the aerodynamic bleed flow model predictions. Test results also show that increased nozzle spacing requires increased bleed flow to attach the plume to the secondary throat which is also consistent with both the cold-flow data and the model predictions.

Although the hot-fire data, overall, were consistent with the cold-flow data, some anomalies did exist. All the test configurations had

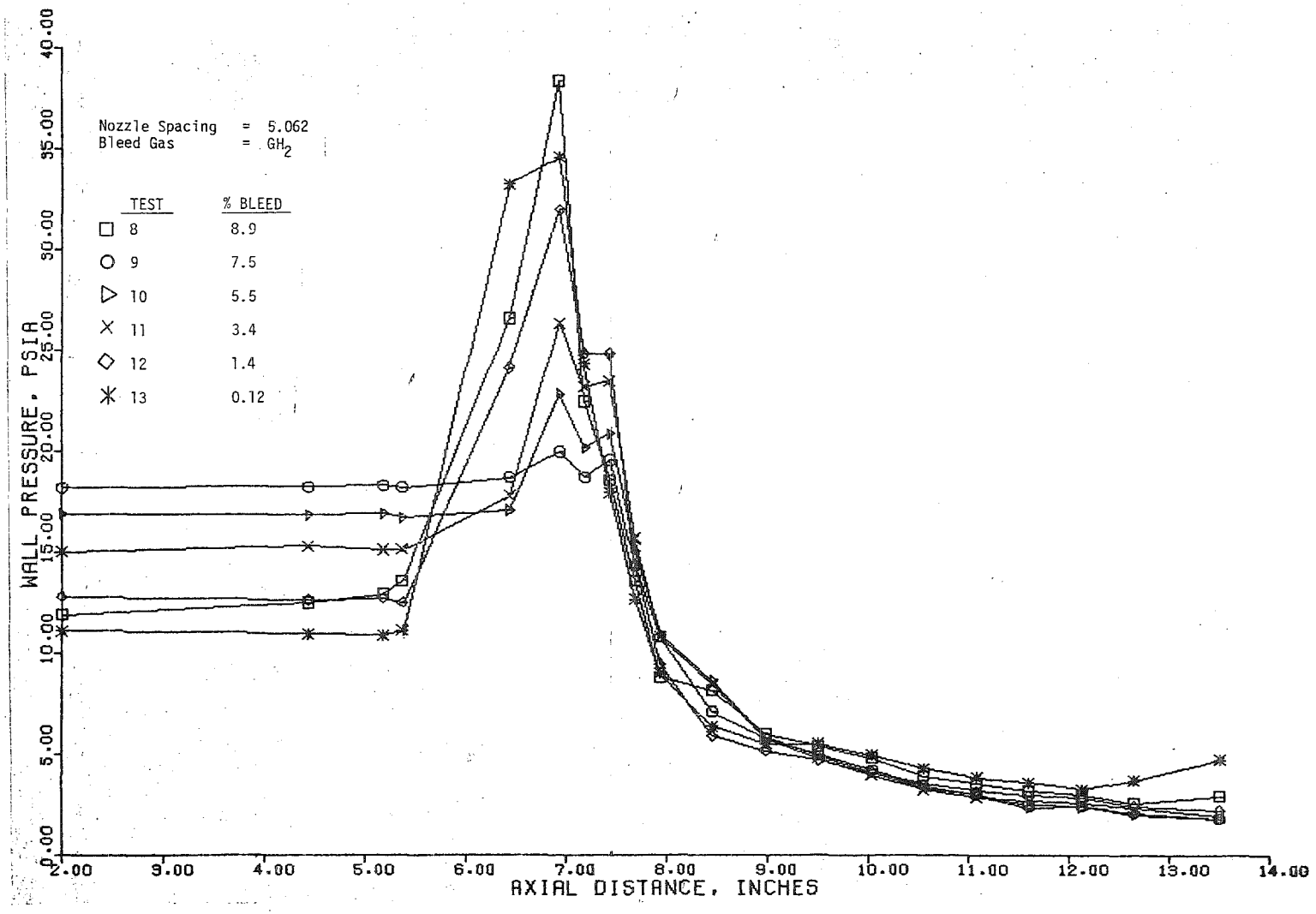

Figure VI-3. Wall Pressure Profile, Nozzle Spacing = 5.062, GH_2 Bleed Flow

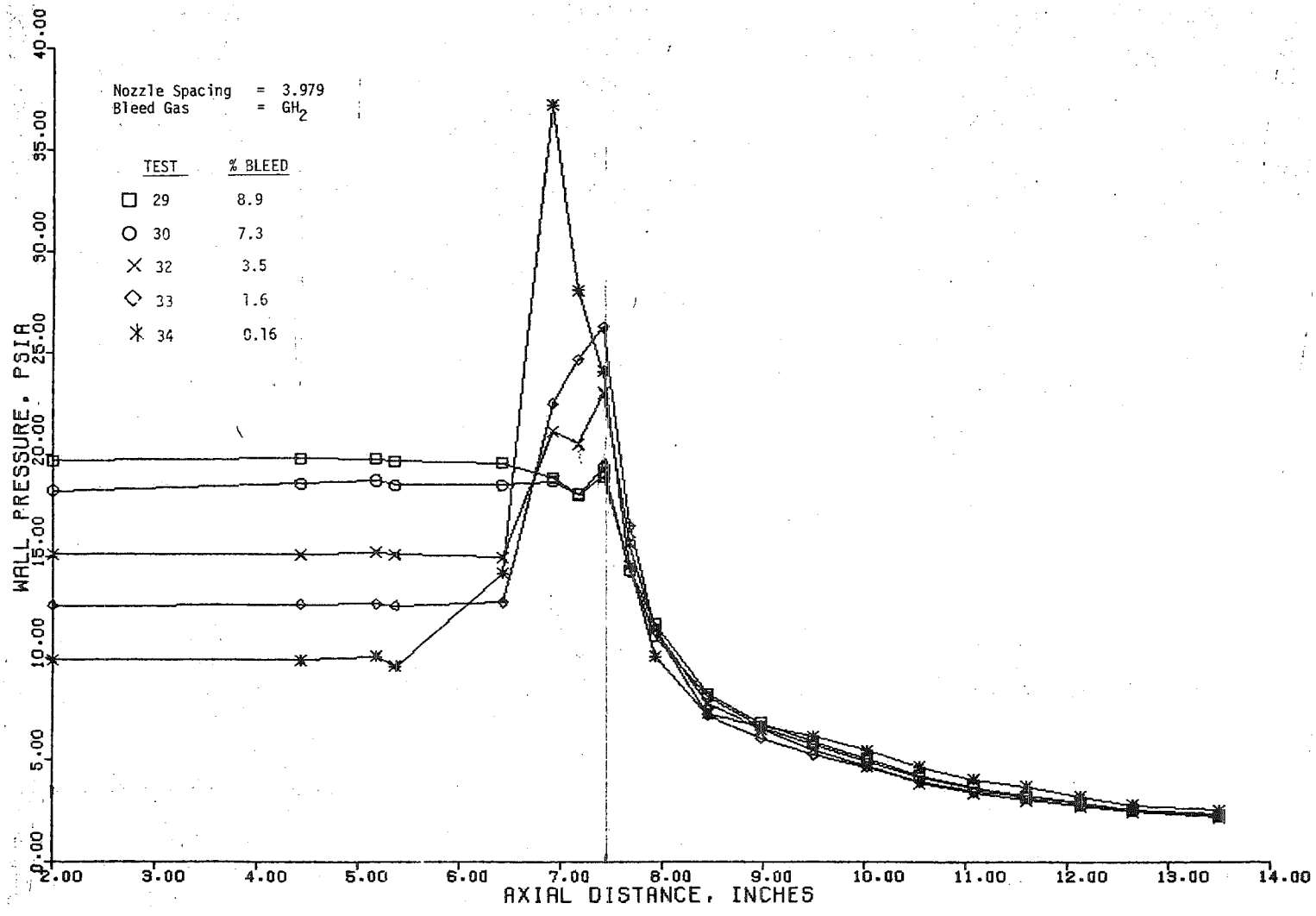

Figure VI-4. Wall Pressure Profile, Nozzle Spacing = 3.979, GH_2 Bleed Flow

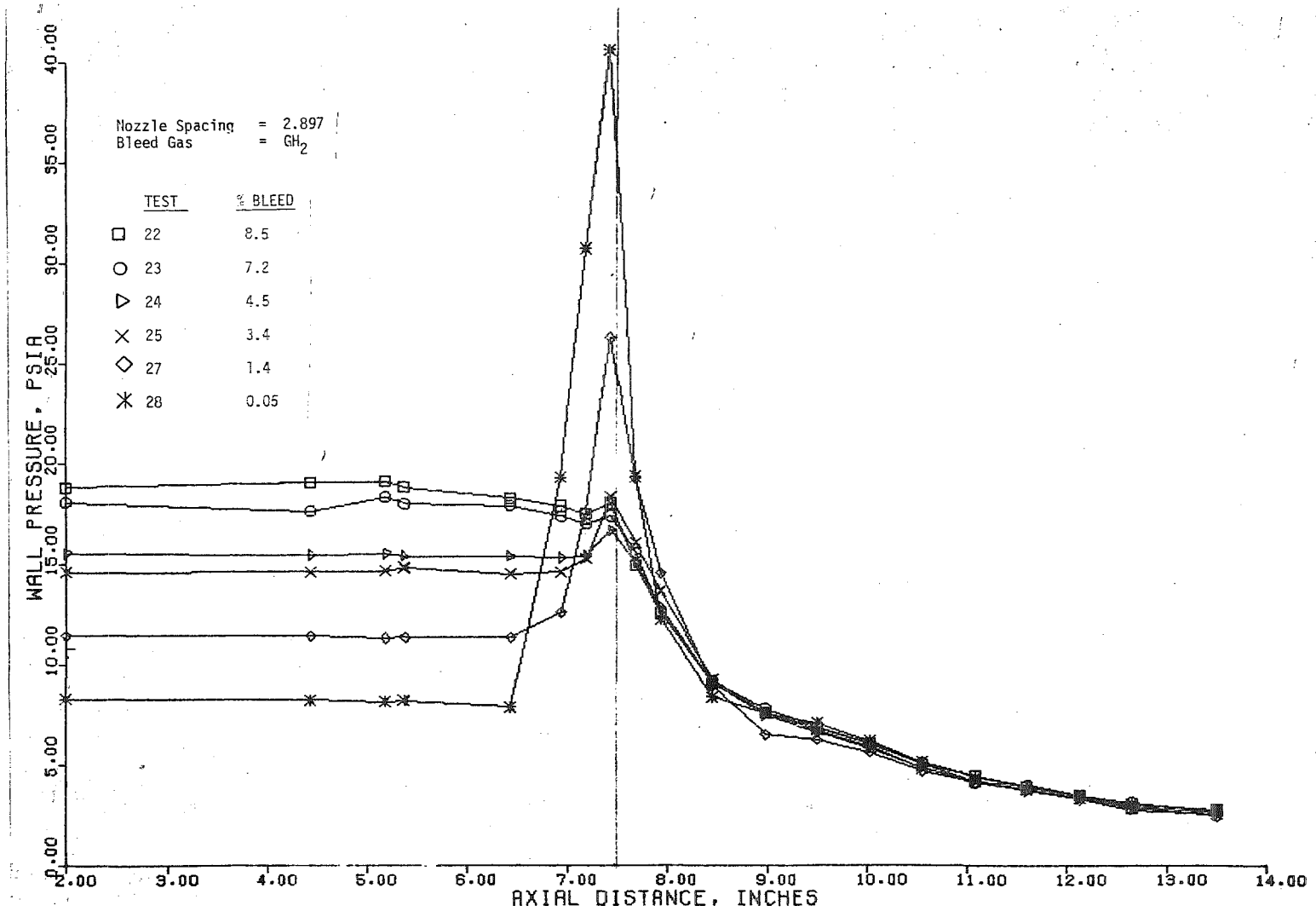

Figure VI-5. Wall Pressure Profile, Nozzle Spacing = 2.897, GH_2 Bleed Flow

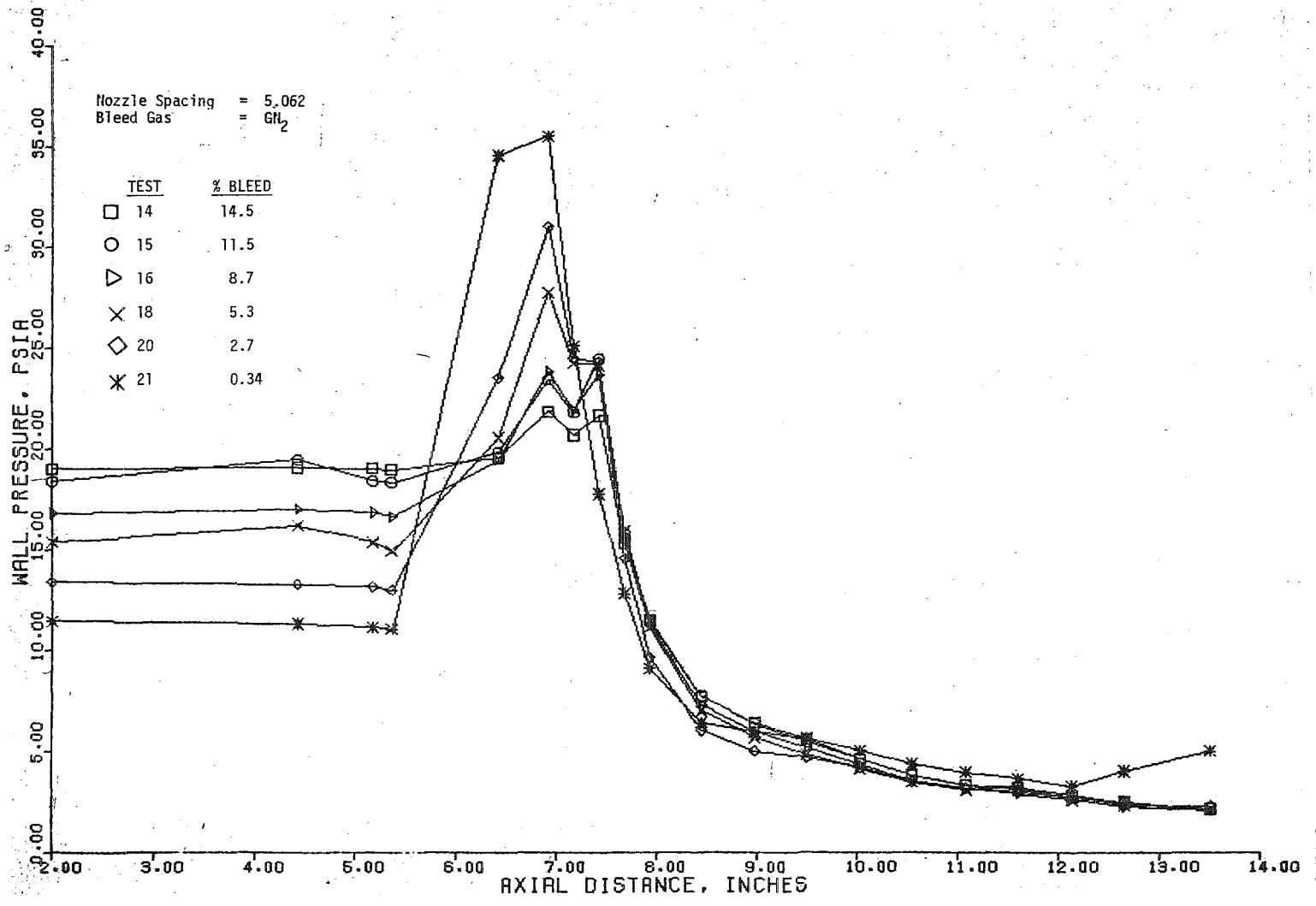

Figure VI-6. Wall Pressure Profile, Nozzle Spacing = 5.062, GN_2 Bleed Flow

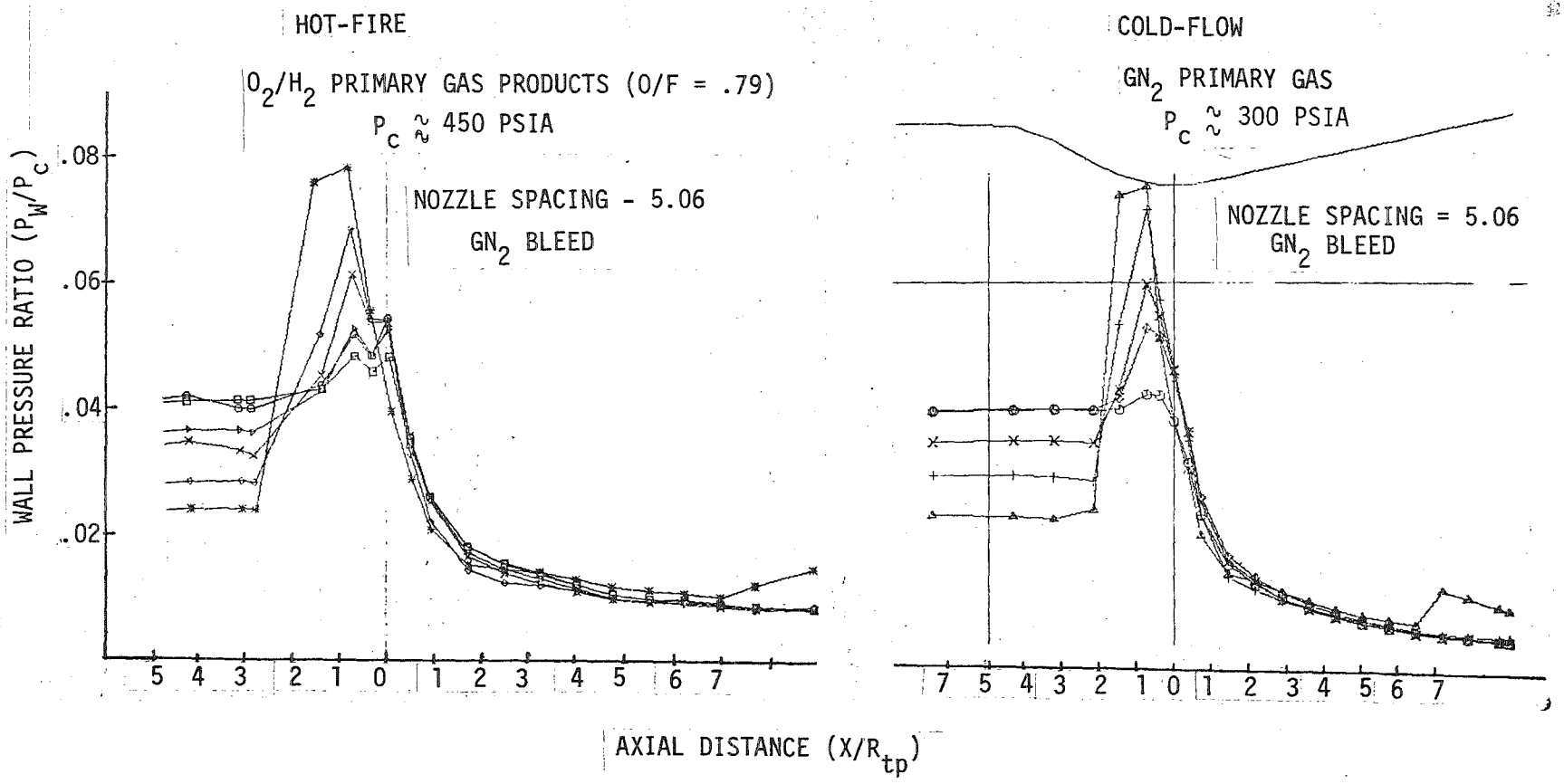

Figure VI-7. Comparison of the Hot-Fire and Cold-Flow Pressure Profiles

some questionable pressure measurements at the secondary throat. The wall pressure would increase due to the plume impingement, decrease, and then increase again at the secondary throat before decreasing as a result of being expanded through the secondary nozzle. Cold-flow data show the secondary wall pressure to increase due to the plume impingement and then continually decrease as the gas exits through the secondary nozle.

Another anomaly is seen in Tests 15, 18, 23, and 34, shown in Figures VI-6, VI-5, and VI-4, respectively. The pressure in the secondary chamber increases and then decreases prior to plume impingement. This trend was not seen during cold-flow testing and is probably the result of small pressure measurement errors.

Test 8, shown in Figure VI-3, is also inconsistent with all other test results. Its measured pressure profile is consistent with a minimum bleed flow, yet the measured bleed flow was the largest with that configuation. This may be due to a leak in the bleed circuit after the flowrate measurement or an erroneous flowrate measurement.

2. Model Comparison

Although some uncertainties do exist with the test data, the experimental results have verified the bleed flow model's predictions. An example of this is shown in Figure VI-8. The bleed flow model predicts nearly exactly the recirculation pressure for a given bleed flow. Also, the model's prediction that more GN_2 bleed would be needed to achieve the same recirculation pressure as with GH_2 was substantiated with the hot-fire test results.

The hot-fire results also verified the correlation of the plume scaling factor (FCTR) with nozzle spacing. Figure VI-9 shows that,

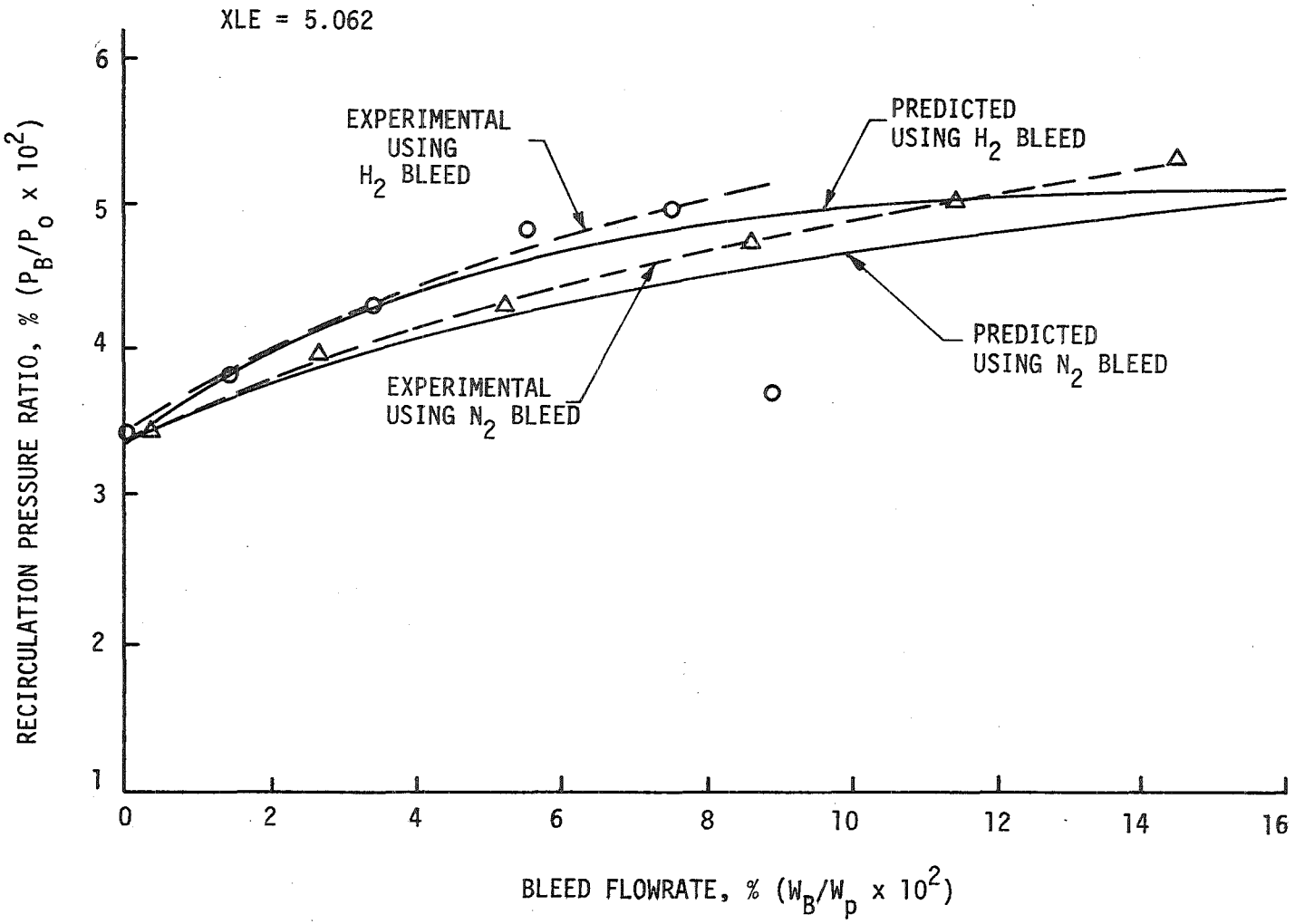

Figure VI-8. Experimental Results Have Verified Aerodynamic Model Predictions

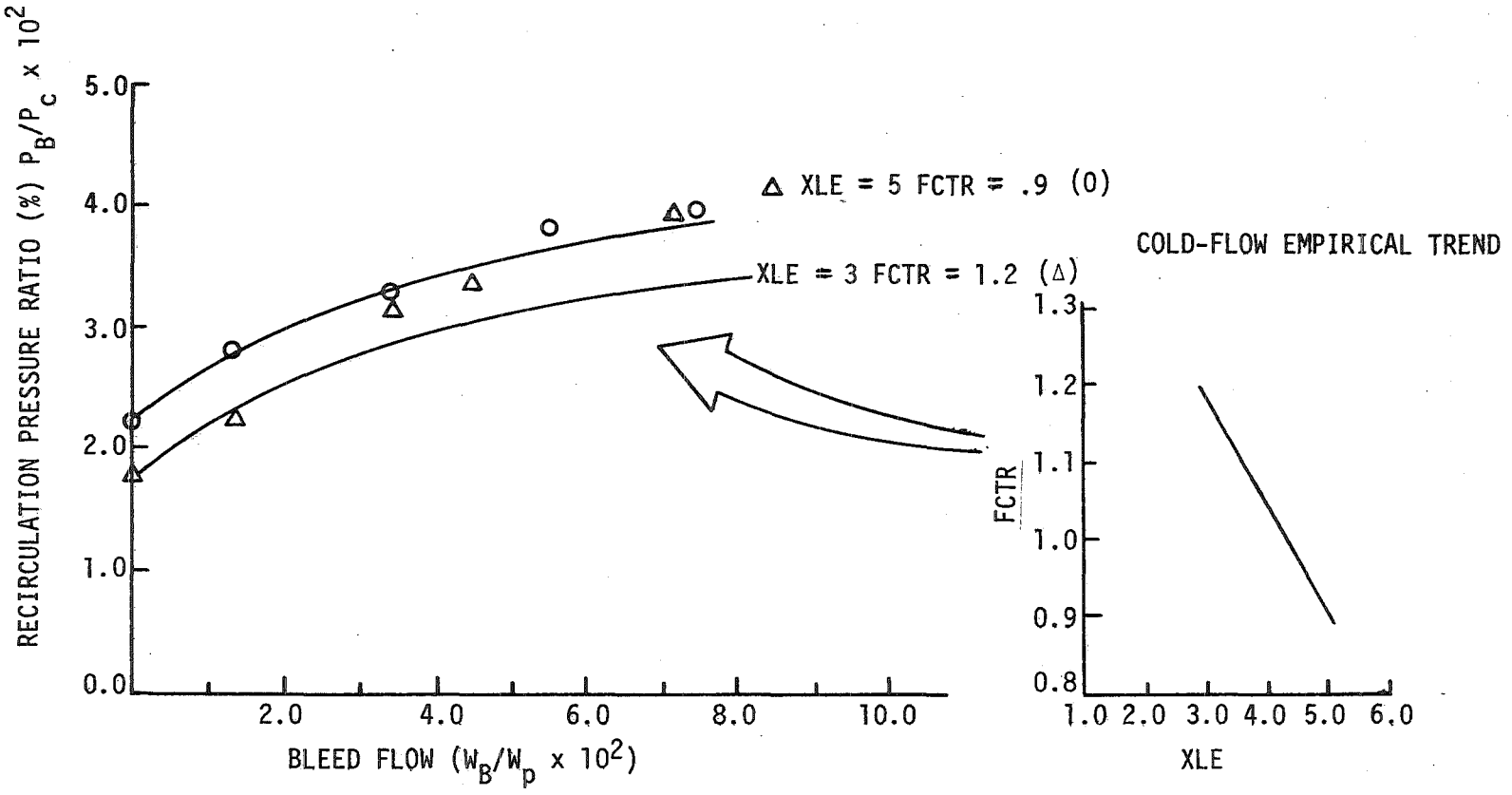

Figure VI-9. Hot-Fire Results Verified Nozzle Spacing Trends Correlated From Cold-Flow Tests

for zero bleed flow, the bleed flow model predicts exactly the recirculation pressure. Some inaccuracy does exist between the data and predictions at the larger bleed flows for small nozzle spacing. This may have resulted due to inaccuracies in the plume correlation. Another important point verified is that a noticeable decrease in bleed flow from that required for blowoff may result in a very small stagnation pressure loss from plume impingement.

3. Engine Performance

Two means of measurement were used to determine engine performance, characteristic velocity (C*), and specific impulse (Isp). Table VI-II presents the method used to determine these parameters. The format for determining specific impulse is the same as that used during previous cold-flow testing (Ref. 1).

Tests 1 through 7 used only the primary nozzle to check out the facility and determine combustion performance. The resulting C* efficiency proved to be very low (70-75%) probably due to the addition of film cooling holes in the outer ring of the primary injector. Testing with the dual throat configuration had similar low primary combustion performance, resulting in a correspondingly low Isp efficiency. As a result, this unusually large combustion inefficiency tended to mask the relatively smaller inefficiencies attributable to the dual throat configuration (i.e., boundary layer and divergence losses).

Nevertheless, the performance determined from the hot-fire test was correlated using the simplified prediction methodology. Estimates of the divergence, boundary layer, and kinetic efficiencies were used to define a perfect injector performance for the test configuration. This value was compared to the measured Isp for a typical test to "back out" an energy release efficiency as shown on

TABLE VI-II

HOT-FIRE TESTS PERFORMANCE MEASUREMENT

CHARACTERISTIC VELOCITY

- MEASURED FLOWRATES
- MEASURED PRIMARY P_C
- MEASURED PRIMARY D_t

$$C^*_{meas} = \frac{P_{c\ meas}\ A_t\ g_c}{\dot{W}_{T\ meas}}$$

$$\% C^* = \frac{C^*_{meas}}{C^*_{ODE\ \begin{matrix} MR\ Test \\ Pc\ Test \\ T_p\ Test \end{matrix}}}$$

SPECIFIC IMPULSE

- MEASURED FLOWRATES
- MEASURED STATIC PRESSURE PROFILE
- MEASURED PRIMARY CHAMBER PRESSURE

$$F_{vac} = P_{c\ meas} \times C_{F_{Primary}} \times A_{t_{Primary}} + \int_{Secondary\ Wall} pdA$$

$$I_{sp_{vac,meas}} = \frac{F_{vac}}{\dot{W}_{T\ meas}}$$

$$\% I_{sp} = \frac{I_{sp\ vac,\ meas}}{I_{sp\ ODE\ \begin{matrix} MR\ Test \\ Pc\ Test \\ T_p\ Test \end{matrix}}}$$

VI, B, Test Results (cont.)

Table VI-III. This method resulted in an indicated energy release efficiency of 76%, which is of the same magnitude as the characteristic velocity efficiency (73%). Therefore, while the hot-fire results cannot be used to provide Vernier calibration of the dual throat performance model, it appears that this measured result is consistent with the model and that the unusually low specific impulse is primarily the result of a low energy release (combustion) efficiency.

TABLE VI-III

PERFORMANCE COMPARISON OF HOT-FIRE TESTS/AERODYNAMIC MODEL

TEST 9 DATA			PERFORMANCE ANALYSIS	
Pc	=	456 psia		
MR	=	0.78	Isp_{ODE}, sec	401.8
% BLEED	=	7.5% (H_2)	η_{DIV}	.985
W_T	=	3.28 lbm/sec		
F_{vac}	=	1261 lbF	η_{KIN}	1.00
Isp_{vac}	=	295 sec	ΔIsp_{BLL}, sec	8.2
$C^*_{Primary}$	=	5570 ft/sec	$Isp_{Perfect\ Injector}$	387.6
% Isp	=	73	$Isp_{measured}$	295
% C*	=	73	η_{ERE}	.76

REFERENCES

1. Lundgreen, R.B., Nickerson, G.R., and O'Brien, C.J., "Dual Throat Thruster Cold Flow Analysis," ALRC Report 32666F, August 1978.

2. O'Brien, C.J., "Dual-Fuel Dual-Throat Engine Preliminary Analysis," Final Report, Contract NAS 8-32967, ALRC Report 32967F, August 1979.

3. Beichel, R., "The Dual-Expander Rocket Engine - Key to Economical Space Transportation," Astronautics and Aeronautics, November 1977.

4. Pieper, J.L., and Hurr, G.B., "Computer Program for Calculating RAO Optimum Nozzle Contours," ALRC Report 9600:M044, September 1971.

5. Nickerson, G.R., et al., "The Two-Dimensional Kinetic (TDK) Rocket Nozzle Analysis Reference Computer Program," prepared for NASA JSC, December 1973.

6. Cline, M.C., "VNAP: A Computer Program for Computation of Two-Dimensional, Time-Dependent Compressible, Viscous, Internal Flow," Los Alamos Scientific Laboratory Technical Report LA-7326, November 1978.

7. Chapman, D.R., "An Analysis of Base Pressure at Supersonic Velocities and Comparison with Experiment," NASA TN 2137, July 1950.

8. Korst, H.H., et al., "Research on Transonic and Supersonic Flow of a Real Fluid at Abrupt Increases in Cross Section," ME Technical Report 392-5, University of Illinois.

9. Bauer, R.C., "Characteristics of Axisymmetric and Two-Dimensional Isoenergetic Jet Mixing Zones," AEDC-TDR-63-253.

10. Bauer, R.C., "An Analysis of Two-Dimensional Laminar and Turbulent Compressible Mixing," AIAA Journal, Volume 4, No. 3, March 1966.

11. Chow, W.L. and Addy, A.L., "Interaction Between Primary and Secondary Streams of Supersonic Ejector Systems and Their Performance Characteristics," AIAA Journal, Volume 2, No. 4, pp. 686-695, April 1964.

12. Herron, R.D., "Jet-Boundary Simulation Parameters for Under-Expended Jets in Quiescent Atmosphere," AIAA Journal, Volume 5, No. 10, p. 1155, October 1968.

13. Murthy, S.N.B., et al., "Aerodynamics of Base Combustion," Progress in Astronautics and Aeronautics, Vol. 10, MIT Press, May 1974.

14. Nash, J.F., "An Analysis of Two-Dimensional Turbulent Base Flow Including the Effect of the Approaching Boundary Layer," Aere Report 1036, 1962, National Physical Lab., Aeronautical Research Council, London.

REFERENCES (cont.)

15. Davis, L.R., "Experimental and Theoretical Determination of Flow Properties in a Reacting Near Wake," AIAA Journal, Vol. 6, No. 5, pp. 843-847, May 1968.

16. Waldman, C.H. and Nickerson, G.R., "Literature Search Abstracts for Dual Nozzle Analysis," S.E.A. Inc. Report, 9 August 1979.

17. Fletcher, L.S., Briggs, D.G. and Page, R.H., "Heat-Transfer in Separated and Reattached Flows - An Annotated Review," Israel J. Tech., 12, pp. 236-261, 1974.

18. Rao, G.V.R., "Exhaust Nozzle Contour for Optimum Thrust," Jet Propulsion, pp. 377-382, June 1958.

19. Nickerson, G.R. and Kempf, D.M., "The Rao Method Optimum Nozzle Contour Program," TRW/Space Technology Laboratories, Memo No. 9552.21-29, 1 October 1964.

20. Mueller, T.J., "Determination of the Turbulent Base Pressure in Supersonic Axisymmetric Flow," AIAA Paper No. 67-446, July 1967.

21. Allman, J.G. and Hoffman, J.D., "Design of Maximum Thrust Nozzle Contours by Direct Optimization Methods," AIAA/SAE 14th Joint Propulsion Conference, Paper No. 78-1048, July 25-27, 1978.

22. Memo 9734:0868, C.V. Owen to C.J. O'Brien, 25 May 1977. Subject: Preliminary Regenerative Cooling Analyses for Tripropellant Engine.

23. Sergeant, R.J., "An Experimental Hot Rocket Model Investigation of a Plug Cluster Nozzle Propulsion System, Part I: Base Thermal and Pressure Environment for a Module Chamber Pressure of 300 psia and Simulated Altitudes to 150,000 feet," CAL No. HM-2045-Y-5(1), September 1967.

24. Rabinowicz, J., "Measurement of Turbulent Heat Transfer Rates on the Aft Portion and Blunt Base of a Hemisphere Cylinder in the Shock Tube," Jet Propulsion, Vol. 28, No. 9, pp. 615-620, 1958.

25. Bulmer, B.M., "Radial Base Heat-Transfer Gradients in Turbulent Flow," J. Spacecraft, Vol. 11, No. 11, pp. 798-800, 1974.

26. Rochelle, W.C. and Kooker, D.E., "Heat-Transfer and Pressure Analysis of Rocket Exhaust Impingement on Flat Plates and Curved Panels," J. Spacecraft, Vol. 6, No. 3, pp. 248-256, 1969.

27. Piesik, E.T., et al., "Rocket-Exhaust Impingement on a Flat Plate at High Vacuum," J. Spacecraft, Vol. 3, No. 11, pp. 1650-1657, 1966.

REFERENCES (cont.)

28. Maddox, A.R., "Impingement of Underexpanded Plumes on Adjacent Surfaces," J. Spacecraft, Vol. 5, No. 6, pp. 718-724, 1968.

29. Van Driest, E.R., "The Problem of Aerodynamic Heating," Aeronautical Engineering Review, Vol. 15, No. 10, pp. 26-41, 1956.

APPENDIX A

PROGRAM INPUT, AERODYNAMIC MODEL

PROGRAM INPUT, AERODYNAMIC MODEL

CARD 1:

The 1st card to be input is used to provide a printed heading for the computer output. Columns 2 through 72 are available for text. This card must always precede each case. The remainder of the input data is read using NAMELIST with the name $DATA, as described below.

$DATA

Geometry; Option 1, Cylindrical Secondary Wall, see Figure 1.

INPUT ITEM	DEFINITION
IWALL = 1,	The secondary nozzle wall is a cylinder
RS	r^*, radius of the secondary nozzle wall
RSP	r^*_p, radius of the primary nozzle
THETAP	θ_p, exit cone half angle, primary nozzle
EPSP	ϵ_p, expansion ratio of the primary nozzle

The items r^* and r^*_p, above, can be input with units of inches, feet, cm, etc. The input item ϵ_p, above, is used only to determine the Mach number at the exit of the primary nozzle (not required if MEPI is input).

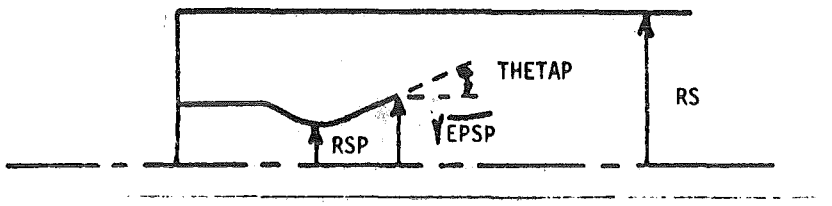

Figure 1. Nozzle Geometry for Option 1

Geometry; Option 2, Full Geometry Option, see Figure 2.

IWALL = 2,	Complete wall geometry specified for both primary and secondary nozzles
	Primary Nozzle
ECP	ϵ_{c_p}, primary nozzle chamber contraction ratio
RIP	R_{I_p}, wall radius connecting chamber and inlet of primary nozzle, divided by r^*_p
THIP	θ_{I_p}, inlet angle for primary nozzle
RWTUP	R_{u_p}, wall radius on upstream side of the throat, primary nozzle, divided by r^*_p
RSP	r^*_p, throat radius of primary nozzle, inches or cm
RWTDP	R_{d_p}, wall radius on downstream side of the throat, primary nozzle, divided by r^*_p
THETAP	θ°_p, exit cone half angle, primary nozzle
EPSP	ϵ_p, expansion ratio of the primary nozzle
	Secondary Nozzle
EC	ϵ_c, secondary nozzle contraction ratio
RI	R_I, wall radius connecting chamber and inlet of primary nozzle, divided by r*
THETAI	θ°_I, inlet angle for secondary nozzle
RWTU	R_u, wall radius on the upstream side of the throat, secondary nozzle, divided by r*
RS	r*, throat radius of secondary nozzle, inches or cm
RWTD	R_d, wall radius on downstream side of the throat, secondary nozzle, divided by r*
THETA	θ°, exit cone half angle, secondary nozzle
EPS	ϵ, expansion ratio of the secondary nozzle

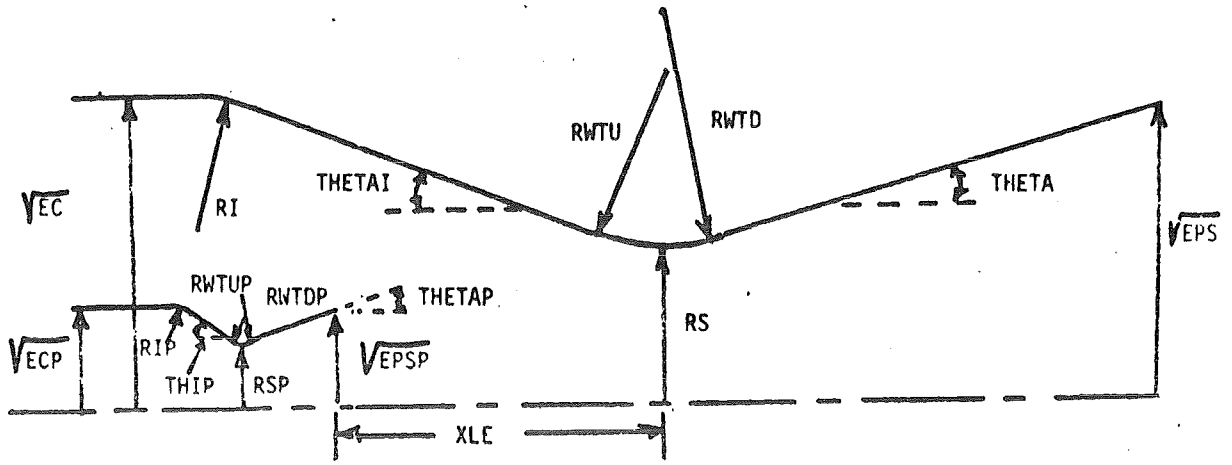

Figure 2. Nozzle Geometry for Option 2

Geometry; Options 3, 4 or 5. Full Geometry Option with Spline Fit Exhaust Contours

For the spline fit wall contour options, contour points are input to replace the conical exit cone of either the primary nozzle, secondary nozzle, or both. Other inputs are the same as in geometry Option 2, described above, except that the inputs for ϵ_p, and/or ϵ are not required. The exit cone half angle is interpreted as the spline contour attachment angle. The spline options are as follows:

	Primary Wall	Secondary Wall
IWALL = 3,	Spline	Cone
IWALL = 4,	Cone	Spline
IWALL = 5,	Spline	Spline

The spline coordinates are input as follows:

X4P(2)*	=	x_{p_i}, axial coordinates for primary wall spline contour
Y4P(2)	=	y_{p_i}, radial coordinates for secondary wall spline contour
N4P	=	n_p, i = 1, 2, ... n_p above. $n_p \leq 20$
TH4P	=	$\theta°_{ep}$, spline contour exit angle for primary nozzle, degrees
X4(2)	=	x_1, axial coordinates for secondary wall spline contour
Y4(2)	=	y_1, radial coordinates for primary wall spline contour
N4	=	n, 1, = 1, 2 ... n above. $N \leq 20$.
TH4	=	$\theta°_e$, spline contour exit angle for secondary nozzle, degrees

*The first point on a spline contour is automatically calculated by the program from the exit contour half angle, $\theta_p°$, or $\theta°$, thus each of these input vectors begins with item 2.

All x,y coordinate values are normalized (i.e. divided) by the corresponding nozzle throat radius.

Relative Positioning of Primary and Secondary Nozzles (IWALL > 2 Cases Only)

XLE — L_e/r^*_p, axial distance from the exit plane of the primary nozzle to the throat plane of the secondary nozzle, divided by r^*_p.

FLOW PROPERTIES AND OPTIONS

INPUT ITEM	DEFINITION	ASSUMED VALUE
FCTR	Factor for scaling plume shape. Used as a multiplier for the parameter M_b/γ in the Herron method.	1.
IPNCH	If IPNCH = 1, geometry inputs for TDK will be punched in the NAMELIST format . If IPNCH = 0, no punched output, only printed output.	0
MEPI	M_{e_p} . (REAL type) exit Mach No., primary nozzle. If M_{E_p} <1 then values will be calculated from ϵ_p assuming one-dimensional flow	0
NW	n_w, number of entries in WSWP $n_w \leq 50$	13
PBPO	Initial guess for the pressure ratio for the plume boundary. If not input, the program will calculate a value corresponding to the area of the secondary nozzle throat divided by the area of the primary nozzle throat using the relationship for one-dimensional flow.	
WLPRN	If a value other than zero is input, print of the secondary and primary nozzle wall tables will be suppressed (to be used on successive cases when the wall geometry does not change.)	0.
WSWP (1)	$(\dot{W}_s/\dot{W}_p)_i$ * 100, percent bleed flow given for these values, i = 1, --, n_w for which base pressure and recirculation temperature and primary mass fraction in the recirculation region , are solved.	0,1,2,3,4,5, 6,7,8,9,10, 12,15

INPUT ITEM		DEFINITION	SUGGESTED VALUE
TRTO	T_r/T_o	Recirculation temperature ratio initial guess NOTE: TRTO is between TOBASE & 1.0	1.0
TOBASE	T_{ob}/T_o	Stagnation temperature ratio of bleed flow (secondary flow) to primary flow	
DELV		Perturbation fraction for Newton solution procedure	.0001
DELVMX		Maximum fractional change of P_b/P_o and T_r/T_o during solution	.3
EPSGGT		Convergence criteria for bleed flow W_s/W_p	.0004
EPSTOB		Convergence criteria for T_{ob}/T_o	.0004
ITERPR		Iteration print option, set equal to 1 for print	0
ITERMX		Max # of iterations	20
CKN		Nash Factor $\hat{N}$	.4
LPBPO	Logical Variable	Find Flow-off Base Pressure (PBPOBF) if true	True
LPLØT	Logical Variable	Draw Plots if true	False
XMINPL		Minimum axial coordinate for plot axis	
XMAXPL		Maximum axial corrdinate for plot axis	
XDISPL		Length of axis (for axial coordinate)	
YMINPL		Minimum radial coordinate for plot axis	
YMAXPL		Maximum radial coordinate for plot axis	
YDISPL		Length of axis (for radial coordinate)	
PBPOBF		Blow-off Base pressure to provide a limit during iteration or initial guess for finding blow-off pressure if LPBPO = .TRUE. (Note: This is then stored in PBPO).	.01

INPUT ITEM	DEFINITION	SUGGESTED VALUE
GGTBF	Blow-off Secondary Mass flow (percent) to provide a limit during iteration. (This is automatically set if LPBPO = .TRUE.)	
CPF	Heat capacity (constant pressure) of primary mass flow	
CPØ	Heat capacity (constant pressure) of secondary mass flow	
MWF	Molecular weight primary mass flow	
MWØ	Molecular weight secondary mass flow	
ITYFR	# of iterations to be taken on mass flow fraction during each base pass.	2
YFRX	Primary mass flow fraction in recirculation region first estimate for YFR.	.5

EXTENDED NOZZLE WALL OPTION

Given an input nozzle wall contour, this option will calculate an extended nozzle wall contour that gives maximum thrust. This is accomplished by first calculating the flow field that is dependent on the given input nozzle wall contour, i.e. the downstream boundary of the flow field is the right running characteristic extending from the nozzle lip to the flow axis. Shocks are ignored. Next, a circular arc of radius R_d is attached tangent to the nozzle lip. The optimization options existing in the program are then used to calculate the maximum thrust wall contour. The following additional input items are required.

IWLØPT = 1 for the extended wall option. The program assumes IWLØPT = 0.

RD = wall radius ratio (R/R_t) of the circular arc, Rd, attached tangent to the nozzle lip.

NOZZLE GEOMETRY

The items RWTU, RWTD, and RSTAR are as previously defined, but apply to the input nozzle wall contour. See Figures 1a,b,c, and d for wall contour options.

IWALL = wall option flag. The value assigned this item determines the type of wall to be specified.

- 0 => arbitrary contour
- 1 => cone; θ, ϵ
- 2 => parabolic contour
- 3 => circular arc contour
- 4 => spline fit contour
- 5 => cone; r_n, x_n

If IWALL = 0 (arbitrary contour)

PW(1) = The wall coordinate points r_1, x_1, are to be input sequentially:

PW(1) = r_1, x_1, r_2, x_2, . . .
. . . r_n, x_n, 0., 0.,

a pair of zero coordinates marks the end of the table. A value of $n \leq 300$ is required. This table is normalized to the throat radius and the origin is at the throat so that necessarily $r_1 = 1$, $x_1 = 0$.

If IWALL = 1 (cone; θ, ϵ)

RWTD = as above.

THJI = exit cone half angle (degrees).

EPS = expansion ratio

If IWALL = 2 or 3 (parabolic contour or circular arc contour)

RWTD = as above

THJI = wall inflection angle (degrees)

RWMAX = nozzle end point radial coordinate, r_n

ZWMAX = nozzle end point axial coordinate, x_n

If IWALL = 4 (spline fit contour)

As in IWALL options 1,2, and 3 the program assumes the throat to begin with a circular arc downstream of the minimum point. The final point on this circular arc is located at an inclination of THJI degrees. The contour exit angle, THE degrees, must also be input. The contour to be spline fit between THJI and THE must be input in tabular form. The first point on the spline fit is automatically located by the program on the circular arc at the point of inclination THJI.

RWTD = As above

THJI = RWTD and the angle THJI define the end point of the circular arc and the beginning of the spline fit (degrees)

NRZS = n, the number of points to be spline fit. $n \leq 40$ is required.

PWRS(2) = radial wall coordinated to be spline fit.

PWRS(2) = $r_2, r_3, \ldots, r_n$

PWZS(2)	=	axial wall coordinates to be spline fit. PWZS(2) = x_2, x_3, . . . , x_n
THE	=	nozzle exit angle
If IWALL = 5		(cone; r_n, x_n)
RWTD	=	As above
RWMAX	=	As above
ZWMAX	=	As above

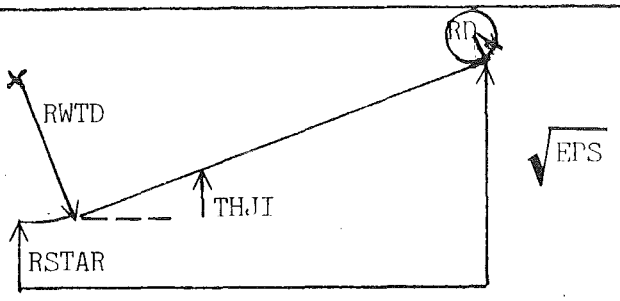

Figure 1a: IWALL = 1 geometry; cone

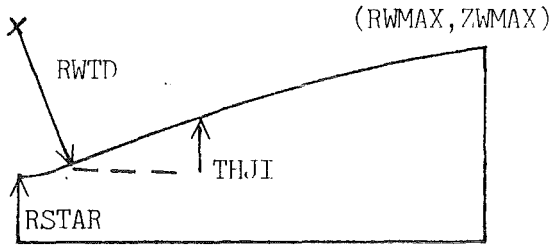

Figure 1b: IWALL = 2 or 3 geometry; parabola or arc

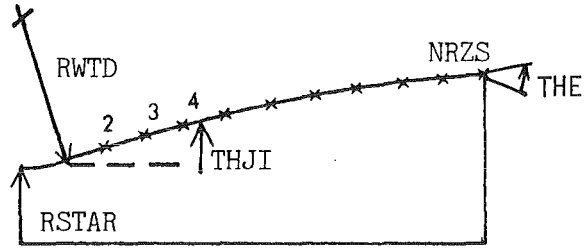

Figure 1c: IWALL = 4 geometry; spline points, x, located at (PWRS,PWZS)

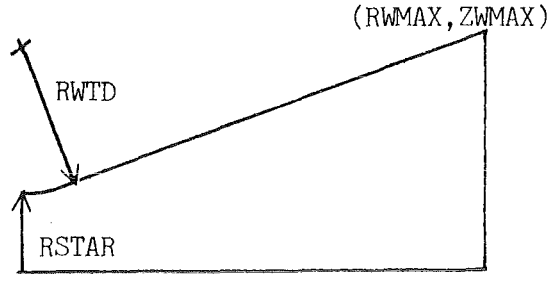

Figure 1d: IWALL = 5 geometry; cone

APPENDIX B

DERIVATION OF DUAL EXPANDER EQUATIONS

DERIVATION OF AREA EQUATION

$$A = 2\pi \delta R$$

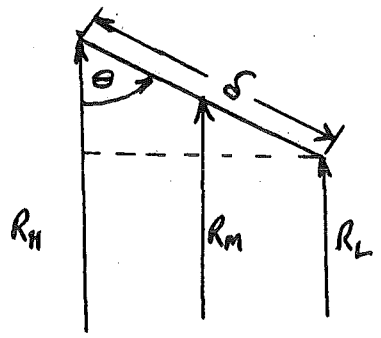

R_H = Outer Radius

R_L = Inner Radius

R_M = Radius @ Mid Point

δ = Gap

Θ = Angle Gap Inclined

$$\delta = \frac{R_H - R_L}{\cos \Theta} = (R_H - R_L) \sec \Theta$$

The projected area of the annulus can be found by

$$A_p = \pi (R_H^2 - R_L^2)$$

The annulus area is then

$$A = \frac{A_p}{\cos \Theta}$$

$$A = \frac{\pi (R_H^2 - R_L^2)}{\cos \Theta} = \frac{\pi (R_H - R_L)(R_H + R_L)}{\cos \Theta}$$

$$R_M = \frac{R_H + R_L}{2}$$

$$R_H - R_L = \delta \cos \Theta$$

Substitute:

$$A = \frac{\pi(\delta \cos \Theta)\, 2 R_M}{\cos \Theta}$$

$$\boxed{A = 2\pi \delta R_M}$$

DERIVATION OF INCLINATION ANGLE EQUATION

$$\cos \Theta_s = 2 \frac{[R_{E_c} - R_{E_p} - D_L \cos \Theta_L]}{\delta_{E_c}}$$

From Figure B-1

$$A_{E_c} = \frac{\pi[r^2_{E_H} - r^2_{E_L}]}{\cos \Theta_s}$$

$$\frac{r_{E_H} + r_{E_L}}{2} = R_{E_c} \Rightarrow r_{E_H} = 2 R_{E_c} - r_{E_L}$$

$$r_{E_L} = R_{E_p} + D_L \cos \Theta_L$$

$$r_{E_H} = 2 R_{E_c} - (R_{E_p} + D_L \cos \Theta_L)$$

$$A_{E_c} = \frac{\pi}{\cos \Theta_s} [(2 R_{E_c} - R_{E_p} - D_L \cos \Theta_L)^2 - (R_{E_p} + D_L \cos \Theta_L)^2]$$

Multiplying out and cancelling terms results

$$A_{E_c} = \frac{\pi}{\cos \Theta_s} [4 R^2_{E_c} - 4 R_{E_c} R_{E_p} - 4 R_{E_c} D_L \cos \Theta_L]$$

$$= \frac{4 \pi R_{E_c}}{\cos \Theta_s} [R_{E_c} - R_{E_p} - D_L \cos \Theta_L]$$

$$\cos \Theta_s = \frac{4 \pi R_{E_c}}{A_{E_c}} [R_{E_c} - R_{E_p} - D_L \cos \Theta_L]$$

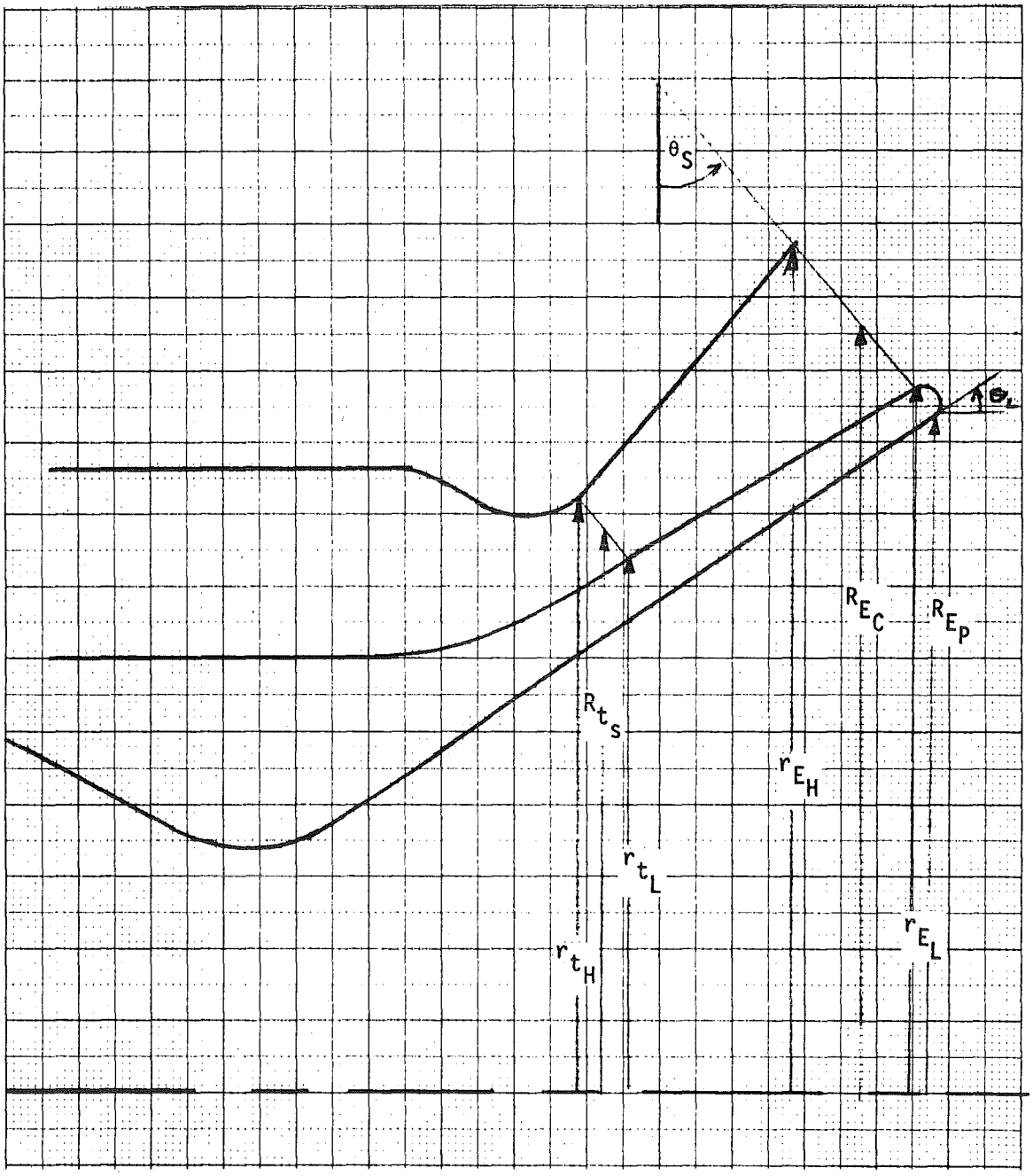

Figure B-1

Substitute:

$$\frac{2\pi R_{E_c}}{A_{E_c}} = \frac{1}{\delta_{E_c}}$$

$$\boxed{\cos\Theta_s = \frac{2\,(R_{E_c} - R_{E_p} - D_L \cos\Theta_L)}{\delta_{E_c}}}$$

DERIVATION OF THROAT RADIUS EQUATION

$$R_{t_s}^2 \left[2 \sec\Theta_s \left(1 - \frac{\sin\Theta_L}{\sin\Theta_s \cos\Theta_c}\right)\right] - R_{t_s}\left[2 \sec\Theta_s \left(R_{E_p} + D_L \cos\Theta_L - \frac{R_{E_c} \sin\Theta_L}{\sin\Theta_s \cos\Theta_c}\right)\right]$$

$$- \frac{A_{t_s}}{2\pi} = 0$$

Start with the relationship from Figure B-1

$$\delta_{t_s} = \frac{r_{t_H} - r_{t_L}}{\cos\Theta_s} \qquad \text{and} \qquad r_{t_H} = 2\,R_{t_s} - r_{t_L}$$

$$\delta_{t_s} = \frac{2\,(R_{t_s} - r_{t_L})}{\cos\Theta_s}$$

From Figure B-2

$$\left.\begin{aligned} r_{t_L} &= r_{E_L} - X_w \sin\Theta_L \\ \frac{X_c}{X_w} &= \cos\Theta_c \end{aligned}\right\} \Rightarrow \quad r_{t_L} = r_{E_L} - \frac{X_c}{\cos\Theta_c} \sin\Theta_L$$

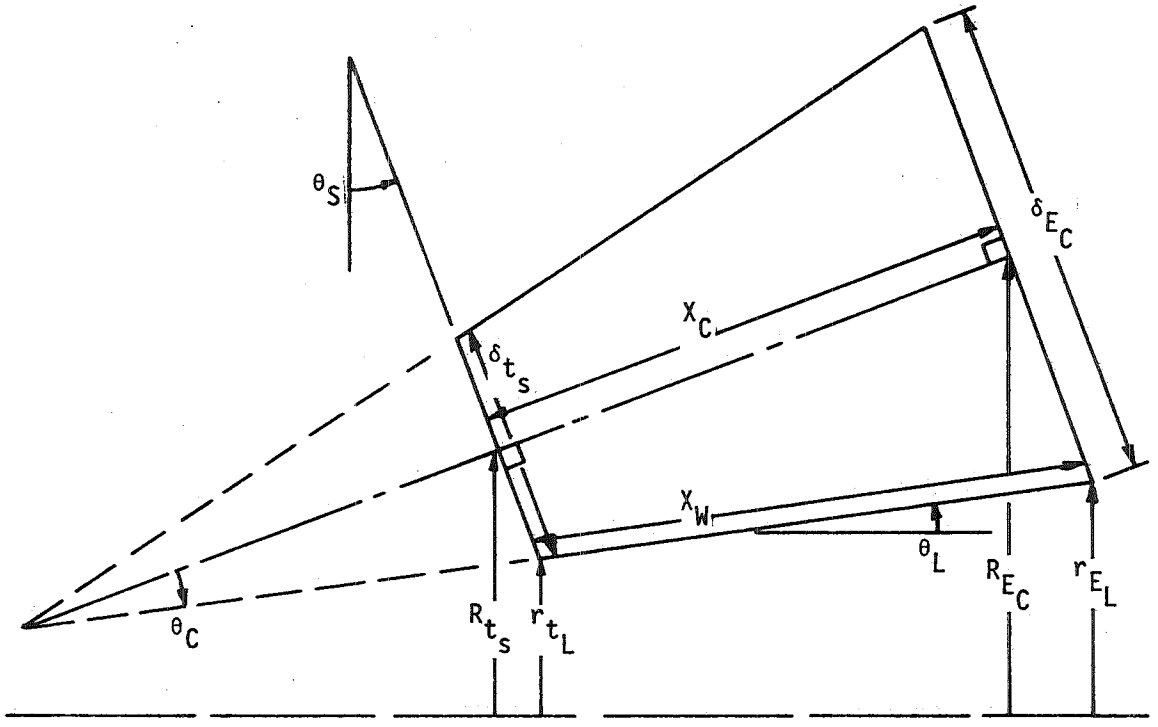

Figure B-2

From Figure B-1

$$r_{E_L} = R_{E_p} + D_L \cos \Theta_L$$

$$r_{t_L} = R_{E_p} + D_L \cos \Theta_L - \frac{X_c \sin \Theta_L}{\cos \Theta_c}$$

Substituting the above into the equation for δ_{t_s}

$$\delta_{t_s} = 2 \left[R_{t_s} - R_{E_p} - D_L \cos \Theta_L + \frac{X_c \sin \Theta_L}{\cos \Theta_c} \right] \sec \Theta_s$$

Also from Figure B-2 it can be seen

$$X_c = \frac{R_{E_c} - R_{t_s}}{\sin \Theta_s}$$

$$\delta_{t_s} = 2 \sec \Theta_s \left[R_{t_s} - R_{E_p} - D_L \cos \Theta_L + \frac{R_{E_c} - R_{t_s}}{\sin \Theta_s} \frac{\sin \Theta_L}{\cos \Theta_c} \right]$$

$$= 2 \sec \Theta_s \left[R_{t_s} \left(1 - \frac{\sin \Theta_L}{\sin \Theta_s \cos \Theta_c} \right) - R_{E_p} - D_L \cos \Theta_L + \frac{R_{E_c} \sin \Theta_L}{\sin_s \cos \Theta_c} \right]$$

$$= R_{t_s} \left[2 \sec \Theta_s \left(1 - \frac{\sin \Theta_L}{\sin \Theta_s \cos \Theta_c} \right) \right] - 2 \sec \Theta_s \left[R_{E_p} + D_L \cos \Theta_L - \frac{R_{E_c} \sin \Theta_L}{\sin_s \cos \Theta_c} \right]$$

Now going back to the area relationship:

$$\delta_{t_s} = \frac{A_{t_s}}{2 \pi R_{t_s}}$$

$$\frac{A_{t_s}}{2\pi R_{t_s}} = R_{t_s}\left[2 \sec \Theta_s \left(1 - \frac{\sin \Theta_L}{\sin \Theta_s \cos \Theta_c}\right)\right] - 2 \sec \Theta_s \left[R_{E_p} + D_L \cos \Theta_L - \frac{R_{E_c} \sin \Theta_L}{\sin \Theta_s \cos \Theta_c}\right]$$

Rearrange to form

$$R_{t_s}^2\left[2 \sec \Theta_s \left(1 - \frac{\sin \Theta_L}{\sin \Theta_s \cos \Theta_c}\right)\right] - R_{t_s}\left[2 \sec \Theta_s \left(R_{E_p} + D_L \cos \Theta_L - \frac{R_{E_c} \sin \Theta_L}{\sin \Theta_s \cos \Theta_c}\right)\right] - \frac{A_{t_s}}{2\pi}$$

$$= 0$$

AREA RATIO RELATIONSHIPS FOR DUAL EXPANDER

MODE I:

Primary flow streamtube area ratio (ε_{P_I})

$$\varepsilon_{P_I} = \frac{A_{E_{P_I}}}{A_{tp}}$$

Secondary flow streamtube area ratio (ε_{S_I})

$$\varepsilon_{S_I} = \frac{A_{E_{S_I}}}{A_{ts}}$$

Overall engine area ratio (ε)

$$\varepsilon = \frac{A_E}{A_{tp} + A_{ts}} = \frac{A_{E_{P_I}} + A_{E_{S_I}}}{A_{tp} + A_{ts}}$$

$$= \frac{\frac{A_{E_{P_I}}}{A_{tp}} A_{tp} + \frac{A_{E_S}}{A_{ts}} A_{ts}}{A_{tp} + A_{ts}} = \frac{\varepsilon_{P_I} A_{tp} + \varepsilon_{SI} A_{ts}}{A_{tp} + A_{ts}}$$

$$= \frac{\left(\varepsilon_{P_I} \frac{A_{tp}}{A_{ts}} + \varepsilon_s\right) A_{ts}}{\left(\frac{A_{tp}}{A_{ts}} + 1\right) A_{ts}}$$

$$\boxed{\varepsilon = \frac{\varepsilon_{P_I} \frac{A_{tp}}{A_{ts}} + \varepsilon_{S_I}}{\left(\frac{A_{tp}}{A_{ts}} + 1\right)}}$$

MODE II:

Secondary nozzle area ratio ($\varepsilon_{S_{II}}$)

$$\varepsilon_{s_{II}} = \frac{A_E}{A_{ts}} = \frac{A_{E_{P_I}} + A_{E_{S_I}}}{A_{ts}}$$

$$= \frac{A_{E_{P_I}}}{A_{tp}} \frac{A_{tp}}{A_{ts}} + \frac{A_{E_{S_I}}}{A_{ts}}$$

$$\boxed{\varepsilon_{s_{II}} = \varepsilon_{P_I} \frac{A_{tp}}{A_{ts}} + \varepsilon_{s_I}}$$

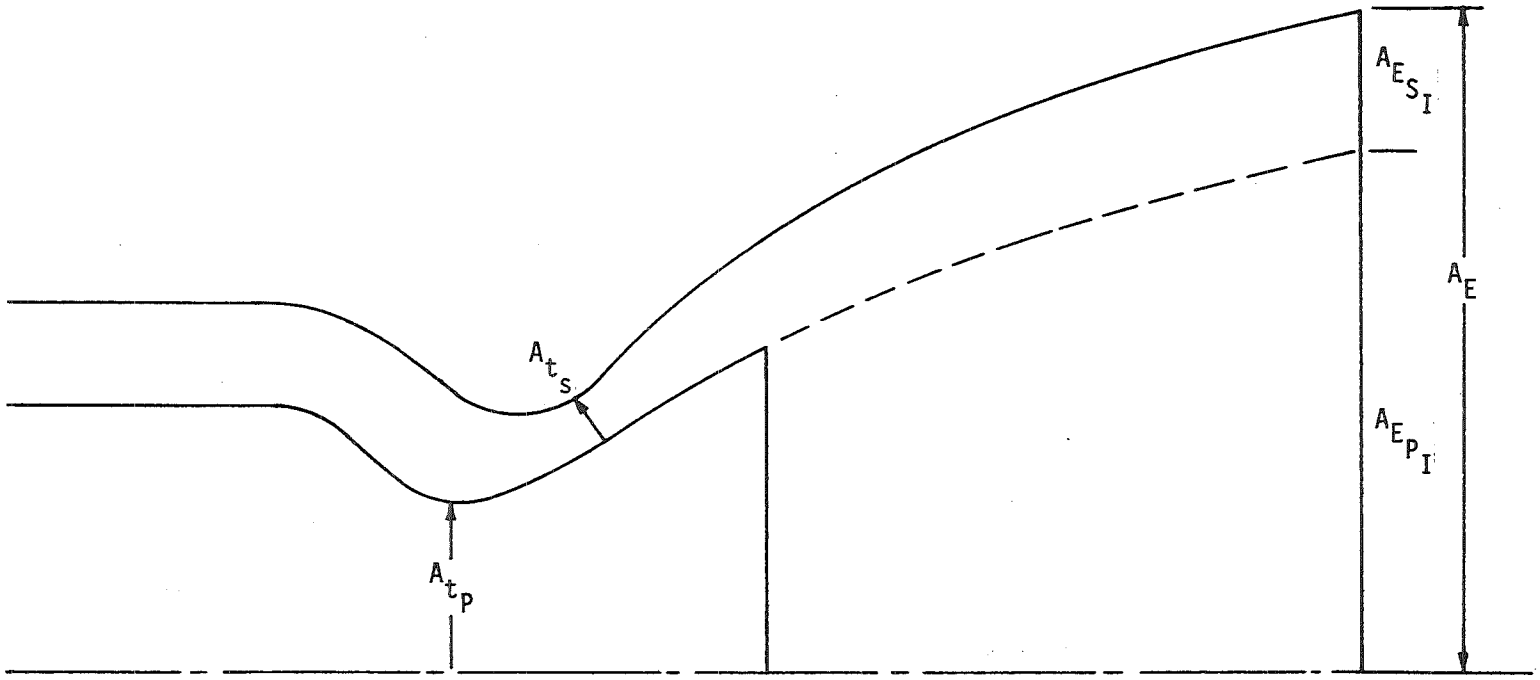

Figure B-3

APPENDIX C

INPUT DESCRIPTION, DUAL EXPANDER SHEAR LAYER MODEL

INPUT DESCRIPTION

DUAL EXPANDER SHEAR LAYER MODEL

The purpose of this computer program is to calculate the base pressure that will occur when a uniform supersonic flow expands around the corner of a bluff body. An example is shown in Figure 1, which corresponds to the Dual Expander engine during Mode II operation.

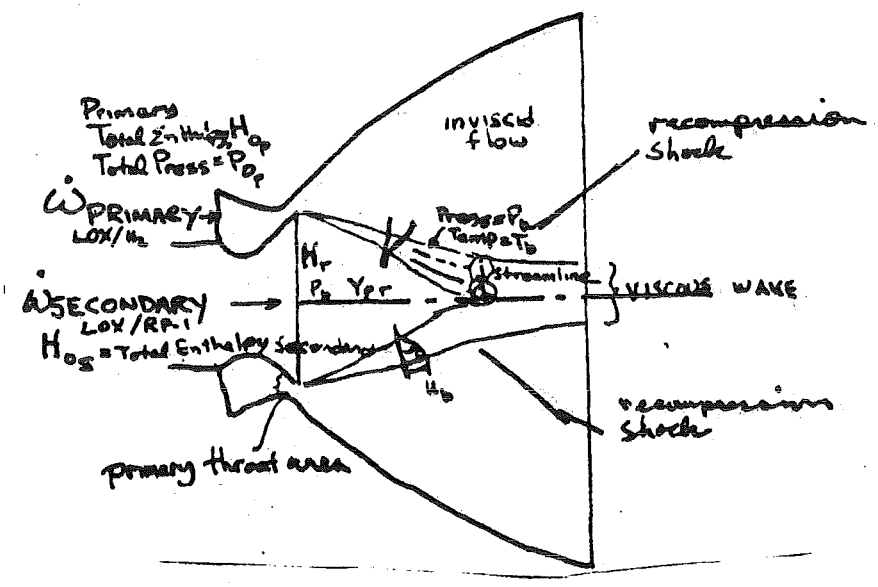

Figure 1. Dual Expander Engine

The method of Korst is used to predict the base pressure. The method applies only to flows that are not fully separated. The shear layer must approach the flow axis and be turned at the so called "neck region". The program allows a bleed flow to be specified, provided this secondary flow is not so great that the flow becomes fully separated. The program allows the molecular weight, specific heat, and total

enthalpy of the secondary stream (bleed) to be different than that of the primary stream. The method of using this program is described below.

Solutions can be obtained for the following situations:

1) zero bleed flow,
2) bleed flow with properties identical to the properties of the primary stream,
3) bleed flow with properties different than the properties of the primary stream.

Case 3), above, is the general case solved by the program and requires the determination of three unknown variables (P_b/P_{op}, H_r/H_{op}, Y_{pr}) of three unknown variables such that three functional constraints are satisfied. Cases 1) and 2), above, are special cases of case 3) and require the determination of only one variable (P_b/P_{op}) such that one function is satisfied. In all three cases, initial estimates of the unknown variables must be supplied. These estimated values must lie within the radius of convergence Newton's method. Estimates can be obtained from solutions previously found. Each run on the computer will use its final values as the first estimate for the succeeding case. This allows parametric studies to be run efficiently by the systematically changing of input.

The program also uses bounds for the unknown variables so as to enhance convergence of the numerical method. Variables H_r/H_{op} and Y_{pr} are automatically bounded by the program and have caused no difficulties thus far. The variable P_b/P_{op}, however, requires carefull consideration. A satisfactory lower bound, 10^{-5}, is assumed; but the upper bound, (P_b/P_{ob}) max, must be input by the uses as described in the following steps.

Step 1) Using γ_p and the approach flow Mach No., M_p, look up the Prandtl- Meyer angle, ν_p, in the Gas Tables.

Step 2) Calculate the Prandtl-Meyer angle, ν, that will turn the flow parallel to the axis by adding the approach flow angle to ν_p, i. e.,

$$\nu = \nu_p + \Theta_b$$

Step 3) Look up the flow pressure ratio for parallel flow, P/P_o, corresponding to ν. (P_b/P_{op}) max must be less than this value, i.e.,

$$(P_b/P_{op}) \text{ max} = .95\ (P/P_o)$$

A good estimate for the base pressure ratio is:

$$P_b/P_{op} = .5\ (P/P_o)$$

One card is read and printed to label the program output. This card is followed by the NAMELIST input data set described below, followed by a listing of cards for a sample case.

NAMELIST NAME	EXPLANATION AND COMMENTS	UNITS	DEFAULT VALUE
$DUALEX			
CPS =	C_{p_s}, Specific heat at constant pressure for the secondary (bleed) flow.	cal/gm ^{o}K	-
CPP =	C_{p_p}, Specific heat at constant pressure for the primary flow.	cal/gm ^{o}K	-
AMWS =	M_{w_s}, Molecular weight for the secondary (bleed) flow.	-	-
AMWP =	M_{w_p}, Molecular weight for the primary flow.	-	-
HØS =	H_{o_s}, Total enthalpy for the secondary (bleed) flow. $H_{o_s} = C_{p_s} T_{o_s}$	cal/gm	-
HØP =	H_{o_p}, Total enthalpy for the primary flow. $H_{o_p} = C_{p_p} T_{o_p}$	cal/gm	-
PØP =	P_{o_p}, Total pressure for the primary flow.	psia	-
WSWP =	$\dot{W}_s/\dot{W}_p$, Ratio of the mass flow rate of the secondary (bleed) flow to the mass flow rate of the primary flow	none	-
SRB =	r_b, Radius of base	inches (or cm)	-
RWRB =	r_w/r_b, Wake radius ratio	none	.5
AREA =	The throat area of the primary stream	in^2 (or cm^2)	$1/\pi$
THETAB =	θ_b, Approach flow angle, i.e. lip angle of the lower wall of the annular nozzle.	degrees	-
AMP =	Mp, Mach No. of the primary flow	none	-

NAMELIST NAME	EXPLANATION AND COMMENTS	UNITS	DEFAULT VALUE
PBPØP1 =	P_b/P_{o_p}, 1st estimate for the ratio of base pressure to the total pressure of the primary flow.	none	-
PMAX =	(P_b/P_{o_p})max, upper bound for P_b/P_{o_p}. Use procedure previously described to calculate this value.	none	1.
HRHØP1	H_r/H_{o_p}, 1st estimate for the ratio of the enthalpy of the gas in the base recirculation region to the total enthalpy of the primary flow.	none	1.
YPR1 =	Y_{p_r}, Mass fraction of bleed flow gas contained in the base recirculation region.	none	1.
AN =	N, Nash factor	none	.4
GCØN =	Convergence criteria for $\bar{\gamma}_d$	none	.001
EJCNV =	Convergence criteria for η_j	none	.0002
WF(1) =	Wi, weighting factors used in testing the convergence of the varables sought by Newton's method.	none	3*1.
EPSI =	Convergence criteria for Newton's method. Convergence occurs when $\sum_{i=1}^{n} (WiFi)^2 < EPSI$	-	10^{-12}
NUN =	n, number of varables to be determined. If n=3, then P_b/P_{o_p}, H_r/H_{o_p}, and Y_{p_r} will be determined. If n=1, then P_b/P_{o_p} will be determined. Always set $H_r/H_{o_p} = 1$, $Y_{p_r} = 1$	-	
PERTV =	Perterbation factor for calculating partial derivitives for Newton's method (see write-up of subroutine NEWT)	-	.02

NAMELIST NAME	EXPLANATION AND COMMENTS	UNITS	DEFAULT VALUE
SK =	k, proportionality factor relating shear layer velocity thickness, δ, to the wake radius ratio, r_w/r_b. The program has been calibrated versus data for air without bleed flow and it was found that $k \doteq 4$, i.e. it is assumed that $r_w/r_b = k\,(x/r_b)/\sigma$ where x/r_b is the non-dimensional shear layer length; σ is the jet spreading parameter. $\sigma = 12 + 2.758M_b$	none	4.
IDBUG	Flag for debuging print-out If IDBUG = 0, no debug print If IDBUG = 1, print debug output	-	0
MAXIT =	Maximum number of iterations allowed for Newton's method.	-	10
MAXITP =	Maximum number of iterations allowed in calculating $\bar{\gamma}_d$	-	25
MAXITE =	Maximum number of iterations allowed in calculating η_j	-	25
LAST =	Flag to avoid error message that results from reading end of file for input. For the last case to be run, set LAST = 1	-	0
$END			

TABLE 1, CARD LISTING FOR A SAMPLE CASE

```
 ** CALIBRATION CASE ** GAMMA=1.4          AIR
$DUALEX
CPS=.2396897,CPP=.2396897,  AMWS=29.,AMWP=29.,
HOS=1.,HOP=1.,POP=1.,
SRB=1.,
THETAB=0.,
AMP=2.3,
AN=1.,
WSWP=0.,
PMAX=.079,PBPOP1=.04,
NUN=1,
AN=.4,
LAST=1,
$END
```

FINAL REPORT DISTRIBUTION LIST

DUAL NOZZLE AERODYNAMIC AND COOLING ANALYSIS

CONTRACT NAS 8-33553

NAME	COPIES
National Aeronautics and Space Administration	
George C. Marshall Space Flight Center Marshall Space Flight Center, AL 35812	
Attn: Administrative Services / AS24D	3
Technology Utilization Office / AT01	1
Associate Director for Management / EM12-34	1
J. L. Sanders / PD13	1
F. W. Braam / EP24	10
Lewis Research Center 21000 Brookpark Road Cleveland, Ohio 44135	
Attn: Library	1
R. Priem / 501-6	1
NASA Headquarters Washington, D.C. 20546	
Attn: F. W. Stephenson / RP	1
Goddard Space Flight Center Greenbelt, Maryland 20771	
Attn: Library	1
John F. Kennedy Space Center Cocoa Beach, Florida 32931	
Attn: Library	1
Lyndon B. Johnson Space Center Houston, Texas 77058	
Attn: Library	1
Langley Research Center Langely Station Hampton, Virginia 23365	
Attn: Library	1
Jet Propulsion Laboratory 4800 Oak Grove Drive Pasadena, CA 91103	
Attn: Library	1
Defense Documentation Center Cameron Station Building 5 5010 Duke Street Alexandria, VA 22314	
Attn: TISIA	2
NASA Scientific Technical Information Facility P.O. Box 8757 Baltimore-Washington International Airport Baltimore, MD 21240	
Attn: Accessioning Dept.	5
U.S. Army Missile Command Redstone Scientific Information Center Redstone Arsenal, AL 35808	
Attn: Document Selection	3
Air Force Rocket Propulsion Laboratory Edwards, CA 93523	
Attn: Library	1
Arnold Engineering Development Center Air Force Systems Command Tullahoma, IN 37388	
Attn: Library	1

NAME	COPIES
Rocketdyne Division of Rockwell International 6633 Canoga Avenue Canoga Park, CA 91304	
Attn: Library	1
Pratt and Whitney Aircraft Group Government Products Division United Technologies Corporation West Palm Beach, FL 33402	
Attn: Library	1
Bell Aerosystems, Inc. Box 1 Buffalo, NY 14240	
Attn: Library	1
Boeing Company Space Division P.O. Box 868 Seattle, WA 98124	
Attn: Library	1
Aerospace Corporation 2350 E. El Segundo Blvd. Los Angeles, CA 90045	
Attn: Library	1
Lockheed Missile and Space Company 1111 Lockheed Way Sunnyvale, CA 94088	
Attn: Library	1
Marquardt Corporation 16555 Saticoy Street Box 2013 South Annex Van Nuys, CA 91409	
Attn: Library	1
Martin-Marietta Aerospace P.O. Box 179 Denver, CO 80201	
Attn: Library	1
McDonnell Douglas Astronautics 5301 Bolsa Avenue Huntington Beach, CA 92647	
Attn: Library	1
Space Division Rockwell International Corporation 12214 Lakewood Blvd. Downey, CA 90241	
Attn: Library	1
Grumman Aerospace Corporation Bethpage, NY 11714	
Attn: Library	1
General Dynamics/Convair P.O. Box 1128 San Diego, CA 92112	
Attn: Library	1
Northrop Corporation 1800 Century Park East Century City, CA 90067	
Attn: Library	1